

Measurement of Z^0 Lepton Coupling Asymmetries *

Michael Burghard Smy
Stanford Linear Accelerator Center
Stanford University
Stanford, CA 94309

SLAC-Report-515
July 1997

Prepared for the Department of Energy
under contract number DE-AC03-76SF00515

Printed in the United States of America. Available from the National Technical Information Service, U.S. Department of Commerce, 5285 Port Royal Road, Springfield, VA 22161.

* Ph.D. thesis, Colorado State University, Fort Collins, Colorado

ABSTRACT OF DISSERTATION

MEASUREMENT OF Z^0 LEPTON COUPLING ASYMMETRIES

Polarized Z^0 's from e^+e^- collisions at the SLAC Linear Collider (SLC) have been used to determine the asymmetry parameters A_e , A_μ and A_τ from the leptonic decay channels. This is the first direct measurement of A_μ . The data have been gathered by the SLC Large Detector (SLD) with the electron polarization averaging 63% during the 1993 data taking period and 77% in 1994-95. A maximum likelihood procedure as well as cross section asymmetries was used to measure the asymmetry parameters from the differential cross sections for equal luminosities of left- and right-handed electron beams. The polarization-dependent muon-pair angular distributions give $A_\mu = 0.102 \pm 0.034$ and the tau-pairs give $A_\tau = 0.195 \pm 0.034$. The initial state electronic couplings in all three leptonic channels as well as the final state angular distribution in the e^+e^- final state measure A_e to be $A_e = 0.152 \pm 0.012$. Assuming lepton universality and defining a global leptonic asymmetry parameter $A_{e-\mu-\tau}$, the measurements yield $A_{e-\mu-\tau} = 0.151 \pm 0.011$. This global leptonic asymmetry value translates directly into $\sin^2 \theta_W^{\text{eff}} = 0.2310 \pm 0.0014$.

Acknowledgments

I wish to thank God for creating a universe with sufficient order to make it intelligible, and for equipping me with a mind powerful enough to catch a glimpse of that order.

I would also like to thank my parents, Alexander and Gudrun, my fiancée Elizabeth, and my sister Heike for their unceasing support and encouragement.

I also thank Dr. H. D. Hochheimer for his support of German exchange students in the Physics Department of Colorado State University.

Furthermore, I am indebted to the High Energy Physics group at Colorado State University, especially to my advisors Dr. John Harton and Dr. Robert Wilson.

Last but not least, I thank the SLD Collaboration, in particular the Tau Group, the Electroweak Physics Group, the Heavy-Flavor Group and the VXD3 Group, as well as the SLC physicists, operators and technical staff.

This work was supported in part by grants from the Department of Energy and Faculty Research Grants from the Colorado State University Graduate School.

Contents

1. INTRODUCTION	1
2. The Standard Model	3
2.1. The Standard Model of the Electroweak Interaction	3
2.2. Calculation of e^+e^- cross section at tree level [1]	12
2.2.1. Definitions	12
2.2.2. Tree level diagrams	14
2.2.3. Propagators	15
2.2.4. QED process	17
2.2.5. Polarized cross section	19
2.2.6. Bhabha scattering at the Z pole	24
2.2.7. Lepton pair production	25
2.3. Fermion Coupling Asymmetries	25
2.3.1. Correction of the asymmetries for photon exchange	29
2.3.2. Event-by-Event Asymmetries and statistical uncertainty	30

CONTENTS

3. The Linear Collider	35
3.1. The Polarized Source	38
3.1.1. Polarized Light Source	38
3.1.2. Electron Gun and Photo cathode	39
3.1.3. The damping rings	44
3.2. Positron generation	45
3.3. The Linear Accelerator	46
3.4. The Arcs	46
3.5. The Final Focus	47
3.6. The Energy Spectrometer	47
4. The Compton Polarimeter	51
4.1. Compton Scattering Kinematics	51
4.2. Polarized Compton scattering	54
4.3. The Compton polarimeter	56
4.3.1. The Compton Polarized Light Source	57
4.3.2. Measurement of the backscattered Electrons	57
4.3.3. Systematic Errors	59
4.3.4. Chromaticity Effect	60
4.4. Polarization	61
5. The Detector	65

CONTENTS

5.1. The Luminosity Monitor (LUM)	67
5.2. The Vertex Detector (VXD)	69
5.2.1. VXD2	70
5.2.2. VXD3	72
5.3. The Drift Chambers	74
5.4. The Čerenkov Ring-Imaging Detector (CRID)	77
5.5. The Liquid Argon Calorimeter (LAC)	78
5.6. The Warm Iron Calorimeter (WIC)	84
6. The Likelihood Function	89
6.1. Likelihood Function for μ and τ pair production	89
6.2. Likelihood Function for $e^+e^- \rightarrow e^+e^-$	95
7. Event selection	103
7.1. Events at SLD	103
7.2. The Pre-Selection	106
7.3. The Bhabha sample	106
7.4. The Muon sample	109
7.5. The Tau sample	110
8. Backgrounds	123
8.1. Assessing the backgrounds	126

CONTENTS

8.2. Measuring the background's angular distribution	127
8.3. Calculating the effect on the lepton asymmetries	144
8.4. Conclusion	154
9. Systematic effects from the τ Lorentz structure	157
9.1. The tracking cuts	161
9.2. The calorimetric cut	164
9.3. Specific decay channels	167
9.4. Cross checks	170
9.5. Conclusion	172
10. Other systematic studies	175
10.1. Thrust Axis Resolution	175
10.1.1. τ events	177
10.1.2. μ and Bhabha events	180
10.1.3. Initial/Final State Radiation	180
10.1.4. Charge Confusion	182
10.1.5. Conclusion	189
10.2. Detector efficiency systematics	189
10.2.1. Effect of a non-uniform selection efficiency for Bhabhas	189
10.2.2. Effect of a detector-induced asymmetry in selection efficiency	191
10.3. Polarization Corrections	195

CONTENTS

10.4. Overview over systematic uncertainties	196
11. The Polarized Lepton Asymmetries	201
11.1. Extraction of the Asymmetries	201
11.2. The Results	203
A. The VXD3	209
A.1. VXD3 Geometry	209
A.1.1. The GEANT Volume Tree of VXD3	211
A.1.2. CCDs	211
A.1.3. Support structure	215
A.1.4. Beam pipe	217
A.1.5. Cryostat	217
A.1.6. Cables and Electronics	219
A.2. VXD3 Material in the GEANT simulation	219
A.2.1. SLD's element list	219
A.2.2. SLD's chemical compound list	223
A.2.3. SLD's material mixture list	230
A.3. Pattern Recognition	236
A.4. Reconstruction Efficiency	238

List of Figures

2.1. The tree level Feynman diagrams representing $e^+e^- \rightarrow f\bar{f}$	8
2.2. The $e^+e^- \rightarrow$ hadrons cross-section as a function of E_{cm}	9
2.3. Tree level diagrams for left-handed electrons.	14
2.4. Tree level diagrams for right-handed electrons.	16
3.1. The SLC layout.	36
3.2. The time history for Z^0 production at SLC/SLD.	37
3.3. The Polarized Light Source.	38
3.4. The polarized gun with a strained GaAs cathode used in the 1993 run.	39
3.5. The energy state diagram for GaAs.	41
3.6. Polarization of photoelectrons as a function of laser wavelength with different cathodes.	42
3.7. The Wire Synchrotron Radiation Detector (WISRD).	48
4.1. Tree-level diagrams for Compton scattering.	51
4.2. Polarized Compton scattering.	54

LIST OF FIGURES

4.3. Compton cross section asymmetry	55
4.4. The Compton Polarimeter.	56
4.5. The Cherenkov and proportional tube chambers of the Compton Polarimeter.	58
4.6. The measured Polarization as a function of Z count.	61
5.1. The SLD detector (isometric view). The end caps have been removed for clarity.	66
5.2. The SLD detector (quadrant view).	66
5.3. The SLD LUM, showing the LMSAT and the MASiC.	68
5.4. The position of LMSAT and MASiC.	68
5.5. The SLD vertex detector.	70
5.6. The new vertex detector "VXD3"	72
5.7. End View comparison of "VXD2" and "VXD3"	73
5.8. Side View comparison of "VXD2" and "VXD3"	73
5.9. SLD's Central Drift Chamber (CDC).	74
5.10. The field map for a drift cell of the CDC.	76
5.11. Exploded view of the barrel LAC.	79
5.12. Exploded view of the end cap LAC.	80
5.13. View of a LAC module, showing the inner EM and outer HAD sections.	82

LIST OF FIGURES

5.14. View of a LAC end cap module, showing the inner EM (top) and outer HAD sections (bottom).	82
5.15. A cell from the barrel LAC in detail.	83
5.16. Cut away view of the WIC.	85
6.1. Initial-state radiation.	90
6.2. μ selection efficiency as a function of the center of mass energy $\sqrt{s'}$. . .	92
6.3. Measured center of mass energy for leptonic events.	93
6.4. τ selection efficiency as a function of the center of mass energy $\sqrt{s'}$. . .	94
6.5. Differential cross section for the various Bhabha terms.	98
6.6. Bhabha selection efficiency as a function of the center of mass energy $\sqrt{s'}$. .	99
7.1. Sketch of event types at SLD.	104
7.2. Typical hadronic event.	105
7.3. Typical Bhabha event.	107
7.4. Bhabha selection cut on sum of the two largest energy clusters.	108
7.5. Typical mu-pair event.	109
7.6. μ selection cut 1 on the invariant mass for all charged tracks.	111
7.7. μ selection cut 2 on the largest energy cluster associated with a charged track.	112
7.8. τ selection cut 1 on the invariant mass for all charged tracks.	113
7.9. Typical Tau event in the 1-1 topology.	114

LIST OF FIGURES

7.10. τ selection cut 2 on the largest energy cluster associated with a charged track.	115
7.11. Typical Tau event in the 1-3 topology.	116
7.12. τ selection cut 3 on the larger hemisphere mass formed by charged tracks.	117
7.13. τ selection cut 4 on the largest momentum for the charged tracks. . .	119
7.14. τ selection cut 4 on the largest momentum for the charged tracks. . .	120
7.15. τ selection cut 5 on the acollinearity computed from the charged tracks.	121
7.16. τ selection cut 5 on the acollinearity computed from the charged tracks.	122
8.1. Shape of the angular distribution of the τ background in the Bhabha sample.	129
8.2. Shape of the angular distribution of the Bhabha and the hadronic background.	130
8.3. Shape of the angular distribution of the τ background in the Bhabha sample for left-handed events.	131
8.4. Shape of the angular distribution of the τ background in the Bhabha sample for right-handed events.	132
8.5. Shape of the angular distribution of the Bhabha background in the τ sample for left-handed events.	133

LIST OF FIGURES

8.6. Shape of the angular distribution of the Bhabha background in the τ sample for right-handed events.	134
8.7. Shape of the angular distribution of the hadronic background in the τ sample for left-handed events.	135
8.8. Shape of the angular distribution of the hadronic background in the τ sample for right-handed events.	136
8.9. Shape of the angular distribution of the two-photon background.	137
8.10. Shape of the angular distribution of the two photon background in the τ sample for left-handed events.	138
8.11. Shape of the angular distribution of the two photon background in the τ sample for right-handed events.	139
8.12. Shape of the angular distribution of the two photon background in the τ sample for left-handed events.	140
8.13. Shape of the angular distribution of the two photon background in the τ sample for right-handed events.	141
8.14. Shape of the angular distribution of the two photon background in the τ sample for left-handed events.	142
8.15. Shape of the angular distribution of the two photon background in the τ sample for right-handed events.	143

LIST OF FIGURES

8.16. Fit for the angular distribution of the τ background in the Bhabha sample.	145
8.17. Fit for the angular distribution of the Bhabha background in the τ sample.	146
8.18. Fit for the angular distribution of the two-photon background in the τ sample.	147
8.19. Fit for the angular distribution of the hadronic background in the τ sample.	148
8.20. Fit for the shifts in A_e due to the presence of τ and μ background as a function of the amount of background.	149
8.21. Fit for the shifts in A_e and A_τ due to the presence of Bhabha background as a function of the amount of background.	151
8.22. Fit for the shifts in A_e and A_τ due to the presence of two-photon background as a function of the amount of background.	153
8.23. Fit for the shifts in A_e and A_τ due to the presence of hadronic background as a function of the amount of background.	155
9.1. τ polarization in KoralZ as a function of the scattering angle.	159
9.2. The beam polarization P_e influences the energy spectrum of the detected π in the τ decay channel $\tau \rightarrow \pi\nu$	160
9.3. τ selection efficiency in KoralZ as a function of the scattering angle.	162

LIST OF FIGURES

9.4. The final state asymmetry A_l as a function of the scattering angle. (tracking cuts)	163
9.5. The final state asymmetry A_l as a function of the scattering angle. (calorimetric cut)	165
9.6. The final state asymmetry A_l as a function of the scattering angle for a beam polarization of magnitude 1.	166
9.7. The efficiencies and the final state asymmetry A_l as a function of the scattering angle in the decay channels $\tau \rightarrow \pi\nu$ and $\tau \rightarrow l\nu\nu$	168
9.8. The efficiencies and the final state asymmetry A_l as a function of the scattering angle in the decay channels $\tau \rightarrow \rho\nu$ and $\tau \rightarrow a_1\nu$	169
9.9. The final state asymmetry A_l as a function of the scattering angle. (tracking cuts with SLD Monte Carlo)	171
10.1. Thrust Axis for a lepton event.	176
10.2. Thrust Axis Resolution for τ events.	179
10.3. Thrust Axis Resolution for μ and Bhabha events.	181
10.4. Charge confusion for τ Monte Carlo.	184
10.5. Like-sign events for τ data.	185
10.6. Like-sign events for μ data.	187
10.7. Like-sign events for Bhabha data.	188
10.8. Bhabha selection efficiency versus $\cos \theta$	190

LIST OF FIGURES

10.9. Maximum momentum of events with high maximum momentum ($\mu^+\mu^-$). 192

10.10. Maximum momentum of events with low maximum momentum ($\gamma\gamma$). 193

11.1. Polar angle distribution for Z decays to e, μ and τ 202

11.2. Future prospects of this analysis. 205

A.1. VXD3 design geometry. 210

A.2. VXD3 GEANT geometry in the xz plane. 212

A.3. VXD3 GEANT geometry in the xy plane. 212

A.4. Detailed VXD3 GEANT geometry. 216

A.5. VXD3 cryostat GEANT geometry. 218

A.6. Drift chamber vector hit. 236

A.7. VXD vector hit in different coordinate systems. 237

A.8. Coordinate system for VXD vector hit. 238

A.9. Reconstruction efficiency for VXD3. 239

List of Tables

2.1. The left, right, vector and axial vector couplings for fermions to the Z^0 gauge boson.	7
2.2. Properties of the Z^0 Boson.	11
3.1. SLC Parameter during 1993 and 1994/95.	37
3.2. Parameters of the SLC damping rings [9; 10]	45
4.1. Systematic Errors for the polarization in the 1994/95 run. [2]	60
5.1. Design parameters for VXD2.	71
5.2. Geometrical properties of the LAC.	81
5.3. Geometrical properties of the WIC.	85
6.1. Coefficients for Lepton production cross section.	95
6.2. Coefficients for the Bhabha cross section.	100
8.1. Monte Carlo estimates of the composition for each sample.	125
8.2. Corrected estimates of the background levels.	126

LIST OF TABLES

8.3. Efficiencies, Purities and Backgrounds for the two-photon and hadronic background data samples.	128
9.1. V-A effect for various τ decay modes.	170
10.1. Systematic Uncertainty Summary in units of 10^{-4}	197
10.2. Systematic Uncertainty in units of 10^{-4}	197
11.1. Lepton Asymmetries from 1993-95 SLD data.	203
A.1. VXD3 GEANT volume tree 1.	213
A.2. VXD3 GEANT volume tree 2.	214
A.3. List of VXD3's GEANT elements.	220
A.4. Cross section comparison for some heavy elements listed in PDB [1].	223
A.5. List of VXD3's GEANT compounds.	224
A.6. Composition of VXD3's GEANT mixtures.	229
A.7. List of VXD3's GEANT mixtures.	230
A.8. Layers of the chip carrier.	232
A.9. Pieces of strip line implemented in GEANT.	235

Chapter 1

INTRODUCTION

The *Standard Model* successfully predicts a large and diverse number of high-energy physics phenomena observed experimentally. However there are still areas in which experimental evidence is crucial to the formulation of correct mechanisms.

The second neutral-current interaction (mediated by the Z^0 boson) is partially parity-violating. Therefore, the coupling of the Z^0 to a fermion pair is characterized by two coupling constants: the strength (analogous to the charge for the electromagnetic interaction and therefore referred to as g hereafter) and the amount of parity violation, called coupling asymmetry parameter A . Maximum parity violation is implied by $|A| = 1$ and no parity violation by $A = 0$. This dissertation presents a measurement of Z^0 -Lepton coupling asymmetries in 12,063 leptonic Z^0 decays at SLD. The study looks at left-right cross section asymmetries and polarized forward-backward asymmetries (see section 2.3) in the muon and tau sample. The asymmetry

1. INTRODUCTION

parameters A_e , A_μ and A_τ are extracted from the muon and tau data sample with an unbinned maximum likelihood fit. For the Bhabha sample A_e is also measured by fitting the differential cross section with an unbinned maximum likelihood method. These asymmetries probe the hypothesis of *lepton universality*, meaning, that all leptons have the same coupling. This universality is required by the standard model. The combined asymmetries can be used to measure the “effective mixing angle” that defines the standard model couplings of the neutral current.

The dissertation is organized as follows: The second chapter discusses the Standard model and derives the tree-level differential cross section for $e^+e^- \rightarrow l^+l^-$. The next three chapters describe the experimental apparatus and do not represent my work; Chapter 3 describes the accelerator, Chapter 4 the polarimeter (to measure electron beam polarization) and Chapter 5 the detector. A discussion of the vertex detector in the upgrade of which I had been involved can be found in Appendix A.

My work on the lepton asymmetry analysis is described in Chapter 6-11: Chapter 6 describes the fitting function, Chapter 7 discusses the event selection, Chapter 8 treats the background sources, Chapter 9 presents the bias arising from the Lorentz structure of the tau decay, Chapter 10 discusses all other systematic errors considered, and Chapter 11 presents the results.

2. THE STANDARD MODEL

The left-handed fermions form isospin doublets, while right-handed fermions are treated as isospin singlet states. The fermion charges are given by the relation

$$Q = I_3 + \frac{Y}{2}$$

where I_3 is the third component of the weak isospin ($I_3 = \frac{1}{2}$ for the upper member of a doublet, $I_3 = -\frac{1}{2}$ for the lower member and $I_3 = 0$ for a singlet).

The gauge bosons of the theory are introduced in a way similar to the A^μ fields in electromagnetism to insure local gauge invariance of the fermionic expectation probabilities. The derivatives ∂^μ in the Lagrangian describing the fermionic fields are replaced by covariant derivatives

$$D_L^\mu = \partial^\mu + ig\vec{W}^\mu \cdot \frac{\vec{\tau}}{2} + ig'B^\mu \frac{Y}{2}$$

for the left-handed doublets and

$$D_R^\mu = \partial^\mu + ig'B^\mu \frac{Y}{2}$$

for the right-handed singlets with g and g' being the energy dependent coupling constants and

$$\tau_1 = \begin{pmatrix} 0 & 1 \\ 1 & 0 \end{pmatrix}, \tau_2 = \begin{pmatrix} 0 & -i \\ i & 0 \end{pmatrix}, \tau_3 = \begin{pmatrix} 1 & 0 \\ 0 & -1 \end{pmatrix}$$

2. THE STANDARD MODEL

being the Pauli matrices. The difference in the electroweak model is that there are 4 such fields W_i^μ ($i=1, 2, 3$) and B^μ that are arranged into the $W^{\pm\mu}$, Z^μ and A^μ fields in the following way

$$\begin{aligned} W^{\pm\mu} &= \frac{1}{\sqrt{2}}(W_1^\mu \pm iW_2^\mu) \\ Z^\mu &= \cos \theta_W W_3^\mu - \sin \theta_W B^\mu \\ A^\mu &= \sin \theta_W W_3^\mu + \cos \theta_W B^\mu \end{aligned} \tag{2.2}$$

where θ_W is the electroweak mixing angle. This generates an interaction Lagrangian for the left- and right-handed neutral current interactions

$$g(j_3)_\mu W_3^\mu + \frac{g'}{2} j_{YL}^\mu B_\mu \quad \text{and} \quad \frac{g'}{2} j_{YR}^\mu B_\mu$$

with the five currents j_i, j_{YR} ($i = 1, 2, 3, YL$) being the fermion currents

$$(j_i)_\mu = c_L^i \bar{f} \gamma^\mu \frac{1 - \gamma^5}{2} f \quad \text{and} \quad (j_{YR})_\mu = c_R \bar{f} \gamma^\mu \frac{1 + \gamma^5}{2} f$$

γ^μ being the Dirac matrices, c_L^i the left-handed couplings and c_R the right-handed one ($c_L^Y = Y = 2(Q - I_3)$, $c_R = 2Q$, $c_L^3 = I_3$). Therefore, we split the neutral current interactions into an electromagnetic and a weak neutral current part

$$(g \sin \theta_W j_3^\mu + g' \cos \theta_W \frac{j_Y^\mu}{2}) A_\mu + (g \cos \theta_W j_3^\mu - g' \sin \theta_W \frac{j_Y^\mu}{2}) Z_\mu.$$

2. THE STANDARD MODEL

This must be equal to

$$ej_{EM}^\mu A_\mu + g_{NC}j_{NC}^\mu Z_\mu$$

and so

$$e = g \sin \theta_W = g' \cos \theta_W \quad \text{and} \quad j_{EM}^\mu = j_3^\mu + \frac{j_Y^\mu}{2}. \quad (2.3)$$

This results in a weak neutral current of

$$g \cos \theta_W j_3^\mu - g' \sin \theta_W \frac{j_Y^\mu}{2} = \frac{g}{\cos \theta_W} (j_3^\mu \cos^2 \theta_W - \sin^2 \theta_W (j_{EM}^\mu - j_3^\mu))$$

that is

$$g_{NC} = \frac{g}{\cos \theta_W} \quad \text{and} \quad j_{NC}^\mu = j_3^\mu - \sin^2 \theta_W j_{EM}^\mu. \quad (2.4)$$

The electroweak neutral-current interaction is therefore

$$-e A_\mu \bar{f} \gamma^\mu (Q \cdot 1 + 0 \cdot \gamma^5) f - \frac{g}{2 \cos \theta_W} Z_\mu \bar{f} \gamma^\mu ((1 - \gamma^5) I_3 - 2Q \sin^2 \theta_W) f$$

Using $g \sin \theta_W = e$ this is

$$-e (A_\mu \bar{f} \gamma^\mu (Q \cdot 1 + 0 \cdot \gamma^5) f + \frac{1}{\sin 2\theta_W} Z_\mu \bar{f} \gamma^\mu ((I_3 - 2Q \sin^2 \theta_W) \cdot 1 + (I_3) \gamma^5) f) \quad (2.5)$$

Therefore, the sizes of the 'Z charges' are $c_L = 2(I_3 - \sin^2 \theta_W Q)$ and $c_R = -2 \sin^2 \theta_W Q$ and $g_V = I_3 - 2 \sin^2 \theta_W Q$ and $g_A = I_3$. The ' γ charges' are $c_L = c_R = Q$ and $g_V = Q$

2. THE STANDARD MODEL

and $g_A = 0$. I have used the definitions

$$c_L \equiv g_V + g_A \text{ and } c_R \equiv g_V - g_A$$

fermion	$c_L = 2(I_3 - \sin^2 \theta_W Q)$		$g_V = I_3 - 2 \sin^2 \theta_W Q$	
	$c_R = 2 \sin^2 \theta_W Q$		$g_A = I_3$	
	c_L	c_R	g_V	g_A
ν_e, ν_μ, ν_τ	+1	0	$+\frac{1}{2}$	$+\frac{1}{2}$
e^-, μ^-, τ^-	$-1 + 2 \sin^2 \theta_W$	$2 \sin^2 \theta_W$	$-\frac{1}{2} + 2 \sin^2 \theta_W$	$-\frac{1}{2}$
u, c, t	$+1 - \frac{4}{3} \sin^2 \theta_W$	$-\frac{4}{3} \sin^2 \theta_W$	$+\frac{1}{2} - \frac{4}{3} \sin^2 \theta_W$	$+\frac{1}{2}$
d, s, b	$-1 + \frac{2}{3} \sin^2 \theta_W$	$+\frac{2}{3} \sin^2 \theta_W$	$-\frac{1}{2} + \frac{2}{3} \sin^2 \theta_W$	$-\frac{1}{2}$

Table 2.1: The left, right, vector and axial vector couplings for fermions to the Z^0 gauge boson. Q is the charge of the fermion, and I_3 is the third component of the weak isospin for the fermion.

Table 2.1 lists the size of the Z charges. The Lagrangian for the charged current interactions can be written as

$$\frac{e}{2 \sin \theta_W} (W_\mu^+ \bar{u}_R \gamma^\mu d_L + W_\mu^- \bar{d}_R \gamma^\mu u_L)$$

where u denotes a fermion with isospin $I_3 = \frac{1}{2}$ and d has isospin $I_3 = -\frac{1}{2}$.

So far the electroweak vector bosons are massless in the theory. To acquire mass an extra field is introduced in the theory, the Higgs field. The latter is such that by spontaneous breaking of the $SU(2)_L \otimes U(1)$ symmetry it gives masses to the $W^{\pm\mu}$, Z^μ

2. THE STANDARD MODEL

fields (the W^\pm , Z^0 bosons) and leaves the A^μ fields (γ , the photon) massless. The W^\pm , Z^0 bosons were discovered by UA-1 [3], and the Z^0 has been extensively studied in e^+e^- collisions at LEP and SLD [2]. The Higgs boson has not yet been observed. The mass of the massive bosons is related to the vacuum expectation value v by

$$M = \frac{vg}{2}$$

The W couples with the $SU(2)_L$, that is, with g , so using Fermi's constant

$$G = \frac{\sqrt{2}g^2}{8M_W^2} = \frac{\sqrt{2}g^2}{8\cos^2\theta_W M_Z^2}$$

I can replace

$$\frac{1}{\sin 2\theta_W} = \frac{g}{2e \cos \theta_W} = \sqrt{2} \frac{\sqrt{G}}{e} M_Z$$

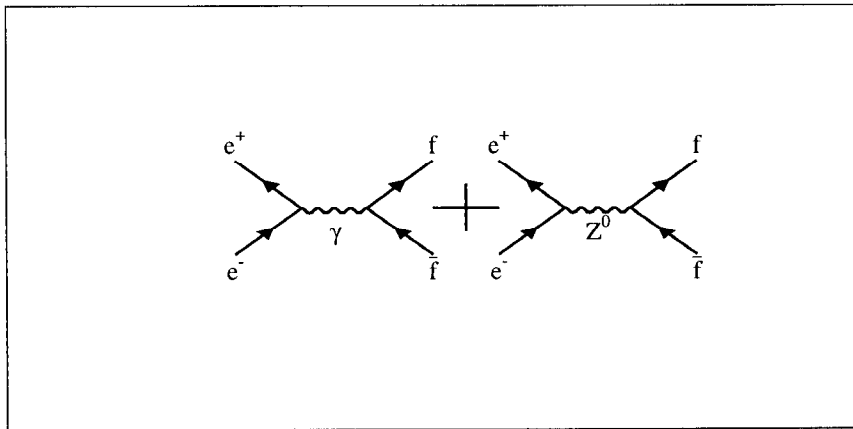


Figure 2.1: The tree level Feynman diagrams representing $e^+e^- \rightarrow f\bar{f}$

2. THE STANDARD MODEL

At SLD we observe e^+e^- collisions at the center of mass energy of $\sqrt{s} \approx 91.28$ GeV slightly above the central value of the Z^0 resonance [2]. In these collisions the initial state annihilates producing the Z^0 boson which decays to final state fermions at a rate roughly 3 orders of magnitude higher than via the electromagnetic interaction at this energy. The process $e^+e^- \rightarrow f\bar{f}$ is illustrated to first order in figure 2.1 as the sum of the photon and Z^0 boson exchange diagrams. The cross section of the process is proportional to the modulus square of the sum of the two matrix elements involved, giving rise to 3 terms: a small electromagnetic term, a large weak interaction term, and an interference term.

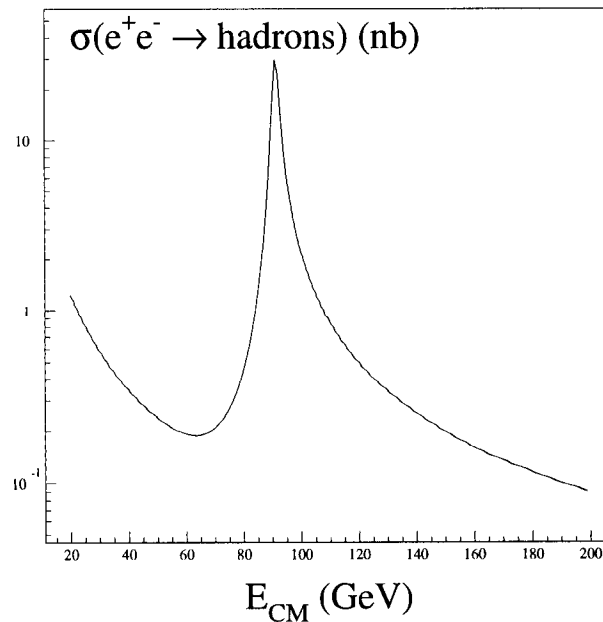


Figure 2.2: The $e^+e^- \rightarrow \text{hadrons}$ cross-section as a function of E_{cm} .

2. THE STANDARD MODEL

Figure 2.2 shows the total cross section for $e^+e^- \rightarrow \text{hadrons}$ as a function of \sqrt{s} . The 2.5 GeV wide Z^0 resonance is clearly dominating the process by a factor of about 800. At $\sqrt{s} \approx 91$ GeV we can neglect the electron and final state fermion masses and approximate helicity with spin for these ultra-relativistic particles. In these assumptions the Born cross section for $e^+e^- \rightarrow f\bar{f}$ can be expressed as follows:

$$\frac{d\sigma}{d\Omega} = K(g_V^{e^2} + g_A^{e^2})(g_V^{f^2} + g_A^{f^2})[(1 + PA_e)(1 + \cos^2\theta) + 2A_f(P + A_e)\cos\theta] \quad (2.6)$$

where g_V and g_A are the vector and axial vector couplings to the Z^0 of the initial and final state particles. P is the signed longitudinal polarization of the electron beam in the convention that left-handed bunches have positive polarization. The angle θ is the angle of the final state fermion momentum with respect to the initial state electron beam. The quantity A_f is:

$$A_f = \frac{c_L^{f^2} - c_R^{f^2}}{c_L^{f^2} + c_R^{f^2}} = \frac{2g_V^f g_A^f}{g_V^{f^2} + g_A^{f^2}} \quad (2.7)$$

and the coefficient K :

$$K = \frac{\alpha^2}{4s \sin^4 2\theta_W} \frac{s^2}{(s - M_Z^2)^2 + \Gamma_Z^2 s^2 / M_Z^2} \quad (2.8)$$

where the $\alpha \approx 1/127.9$ (at the Z^0 energy scale) is the electromagnetic fine struc-

2. THE STANDARD MODEL

ture constant. $M_Z \approx 91.19 \text{ GeV}/c^2$ is the Z^0 mass, and $\Gamma_Z \approx 2.49 \text{ GeV}/c^2$ is the Z^0 width. More data related to the Z^0 boson is listed in table 2.2. The weak mixing angle is roughly $\theta_W \approx 28.7^\circ$. This corresponds to a leptonic coupling asymmetry parameter A_l (see equation 2.7 and table 2.1)

$$A_l = \frac{2(1 - 4 \sin^2 \theta_W)}{1 + (1 - 4 \sin^2 \theta_W)^2} = 0.154 \quad \text{or} \quad \frac{g_V^l}{g_A^l} = \frac{1}{1 - 4 \sin^2 \theta_W} = 12.9.$$

The amount A_f deviates from zero indicates how much parity violation is in the Z^0 $-f\bar{f}$ coupling. Table 2.1 lists the Z^0 couplings to various fermions.

Z^0 Mass (M_Z)	$91.1863 \pm 0.0019 \text{ GeV}/c^2$
Z^0 Decay Width (Γ_Z)	$2.4947 \pm 0.0026 \text{ GeV}$
Z^0 decay branching fractions	
e^+e^-	$(3.3627 \pm 0.0065)\%$
$\mu^+\mu^-$	$(3.3587 \pm 0.0088)\%$
$\tau^+\tau^-$	$(3.3527 \pm 0.0107)\%$
invisible	$(20.034 \pm 0.078)\%$
hadrons	$(69.89 \pm 0.11)\%$
$(u\bar{u} + c\bar{c})/2$	$(9.6 \pm 1.3)\%$
$(d\bar{d} + s\bar{s} + b\bar{b})/3$	$(16.9 \pm 0.9)\%$
$c\bar{c}$	$(12.035 \pm 0.371)\%$
$b\bar{b}$	$(15.215 \pm 0.080)\%$

Table 2.2: Properties of the Z^0 Boson. [2]

2. THE STANDARD MODEL

2.2. Calculation of e^+e^- cross section at tree level [1]

2.2.1. Definitions

The most general lepton current for exchange of spin 1 bosons is

$$j^\mu = \bar{l}\gamma^\mu(g_V^l - g_A^l\gamma^5)l$$

with a vector coupling constant g_V^l and an axial vector coupling constant g_A^l . Using the definitions

$$c_L^l \equiv g_V^l + g_A^l \text{ and } c_R^l \equiv g_V^l - g_A^l$$

I get the relations

$$c_{L,R}^l = g_V^l \pm g_A^l \text{ and } 2g_{V,A}^l = c_L^l \pm c_R^l$$

$$2q_l^2 \equiv 2((g_V^l)^2 + (g_A^l)^2) = (c_L^l)^2 + (c_R^l)^2$$

$$(g_V^l)^2 - (g_A^l)^2 = c_L^l c_R^l \text{ and } (c_L^l)^2 - (c_R^l)^2 = 4g_V^l g_A^l$$

Finally, I define

$$a_l = \frac{g_A^l}{g_V^l} \text{ and } A_l \equiv \frac{(c_L^l)^2 - (c_R^l)^2}{(c_L^l)^2 + (c_R^l)^2} = \frac{2g_V^l g_A^l}{(g_V^l)^2 + (g_A^l)^2} = \frac{2g_V^l g_A^l}{q_l^2} = \frac{2a_l}{1 + a_l^2}$$

2. THE STANDARD MODEL

or

$$A_l = 1 - \frac{2(c_R^l)^2}{(c_L^l)^2 + (c_R^l)^2} = -1 + \frac{2(c_L^l)^2}{(c_L^l)^2 + (c_R^l)^2}$$

Therefore

$$c_{L,R}^l = g_V^l \pm a_l g_V^l = (1 \pm a_l) g_V^l$$

$$(c_{L,R}^l)^2 = (1 \pm A_l) \frac{(c_L^l)^2 + (c_R^l)^2}{2} = (1 \pm A_l) q_l^2$$

Using the projector operators

$$\Lambda_L \equiv \frac{1 - \gamma^5}{2} \text{ and } \Lambda_R \equiv \frac{1 + \gamma^5}{2}$$

and the identities

$$\gamma^\mu \Lambda_L = \Lambda_R \gamma^\mu \text{ and } \gamma^\mu \Lambda_R = \Lambda_L \gamma^\mu$$

together with

$$\Lambda_{L,R}^2 = \Lambda_{L,R} \text{ and } \Lambda_{L,R} \Lambda_{R,L} = 0$$

the lepton current is

$$j^\mu = c_L^l \bar{l} \Lambda_R \gamma^\mu \Lambda_L l + c_R^l \bar{l} \Lambda_L \gamma^\mu \Lambda_R l$$

in short notation

$$j^\mu = c_L^l \bar{l}_R^+ \gamma^\mu l_L^- + c_R^l \bar{l}_L^+ \gamma^\mu l_R^-$$

2. THE STANDARD MODEL

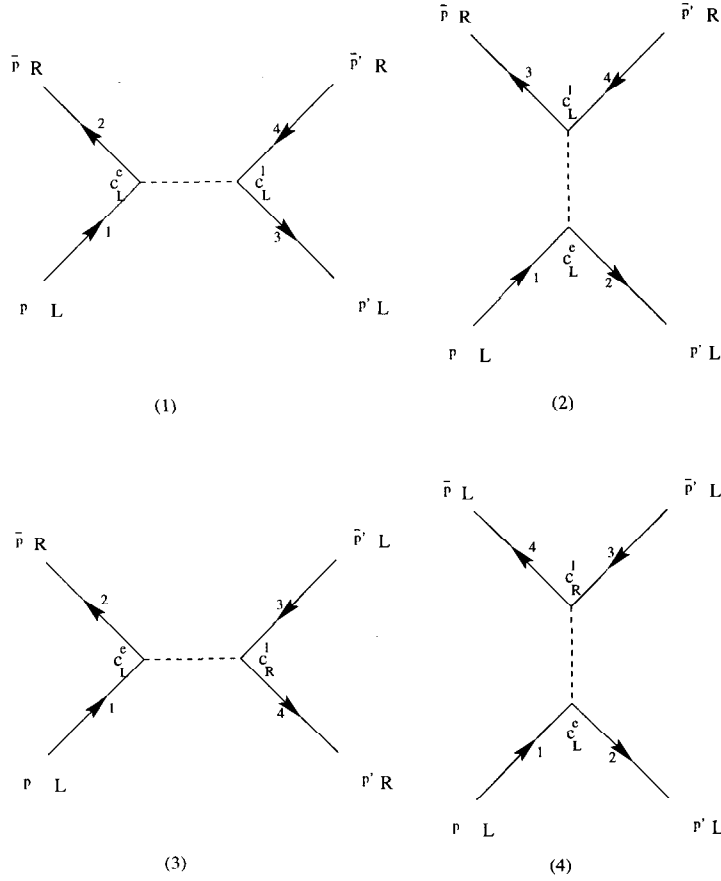


Figure 2.3: Tree level diagrams for left-handed electrons.

2.2.2. Tree level diagrams

I consider now the process $e^+e^- \rightarrow l^+l^-$. To consider the most general case, I assume that the leptons cannot be distinguished from the electrons, that is, they have the same mass as electrons. When finished, I can extract the result of lepton pair production by setting the t-channel and s-t interference terms to 0. I can also extract Bhabha scattering, by setting the lepton coupling constants equal to the

2. THE STANDARD MODEL

electron coupling constants. At high energies, any vector interaction and any axial vector interaction will preserve the helicity. If I require the electron helicity to be left-handed, without regarding the helicity of the other three particles, I get contributions from the diagrams shown in figure 2.3.

The diagrams (1) and (2) can interfere, because they describe the same helicity state, but (3) and (4) cannot interfere. Diagrams (2) and (4) really describe electron-lepton scattering. If leptons cannot be distinguished from electrons, then this does not matter.

The diagrams for right-handed electrons (figure 2.4) will have the same structure as for the left-handed electrons, because they can be obtained by interchanging the initial and final state particles and reversing the arrows. Conservation of momentum ensures that the important Lorentz invariants s , t and u will not change.

2.2.3. Propagators

The photon propagator transferring the four-momentum q^μ is

$$\frac{g^{\mu\nu}}{q^2}$$

while the Z propagator is

$$\frac{g^{\mu\nu} - \frac{q^\mu q^\nu}{M_Z^2}}{q^2 - M_Z^2 + i\epsilon}$$

2. THE STANDARD MODEL

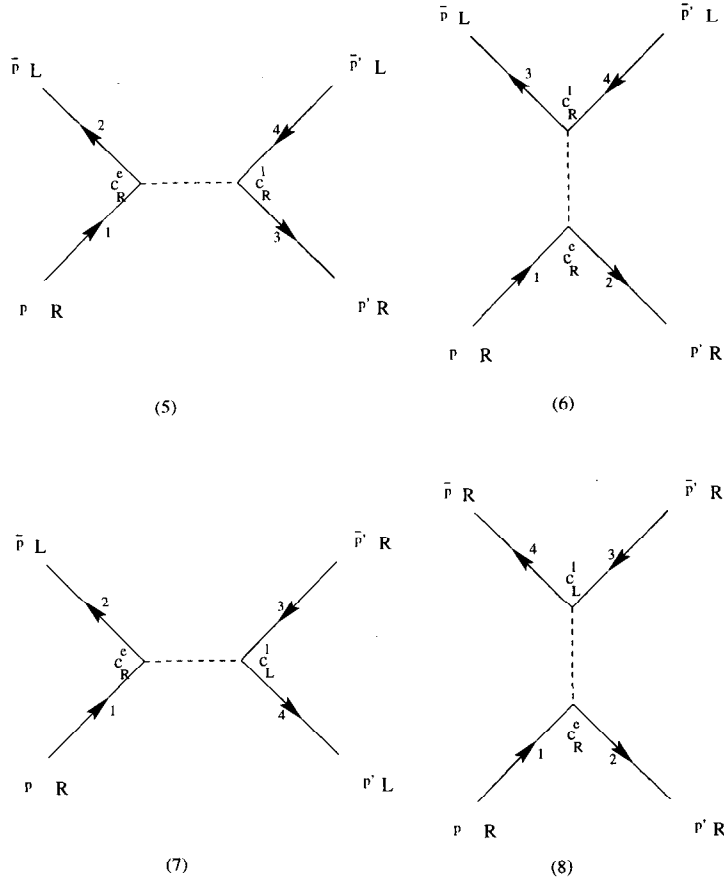


Figure 2.4: Tree level diagrams for right-handed electrons.

Because $\gamma_\mu p^\mu l_{L,R} = m l_{L,R}$ the second term ($\frac{q^\mu q^\nu}{M_Z^2}$) can be neglected. Taking into account the finite width Γ_Z of the Z boson the propagator becomes

$$\frac{g^{\mu\nu}}{q^2 - M_Z^2 + i \frac{s}{M_Z} \Gamma_Z}$$

For diagrams (1), (3), (5) and (7) $q^2 = s$ which is roughly M_Z^2 so the imaginary part in the denominator is important. For the other diagrams $q^2 = t$ which is always

2. THE STANDARD MODEL

smaller than zero, so the real part of the t propagator is always large. I will carry the imaginary part, but in the final result, it can safely be set to 0.

If the amplitude of a polarized QED process is known, I can therefore immediately calculate the amplitude of the Z-exchange process by multiplying it with rc_1c_2 where r is the ratio of the propagators multiplied with the squared coupling constants. For an s-channel process I define

$$r(s) = \frac{1}{\sin^2 2\theta_W} \frac{s}{s - M_Z^2 + i \frac{s}{M_Z} \Gamma_Z} = \frac{\sqrt{2}GM_Z^2}{s - M_Z^2 + i \frac{s}{M_Z} \Gamma_Z} \frac{s}{e^2}$$

For a t-channel process I define

$$r(t) = \frac{1}{\sin^2 2\theta_W} \frac{s}{t - M_Z^2 + i \frac{s}{M_Z} \Gamma_Z}$$

which converts the multiplication factor from rc_1c_2 to rc_1c_2t/s .

2.2.4. QED process

To derive the QED cross section, it is helpful to use the Mandelstam variables

$$\begin{aligned} s &= (p + \bar{p})^2 = (p' + \bar{p}')^2 = 2p \cdot \bar{p} = 4E^2 \\ t &= (p - p')^2 = (\bar{p} - \bar{p}')^2 = -\frac{s}{2} + \frac{s}{2} \cos \theta \equiv -\frac{s}{2}(1 - x) \\ u &= (p - \bar{p}')^2 = (\bar{p} - p')^2 = -\frac{s}{2} - \frac{s}{2} \cos \theta \equiv -\frac{s}{2}(1 + x) \end{aligned}$$

2. THE STANDARD MODEL

The s channel QED matrix element is

$$M^{(s)} = -\frac{e^2}{s} \bar{c}(-\bar{p})\gamma^\mu c(p)\bar{l}(p')\gamma_\mu l(-\bar{p}')$$

The spin-averaged square is

$$|\overline{M^{(s)}}|^2 = \frac{e^4}{s^2} L_e^{\mu\nu}(-\bar{p}, p) L_{l\mu\nu}(p', -\bar{p}')$$

with

$$L_i^{\mu\nu}(p, q) = \frac{1}{2} \sum_{1 \text{ spins}} (\bar{l}(p)\gamma^\mu l(q))(\bar{l}(p)\gamma^\nu l(q))^* = \frac{1}{2} \text{Tr}(\not{p}\gamma^\mu \not{q}\gamma^\nu) = 2(q^\mu p^\nu + q^\nu p^\mu - g^{\mu\nu} q \cdot p)$$

where I neglected the lepton mass. This results in

$$|\overline{M^{(s)}}|^2 = 2\frac{e^4}{s^2} ((2p \cdot p')(2\bar{p} \cdot \bar{p}') + (2p \cdot \bar{p}')(2\bar{p} \cdot p')) = 2e^4 \frac{t^2 + u^2}{s^2} = e^4(1 + x^2)$$

with $x = \cos \theta$. Flipping the helicity of the electron beam means flipping the spin of the exchange boson which means, that effectively the sign of x gets flipped, which interchanges u and t . Flipping the helicity of the outgoing lepton has the same effect.

The amplitudes of processes (1), (5) and of processes (3), (7) are therefore

$$\sqrt{2}e^2 \frac{u}{s} \text{ and } \sqrt{2}e^2 \frac{t}{s}$$

2. THE STANDARD MODEL

The processes (2), (6) and (4), (8) are (by s-t crossing)

$$\sqrt{2}e^2\frac{u}{t} \text{ and } \sqrt{2}e^2\frac{s}{t}$$

2.2.5. Polarized cross section

At SLC/SLD, the polarized (left- or right-handed) cross section can be measured.

I can calculate the left-handed averaged squared matrix element

$$\frac{\overline{|M_L|^2}}{e^4} = 2 \left(\left| \frac{u}{s} (1 + c_L^e c_L^l (r(s) + r(t))) + \frac{u}{t} \right|^2 + \left| \frac{t}{s} (1 + c_L^e c_R^l r(s)) \right|^2 + \left| \frac{s}{t} + c_L^e c_R^l r(t) \right|^2 \right)$$

This is spelled out ($\Re(z)$ is the real part of z)

$$\begin{aligned} \frac{\overline{|M_L|^2}}{e^4} = & 2 \left(\frac{u^2}{s^2} (1 + 2c_L^e c_L^l \Re(r(s) + r(t)) + (c_L^e c_L^l)^2 |r(s) + r(t)|^2) + \right. \\ & 2\frac{u^2}{st} (1 + c_L^e c_L^l \Re(r(s) + r(t))) + \frac{u^2}{t^2} + \frac{t^2}{s^2} (1 + 2c_L^e c_R^l \Re(r(s)) + \\ & \left. (c_L^e c_R^l)^2 |r(s)|^2) + \frac{s^2}{t^2} + 2c_L^e c_R^l \Re(r(t))\frac{s}{t} + (c_L^e c_R^l)^2 |r(t)|^2 \right) \end{aligned}$$

The differential cross section is computed from the matrix element by

$$\left(\frac{d\sigma}{dx} \right)_L = \frac{\overline{|M_L|^2}}{32\pi s} = \frac{\overline{|M_L|^2}}{e^4} \frac{\pi\alpha^2}{2s}$$

2. THE STANDARD MODEL

It is useful, to order the differential cross section in 10 terms: 3 γ -exchange terms, 3 Z -exchange terms and 4 interference terms; or 3 s -channel terms, 3 t -channel terms and 4 interference terms.

$$\begin{aligned}
 \left(\frac{d\sigma_{\gamma(s)}}{dx}\right)_L &= \frac{\pi\alpha^2}{s} \frac{t^2 + u^2}{s^2} \\
 \left(\frac{d\sigma_{\gamma(s)\gamma(t)}}{dx}\right)_L &= \frac{\pi\alpha^2}{s} 2 \frac{u^2}{ts} \\
 \left(\frac{d\sigma_{\gamma(t)}}{dx}\right)_L &= \frac{\pi\alpha^2}{s} \frac{s^2 + u^2}{t^2} \\
 \left(\frac{d\sigma_{\gamma(s)Z(s)}}{dx}\right)_L &= \frac{\pi\alpha^2}{s} 2\Re(r(s))c_L^e \frac{c_L^l u^2 + c_R^l t^2}{s^2} \\
 \left(\frac{d\sigma_{\gamma(t)Z(s)}}{dx}\right)_L &= \frac{\pi\alpha^2}{s} 2\Re(r(s))c_L^e c_L^l \frac{u^2}{st} \\
 \left(\frac{d\sigma_{\gamma(s)Z(t)}}{dx}\right)_L &= \frac{\pi\alpha^2}{s} 2\Re(r(t))c_L^e c_L^l \frac{u^2}{s^2} \\
 \left(\frac{d\sigma_{\gamma(t)Z(t)}}{dx}\right)_L &= \frac{\pi\alpha^2}{s} 2\Re(r(t))c_L^e \left(c_L^l \frac{u^2}{st} + c_R^l \frac{s}{t} \right) \\
 \left(\frac{d\sigma_{Z(s)}}{dx}\right)_L &= \frac{\pi\alpha^2}{s} |r(s)|^2 (c_L^e)^2 \frac{(c_L^l)^2 u^2 + (c_R^l)^2 t^2}{s^2} \\
 \left(\frac{d\sigma_{Z(s)Z(t)}}{dx}\right)_L &= \frac{\pi\alpha^2}{s} 2\Re(r(s)r^*(t))(c_L^e c_L^l)^2 \frac{u^2}{s^2} \\
 \left(\frac{d\sigma_{Z(t)}}{dx}\right)_L &= \frac{\pi\alpha^2}{s} |r(t)|^2 (c_L^e)^2 \left((c_L^l)^2 \frac{u^2}{s^2} + (c_R^l)^2 \right)
 \end{aligned}$$

Now computing u , s and t

$$\begin{aligned}
 \frac{u^2}{s^2} &= \frac{(x+1)^2}{4} \\
 \frac{t^2}{s^2} &= \frac{(x-1)^2}{4} \\
 \frac{u^2 + t^2}{s^2} &= \frac{1+x^2}{2}
 \end{aligned}$$

2. THE STANDARD MODEL

$$\begin{aligned}\frac{s^2 + u^2}{t^2} &= \frac{4 + (x+1)^2}{(x-1)^2} \\ \frac{u^2}{ts} &= \frac{(x+1)^2}{2(x-1)} \\ \frac{s}{t} &= \frac{2}{x-1}\end{aligned}$$

and using the identities (valid for all complex numbers e and o)

$$\begin{aligned}c_{L,R}^l &= (1 \pm a_l)g_V^l \\ c_{L,R}^l(e+o) + c_{R,L}^l(e-o) &= 2(e \pm a_l o)g_V^l \\ (c_{L,R}^l)^2 &= (1 \pm A_l)q_l^2 \\ (c_{L,R}^l)^2(e+o) + (c_{R,L}^l)^2(e-o) &= 2(e \pm A_l o)q_l^2\end{aligned}$$

and exploiting the symmetry between $(d\sigma/dx)_L$ and $(d\sigma/dx)_R$ I get the polarized cross sections

$$\begin{aligned}\left(\frac{d\sigma_{\gamma(s)}}{dx}\right)_{L,R} &= \frac{\pi\alpha^2}{2s}(1+x^2) \\ \left(\frac{d\sigma_{\gamma(s)\gamma(t)}}{dx}\right)_{L,R} &= \frac{\pi\alpha^2}{2s}2\frac{(x+1)^2}{x-1} \\ \left(\frac{d\sigma_{\gamma(t)}}{dx}\right)_{L,R} &= \frac{\pi\alpha^2}{2s}2\frac{4+(x+1)^2}{(x-1)^2} \\ \left(\frac{d\sigma_{\gamma(s)Z(s)}}{dx}\right)_{L,R} &= \frac{\pi\alpha^2}{2s}2\Re(r(s))(1 \pm a_e)g_V^e g_V^l (1+x^2 \pm a_l 2x) \\ \left(\frac{d\sigma_{\gamma(t)Z(s)}}{dx}\right)_{L,R} &= \frac{\pi\alpha^2}{2s}2\Re(r(s))(1 \pm a_e)(1 \pm a_l)g_V^e g_V^l \frac{(x+1)^2}{(x-1)}\end{aligned}$$

2. THE STANDARD MODEL

$$\begin{aligned}
\left(\frac{d\sigma_{\gamma(s)Z(t)}}{dx}\right)_{L,R} &= \frac{\pi\alpha^2}{2s} \Re(r(t))(1 \pm a_e)(1 \pm a_l)g_V^e g_V^l (x+1)^2 \\
\left(\frac{d\sigma_{\gamma(t)Z(t)}}{dx}\right)_{L,R} &= \frac{\pi\alpha^2}{2s} 2\Re(r(t))(1 \pm a_e)g_V^e g_V^l \frac{(1 \pm a_l)(x+1)^2 + (1 \mp a_l)4}{x-1} \\
\left(\frac{d\sigma_{Z(s)}}{dx}\right)_{L,R} &= \frac{\pi\alpha^2}{2s} |r(s)|^2 (1 \pm A_e)q_e^2 q_l^2 (1 + x^2 \pm A_l 2x) \\
\left(\frac{d\sigma_{Z(s)Z(t)}}{dx}\right)_{L,R} &= \frac{\pi\alpha^2}{2s} \Re(r(s)r^*(t))(1 \pm A_e)(1 \pm A_l)q_e^2 q_l^2 (x+1)^2 \\
\left(\frac{d\sigma_{Z(t)}}{dx}\right)_{L,R} &= \frac{\pi\alpha^2}{2s} |r(t)|^2 (1 \pm A_e) \frac{q_e^2 q_l^2}{2} ((1 \pm A_l)(x+1)^2 + (1 \mp A_l) \cdot 4)
\end{aligned}$$

For the final result I compute

$$\Re(r(s)) = \Re\left(\frac{1}{\sin^2 2\theta_W} \frac{s}{s - M_Z^2 + i \frac{s}{M_Z} \Gamma_Z}\right) = \frac{1}{\sin^2 2\theta_W} \frac{s(s - M_Z^2)}{(s - M_Z^2)^2 + \frac{s^2}{M_Z^2} \Gamma_Z^2}$$

$$\Re(r(t)) = \Re\left(\frac{1}{\sin^2 2\theta_W} \frac{s}{t - M_Z^2 + i \frac{s}{M_Z} \Gamma_Z}\right) = \frac{1}{\sin^2 2\theta_W} \frac{s(t - M_Z^2)}{(t - M_Z^2)^2 + \frac{s^2}{M_Z^2} \Gamma_Z^2}$$

$$\Re(r(s)r(t)^*) = \frac{1}{\sin^4 2\theta_W} \frac{s^2(s - M_Z^2)(t - M_Z^2) + \frac{s^2}{M_Z^2} \Gamma_Z^2}{((s - M_Z^2)(t - M_Z^2) + \frac{s^2}{M_Z^2} \Gamma_Z^2)^2 + \frac{s^2}{M_Z^2} \Gamma_Z^2 (t - s)^2}$$

$$|r(s)|^2 = \frac{1}{\sin^4 2\theta_W} \frac{s^2}{(s - M_Z^2)^2 + \frac{s^2}{M_Z^2} \Gamma_Z^2}$$

$$|r(t)|^2 = \frac{1}{\sin^4 2\theta_W} \frac{s^2}{(t - M_Z^2)^2 + \frac{s^2}{M_Z^2} \Gamma_Z^2}$$

SLC doesn't produce electron beams with polarization 1. A smaller polarization is introduced in the cross section by replacing each odd power of '+1' with P and each even power with 1.

2. THE STANDARD MODEL

$$\begin{aligned}
\frac{d\sigma_{\gamma(s)}}{dx} &= \frac{\pi\alpha^2}{2s}(1+x^2) \\
\frac{d\sigma_{\gamma(s)\gamma(t)}}{dx} &= \frac{\pi\alpha^2}{2s}2\frac{(x+1)^2}{x-1} \\
\frac{d\sigma_{\gamma(t)}}{dx} &= \frac{\pi\alpha^2}{2s}2\frac{4+(x+1)^2}{(x-1)^2} \\
\frac{d\sigma_{\gamma(s)Z(s)}}{dx} &= \frac{\pi\alpha^2}{2s\sin^2 2\theta_W}2\frac{s(s-M_Z^2)}{(s-M_Z^2)^2+\frac{s^2}{M_Z^2}\Gamma_Z^2}g_V^e g_V^l((1+PA_e)(1+x^2)+(P+a_e)a_l 2x) \\
\frac{d\sigma_{\gamma(t)Z(s)}}{dx} &= \frac{\pi\alpha^2}{2s\sin^2 2\theta_W}2\frac{s(s-M_Z^2)}{(s-M_Z^2)^2+\frac{s^2}{M_Z^2}\Gamma_Z^2}g_V^e g_V^l(1+a_e a_l+P(a_e+a_l))\frac{(x+1)^2}{(x-1)} \\
\frac{d\sigma_{\gamma(s)Z(t)}}{dx} &= \frac{\pi\alpha^2}{2s\sin^2 2\theta_W}\frac{s(t-M_Z^2)}{(t-M_Z^2)^2+\frac{s^2}{M_Z^2}\Gamma_Z^2}g_V^e g_V^l(1+a_e a_l+P(a_e+a_l))(x+1)^2 \\
\frac{d\sigma_{\gamma(t)Z(t)}}{dx} &= \frac{\pi\alpha^2}{2s\sin^2 2\theta_W}2\frac{s(t-M_Z^2)}{(t-M_Z^2)^2+\frac{s^2}{M_Z^2}\Gamma_Z^2} \\
&\quad \frac{g_V^e g_V^l(1+a_e a_l+P(a_e+a_l))(x+1)^2+(1-a_e a_l+P(a_e-a_l))4}{x-1} \\
\frac{d\sigma_{Z(s)}}{dx} &= \frac{\pi\alpha^2}{2s\sin^4 2\theta_W}\frac{s^2}{(s-M_Z^2)^2+\frac{s^2}{M_Z^2}\Gamma_Z^2}q_e^2 q_l^2((1+PA_e)(1+x^2)+(P+A_e)A_l 2x) \\
\frac{d\sigma_{Z(s)Z(t)}}{dx} &= \frac{\pi\alpha^2}{2s\sin^4 2\theta_W}\frac{s^2((s-M_Z^2)(t-M_Z^2)+\frac{s^2}{M_Z^2}\Gamma_Z^2)}{((s-M_Z^2)(t-M_Z^2)+\frac{s^2}{M_Z^2}\Gamma_Z^2)^2+\frac{s^2}{M_Z^2}\Gamma_Z^2(t-s)^2} \\
&\quad \frac{q_e^2 q_l^2(1+A_e A_l+P(A_e+A_l))(x+1)^2}{2} \\
\frac{d\sigma_{Z(t)}}{dx} &= \frac{\pi\alpha^2}{2s\sin^4 2\theta_W}\frac{s^2}{(t-M_Z^2)^2+\frac{s^2}{M_Z^2}\Gamma_Z^2} \\
&\quad \frac{q_e^2 q_l^2}{2}((1+A_e A_l+P(A_e+A_l))(x+1)^2+(1-A_e A_l+P(A_e-A_l))\cdot 4)
\end{aligned} \tag{2.9}$$

This is the most general tree-level result. From this, both the Bhabha cross section and the lepton (or any other fermion) pair production cross section can be derived.

This is done in the next two subsections.

2. THE STANDARD MODEL

2.2.6. Bhabha scattering at the Z pole

I can always neglect the Z width in the t-channel:

$$\begin{aligned}\Re(r(t)) &= \frac{1}{\sin^2 2\theta_W} \frac{s}{t - M_Z^2} \\ \Re(r(s)r(t)^*) &= \frac{1}{\sin^4 2\theta_W} \frac{s(s - M_Z^2)}{(t - M_Z^2)^2 + \frac{s^2}{M_Z^2} \Gamma_Z^2} \frac{s}{t - M_Z^2} \\ |r(t)|^2 &= \frac{1}{\sin^4 2\theta_W} \frac{s^2}{(t - M_Z^2)^2}\end{aligned}$$

Furthermore, initial and final state lepton species are the same, so I set $g_{V,A} \equiv g_{V,A}^e =$

$g_{V,A}^l$. This results in $\frac{d\sigma}{dx} = \sum_{b_{1,2}=Z,\gamma} \sum_{c_{1,2}=s,t} \frac{d\sigma_{b_1(c_1)b_2(c_2)}}{dx}$ with $\frac{d\sigma_{b(c)}}{dx}$ being

$$\begin{aligned}\frac{d\sigma_{\gamma(s)}}{dx} &= \frac{\pi\alpha^2}{2s}(1+x^2) \\ \frac{d\sigma_{\gamma(s)\gamma(t)}}{dx} &= \frac{\pi\alpha^2}{2s} \frac{(x+1)^2}{x-1} \\ \frac{d\sigma_{\gamma(t)}}{dx} &= \frac{\pi\alpha^2}{2s} \frac{4+(x+1)^2}{(x-1)^2} \\ \frac{d\sigma_{\gamma(s)Z(s)}}{dx} &= \frac{\pi\alpha^2}{2s \sin^2 2\theta_W} 2 \frac{s(s - M_Z^2)}{(s - M_Z^2)^2 + \frac{s^2}{M_Z^2} \Gamma_Z^2} g_V^2 ((1 + PA_e)(1 + x^2) + (P + a_e)a_l 2x) \\ \frac{d\sigma_{\gamma(t)Z(s)}}{dx} &= \frac{\pi\alpha^2}{2s \sin^2 2\theta_W} 2 \frac{s(s - M_Z^2)}{(s - M_Z^2)^2 + \frac{s^2}{M_Z^2} \Gamma_Z^2} q_e^2 (1 + PA_e) \frac{(x+1)^2}{(x-1)} \\ \frac{d\sigma_{\gamma(s)Z(t)}}{dx} &= \frac{\pi\alpha^2}{2s \sin^2 2\theta_W} \frac{s}{t - M_Z^2} q_e^2 (1 + PA_e)(x+1)^2 \\ \frac{d\sigma_{\gamma(t)Z(t)}}{dx} &= \frac{\pi\alpha^2}{2s \sin^2 2\theta_W} 2 \frac{s}{t - M_Z^2} \frac{q_e^2 (1 + PA_e)(x+1)^2 + g_V^2 (1 - a_e^2) \cdot 4}{x-1} \\ \frac{d\sigma_{Z(s)}}{dx} &= \frac{\pi\alpha^2}{2s \sin^4 2\theta_W} \frac{s^2}{(s - M_Z^2)^2 + \frac{s^2}{M_Z^2} \Gamma_Z^2} q_e^4 ((1 + PA_e)(1 + x^2) + (P + A_e)A_e 2x) \\ \frac{d\sigma_{Z(s)Z(t)}}{dx} &= \frac{\pi\alpha^2}{2s \sin^4 2\theta_W} \frac{s(s - M_Z^2)}{(s - M_Z^2)^2 + \frac{s^2}{M_Z^2} \Gamma_Z^2} \frac{s}{t - M_Z^2} q_e^4 (1 + A_e^2 + 2PA_e)(x+1)^2 \\ \frac{d\sigma_{Z(t)}}{dx} &= \frac{\pi\alpha^2}{2s \sin^4 2\theta_W} \frac{s^2}{(t - M_Z^2)^2} \frac{q_e^4}{2} ((1 + A_e^2 + 2PA_e)(x+1)^2 + (1 - A_e^2) \cdot 4)\end{aligned}\tag{2.10}$$

2.2.7. Lepton pair production

Here, only the s channel contributes

$$\begin{aligned}
 \frac{d\sigma_{\gamma(s)}}{dx} &= \frac{\pi\alpha^2}{2s}(1+x^2) \\
 \frac{d\sigma_{\gamma(s)Z(s)}}{dx} &= \frac{\pi\alpha^2}{2s\sin^2 2\theta_W} 2 \frac{s(s-M_Z^2)}{(s-M_Z^2)^2 + \frac{s^2}{M_Z^2}\Gamma_Z^2} g_V^e g_V^l ((1+Pa_e)(1+x^2) + (P+a_e)a_l 2x) \\
 \frac{d\sigma_{Z(s)}}{dx} &= \frac{\pi\alpha^2}{2s\sin^4 2\theta_W} \frac{s^2}{(s-M_Z^2)^2 + \frac{s^2}{M_Z^2}\Gamma_Z^2} q_e^2 q_l^2 ((1+PA_e)(1+x^2) + (P+A_e)A_l 2x)
 \end{aligned} \tag{2.11}$$

2.3. Fermion Coupling Asymmetries

One very important tool to test Standard Model (SM) predictions is from normalized differences of cross-sections that are sensitive to space and/or spin-space inversions. The quantities are called asymmetries and exist in 3 categories: sensitive to space inversion, the ‘‘Forward-Backward Asymmetry’’ (A_{FB}); sensitive to spin-space inversion, the ‘‘Left-Right Asymmetry’’ (A_{LR}); and sensitive to both space inversion and spin-space inversion, the ‘‘Polarized Forward-Backward Asymmetry’’ (\tilde{A}_{FB}^f).

SLD measures the left-right asymmetry A_{LR} [5] by using the unique SLC capability of delivering highly polarized electron beams:

$$A_{LR}^0 = \frac{\sigma(e^+e_L^- \rightarrow Z^0 \rightarrow f\bar{f}) - \sigma(e^+e_R^- \rightarrow Z^0 \rightarrow f\bar{f})}{\sigma(e^+e_L^- \rightarrow Z^0 \rightarrow f\bar{f}) + \sigma(e^+e_R^- \rightarrow Z^0 \rightarrow f\bar{f})} \tag{2.12}$$

2. THE STANDARD MODEL

In the measurement both left and right final-state polarizations are accepted. A_{LR}^0 relates to the effective weak mixing angle as:

$$A_{LR}^0 = A_e = \frac{2g_V^e g_A^e}{g_V^{e^2} + g_A^{e^2}} = \frac{2[1 - 4 \sin^2 \theta_W^{\text{eff}}(M_Z^2)]}{1 + [1 - 4 \sin^2 \theta_W^{\text{eff}}(M_Z^2)]^2} \approx 0.145 \quad (2.13)$$

The dependence of $\sin^2 \theta_W^{\text{eff}}$ on energy, indicates the “running” of all constants with energy. Since the SLD experiment is based at $\sqrt{s} \approx M_Z$, then the $\sin^2 \theta_W^{\text{eff}}$ used must be the one at that energy. The measured value is corrected to $\sqrt{s} = M_Z$. It is an effective value; part of the radiative corrections [4; 7] are absorbed into it. What SLD measures with the highly polarized electron beams of SLC is

$$A_{LR}^{\text{meas}} = \frac{1}{|P_e|} \frac{N_L^{\text{meas}} - N_R^{\text{meas}}}{N_L^{\text{meas}} + N_R^{\text{meas}}} \quad (2.14)$$

where $N_{L,R}$ are the number of Z^0 decays produced in left/right handed electron beams. As it can be observed A_{LR} is independent of the final state couplings to the Z^0 . Therefore, the measurement can include all final states to improve statistical power. Since the error is dominated by the statistical error, this directly improves the precision of the measurement.

The SLD measurements of A_{LR} are based on the 1992, 1993 and 1994-95 physics runs. The combined result comprising of the hadronic left-right asymmetry and lepton

2. THE STANDARD MODEL

final state asymmetries measurements (which are discussed here) is:

$$\begin{aligned} A_{LR}^0 &= 0.1542 \pm 0.0037 \\ \sin^2 \theta_W^{\text{eff}} &= 0.23061 \pm 0.00047 \end{aligned} \quad (2.15)$$

The Forward-Backward Asymmetries A_{FB}^f and \tilde{A}_{FB}^f

The Forward-Backward Asymmetry is defined as:

$$A_{FB}^f = \frac{\sigma_F^f - \sigma_B^f}{\sigma_F^f + \sigma_B^f} = \frac{3}{4} A_e A_f, \quad (2.16)$$

where:

$$\sigma_F^f = \sigma^f(\cos \theta > 0) = \int_0^1 d(\cos \theta) \frac{d\sigma}{d \cos \theta} \quad (2.17)$$

is the forward integrated cross section, and similarly, σ_B^f the backward integrated cross section for the respective fermion.

The A_{FB} asymmetry depends on both the initial and the final state couplings to the Z^0 . The final state coupling asymmetry can be extracted only if the initial state asymmetry is known and vice versa.

With the benefit of longitudinally polarized electron beams, a double asymmetry may be formed:

2. THE STANDARD MODEL

$$\tilde{A}_{FB}^f = \frac{(\sigma_F^L + \sigma_B^R) - (\sigma_F^R + \sigma_B^L)}{(\sigma_F^L + \sigma_B^R) + (\sigma_F^R + \sigma_B^L)} = \frac{3}{4} |P_e| A_f. \quad (2.18)$$

In this case $\sigma_F^{L(R)}$ is the forward cross section for left (right) polarized electron beams. It is evident from the expression of \tilde{A}_{FB}^f that it is dependent only on the final state couplings to the Z^0 . This is a unique and very interesting feature at SLD that the final state couplings may be accessed directly. Measurements of \tilde{A}_{FB}^b [8; 10] and \tilde{A}_{FB}^c [9; 10] for the heavy quarks b and c have been performed at SLD, using the single heavy-hadron decays that occur in jets initiated by heavy quarks. The hadron is detected by its weak decay. In light flavor events, “ u, d, s ”, there is a large multiplicity factor of particles containing the same flavor and it is difficult to establish the one containing the initiating quark. The measurements of \tilde{A}_{FB}^μ and \tilde{A}_{FB}^τ are part of this analysis.

If we form \tilde{A}_{FB}^f from the differential cross sections, its angular dependence is given by

$$\tilde{A}_{FB}^f(\cos\theta) = |P_e| A_f \frac{2 \cos\theta}{1 + \cos^2\theta}. \quad (2.19)$$

This differential \tilde{A}_{FB}^f can be used to increase the statistical power of the measurement of A_f .

2. THE STANDARD MODEL

2.3.1. Correction of the asymmetries for photon exchange

The left-right asymmetry of the photon term is 0 while the one of the interference term is $a_e = \frac{g_A^e}{g_V^e} \approx 12.9$. If the three terms have the weights f_γ , $f_{Z-\gamma}$ and f_Z then the measured asymmetry will be

$$A_{LR}^{meas} = \frac{a_e f_{Z-\gamma} + A_e f_Z}{f_\gamma + f_{Z-\gamma} + f_Z}$$

A similar equation holds for \tilde{A}_{FB}^f , so

$$\begin{aligned} A_e &= f_{Z-\gamma}(A_{LR}^{meas} - a_e) + (f_\gamma + f_Z)A_{LR}^{meas} \\ A_f &= f_{Z-\gamma}\left(\frac{4}{3|P|}\tilde{A}_{FB}^f - a_f\right) + (f_\gamma + f_Z)\frac{4}{3|P|}\tilde{A}_{FB}^f \end{aligned} \quad (2.20)$$

At tree level, $f_{Z-\gamma} \propto g_V^e g_V^f$ which is very small for leptons and highly sensitive to the electroweak mixing angle $\sin^2 \theta_W^{\text{eff}}$. To remove this sensitivity we replace $f_{Z-\gamma}$ with

$$\frac{f_{Z-\gamma}}{a_e a_f} \propto g_A^e g_A^f:$$

$$\begin{aligned} A_e &= \frac{f_{Z-\gamma}}{a_e a_f}(A_{LR}^{meas} - a_e) + (f_\gamma + f_Z)A_{LR}^{meas} \\ A_f &= \frac{f_{Z-\gamma}}{a_e a_f}\left(\frac{4}{3|P|}\tilde{A}_{FB}^f - a_f\right) + (f_\gamma + f_Z)\frac{4}{3|P|}\tilde{A}_{FB}^f \end{aligned} \quad (2.21)$$

2. THE STANDARD MODEL

and we obtain a_e and a_f from

$$\begin{aligned} a_e &= \frac{1 - \sqrt{1 - A_e^2}}{A_e} \\ a_f &= \frac{1 - \sqrt{1 - A_f^2}}{A_f} \end{aligned} \tag{2.22}$$

2.3.2. Event-by-Event Asymmetries and statistical uncertainty

If I measure A_{LR} with equation 2.14, the statistical uncertainty will be

$$\sigma^2 = \frac{1}{P^2} \frac{1}{N_L + N_R} \frac{4N_L N_R}{(N_L + N_R)^2} = \frac{1}{P^2} \frac{1}{N_L + N_R} \frac{(N_L + N_R)^2 - (N_L - N_R)^2}{(N_L + N_R)^2}$$

$$\sigma^2 = \frac{1}{P^2} \frac{1}{N_L + N_R} \left(1 - P^2 (A_{LR}^{meas})^2\right)$$

within 1.4 % ($PA_{LR}^{meas} \approx 0.119$) this is equal to

$$\sigma_i^2 = \frac{1}{P_i^2} \frac{1}{N_L^i + N_R^i} = \frac{1}{|P_i|} \frac{A_{LR}^i}{N_L^i - N_R^i}$$

(with the added index i indicate that I consider now several independent measurements of A_{LR}). I can now form a weighted average:

$$\overline{A_{LR}^{meas}} = \frac{\sum_i \frac{A_{LR}^i}{\sigma_i^2}}{\sum_i \frac{1}{\sigma_i^2}} = \frac{\sum_i (N_L^i P_i + N_R^i P_i)}{\sum_i (N_L^i P_i^2 + N_R^i P_i^2)} = \frac{\sum_{\text{all events}} P_i}{\sum_{\text{all events}} P_i^2} = \frac{\overline{P}}{\overline{P^2}}$$

2. THE STANDARD MODEL

which has an uncertainty of

$$\frac{1}{\sigma^2} = \sum_i \frac{1}{\sigma_i^2} = \sum_{\text{all events}} P_i^2 = N\overline{P^2}$$

For the polarized forward-backward asymmetry things are very similar. Instead of the weight $|P_i|$ we have $\left| \frac{P_i \cos \theta_i}{1 + \cos^2 \theta_i} \right|$ and the sign in the asymmetry is the sign of $P_i \cos \theta_i$.

Therefore, the event-by-event asymmetries are

$$\begin{aligned} \overline{A_{LR}^{meas}} &= \frac{\sum_{\text{all events}} P_i}{\sum_{\text{all events}} P_i^2} = \frac{\overline{P}}{\overline{P^2}} \\ \frac{1}{\sigma^2} &= \sum_{\text{all events}} P_i^2 = N\overline{P^2} \\ \overline{\tilde{A}_{FB}} &= \frac{\sum_{\text{all events}} \frac{P_i 2x_i}{1 + x_i^2}}{\sum_{\text{all events}} \left(\frac{P_i 2x_i}{1 + x_i^2} \right)^2} = \frac{\frac{\overline{P2x}}{1+x^2}}{\left(\frac{\overline{P2x}}{1+x^2} \right)^2} \\ \frac{1}{\sigma^2} &= \sum_{\text{all events}} \left(\frac{P_i 2x_i}{1 + x_i^2} \right)^2 = N \overline{\left(\frac{P2x}{1+x^2} \right)^2} \end{aligned}$$

$$(x = \cos \theta) \tag{2.23}$$

Bibliography

- [1] F. Halzen and A.D. Marten, *Quarks and Leptons: an Introductory Course in Elementary Particle Theory*, (Wiley, New York, 1984)
- [2] S.L. Glashow, Nucl. Phys. **22**, 519 (1961);
S. Weinberg, Phys. Rev. Lett. **19**, 1264 (1967);
A. Salam, in *Elementary Particle Theory*, edited by N. Svartholm (Almqvist and Wiksell, Stockholm, 1968)
- [3] UA-1 collaboration (G. Arnison et al.) Phys. Lett. **166B**, 484 (1986)
- [4] The LEP collaborations and the LEP electroweak working group, *A Combination of Preliminary Electroweak Measurements and Constraints on the Standard Model*, unpublished, see also *CERN-PPE/96-183*
- [5] SLD Collaboration (K. Abe et al.) Phys. Rev. Lett. **73**, 25 (1994)
- [6] A. Lath, Ph.D Thesis, Mass. Institute of Technology (1994), SLAC Report 454
- [7] B. W. Lynn and C. Verzegnassi, Phys. Rev. **D35**, 3326 (1987)

BIBLIOGRAPHY

- [8] SLD Collaboration (K. Abe et al.) Phys. Rev. Lett. **74**, 2890 (1995)
- [9] SLD Collaboration (K. Abe et al.) Phys. Rev. Lett. **75**, 3609 (1995)
- [10] SLD Collaboration (K. Abe et al.) Phys. Rev. Lett. **74**, 2895 (1995)

Chapter 3

The Linear Collider

The data used in this analysis were collected by the SLD collaboration at the Stanford Linear Accelerator Center (SLAC) in Stanford, California. The SLAC Linear Collider [2] (SLC)¹ is a unique single-pass electron-positron collider that produces longitudinally-polarized Z^0 's. The SLC Large Detector (SLD) is a full coverage multipurpose detector placed at the interaction region. This chapter presents an overview of the main features of the SLC.

The SLC is the world's only linear collider (Fig. 3.1). The 2 mile long linear accelerator (linac) was constructed in the 1960's to study the interior structure of the nucleon by scattering 20 GeV electrons on fixed targets [3]. It was upgraded in the 1980's to act as a single pass electron-positron collider with sufficient energy to

¹A good description of the SLC may be found in T. Junk's PhD thesis "Measurement of the Polarized Forward-Backward Asymmetry of B Quarks Using Momentum-Weighted Track Charge at SLD" [2]

3. THE LINEAR COLLIDER

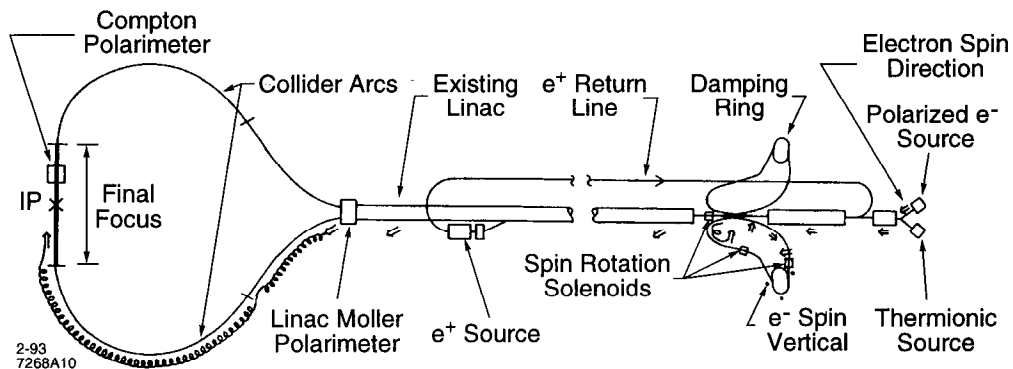


Figure 3.1: The SLC layout.

produce Z^0 bosons at resonance. The addition of a polarized electron source gives the SLC the unique capability to control the Z^0 polarization, which (as described in the previous chapter) is a useful tool for studying the electroweak interaction. The main components of SLC are the polarized source, the damping rings, the linac, the arcs, and the final focus. As time progresses, the SLC continues to be more efficient in producing Z^0 's (see Fig. 3.2). While in 1992 the typical luminosity was about 30Z/hour, it is now (1994/95 run and 1996 run) more like 60Z/hour. It is projected that another 250k Z^0 's will be produced in the remaining scheduled run. Performance parameters of SLC for the time period relevant to this analysis (1993-95) are listed in table 3.1. The higher luminosity in the 1994/95 run was made possible by improvements of the damping rings and the final focus optics. The higher polarization results from the use of a thin strained GaAs photo cathode in the electron gun.

3. THE LINEAR COLLIDER

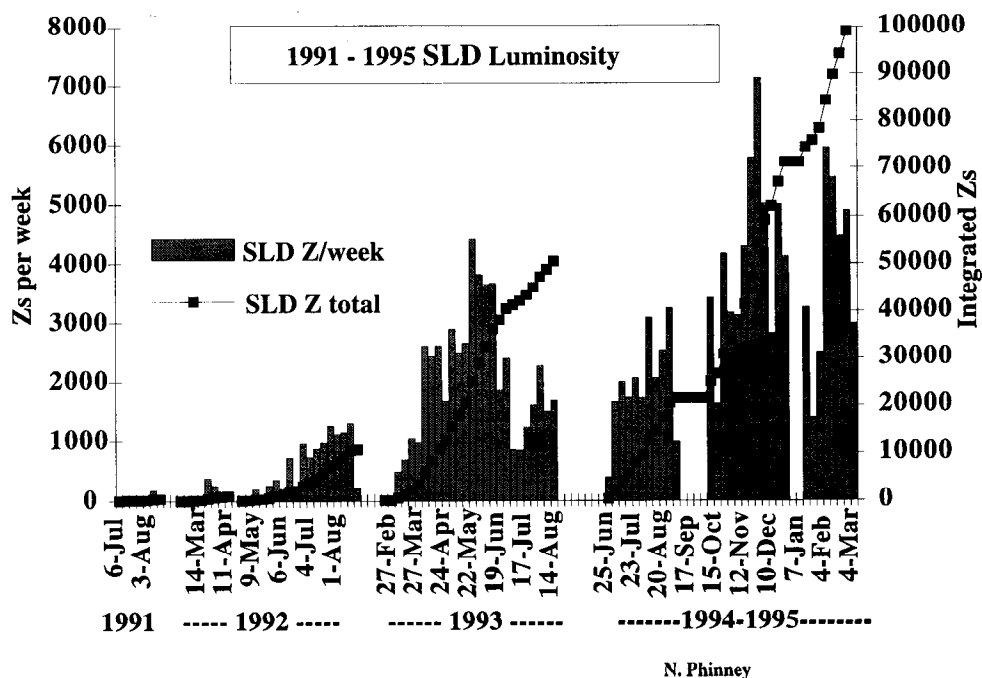


Figure 3.2: The time history for Z^0 production at SLC/SLD.

Parameter	1993	1994/95
Number of e^+ /bunch	$3.0 \cdot 10^{10}$	$3.5 \cdot 10^{10}$
Number of e^- /bunch	$3.0 \cdot 10^{10}$	$3.5 \cdot 10^{10}$
beam spot size σ_x	$2.6 \mu\text{m}$	$2.3 \mu\text{m}$
beam spot size σ_y	$0.8 \mu\text{m}$	$0.5 \mu\text{m}$
center of mass energy E_{cm}	91.26 GeV	91.28 GeV
Energy spread	0.25 %	0.12 %
Polarization P_e	$(63.0 \pm 1.1)\%$	(77.22 ± 0.51)
Luminosity	$3.8 \cdot 10^{29} \frac{1}{\text{cm}^2\text{sec}}$	$6.0 \cdot 10^{29} \frac{1}{\text{cm}^2\text{sec}}$
Z^0 count	$5.0 \cdot 10^4$	$1.0 \cdot 10^5$

Table 3.1: SLC Parameter during 1993 and 1994/95.

3. THE LINEAR COLLIDER

3.1. The Polarized Source

The rate at which new pulses of electrons are injected into the SLC is limited to 120 Hz, because the pulses have to be stored for 8 msec in a damping ring to reduce their volume in phase space and packing more pulses in the damping ring introduces bunch lengthening instabilities [4]. Also the electrical power needed increases linearly with the repetition rate, because new RF pulses are generated for each cycle. At the start of each 120 Hz cycle, the polarized electron source produces two longitudinally polarized bunches of approximately 6×10^{10} electrons.

3.1.1. Polarized Light Source

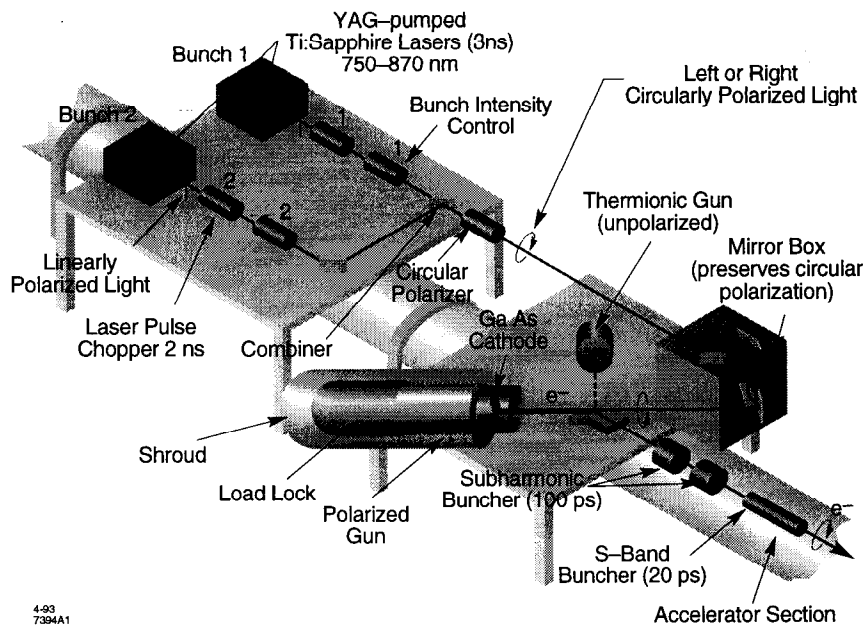


Figure 3.3: The Polarized Light Source.

3. THE LINEAR COLLIDER

As described below the electron beam is generated by photo-emission of electrons from a GaAs cathode. To polarize the beam it is necessary to use circularly polarized light. The sign of the polarization of the electron beam can then be controlled by the helicity of the photons. The Polarized Light Source (PLS) is shown in figure 3.3. Circular polarization of the laser beam is achieved by passing the linearly polarized beam through a Pockels cell. The sign of the voltage applied to the Pockels cell determines the photon helicity. To minimize any systematic effects due to differences in left- and right-handed luminosity caused by periodic behavior of the accelerator, the photon helicity is chosen according to a pseudo-random sequence.

3.1.2. Electron Gun and Photo cathode

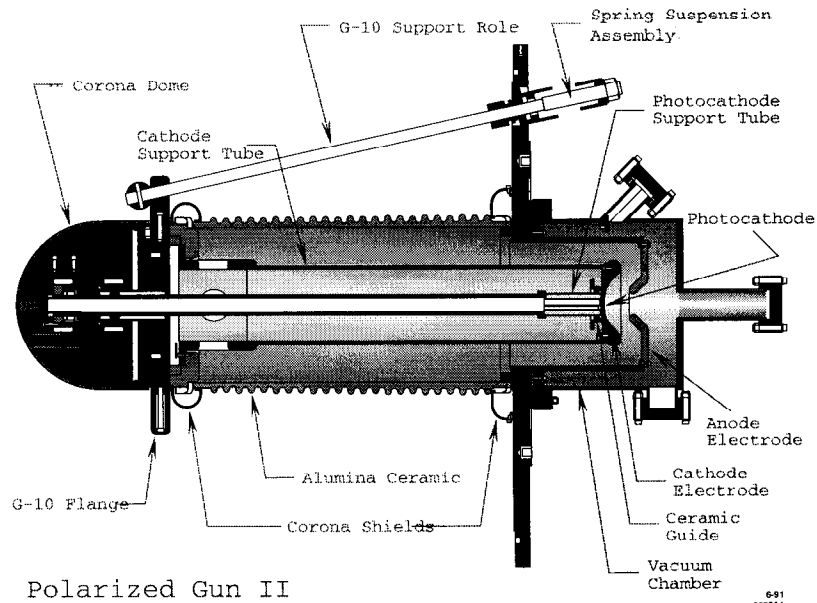


Figure 3.4: The polarized gun with a strained GaAs cathode used in the 1993 run.

3. THE LINEAR COLLIDER

The SLC's unique capability of colliding longitudinally polarized electrons with (unpolarized) positrons to produce polarized Z^0 's is made possible by the use of GaAs photo-cathodes [5] in the electron gun shown in figure 3.4. The circularly polarized laser-light is used to selectively excite electron transitions into longitudinally-polarized states in the conduction band. An energy state diagram is shown in Figure 3.5.

The strongest transition 3 leads to a $\sigma_e = -\frac{1}{2}$ state for a photon of spin $\sigma_\gamma = +1$ and to a $\sigma_e = +\frac{1}{2}$ state for a photon of spin $\sigma_\gamma = -1$, so the electron spin is controlled by the photon spin which is controlled by the sign of the Pockels cell voltage. The transitions 2 and 1 on the other hand produce spin states opposite to the ones of transition 3 and thereby reduce the magnitude of polarization. The strength of the three transitions can be calculated from the Clebsch-Gordan coefficients. The spin $\frac{1}{2}$ of the conduction band electrons and the spin 1 of the photons combines to a spin $\frac{3}{2}$ and a spin $\frac{1}{2}$ system in the valence band.

$$\begin{aligned}
 \left| \frac{3}{2}, +\frac{3}{2} \right\rangle &= \left| +1 \right\rangle \left| +\frac{1}{2} \right\rangle \\
 \left| \frac{3}{2}, +\frac{1}{2} \right\rangle &= \sqrt{\frac{1}{3}} \left| +1 \right\rangle \left| -\frac{1}{2} \right\rangle + \sqrt{\frac{2}{3}} \left| 0 \right\rangle \left| +\frac{1}{2} \right\rangle \\
 \left| \frac{3}{2}, -\frac{1}{2} \right\rangle &= \sqrt{\frac{1}{3}} \left| -1 \right\rangle \left| +\frac{1}{2} \right\rangle + \sqrt{\frac{2}{3}} \left| 0 \right\rangle \left| -\frac{1}{2} \right\rangle \\
 \left| \frac{3}{2}, -\frac{3}{2} \right\rangle &= \left| -1 \right\rangle \left| -\frac{1}{2} \right\rangle \\
 \left| \frac{1}{2}, +\frac{1}{2} \right\rangle &= \sqrt{\frac{2}{3}} \left| +1 \right\rangle \left| -\frac{1}{2} \right\rangle - \sqrt{\frac{1}{3}} \left| 0 \right\rangle \left| +\frac{1}{2} \right\rangle \\
 \left| \frac{1}{2}, -\frac{1}{2} \right\rangle &= \sqrt{\frac{2}{3}} \left| -1 \right\rangle \left| +\frac{1}{2} \right\rangle - \sqrt{\frac{1}{3}} \left| 0 \right\rangle \left| -\frac{1}{2} \right\rangle
 \end{aligned}$$

3. THE LINEAR COLLIDER

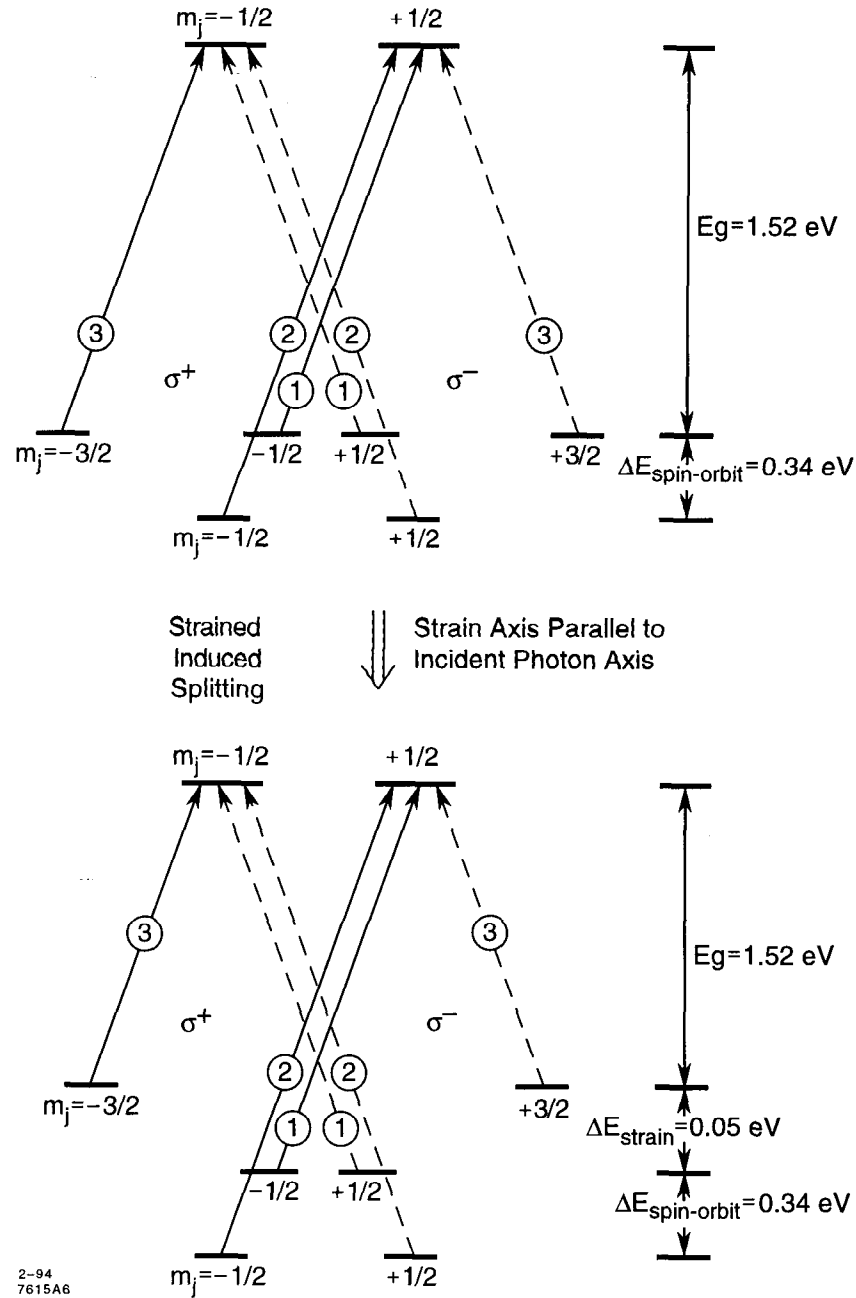


Figure 3.5: The energy state diagram for bulk GaAs (top) and the changes it undergoes when the lattice is strained (bottom). The polarization is due to the preference of certain excitation modes; the relative sizes of the matrix elements are shown in the circles. For the bulk GaAs, the maximum theoretical polarization is 50%. For the strained lattice, the maximum theoretical polarization is 100%.

3. THE LINEAR COLLIDER

The $|0\rangle$ state does not exist for the photons, so the strength of transition 3:transition 2:transition 1 is 3:2:1. Transition 2 is suppressed, since it is off-resonance, but transition 1 has the same resonance frequency as 3.

For the 1992 physics run, a bulk GaAs cathode was used. The probability of photo-emission with the right spin orientation is $p_{\text{right}} = \frac{3}{4}$ and the probability for the opposite one is $p_{\text{wrong}} = \frac{1}{4}$. The cathode had therefore a theoretical maximum polarization of

$$P_{\text{max}} = \frac{p_{\text{right}} - p_{\text{wrong}}}{p_{\text{right}} + p_{\text{wrong}}} = 2p_{\text{right}} - 1 = 50\%$$

The average polarization was measured [6] to be 22 %.

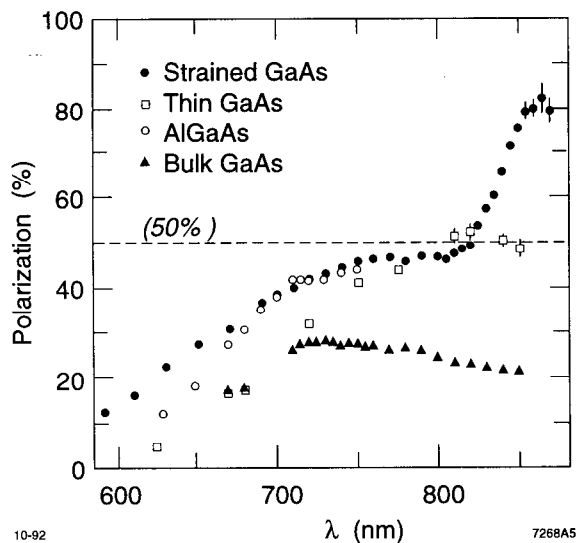


Figure 3.6: Polarization of photoelectrons as a function of laser wavelength with different cathodes.

3. THE LINEAR COLLIDER

To achieve higher beam polarization, thin strained GaAs cathodes [5] were developed. The idea is to suppress the transition 1 which limits the polarization. This is done by breaking the crystal symmetry with a mechanical strain parallel to the incident photons. The degeneracy of the spin states is lifted due to the strain that is induced by growing the GaAs on a GaAsP substrate, which has a slightly smaller lattice constant than GaAs. Therefore transition 1 is moved off-resonance by 0.05 eV. Since this energy splitting is very small, the energy of the photons (that is the laser wavelength) has to be tuned for optimal polarization. Optimal polarization is achieved if the photons have just enough energy for transition 3 which lowers the quantum efficiency and thereby the electron current. The wavelength is tuned to a value where the cathode is just about able to supply sufficient current. The thickness of the GaAs layer is also important since the strain of the lattice relaxes with growing distance from the GaAsP [5]. Figure 3.6 compares the achieved polarizations with different photo cathodes.

For the 1993 and 1994/95 runs, a strained-lattice cathode was used. The theoretical maximum polarization is 100%. During the 1993 run the polarization was approximately 65% [7]. In the 1994/95 run a thin strained GaAs cathode was used to achieve a polarization of $\sim 80\%$.

3. THE LINEAR COLLIDER

3.1.3. The damping rings

The bunches coming from the polarized source, approximately 1 mm in length, are accelerated in the linac to 1.19 GeV and stored in the north damping ring of the SLC. Damping rings are used to compress the bunches and reduce energy fluctuations. This is desirable, because as a consequence of Liouville's theorem, the volume of phase space (that is the product of position and momentum uncertainty) occupied by a bunch is constant for a non-dissipative accelerator. Introducing synchrotron radiation as a dissipative element reduces this volume and makes a smaller spot size at the interaction point possible. The radiative losses are compensated by short accelerator sections. The particles settle in stable orbits determined by the damping ring parameters and the angular divergence and bunch length decreases. To prevent depolarization of the electrons in the damping rings, spin rotators convert the longitudinal polarization into a transverse one.

The positrons (discussed in the next section) are also damped in the South Damping Ring (SDR). Since they are unpolarized, there are no spin rotators. A transverse polarization builds up, but since the storage time (16.7 msec) is very small compared to the Sokolov-Ternov polarization buildup time [8], which is ~ 960 sec, it is negligible. Some parameters of the damping rings are listed in table 3.2.

3. THE LINEAR COLLIDER

Energy	1.19 GeV
Circumference	35.270 m
Revolution Frequency	8500.411 kHz
RF Frequency	714.000 MHz
Bending Radius	2.0372 m
Energy Loss/turn	93 keV
Damping Time τ_x	3.32 ± 0.28 msec (e^-) 3.60 ± 0.15 msec (e^+)
Damping Time τ_y	4.11 ± 0.31 msec (e^-) 4.17 ± 0.14 msec (e^+)

Table 3.2: Parameters of the SLC damping rings [9; 10]

3.2. Positron generation

The polarized source produces a polarized and an unpolarized electron bunch. After damping, the two electron bunches are extracted from the damping rings and accelerated. The second e^- bunch (called the "scavenger bunch") is accelerated to 31 GeV and then diverted onto a Tungsten-Rhenium alloy target 1.33 miles down the accelerator. The resulting shower is filtered for positrons, which, after being focused by a pulsed solenoid and accelerated to 200 MeV by a short booster, are brought back to the front-end of the accelerator to be used in the next cycle. In the next cycle they are accelerated to 1.19 GeV by the linac and enter the south damping ring.

3. THE LINEAR COLLIDER

3.3. The Linear Accelerator

After damping, the two electron bunches and the positron bunch are further accelerated (the positron bunch leads the other two) by the two miles long linear accelerator. The e^+ bunch together with the first e^- bunch is accelerated to 46.7 GeV. The required energy in form of microwave pulses comes from pulsed 38 MW, 2.856 GHz klystrons which produce 120 of 5 μ sec long RF pulses every second.

3.4. The Arcs

At the end of the linac, positrons and electrons, having acquired 46.6 GeV, reach the Beam Switch Yard BSY. The BSY consists of dipole magnets directing electrons into the North SLC arc (NARC) and positrons into the South SLC arc (SARC). These 1 km long arcs consist of a sequence of dipole and quadrupole magnets to keep the beams focused and bend them towards the interaction point (IP) where they collide. Unfortunately the arcs are not flat, but rather follow SLAC's topography which rotates the electron spin in a complicated way. Collimators at the end of the linac and at different places in the arcs cut out particles with a wrong energy or position. During their travel through the arcs, the electrons and positrons lose energy through synchrotron radiation (about 1 GeV), and by the time the two bunches collide the mean energy per bunch is ~ 45.6 GeV (half of the Z^0 rest mass).

3. THE LINEAR COLLIDER

3.5. The Final Focus

The last part of the beam pipe before the IP is almost straight to keep beam-related backgrounds under control. These pieces of beam pipe have magnets to focus the beam before they hit the IP. The use of superconducting quadrupole magnets for the Final Focus triplet allows for a higher field strength (as compared with iron-yoke magnets) and makes the operation within the solenoidal field of SLD possible. [11]. SLC focuses the beam very hard; it has a spot size of $0.5 \mu\text{m}$ by $2.3 \mu\text{m}$. On the one hand, this increased the luminosity. On the other hand together with SLD's precise vertex detector (especially for the upgrade, "VXD3", that was installed before the 1996 run) this allows for very precise measurements of decay lengths. The final focus was upgraded before the 1994/95 run to reduce the chromatic effects on the focal length [12].

3.6. The Energy Spectrometer

The energy of the two beams is measured by the Wire Synchrotron Radiation Detector (WISRD) [13]. It is in the electron (positron) extraction line just before the beam dump. The WISRD is sketched out in figure 3.7. First a strong horizontal bend causes the beam to emit a horizontal swath of synchrotron radiation. Then a soft vertical bend deflects the beam downwards and spreads it out according to the energy spread in the beam. A second strong horizontal bend causes another swath of

3. THE LINEAR COLLIDER

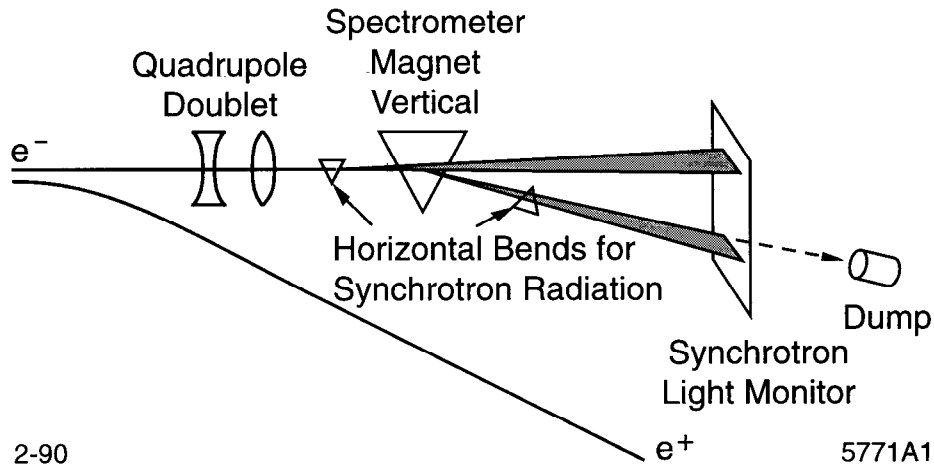


Figure 3.7: The Wire Synchrotron Radiation Detector (WISRD).

synchrotron radiation. The separation between the swathes is inversely proportional to the energy of the beam, while its energy spread can be deduced from the difference in widths of the two swathes.

The synchrotron radiation is measured by proportional wire chambers that are separated by 15 m from the magnets. The wire spacing is $100 \mu\text{m}$ which results in an energy resolution of 22 MeV. The energy spread is measured less accurately, so it is better to estimate it from wire scans in high-dispersion locations in the arcs. The energy spread is typically between 50 and 100 MeV.

Bibliography

- [1] T. Junk, Ph.D Thesis, (November 1995) SLAC-Report-95-476

- [2] SLAC Linear Collider Conceptual Design Report, SLAC-REPORT-229 (1980)
This report is bit out-dated, but still gives an overview of the design options of the major SLC components

- [3] D. Dupen, SLAC-62, (1966)

- [4] Y.-C. Chao et. al., SLAC-PUB-5868 (1992)
Presented at the 15th Int'l conf. on High Energy Accelerators, Hamburg, Germany, Jul 20-24, 1992

- [5] R. Prepost, Proceedings of the 21st SLAC Summer Institute on Particle Physics
SLAC-REPORT-444, p. 57 (1994)

- [6] SLD Collaboration (K. Abe et.al.), Phys. Rev. Lett., **70**, 2515 (1993)

- [7] SLD Collaboration (K. Abe et.al.), Phys. Rev. Lett., **73**, 24 (1995)

BIBLIOGRAPHY

- [8] A.A. Sokolov and I.M. Ternov, Sov. Phys. Doklady **8**, 1203 (1964)

- [9] H. Wiedemann, SLAC-CN-58 (1981)

- [10] C. Simopoulos and R. L. Holtzapple, SLAC-PUB-6813 (1995)

- [11] R. Erickson, T.H. Feiguth, J.J. Murray, SLAC-PUB-4199 (1987)
published in Washington PAC, p. 142 (1987)

- [12] F. Zimmermann et.al., SLAC-PUB-6790 (1995)
presented at the IEEE Particle Accelerator Conference (PAC 95)

- [13] G. Blaylock, SLD Physics Note # 22 (1993)
also, G. Blaylock, D. Briggs, B. Collins and M. Petree SLAC-PUB-5649 (1992)
Presented at the Technical Conf. and Expo, San Francisco, CA,
(January 15-17 1992)

Chapter 4

The Compton Polarimeter

4.1. Compton Scattering Kinematics

The Compton Scattering has two diagrams at tree-level shown in figure 4.1, one s -channel and one u -channel.¹

¹Good descriptions of the Compton polarimeter may be found in T. Junk's PhD thesis "Measurement of the Polarized Forward-Backward Asymmetry of B Quarks Using Momentum-Weighted Track Charge at SLD" [2] or in R. Ben-David's PhD thesis "The First Measurement of the Left-Right Cross Section Asymmetry in Z^0 Boson Production" [2]

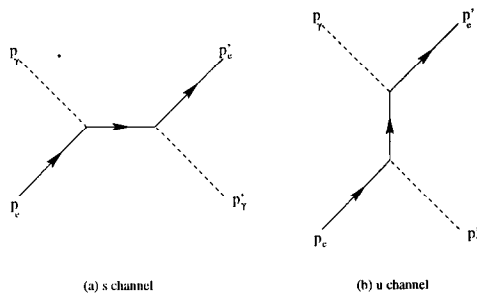


Figure 4.1: Tree-level diagrams for Compton scattering. At high energy, the s -channel is highly suppressed (in the totally backscattered case).

4. THE COMPTON POLARIMETER

In the center-of-mass system of the electron, the scattering is described by the following four vectors:

$$\bar{M} = \begin{pmatrix} m_e \\ 0 \\ 0 \end{pmatrix} \quad \bar{k} = \begin{pmatrix} k \\ 0 \\ -k \end{pmatrix} \quad \bar{M}' = \begin{pmatrix} E' \\ k' \sin \theta \hat{T} \\ k' \cos \theta - k \end{pmatrix} \quad \bar{k}' = \begin{pmatrix} k' \\ -k' \sin \theta \hat{T} \\ -k' \cos \theta \end{pmatrix}$$

where $\cos \theta \equiv \frac{t}{2kk'} + 1$ is the scattering angle, \hat{T} is the direction of the transverse momentum of the final state and t is the degree of freedom of the scattering process.

In the lab frame, the four vectors are given by

$$\bar{p}_e = \begin{pmatrix} E_e \\ 0 \\ p_e \end{pmatrix} \quad \bar{p}_\gamma = \begin{pmatrix} E_\gamma \\ 0 \\ -E_\gamma \end{pmatrix} \quad \bar{p}'_e = \begin{pmatrix} E'_e \\ p_T \hat{T} \\ p_L \end{pmatrix} \quad \bar{p}'_\gamma = \begin{pmatrix} E_e - E'_e + E_\gamma \\ -p_T \hat{T} \\ p_e - (E_\gamma + p_L) \end{pmatrix}$$

From the constraints $M'^2 = \bar{p}'_e{}^2 = m_e^2$ and $\bar{p}'_\gamma{}^2 = 0$ I get

$$k' = \frac{k}{1 + \frac{k}{m_e}(1 - \cos \theta)} = k \left(1 + \frac{t}{2m_e k} \right) \quad \text{or} \quad t = 2m_e(k' - k)$$

$$E'_e + p_L = \frac{(E'_e - E_\gamma)(E_e + p_e) - m_e^2}{p_e - E_\gamma} \quad (4.1)$$

so $\cos \theta = \frac{m_e}{k} \frac{1}{1 + \frac{2m_e k}{t}} + 1$. The Mandelstam variables u , s and t are

$$\begin{aligned} s &= m_e^2 \left(1 + \frac{2k}{m_e} \right) = m_e^2 + 2m_e k \equiv m_e^2 + 2E_\gamma(E_e + p_e) \\ u &= m_e^2 \left(1 - \frac{2k'}{m_e} \right) = m_e^2 - 2m_e k' \equiv m_e^2 - 2E_\gamma(E'_e + p_L) \\ t &= -2kk'(1 - \cos \theta) = 2m_e(k' - k) \equiv 2(m_e^2 - (E_e + p_e)E'_e + p_e(E'_e + p_L)) \end{aligned} \quad (4.2)$$

4. THE COMPTON POLARIMETER

So, the energy of the scattered electron is

$$E'_e = E_e + (p_e - E_\gamma) \frac{t}{2m_e k} \quad (4.3)$$

The cross section in the center-of-mass frame is given by the Klein-Nishina formula [3].

$$\frac{d\sigma}{d\cos\theta} = \frac{\pi\alpha^2}{m_e^2} \left(\frac{k'}{k}\right)^2 \left(\frac{k'}{k} + \frac{k}{k'} - \sin^2\theta\right) \quad (4.4)$$

which is in the lab frame

$$\frac{d\sigma}{dE'_e} = \frac{\pi\alpha^2}{m_e k} \frac{1}{p_e - E_\gamma} \left(\frac{k'}{k} + \frac{k}{k'} + m_e \left(\frac{1}{k} - \frac{1}{k'}\right) \left(m_e \left(\frac{1}{k} - \frac{1}{k'}\right) + 2\right)\right) \quad (4.5)$$

The values of k and k' and can be calculated with

$$\begin{aligned} k &= \frac{E_e + p_e}{m_e} E_\gamma \approx 2\gamma E_\gamma \\ \frac{k'}{k} &= \frac{(E'_e - E_\gamma) - \frac{m_e^2}{E_e + p_e}}{p_e - E_\gamma} \approx \frac{E'_e}{E_e} \end{aligned} \quad (4.6)$$

There is a kinematic limit for the energy of the backscattered electron, since $|\cos\theta| < 1$. This restricts E'_e to

$$E_e > E'_e > \frac{\frac{m_e^2}{E_e + p_e} + E_\gamma}{1 + \frac{m_e^2}{2(E_e + p_e)E_\gamma}} + \frac{E_e}{1 + \frac{2(E_e + p_e)E_\gamma}{m_e^2}} \approx \frac{E_e}{1 + \frac{4E_e E_\gamma}{m_e^2}} \quad (4.7)$$

4. THE COMPTON POLARIMETER

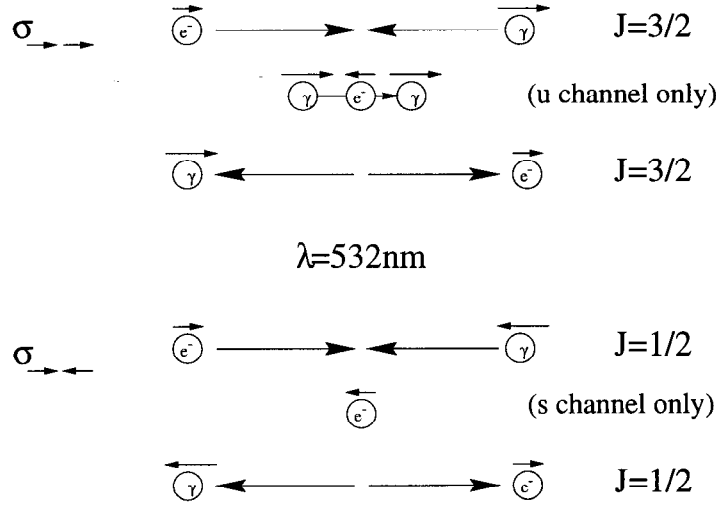


Figure 4.2: Polarized Compton scattering schematically: The $J = \frac{3}{2}$ cross section can only be mediated by the u channel, since a s channel electron exchange would involve a spin $\frac{3}{2}$ electron. The $J = \frac{1}{2}$ cross section can only be mediated by the s channel, since a u channel electron exchange would involve a spin $\frac{3}{2}$ electron.

4.2. Polarized Compton scattering

If both the incoming electrons and photons are polarized, then the two values for the total angular momentum J (see figure 4.2) select the channel by which the process was mediated (see also figure 4.1).

Because the spin of the electron propagator has to be $\frac{1}{2}$, the $J = \frac{3}{2}$ case must be mediated by the u channel and has a larger cross section than the $J = \frac{1}{2}$ case which must be mediated by the s channel. The differential cross section for the Compton scattering of polarized electrons and polarized photons can be written as:

$$\frac{d\sigma}{dE'_e} = \frac{d\sigma_u}{dE'_e} (1 + P_\gamma P_e A_c(E'_e)) \quad (4.8)$$

4. THE COMPTON POLARIMETER

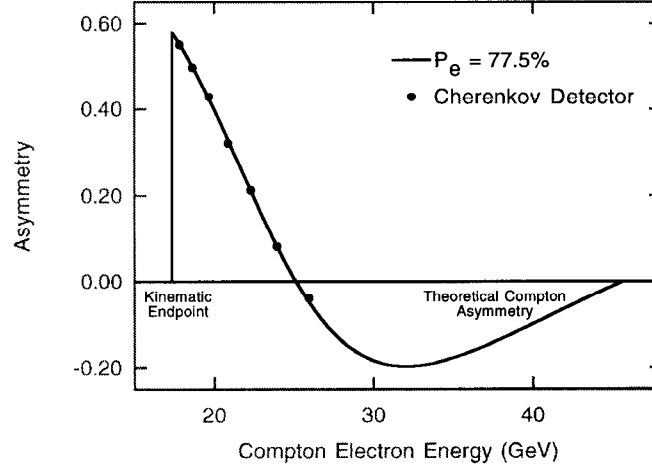


Figure 4.3: The measured (points) and theoretical Compton cross section asymmetry (line) between the $J = \frac{3}{2}$ and the $J = \frac{1}{2}$ state. The electron polarization is $P_e = 77\%$. The distance on the horizontal axis corresponds to the energy of the scattered electrons.

where σ_u is the unpolarized Compton scattering cross section, P_γ is the measured photon polarization, P_e is the unknown electron polarization, and A_c is the Compton asymmetry, which depends upon the energy of the scattered electron [4]. A_c is given by [7]

$$A_c = \frac{(ab^3 - a^3b) + m_e^2(ab^2 + a^2b - a^3 - b^3)}{(ab^3 + a^3b) + m_e^2(2ab^2 - 2a^2b) + m_e^4(a - b)^2}$$

where $a = -\frac{s-m_e^2}{2}$ and $b = \frac{u-m_e^2}{2}$. The Compton cross section asymmetry

$$A_{Compton} = \frac{d\sigma_{3/2} - d\sigma_{1/2}}{d\sigma_{3/2} + d\sigma_{1/2}} = P_e P_\gamma A_c$$

4. THE COMPTON POLARIMETER

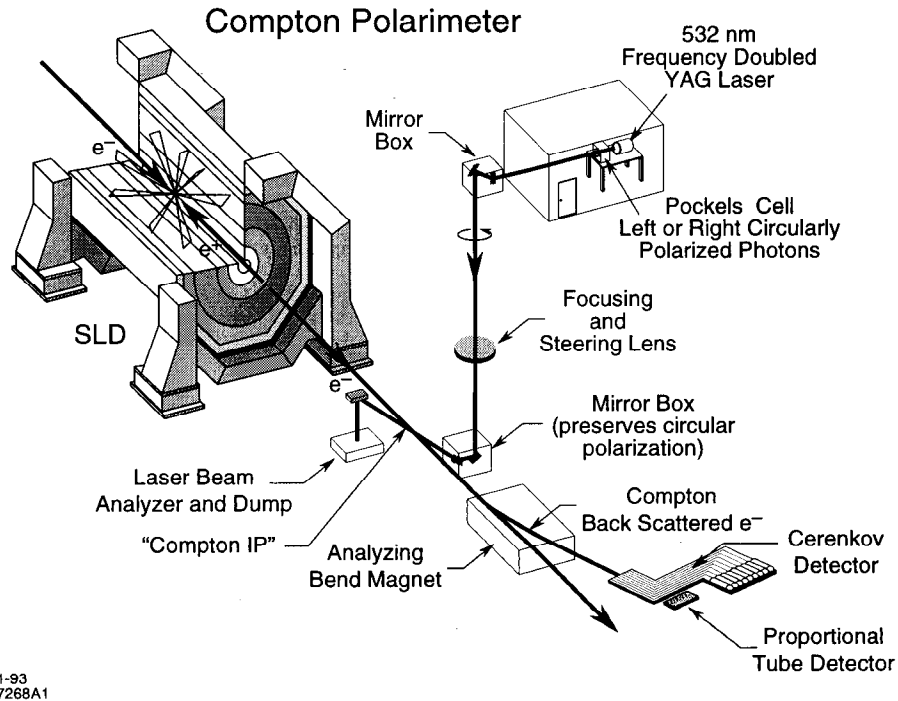


Figure 4.4: The Compton Polarimeter.

is shown in figure 4.3. Because A_c (and the analyzing power for each channel from it) can be precisely calculated (taking into account one loop and bremsstrahlung corrections [7] that have been implemented in figure 4.3), the precision of the polarization P_e that is measured this way is limited only by systematics of the detector.

4.3. The Compton polarimeter

The polarization of the electron bunch near the IP is measured by a Compton scattering polarimeter [4]. This polarimeter has two main components: a laser with polarizing optics, and an electron spectrometer (Figure 4.4).

4. THE COMPTON POLARIMETER

4.3.1. The Compton Polarized Light Source

Since the Compton asymmetry is sensitive to the product of electron beam polarization and photon polarization, it is necessary to produce polarized photons and measure the magnitude of the polarization. The photons originate from a frequency doubled, pulsed Nd:YAG laser which produces 50 mJ pulses of 7 nsec duration at a wavelength of $\lambda = 532$ nm. The laser fires every 11th beam crossing. The other 10 beam crossings are used to measure the beam background. After passing through a linear polarizer, the photons get circularly polarized by two Pockels cells [5]. The laser polarization is monitored during the run. It leads to a correction of P_e of 0.37% (for the 1994/95 run) and a systematic error of 0.28%.

4.3.2. Measurement of the backscattered Electrons

The circularly polarized laser beam is focused onto the electron bunches just after they pass through the IP (approximately 30 m downstream). Polarized photons undergo Compton scattering with some of the electrons, causing them to lose momentum. The electrons pass through a precision dipole magnet, where the scattered electrons are bent away from the main bunch. The momentum spectrum of the scattered electrons is determined by measuring their deflection angle with Cherenkov and proportional tube chambers shown in figure 4.5. The electrons pass through a lead preradiator, where they shower. The generated particles produce Cherenkov light

4. THE COMPTON POLARIMETER

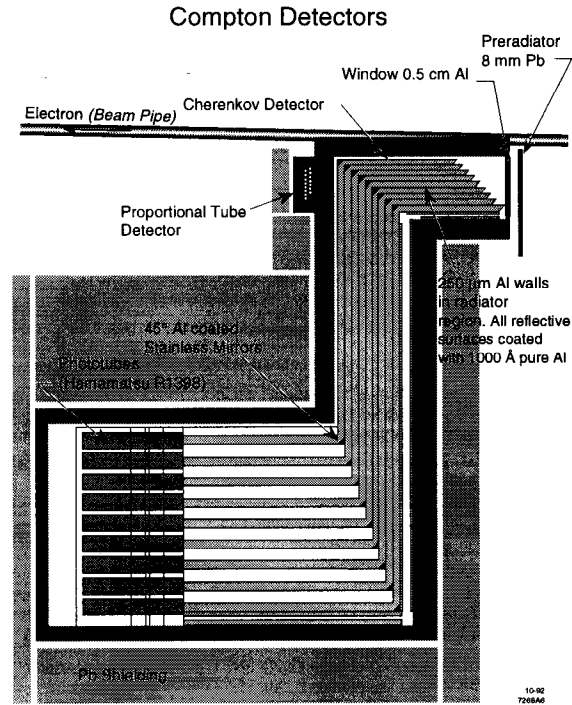


Figure 4.5: The Cherenkov and proportional tube chambers of the Compton Polarimeter.

in seven radiators the light of which is guided to seven Hamamatsu R1398 photo multiplier tubes.

The energy of the electrons is $E_e = 45.64$ GeV, a laser wavelength of $\lambda = 532$ nm corresponds to a photon energy of $E_\gamma = 2.331$ eV. Therefore k is equal to $k = 416.3$ keV and k' is in the range of $416.3 \text{ keV} > k' > 158.3 \text{ keV}$ (see equation 4.7). From equation 4.7 the kinematic constraint on E_e' is

$$17.36 \text{ GeV} < E_e' < 45.64 \text{ GeV}$$

4. THE COMPTON POLARIMETER

If the electrons have the maximum energy, they are bent by 20 mrad, while the ones with minimum energy are bent by 52.59 mrad. Since the Compton detector is 355 cm downstream from the bend point, the maximum deflection from the unscattered electrons is

$$d_{max} = 11.57 \text{ cm}$$

At $\cos \theta = 0$ (corresponds to $E'_e = 25.15 \text{ GeV}$ and a bend of 36.29 mrad) the Compton asymmetry vanishes. The deflection at this point is

$$d_0 = 5.78 \text{ cm}$$

These two points serve to locate the image of the energy spectrum on the array of Cherenkov detectors and to determine its distance scale. The detector is positioned, so that the kinematic endpoint lays within the acceptance of channel 7 and the zero asymmetry point within the acceptance of channel 2.

4.3.3. Systematic Errors

Since the statistical precision of the measurement is high, it is dominated by systematics. The largest contribution to the systematic error comes from the uncertainty in the linearity of the detector response. This systematic error and others are listed in table 4.1 for the 1994/95 run.

4. THE COMPTON POLARIMETER

Item	rel. Correction	rel. Uncertainty
Analyzing Power		
Calibration	0.7086	0.29%
Laser Polarization	+0.37%	0.20%
Electronics Noise	-0.19%	0.20%
Linearity	-0.22%	0.50%
SLC IP	+0.09%	0.17%
Total		0.67%

Table 4.1: Systematic Errors for the polarization in the 1994/95 run. [2]

4.3.4. Chromaticity Effect

The diameter of the laser beam at the CIP is larger than the electron beam and therefore the Compton polarimeter determines the average polarization. However, the polarization depends on the electron energy. The luminosity depends on the energy as well, since chromatic aberration of the final focus optics leads to a defocusing of the electrons in the energy tails. Therefore, the luminosity-weighted average will be bigger (the polarization is of course optimized for the electrons with the central-value energy) than the simple average. This “chromaticity effect” leads to a correction of $1.7\% \pm 1.1\%$ for the 1993 run and $0.20\% \pm 0.14\%$ for the 1994/95 run. The reduction in error for the 1994/95 runs was achieved by reducing the energy dependence of the polarization (reducing the effective number of turns in the arc) which moves the simple average closer to the luminosity-weighted average and thereby reducing a large part of the systematic error of the polarization.

4. THE COMPTON POLARIMETER

Beam Polarization SLD 1992 - 1995 Data

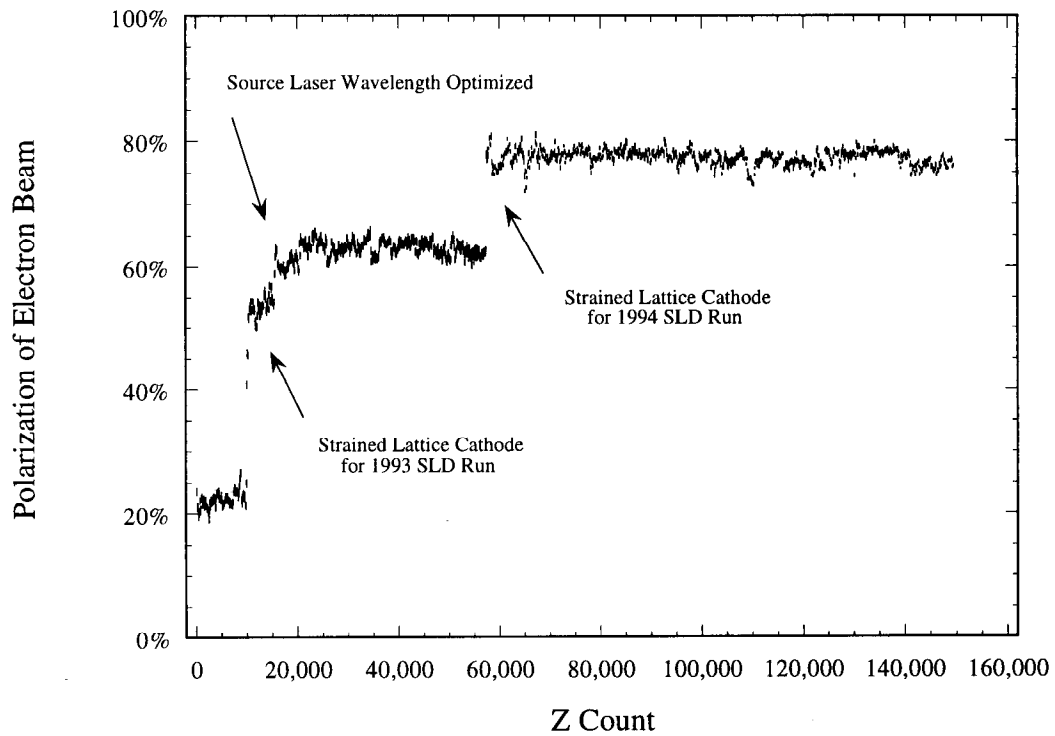


Figure 4.6: The measured Polarization as a function of Z count.

4.4. Polarization

For the 1993 physics run, the average longitudinal polarization at the IP was $(63.0 \pm 1.1)\%$; during the 1994-95 run the average was $(77.22 \pm 0.51)\%$ [2]. The polarization history is shown in figure 4.6. The improvements of the polarized source (from bulk GaAs cathode to thin GaAs cathode to strained GaAs cathode to strained thin GaAs cathode) are clearly visible.

Bibliography

- [1] T. Junk, Ph.D Thesis, (November 1995) SLAC-Report-95-476
- [2] R. Ben-David, Ph.D Thesis, (May 1994) SLAC Report 442
- [3] O. Klein and Y. Nishina, Z.Phys. **52**, 823 (1929);
Y. Nishina, Z.Phys., **52**, 869 (1929);
- [4] A. Lath, Ph.D Thesis, Mass. Institute of Technology (1994), SLAC Report 454
- [5] A. Lath and M. Woods, SLD Note #236 (1994)
- [6] M. Fero, D. Calloway, R. Elia and A. Lath, SLD Note #221 (October 1992)
- [7] H. Veltman, Phys.Rev. **D40**, 2810 (1989)
- [8] A. Lath, D. Freytag, *Compton Analysis: LeCroy Model 2249W ADC Linearity Study*, SLD Note #234 (April 1994)
- [9] M. Fero, P. Reinertsen, B. Schumm, M. Swartz, E. Torrence, SLD Note #50 (June 1996)

Chapter 5

The Detector

The SLC Large Detector (SLD)¹ was proposed in 1984 [3]. It is the only detector of SLC, since this accelerator has only one interaction point (IP). It was designed as a general purpose detector with nearly complete solid angle coverage around the IP. Figures 5.1 and 5.2 show a cut-away (with the end cap portions removed) and a quadrant view of SLD.

Like other detectors in a e^+e^- collider environment, SLD has two main geometric regions: The *barrel* is a cylinder of 4.5 m radius and 10 m length. The *end caps* close off the two faces of the cylinder, nearly completing the solid angle coverage. The e^+e^- beams enter along the axis of the cylinder, and the various barrel subsystems are arranged radially within the cylinder. At small angles to the beam, there is no

¹A good description of the SLD may be found in K. Baird's PhD thesis "Strange Particle Production in Hadronic Z^0 Decays" [1] or in T. Junk's PhD thesis "Measurement of the Polarized Forward-Backward Asymmetry of B Quarks Using Momentum-Weighted Track Charge at SLD" [2]

5. THE DETECTOR

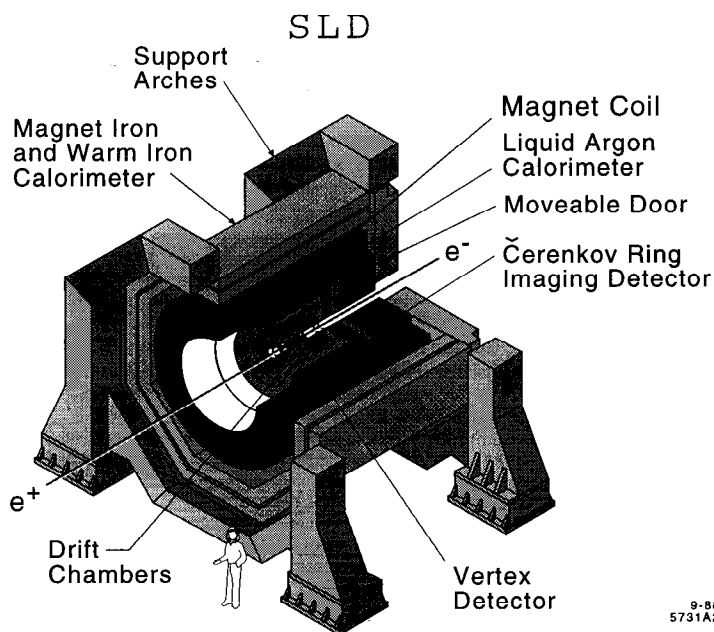


Figure 5.1: The SLD detector (isometric view). The end caps have been removed for clarity.

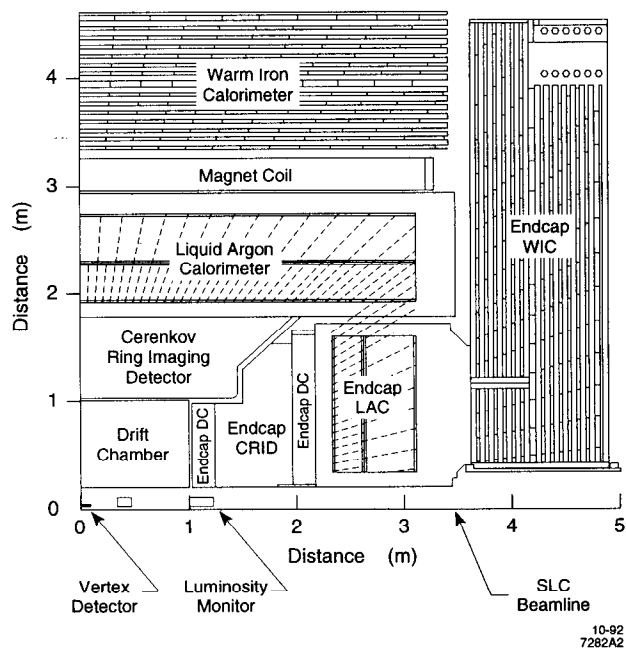


Figure 5.2: The SLD detector (quadrant view).

5. THE DETECTOR

detector coverage due to the location of the beam-pipe and its support structures. Nevertheless, the detector covers 98% of the solid angle. The outer support structure of SLD is the Warm-Iron Calorimeter (WIC) providing the flux return for the coil (not superconducting) which produces a magnetic field of 0.6 T. Except for the WIC, all of SLD's subsystems are inside the coil.

5.1. The Luminosity Monitor (LUM)

The Luminosity Monitor precisely monitors the total luminosity as well as small luminosity differences between left- and right-handed polarized beams [4] that may be present. In addition, it extends the electromagnetic calorimetry coverage down to very small polar angles (the Liquid Argon Calorimeter provides electromagnetic shower (EM) coverage for 98% of the solid angle as described in Section 5.5))

The LUM, shown in figure 5.3, is divided into two separate modules, both of which are inside the Central Drift Chamber (CDC) as shown in figure 5.4. The LMSAT, Luminosity-Monitor/Small-Angle Trigger, mounts directly onto the Superconducting Final-Focus triplet assembly and covers the polar angle region between 28 and 68 mrad. The MASiC, Medium Angle Silicon Calorimeter, provides coverage from 68 to 200 mrad. The end cap LAC, covers the region above 200 mrad.

5. THE DETECTOR

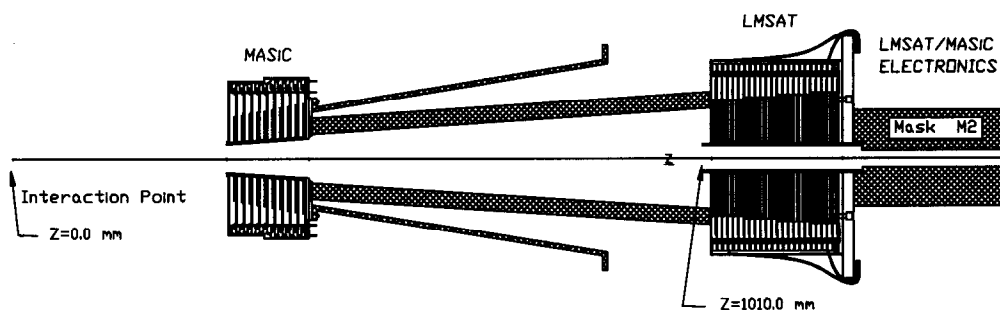


Figure 5.3: The SLD LUM, showing the LMSAT and the MASiC.

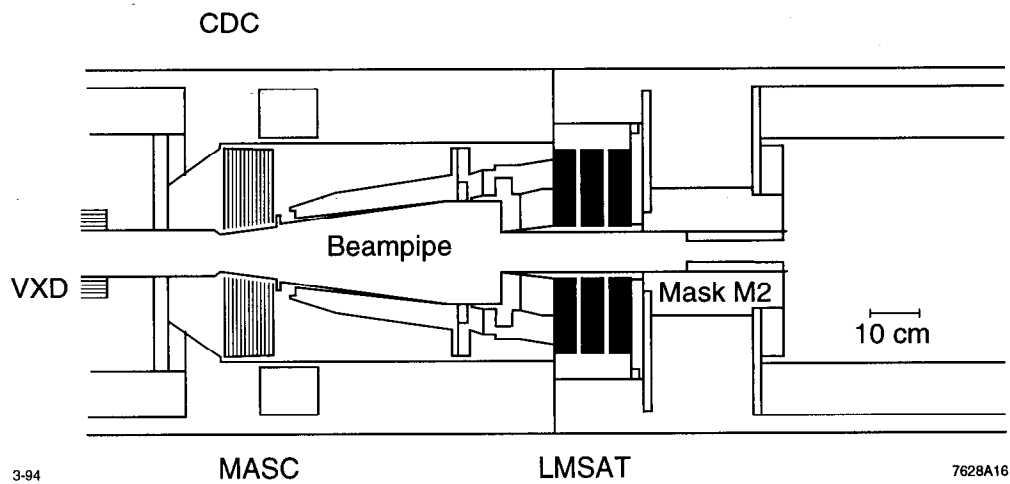


Figure 5.4: The position of LMSAT and MASiC.

5. THE DETECTOR

5.2. The Vertex Detector (VXD)

The VXD uses Charge-Coupled Devices (CCDs) to measure charged tracks with high precision. A CCD (which is also used for compact video cameras) is a semiconductor consisting of an array of tiny "pixels" which collect charge carriers produced by photons or, as in this case, by charged particles passing through the CCD. The accumulated charges are trapped in a small potential well. The potential wells of the pixels can be manipulated to transfer the charge content of one pixel to a neighboring one. The CCD pixels are read out by shifting simultaneously all the columns of the array one pixel down. The bottom row is copied into an additional row of pixels, which is the output register. Then the output register is shifted left by one pixel, and the leftmost pixel is read out. Then the output register is shifted again and one by one all the pixels it contains are read out. Again, the pixel array is shifted down by one pixel and the next row is copied into the output register. In this way, all the CCD pixels are read out sequentially. A hit by a charged particle in the CCD active area will produce a charge cluster that is collected by a few pixels. (being spread out in an extended depletion region to increase the accuracy of its measured position) From the pixel address (its row and column), the position of the hit can be deduced. [5]

5. THE DETECTOR

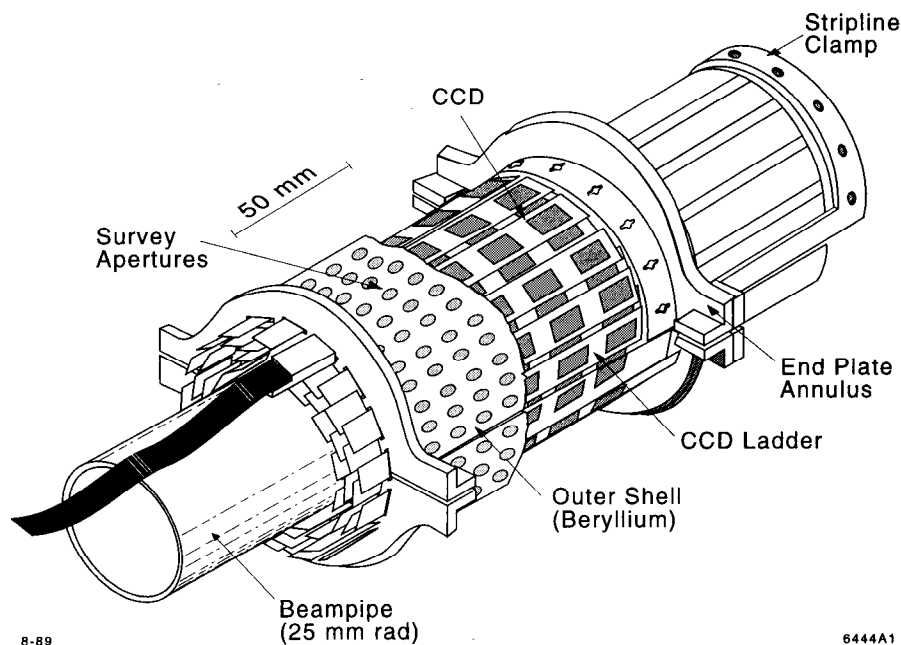


Figure 5.5: The SLD vertex detector.

5.2.1. VXD2

The VXD2, shown in figure 5.5, has 60 ladders of 9.2 cm length that are arranged into four concentric cylinders held in place by a beryllium shell. Eight CCDs are mounted on each ladder, four on each side (to maintain the symmetry of the polar angle). Each CCD is a square of about 1 cm length, and contains 240,000 pixels. The pixels are squares and have a length of $22 \mu\text{m}$. On the average, 2.3 VXD hits are obtained for each charged track passing through the detector. The inner layer of CCDs is at a distance of 29.5 mm from the IP, and the outer layer is at a distance

5. THE DETECTOR

of 41.5 mm. Each layer's material is 1.1% of a radiation length (X_0)². Inside the inner-most CCD layer is the VXD cooling jacket (VXD2 is operated at 170 K to reduce the effects of radiation damage) and the thin beryllium cylinder which serves as the beam pipe. The total radiation thickness of the material between the IP and the first CCD layer is 0.71% X_0 . The vertex detector design parameters are listed in table 5.1

CCD count	480
Pixels/CCD	400 × 600
Pixel size	22 μm × 22 μm
Active area per CCD	8.5 mm × 12.7 mm
Readout time	160 msec (19 beam crossings)
Operating temperature	170 K
Layer 1 radius	29.5 mm
Layer 2 radius	33.5 mm
Layer 3 radius	37.5 mm
Layer 4 radius	41.5 mm
Radiation thickness per layer	0.01064 X_0
Expected hits/track	2.3
Two-hit coverage	$ \cos \theta < 0.75$
One-hit coverage	$ \cos \theta < 0.82$
Impact parameter resolution	$\sim 12\mu\text{m} (r\phi)$ and $38\mu\text{m} (rz)$ [7]

Table 5.1: Design parameters for VXD2.

²1 radiation length (X_0) is the mean distance over which a high energy electron loses all but 1/e of its energy by bremsstrahlung [1].

5. THE DETECTOR

5.2.2. VXD3

The VXD detector was upgraded recently. The new detector, "VXD3" (shown in figure 5.6 and described in appendix A), has fully-overlapping layers of CCD ladders in order to provide at least three spatial points for each charged track. The ladders are longer than VXD2's to cover smaller polar angles. Figures 5.7 and 5.8 compare the end and side views of the VXD2 and the new VXD3. VXD3 took data in the 1996 run. (about 50000 hadronicZ's)

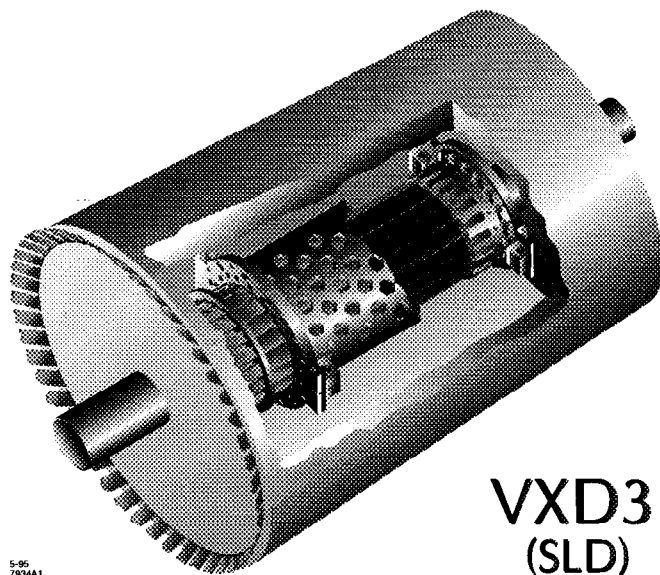
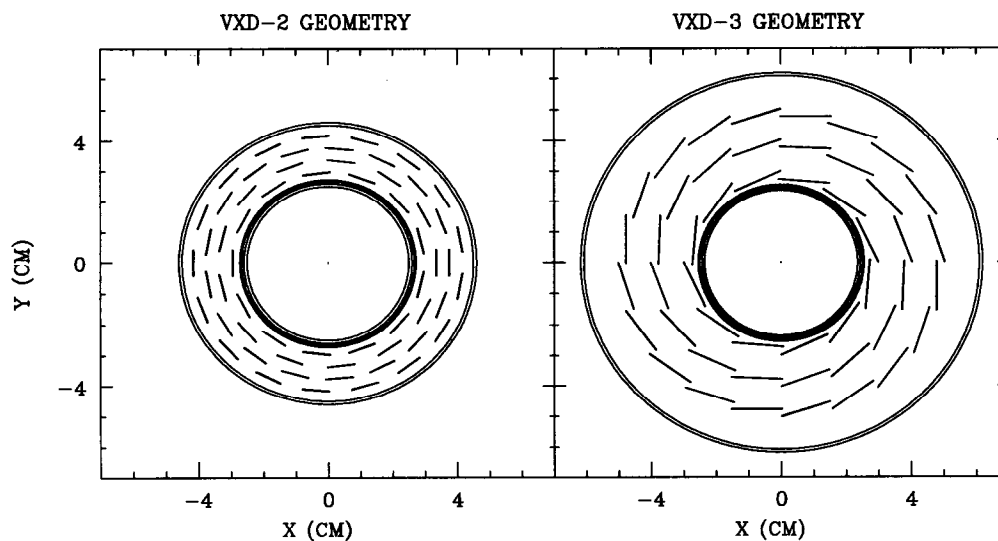


Figure 5.6: The new vertex detector "VXD3". It has three layers of overlapping, long CCDs which insure at least three spatial points for each charged tracks.

5. THE DETECTOR



HANDYPAK 14:43:29 4SEP96

Figure 5.7: An end view comparison of the current "VXD2" vertex detector and the new "VXD3" tracker. The overlapping CCDs insure that at least three spatial points are obtained for charged tracks that traverse all three layers.

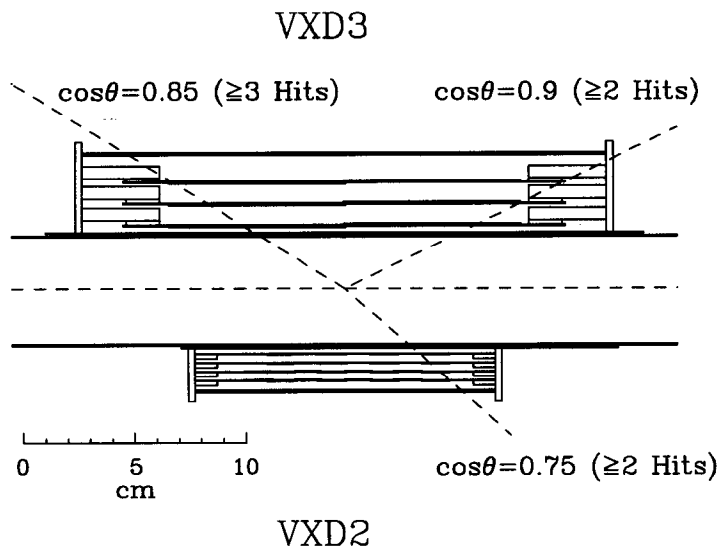


Figure 5.8: A side view comparison of VXD2 and VXD3. The new tracker will provide coverage to higher $\cos \theta$.

5. THE DETECTOR

5.3. The Drift Chambers

There are two separate drift chamber subsystems for the SLD - the Central Drift Chamber (CDC) and the Endcap Drift Chambers (EDCs). The CDC covers roughly 80% of the solid angle ($|\cos\theta| < 0.8$), and operates in a uniform solenoidal magnetic field of 0.6 T. Its shape is that of a cylindrical annulus. It is 2 m long, its inner radius is 20 cm and its outer radius is 1 m. The CDC has 10 "superlayers" of drift cells, each approximately 6 cm wide by 5 cm high. These superlayers are staggered in orientation (figure 5.9). Axial superlayers (with the sense wires oriented along the cylinder axis) alternate with stereo superlayers (the sense wires are tilted at an angle of 41 mrad).

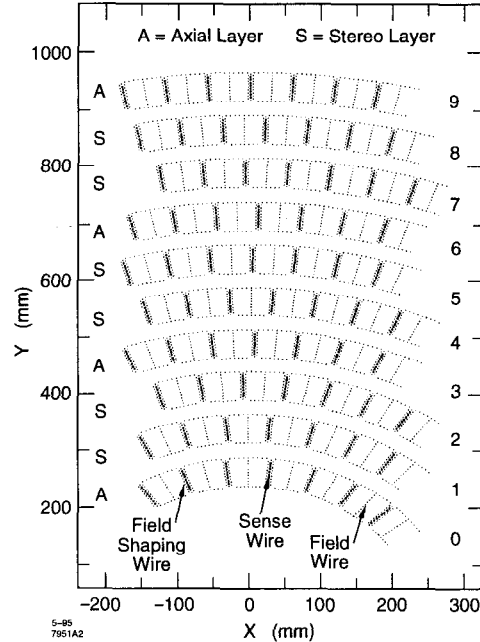


Figure 5.9: SLD's Central Drift Chamber (CDC).

5. THE DETECTOR

Each cell contains a set of field shaping wires, guard wires, and sense wires (figure 5.10). A charged track passing through a cell leaves a trail of ions in the drift gas (a mixture of CO₂ (75%), argon (21%), Isobutane (4%), and water (0.2%)). The field shaping wires generate a roughly homogeneous drift field which directs the ions towards the 8 sense wires. The $r\phi$ position of the hit is known from the wire address and drift time (the time from e^+e^- collision to the time when the pulse is detected on the wire which is related to the separation of the track from the wire). The sense wires are instrumented on both ends, so a charge division provides some information of the z position (along the wire). The precision of the z position is about 2 cm.

Since there are 8 sense wires, the 8 measurements can be combined into a vector hit (a linear approximation of the track segment). The sense wires in the cell are not staggered, so the vector hit is ambiguous (the mirror image of the vector hit cannot be distinguished from it). Once vector hits are obtained, a pattern recognition program combines vector hits from adjacent cells into track candidates. A detailed fit using individual wire hit information (at this stage, the stereo layer information gives more precise z information), electric and magnetic field variations, and energy loss gives the six track parameters: the three coordinates of the distance of closest approach to the origin x , y and z , the azimuthal angle ϕ of the track, its curvature κ (related to the transverse momentum p_T by $\kappa = \frac{1}{p_T}$) and the dip angle $\tan \lambda$ (related to the polar angle $\cos \theta$ by $\cos^2 \theta = \cos^2(\frac{\pi}{2} - \lambda) = \frac{\tan^2 \lambda}{1 + \tan^2 \lambda}$). The transverse

5. THE DETECTOR

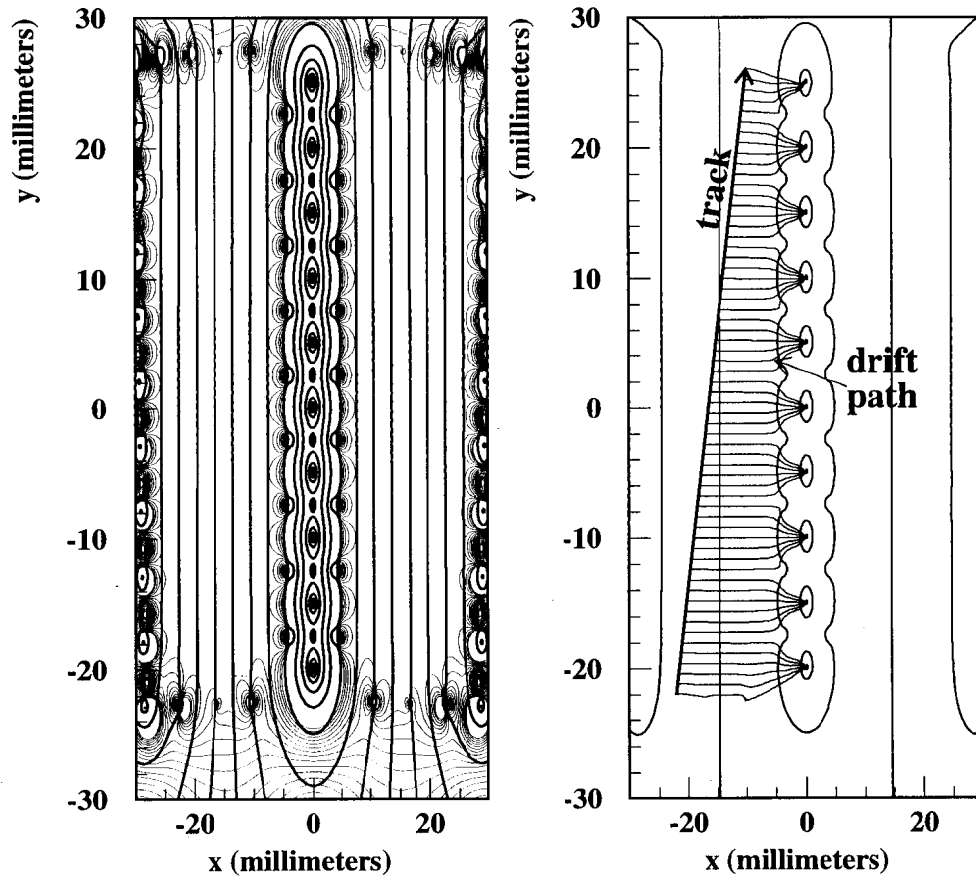


Figure 5.10: The field map for a drift cell of the CDC. The left figure shows lines of constant potential (bold) and lines of constant field strength(thin) within a CDC cell. The right figure shows a drift path of charges caused by the passing of a charged track through the cell.

5. THE DETECTOR

momentum is the projection of the momentum in the plane perpendicular to the beam axis (or B-field direction). The total momentum is then $p = p_T \sqrt{1 + \tan^2 \lambda}$. The momentum resolution function for the CDC has been measured to be $(dp_T/p_T)^2 = 0.0050^2 + (0.010/p_T)^2$, where p_T is in units of GeV/c. The first term in the resolution function is the multiple scattering error, and the second term is the measurement error term [8].

5.4. The Čerenkov Ring-Imaging Detector (CRID)

The Čerenkov Ring-Imaging Detector (CRID)³ identifies charged particles over a large momentum range. As with most subsystems, it is divided into a barrel region and two end caps.

The principle by which the CRID(s) operate is the following: For a charged particle traveling with velocity $v = \beta c$ in a medium of index of refraction n , Čerenkov photons are emitted at an angle of $\cos \theta_c = \frac{1}{\beta n}$ with respect to the particle's flight direction. The relation for $\cos \theta_c$ implies a threshold condition $\beta_{threshold} = 1/n$. If the particle's velocity is below that, no photons are emitted. If it is above threshold, these photons can be emitted at any point along the particle's trajectory, so the Čerenkov radiation forms a cone. All the photons are emitted at the same angle, so a spherical mirror will focus the cone into a ring that is located in the mirror's focal plane.

³A good description of the SLD CRID may be found in K. Baird's PhD thesis "Strange Particle Production in Hadronic Z^0 Decays" [1] or in M. Dima's PhD thesis "Production of Strange Vector Mesons at the Z^0 Resonance" [9]

5. THE DETECTOR

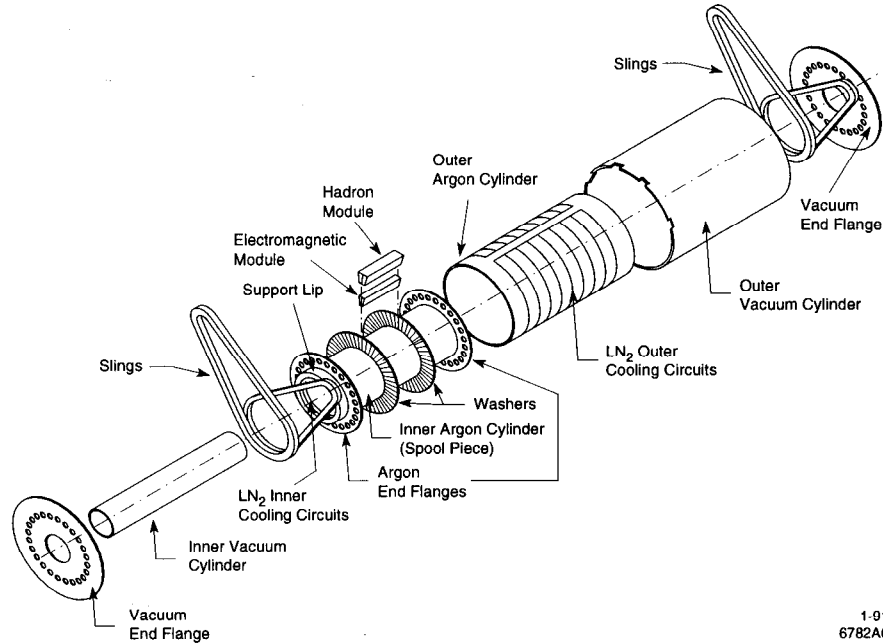


Figure 5.11: Exploded view of the barrel LAC.

Hadronic showers have in addition an invisible energy resulting from neutrinos, muons, nuclear binding energy losses and similar processes. The invisible energy is about 40 % of the total energy. The ratio $\frac{F_{EM}}{F_{HAD}}$ is therefore not unity. If the hadronic response is equalized to the electromagnetic one, the calorimeter is called a *compensating* one. A compensating calorimeter will have better resolution, because the electromagnetic component in the hadronic showers will not matter.

The Liquid Argon Calorimeter (LAC) is a lead-argon sampling calorimeter [3]. Again, the LAC can be broken into three sections: a barrel and two end caps. The barrel, which has an inner radius of 1.8 m and an outer radius of 2.9 m, continuously covers the solid angle between $\theta = 35^\circ$ and $\theta = 145^\circ$ (here, θ is the measured angle

5. THE DETECTOR

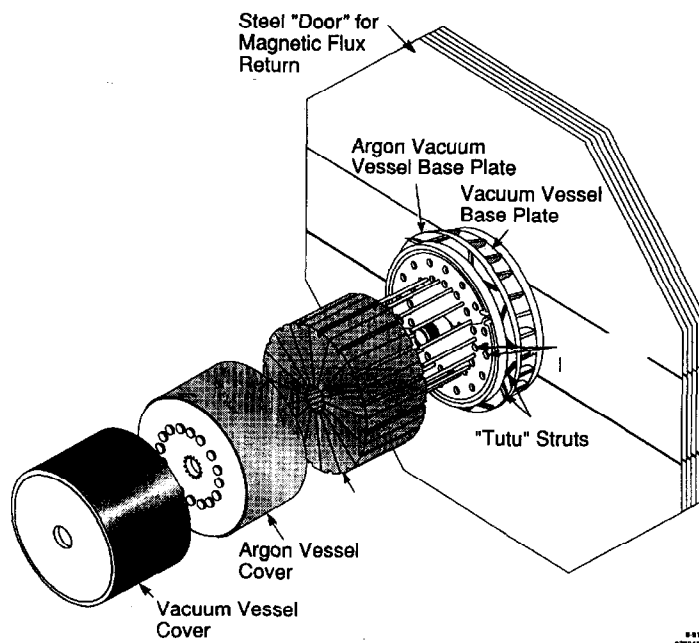


Figure 5.12: Exploded view of the end cap LAC.

with respect to the electron beam direction). An exploded view of the barrel is shown in figure 5.11. The two end cap sections butt against the barrel, and provide coverage between 8° and 35° with respect to the beam pipe. An exploded view of an end cap LAC is pictured in figure 5.12. Overall, the LAC covers 98% of the solid angle around the IP.

Using a liquid argon system for calorimetry has some advantages: It allows for arbitrary transverse segmentation, the dead regions can be minimized, the LAC works inside SLD's magnetic field of 0.6 T, it is radiation hard and it is a sampling medium with a gain of unity. The energy resolution is excellent even with thin absorber layers, because argon is a dense sampling medium

5. THE DETECTOR

Layer	#Radiation Lengths	#Interaction Lengths	Angular Segmentation
EM1	6.0	0.24	33 mrad × 28 mrad
EM2	15.0	0.60	33 mrad × 28 mrad
HAD1	25	1.00	66 mrad × 56 mrad
HAD2	25	1.00	66 mrad × 56 mrad
total	71	2.84	

Table 5.2: Geometrical properties of the LAC. All the thicknesses listed are at normal incidence. The angular segmentation is listed as $\Delta\theta \times \Delta\phi$.

The barrel as well as the end cap LAC are inside one dewar that holds the liquid argon. The LAC has an “onion skin” structure. The two innermost layers are relatively thin, and measure the energy from electromagnetic showers. The two outer layers are denser in composition, and measure the energy in hadronic showers due to the interaction of neutral or charged hadrons. Overall, there are 21 radiation lengths of material in the electromagnetic (EM) sections of the LAC, and 2 interaction lengths in the hadronic (HAD) sections. In total, there are $2.8\lambda_0$ of material in the LAC. Table 5.2 lists the amount of material in all four sections of the LAC.

The barrel and end cap portions of the LAC are segmented in polar angle and azimuthal angle, thus allowing for spatial determination of the energy shower. The segmentation and module thicknesses were chosen to maximize the amount of particle energy sampled, and to be able to differentiate between electromagnetic and hadronic particles. The energy resolution of the LAC has been shown to be $\sim 15\%/\sqrt{E}$ GeV for EM showers and $\sim 60\%/\sqrt{E}$ GeV for hadronic showers [10].

The LAC is divided into modules, an illustration of which is shown in figure 5.13.

5. THE DETECTOR

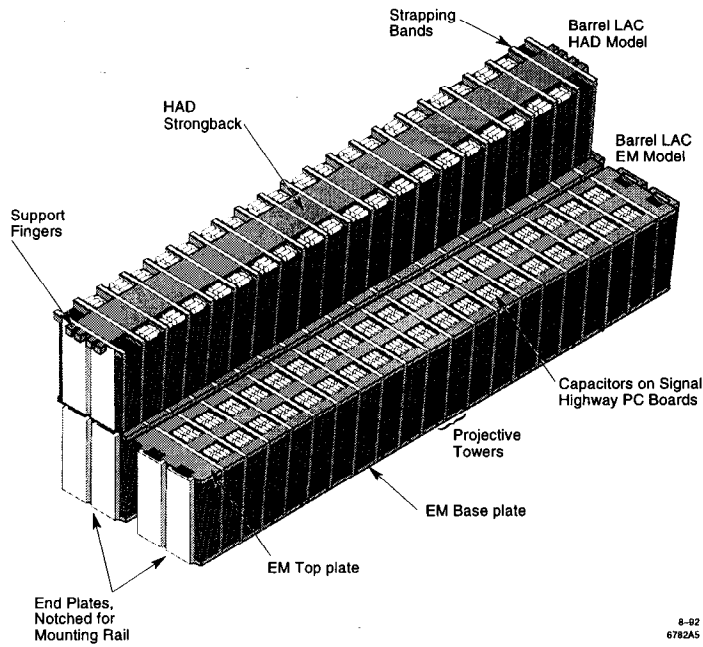


Figure 5.13: View of a LAC module, showing the inner EM and outer HAD sections.

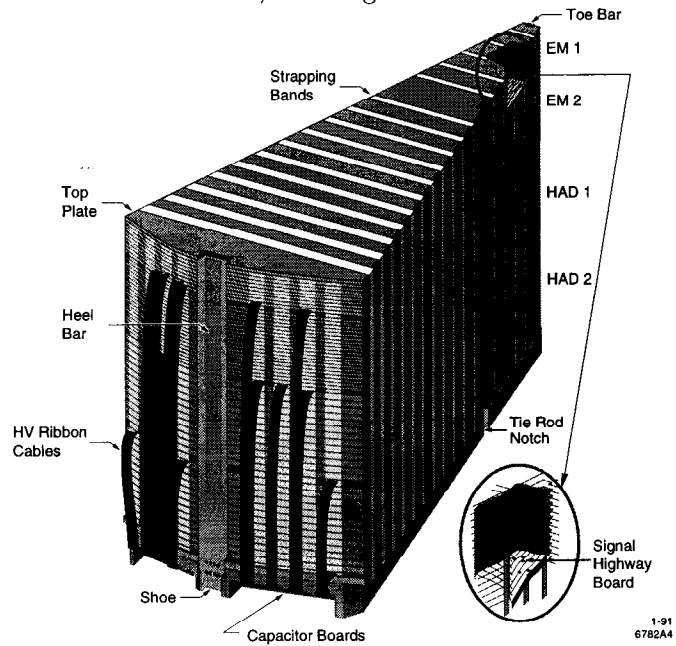


Figure 5.14: View of a LAC end cap module, showing the inner EM (top) and outer HAD sections (bottom).

5. THE DETECTOR

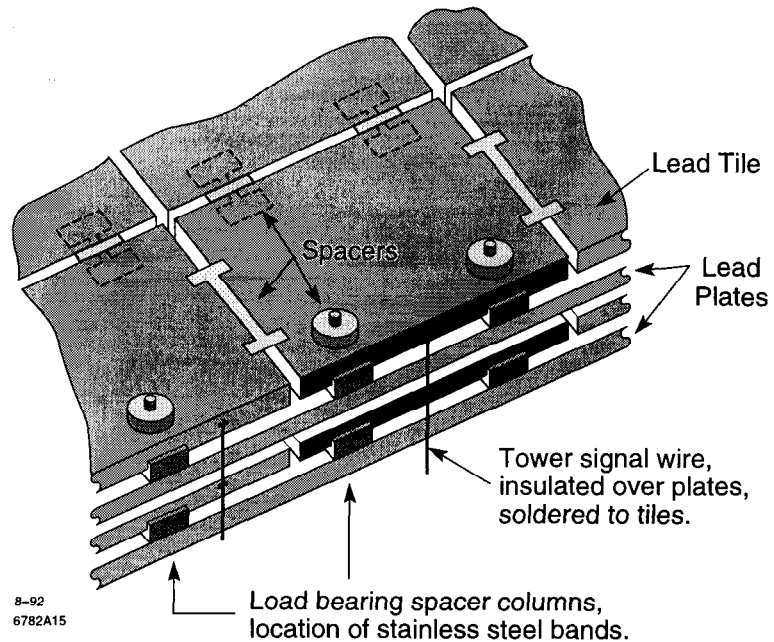


Figure 5.15: A cell from the barrel LAC in detail.

An end cap module (see figure 5.14) contains both the electromagnetic and hadronic section. Each module consists of alternating layers of lead plates, tiles and argon. This structure is shown in figure 5.15. The layers are separated from each other by non-conducting spacers and immersed in a liquid argon bath. Negative high voltage is applied to the tiles while the plates are grounded. Particles which interact with the lead produce a secondary shower of low energy particles which then ionize the argon. The high voltage produces a field which sweeps the liberated charges out of the argon and onto the lead tiles. The tiles are projective and form the so-called towers. (units of constant cross-section when viewed from the IP). Each tower is connected to an amplifier to measure the charge deposited. As the argon supplies no charge

5. THE DETECTOR

amplification, the charge observed is proportional to the energy deposited.

The lead plates and tiles in the EM sections are 2.00 mm thick and are separated by 2.75 mm of liquid argon filled gaps. EM1 consists out of the first 16 layers and EM2 out of the last 40 layers. Together EM1 and EM2 contain 98-99% of a 50 GeV electromagnetic shower. The barrel EM divides the $\theta \times \phi$ plane into 68×192 towers. The end cap divides the azimuth into 192 towers at small $|\cos \theta|$ falling to 96 and to 48 towers near the beam line. The hadronic sections have also 2.75 mm gaps of liquid argon, but the lead plate and tiles have an increased thickness of 6.00 mm.

5.6. The Warm Iron Calorimeter (WIC)

The WIC (Figure 5.16) serves four functions at SLD: as the flux return for the solenoid, as a calorimeter to measure residual hadronic energy that has "leaked" through the LAC, as a muon-identification system and as support structure for the rest of the detector components. The WIC consists of 18 layers of Iarrocì streamer tubes sandwiched between 5 cm thick steel plates [12]. These tubes are instrumented with square readout pads for calorimetric purposes, and with long conducting strips in order to perform muon tracking. These strips are laid in two separate arrays at 90° with respect to each other in order to measure the trajectory of the muon in 2D. The amount of material in the WIC is summarized in table 5.3.

5. THE DETECTOR

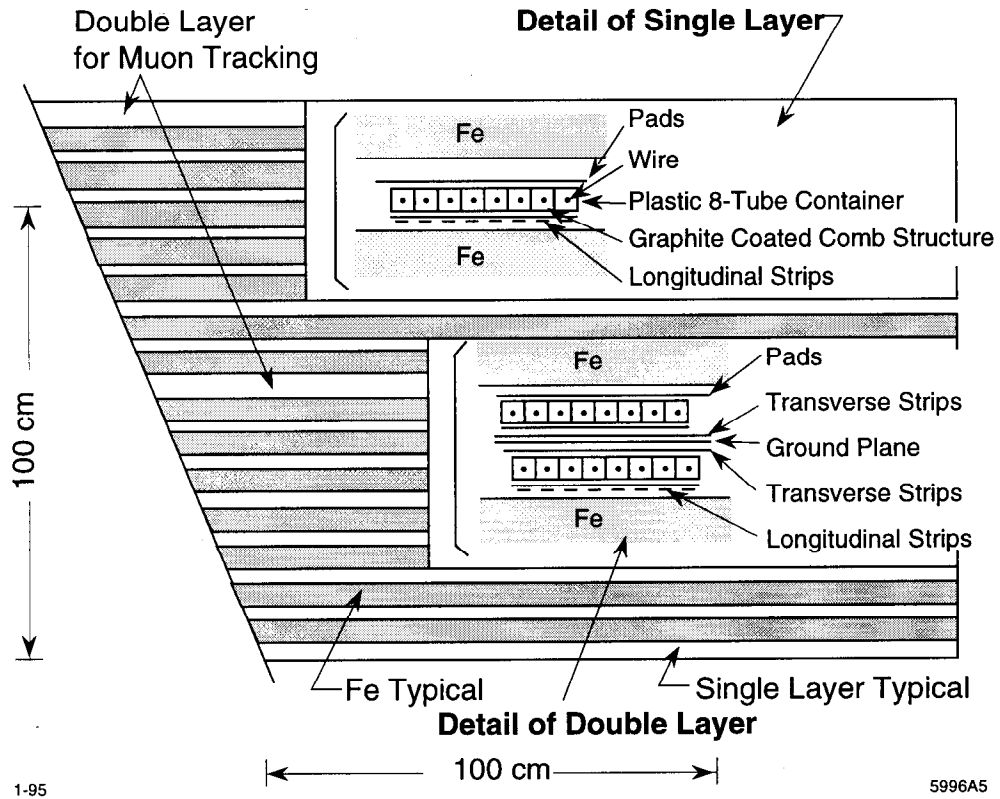


Figure 5.16: Cut away view of the WIC.

Layer	#Radiation Lengths	#Interaction Lengths	Angular Segmentation
LAC	71	2.8	
WIC 1	50	2.0	66 mrad
WIC 2	50	2.0	66 mrad
Total	171	6.8	

Table 5.3: Geometrical properties of the WIC. All the thicknesses listed are at normal incidence. The angular segmentation is listed as $\Delta\phi$.

Bibliography

- [1] K. Baird, Ph.D Thesis, (April 1996), SLAC-Report-483
- [2] T. Junk, Ph.D Thesis, (November 1995), SLAC-Report-95-476
- [3] SLD Collaboration (G. Agnew et al., SLD Design Report SLAC-0273 (1984)
- [4] K. Pitts, Ph.D Thesis, University of Oregon (1994), SLAC Report 446
- [5] C. Damerell, *Vertex Detectors*, RAL-86-077 (July 1986)
- [6] The Particle Data Group, Phys. Rev. **D50**, Part I (1994)
- [7] M. Strauss, SLAC Pub 6686, (1994)
- [8] M. Hildreth et al., SLAC Pub 6656, (1994)
- [9] M. Dima, Ph.D Thesis, Colorado State University (1996), SLAC-R-0505
- [10] SLD Collaboration (K. Abe et al.), Nucl. Inst. and Meth. **A328** (1993) 472
- [11] S. Martirena, Ph.D Thesis, (April 1994), SLAC-Report-439

BIBLIOGRAPHY

- [12] D. C. Williams, Ph.D Thesis, Mass. Institute of Technology (1994),
SLAC Report 445,
SLD Collaboration (K. Abe et al.), Phys. Rev. Lett. **74** (1995) 2895

Chapter 6

The Likelihood Function

The leptonic coupling asymmetry parameters A_e , A_μ and A_τ are extracted from the polarized angular distributions of $e^+e_{L,R}^- \rightarrow e^+e^-$, $e^+e_{L,R}^- \rightarrow Z \rightarrow \mu^+\mu^-$ and $e^+e_{L,R}^- \rightarrow Z \rightarrow \tau^+\tau^-$. This is done with an unbinned maximum likelihood fit of the theoretical cross section to these distributions with the coupling asymmetries as free parameters.

6.1. Likelihood Function for μ and τ pair production

The tree-level cross section is the sum of three terms (see equation 2.11)

$$\begin{aligned}
 \frac{d\sigma_{\gamma(s)}}{dx} &= f_{\gamma(s)}(1+x^2) \\
 \frac{d\sigma_{\gamma(s)Z(s)}}{dx} &= f_{\gamma(s)Z(s)} \frac{g_V^e g_V^l}{g_A^e g_A^l} \left(\left(1 + P \frac{g_A^e}{g_V^e}\right) (1+x^2) + \left(P + \frac{g_A^e}{g_V^e}\right) \frac{g_A^l}{g_V^l} 2x \right) \\
 \frac{d\sigma_{Z(s)}}{dx} &= f_{Z(s)} ((1 + PA_e)(1+x^2) + (P + A_e)A_l 2x)
 \end{aligned} \tag{6.1}$$

6. THE LIKELIHOOD FUNCTION

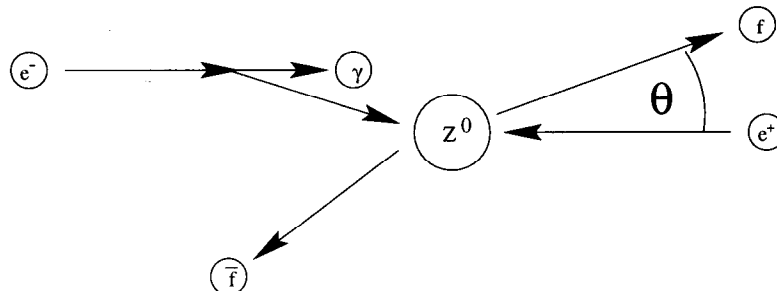


Figure 6.1: Initial-state radiation. The center-of-mass energy at the boson production vertex is reduced by the amount of energy carried away by a photon emitted along the beam pipe.

with $x = \cos \theta$ and the tree-level coefficients

$$\begin{aligned}
 f_{\gamma(s)}^{\text{tree}} &= \frac{\pi\alpha^2}{2s} \\
 f_{\gamma(s)Z(s)}^{\text{tree}} &= \frac{\pi\alpha^2}{2s2\sin^2\theta_W\cos^2\theta_W} 2\frac{s(s-M_Z^2)}{(s-M_Z^2)^2 + \frac{s^2}{M_Z^2}\Gamma_Z^2} g_A^e g_A^l \\
 f_{Z(s)}^{\text{tree}} &= \frac{\pi\alpha^2}{2s(2\sin^2\theta_W\cos^2\theta_W)^2} \frac{s^2}{(s-M_Z^2)^2 + \frac{s^2}{M_Z^2}\Gamma_Z^2} (g_V^{e^2} + g_A^{e^2})(g_V^{l^2} + g_A^{l^2}) \quad (6.2)
 \end{aligned}$$

Higher order diagrams describe initial- and final-state (photon) radiation as well as fermion loops and vertex corrections. The Z line shape (Z production cross section as a function of center-of-mass energy \sqrt{s}) is modified considerably by initial-state radiation. Above the pole of the resonance, the probability of emitting a photon going (roughly) along the beam pipe and producing an on-shell Z boson is quite high (see figure 6.1). Therefore, the Z production cross section falls more slowly with increasing center-of-mass energy than expected from a tree-level calculation. At and below the pole of the resonance, initial state radiation can occur as well, which increases the

6. THE LIKELIHOOD FUNCTION

probability of a virtual photon exchange compared to the probability of exchanging a virtual Z boson. The SLC center-of-mass energy is slightly above the pole, so the tree-level calculation predicts positive $Z - \gamma$ interference terms. Due to initial-state radiation, these terms become negative (on the average, the effective center-of-mass energy $\sqrt{s'}$ at the boson production vertex is below the Z mass).

Radiative corrections are done to this cross section under the assumption that the shapes of each of the three terms remain the same and only the coefficients (6.2) get modified. Radiative corrections need to take into account initial- and final-state radiation and loops that modify the coupling constant α . I used the program MIZA [1] to calculate the unpolarized cross-section for each of the three terms which are directly proportional to the coefficients (6.2). MIZA removes some of the dependence on the standard model by replacing (6.2) with

$$\begin{aligned}
 f_{\gamma(s)}^{\text{tree}} &= \frac{\pi\alpha^2}{2s} \\
 f_{\gamma(s)Z(s)}^{\text{tree}} &= \frac{\pi\alpha^2}{2s^2 \sin^2 \theta_W \cos^2 \theta_W} 2 \frac{s(s - M_Z^2)}{(s - M_Z^2)^2 + s^2 \Gamma_Z^2 / M_Z^2} g_A^e g_A^l \\
 f_{Z(s)}^{\text{tree}} &= \frac{9\pi}{2} \frac{s}{(s - M_Z^2)^2 + s^2 \Gamma_Z^2 / M_Z^2} \frac{\Gamma_{ee} \Gamma_{ll}}{M_Z^2}
 \end{aligned} \tag{6.3}$$

These expressions are now convoluted with the QED initial state radiator times the μ pair selection efficiency $\epsilon_\mu(s')$ which is determined from SLD Monte Carlo. s' is the center-of-mass squared energy after initial state radiation has taken place. The efficiency can be seen in figure 6.2

6. THE LIKELIHOOD FUNCTION

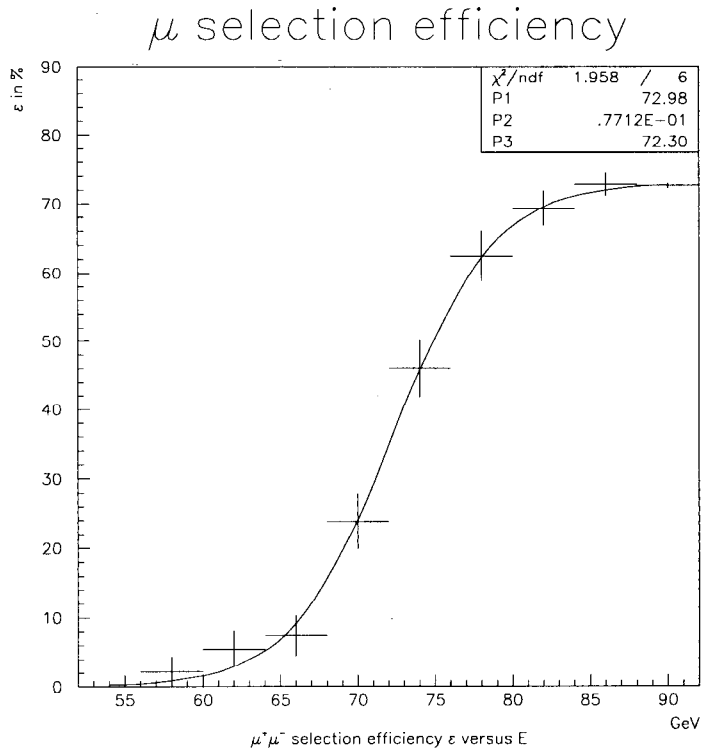


Figure 6.2: μ selection efficiency as a function of the center of mass energy $\sqrt{s'}$. The fit is the parameterization function $\frac{p_1}{1+e^{-4p_2(x-p_3)}}$, so p_1 is the efficiency in the peak region, p_3 is the cut-off energy and p_2 is the slope at the cut-off energy.

Both the energy spread of the SLC beams and the change of the central value of the energy over the course of the run need to be taken into account as well. The energy spread of SLC is about 200 MeV. To investigate the change of the central value of the energy, I plotted the distribution of this central value in the center of mass frame in figure 6.3 and fit this distribution with a Gaussian. I integrate all three coefficients over a normalized Gaussian of width 200 MeV and vary the central value of this normalized Gaussian by $\pm\sigma = \pm 57.76\text{MeV}$ (see figure 6.3) to estimate the

6. THE LIKELIHOOD FUNCTION

Measured SLC cms Energy

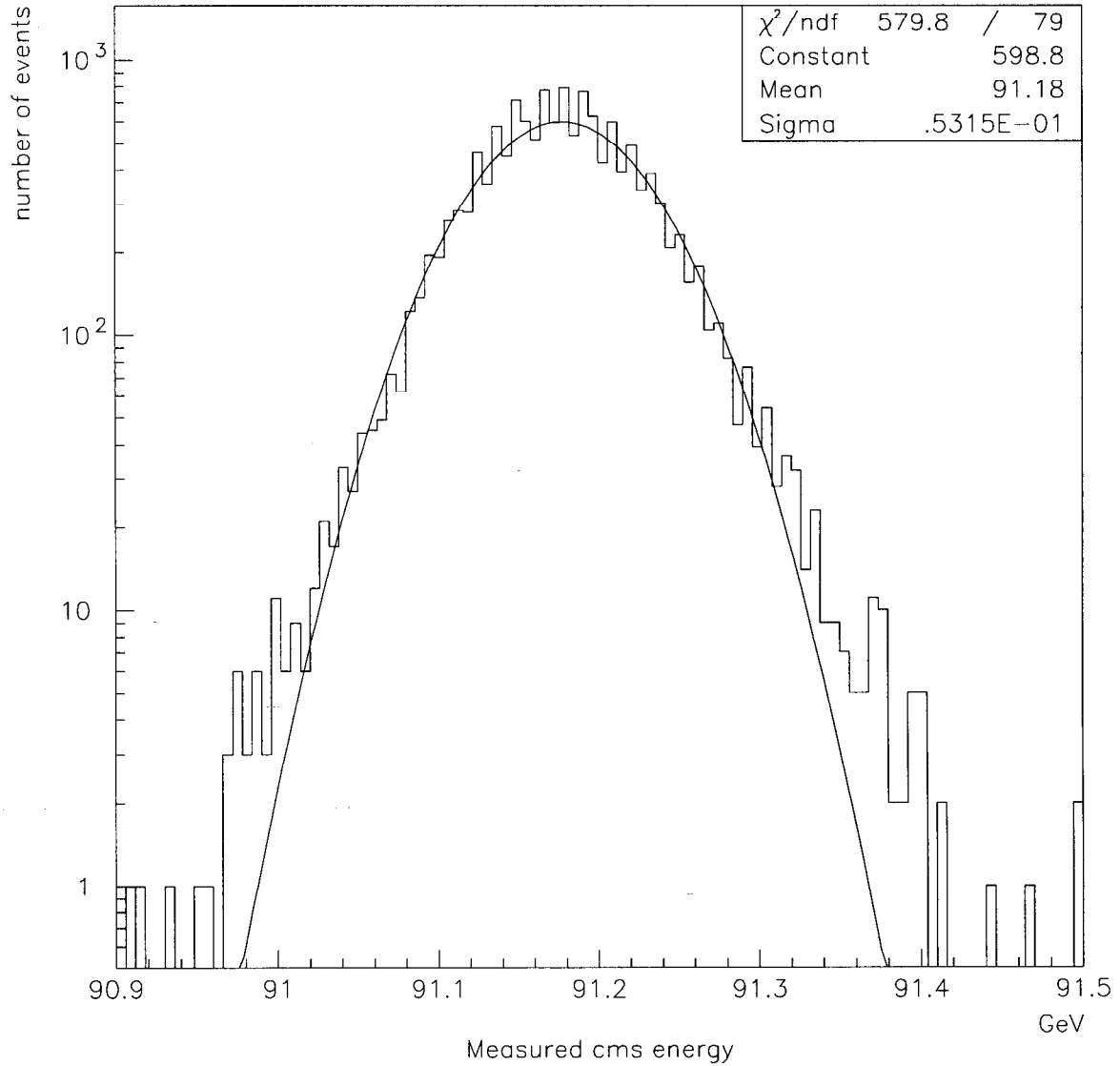


Figure 6.3: Measured center of mass energy for events passing the pre-selection cuts. The corrected mean value is 91.28 GeV. I use a width of 57.76 MeV (rather than 53.15 MeV) as measured by the polarimeter group [3], since it is determined from a larger (hadronic) sample.

6. THE LIKELIHOOD FUNCTION

τ selection efficiency

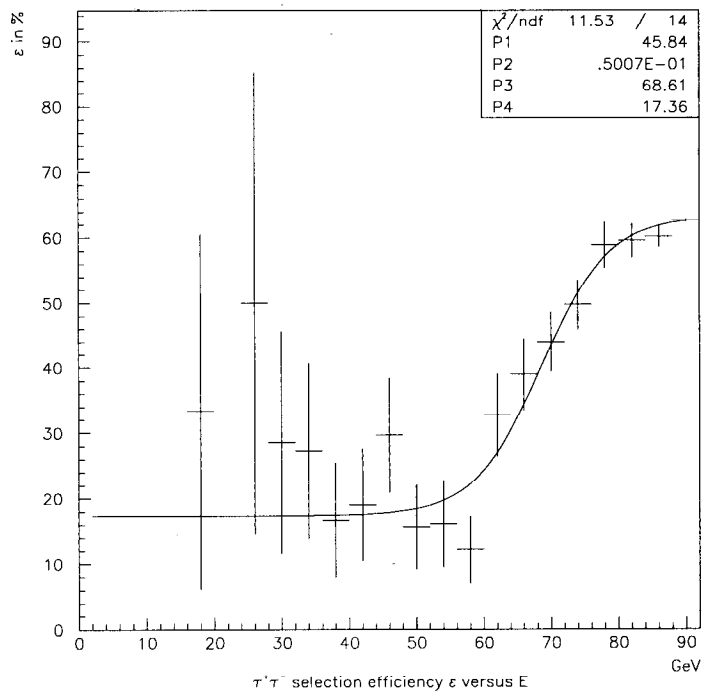


Figure 6.4: τ selection efficiency as a function of the center of mass energy $\sqrt{s'}$. The fit is the parameterization function $\frac{p_1}{1+e^{-4p_2(x-p_3)}} + p_4$, so p_1 is the efficiency in the peak region, p_3 is the cut-off energy and p_2 is the slope at the cut-off energy. p_4 is the residual efficiency at low energies.

systematic uncertainty due to variation in the central value of the energy.

For the purpose of measuring the lepton coupling asymmetries A_l , the value for the total cross section is irrelevant, so the sum of the coefficients (6.3) is normalized to 100. The coefficients for μ pair production I obtained are listed in table 6.1.

For τ pair production, the same procedure is followed as for the μ 's. The τ selection efficiency is plotted in figure 6.4. I integrate again over the Gaussian of figure 6.3 and obtain the coefficients for τ pair production. The coefficients for μ and

6. THE LIKELIHOOD FUNCTION

Coefficient	tree-level	Muon	Tau
$f_{\gamma(s)}$	0.591	1.428 ± 0.012	0.913 ± 0.010
$f_{\gamma(s)Z(s)}$	1.127	-1.568 ± 0.674	-1.524 ± 0.563
$f_{Z(s)}$	98.282	100.140 ± 0.662	100.611 ± 0.555

Table 6.1: Coefficients for Lepton production cross section. Note the sign change of the $Z - \gamma$ interference term.

τ pairs are summarized in table 6.1.

6.2. Likelihood Function for $e^+e^- \rightarrow e^+e^-$

The presence of t -channel diagrams modifies (6.1) to (see equation 2.10)

$$\begin{aligned}
 \frac{d\sigma_{\gamma(s)}}{dx} &= f_{\gamma(s)}(1+x^2) \\
 \frac{d\sigma_{\gamma(s)\gamma(t)}}{dx} &= f_{\gamma(s)\gamma(t)} \frac{(x+1)^2}{x-1} \\
 \frac{d\sigma_{\gamma(t)}}{dx} &= f_{\gamma(t)} \frac{4+(x+1)^2}{(x-1)^2} \\
 \frac{d\sigma_{\gamma(s)Z(s)}}{dx} &= f_{\gamma(s)Z(s)} g_V^2 \left(\left(1 + P \frac{g_A^e}{g_V^e}\right) (1+x^2) + \left(P + \frac{g_A^e}{g_V^e}\right) \frac{g_A^e}{g_V^e} 2x \right) \\
 \frac{d\sigma_{\gamma(t)Z(s)}}{dx} &= f_{\gamma(t)Z(s)} (g_V^{e2} + g_A^{e2}) (1 + PA_e) \frac{(x+1)^2}{(x-1)} \\
 \frac{d\sigma_{\gamma(s)Z(t)}}{dx} &= f_{\gamma(s)Z(t)} \frac{2}{x-D} (g_V^{e2} + g_A^{e2}) (1 + PA_e)(x+1)^2 \\
 \frac{d\sigma_{\gamma(t)Z(t)}}{dx} &= f_{\gamma(t)Z(t)} \frac{2}{x-D} \frac{(g_V^{e2} + g_A^{e2}) (1 + PA_e)(x+1)^2 + (g_V^{e2} - g_A^{e2}) \cdot 4}{x-1} \\
 \frac{d\sigma_{Z(s)}}{dx} &= f_{Z(s)} (g_V^{e2} + g_A^{e2})^2 ((1 + PA_e)(1+x^2) + (P + A_e)A_e 2x) \\
 \frac{d\sigma_{Z(s)Z(t)}}{dx} &= f_{Z(s)Z(t)} \frac{2}{x-D} (g_V^{e2} + g_A^{e2})^2 (1 + A_e^2 + 2PA_e)(x+1)^2 \\
 \frac{d\sigma_{Z(t)}}{dx} &= f_{Z(t)} \left(\frac{2}{x-D}\right)^2 (g_V^{e2} + g_A^{e2})^2 ((1 + A_e^2 + 2PA_e)(x+1)^2 + (1 - A_e^2) \cdot 4)
 \end{aligned} \tag{6.4}$$

6. THE LIKELIHOOD FUNCTION

with

$$\begin{aligned}
D^{\text{tree}} &= 1 + 2 \frac{M_Z^2}{s} \\
f_{\gamma(s)}^{\text{tree}} &= \frac{\pi\alpha^2}{2s} \\
f_{\gamma(s)\gamma(t)}^{\text{tree}} &= \frac{\pi\alpha^2}{2s} 2 \\
f_{\gamma(t)}^{\text{tree}} &= \frac{\pi\alpha^2}{2s} 2 \\
f_{\gamma(s)Z(s)}^{\text{tree}} &= \frac{\pi\alpha^2}{2s 2 \sin^2 \theta_W \cos^2 \theta_W} 2 \frac{s(s - M_Z^2)}{(s - M_Z^2)^2 + \frac{s^2}{M_Z^2} \Gamma_Z^2} \\
f_{\gamma(t)Z(s)}^{\text{tree}} &= \frac{\pi\alpha^2}{2s 2 \sin^2 \theta_W \cos^2 \theta_W} 2 \frac{s(s - M_Z^2)}{(s - M_Z^2)^2 + \frac{s^2}{M_Z^2} \Gamma_Z^2} \\
f_{\gamma(s)Z(t)}^{\text{tree}} &= \frac{\pi\alpha^2}{2s 2 \sin^2 \theta_W \cos^2 \theta_W} \\
f_{\gamma(t)Z(t)}^{\text{tree}} &= \frac{\pi\alpha^2}{2s 2 \sin^2 \theta_W \cos^2 \theta_W} 2 \\
f_{Z(s)}^{\text{tree}} &= \frac{\pi\alpha^2}{2s (2 \sin^2 \theta_W \cos^2 \theta_W)^2} \frac{s^2}{(s - M_Z^2)^2 + \frac{s^2}{M_Z^2} \Gamma_Z^2} \\
f_{Z(s)Z(t)}^{\text{tree}} &= \frac{\pi\alpha^2}{2s (2 \sin^2 \theta_W \cos^2 \theta_W)^2} \frac{s(s - M_Z^2)}{(s - M_Z^2)^2 + \frac{s^2}{M_Z^2} \Gamma_Z^2} \\
f_{Z(t)}^{\text{tree}} &= \frac{\pi\alpha^2}{2s (2 \sin^2 \theta_W \cos^2 \theta_W)^2} \frac{1}{2}
\end{aligned} \tag{6.5}$$

Radiative corrections again use the assumption that the shapes of each of all the terms remain the same and only the coefficients (6.5) get modified. I used the program MIBA [2] to calculate the unpolarized cross-section for each of the ten terms which are no longer directly proportional to the coefficients (6.2) but can still be calculated. For this purpose, I integrated the terms 6.4 over a symmetric range of $|\cos \theta| < c$

6. THE LIKELIHOOD FUNCTION

with $c = 0.7$.

$$\begin{aligned}
 \sigma_{\gamma(s)} &= f_{\gamma(s)} 2c \left(1 + \frac{c^2}{3}\right) \\
 \sigma_{\gamma(s)\gamma(t)} &= f_{\gamma(s)\gamma(t)} 2 \left(3c + 2 \log \frac{1-c}{1+c}\right) \\
 \sigma_{\gamma(t)} &= f_{\gamma(t)} 2 \left(c + 2 \log \frac{1-c}{1+c} + \frac{8c}{1-c^2}\right) \\
 \sigma_{\gamma(s)Z(s)} &= f_{\gamma(s)Z(s)} g_V^2 \left(1 + P \frac{g_A^e}{g_V^e}\right) 2c \left(1 + \frac{c^2}{3}\right) \\
 \sigma_{\gamma(t)Z(s)} &= f_{\gamma(t)Z(s)} (g_V^{e^2} + g_A^{e^2}) (1 + PA_e) 2 \left(3c + 2 \log \frac{1-c}{1+c}\right) \\
 \sigma_{\gamma(s)Z(t)} &= f_{\gamma(s)Z(t)} (g_V^{e^2} + g_A^{e^2}) (1 + PA_e) 2 \left((D+2)2c + (1+D)^2 \log \frac{D-c}{D+c}\right) \\
 \sigma_{\gamma(t)Z(t)} &= f_{\gamma(t)Z(t)} \times \\
 &\quad \left[\left(g_V^{e^2} + g_A^{e^2}\right) (1 + PA_e) \left(2c + \frac{4}{1-D} \log \frac{1-c}{1+c} + \frac{(1+D)^2}{1-D} \log \frac{D-c}{D+c}\right) \right. \\
 &\quad \left. + \left(g_V^{e^2} - g_A^{e^2}\right) \frac{8}{1-D} \left(\log \frac{1-c}{1+c} - \log \frac{D-c}{D+c}\right) \right] \\
 \sigma_{Z(s)} &= f_{Z(s)} (g_V^{e^2} + g_A^{e^2})^2 (1 + PA_e) 2c \left(1 + \frac{c^2}{3}\right) \\
 \sigma_{Z(s)Z(t)} &= f_{Z(s)Z(t)} (g_V^{e^2} + g_A^{e^2})^2 (1 + A_e^2 + 2PA_e) \times \\
 &\quad 2 \left((D+2)2c + (1+D)^2 \log \frac{D-c}{D+c}\right) \\
 \sigma_{Z(t)} &= f_{Z(t)} (g_V^{e^2} + g_A^{e^2})^2 \times \\
 &\quad 8 \left[(1 + A_e^2 + 2PA_e) \left(c + (1+D) \log \frac{D-c}{D+c} + (1+D)^2 \frac{c}{D^2 - c^2}\right) + \right. \\
 &\quad \left. (1 - A_e^2) 4 \frac{c}{D^2 - c^2} \right] \tag{6.6}
 \end{aligned}$$

MIBA like MIZA removes some of the dependence on the standard model by using Γ_{ee} instead of the weak coupling constant for the pure Z exchange terms.

Alternatively, I used dMIBA [2] which calculates differential rather than integrated

6. THE LIKELIHOOD FUNCTION

Bhabha differential cross section

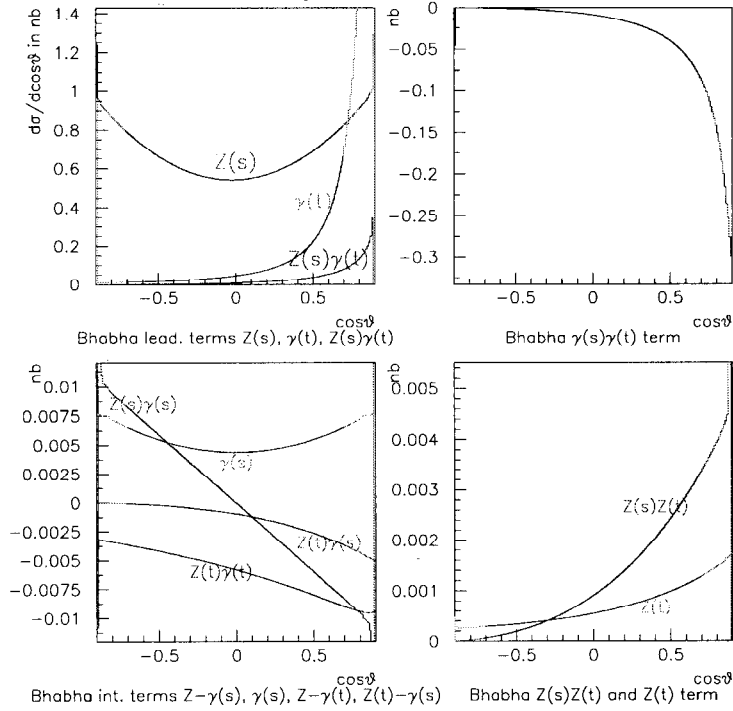


Figure 6.5: Differential cross section for the various Bhabha terms. The histogram for each of the terms is a dMIBA [2] calculation, the smooth function is a tree-level fit with the strength of the term as the only parameter.

cross sections to fit the angular distributions arising from the ten different terms to the tree-level formulas. The resulting coefficients are the same as for MIBA. The results can be seen in figure 6.5. The coupling constant α for some terms runs with t which in turn is a function of $\cos\theta$. Figure 6.5 also shows, that the assumption that the radiative corrections do not affect the shapes of the ten terms is a very good approximation over the interesting range of $\cos\theta$. Finally, the dMIBA fit supplied me with a value for D . Like for the μ 's and τ 's I computed a Bhabha selection efficiency

6. THE LIKELIHOOD FUNCTION

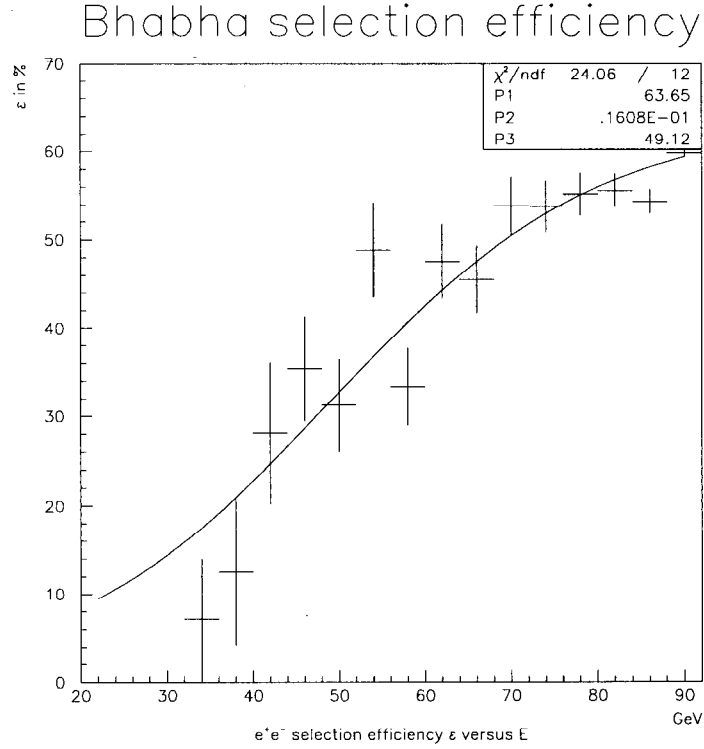


Figure 6.6: Bhabha selection efficiency as a function of the center of mass energy \sqrt{s} . The fit is the parameterization function $\frac{p_1}{1+e^{-4p_2(x-p_3)}}$, so p_1 is the efficiency in the peak region, p_3 is the cut-off energy and p_2 is the slope at the cut-off energy.

(plotted in figure 6.6) which was then folded in the initial state radiator function.

Since the coefficients will depend on the center of mass energy, I computed them for the peak energy of $\sqrt{s} = 91.28\text{GeV}$ as well as for the 1σ variation of $\sqrt{s} = 91.22\text{GeV}$ and $\sqrt{s} = 91.34\text{GeV}$. The dMIBA/MIBA coefficients are listed in table 6.2.

Varying the center of mass energy results in a variation of A_e from the e^+e^- final state of

$$\Delta A_e^e = 8 \cdot 10^{-4}$$

6. THE LIKELIHOOD FUNCTION

Coefficient	Tree Level	dMIBA
D	3.00	3.07
$f_{\gamma(s)}$	3.254	4.384 ± 0.005
$f_{\gamma(s)\gamma(t)}$	6.507	8.911 ± 0.012
$f_{\gamma(t)}$	6.507	8.893 ± 0.021
$f_{\gamma(s)Z(s)}$	24.809	-23.756 ± 15
$f_{\gamma(t)Z(s)}$	24.809	-32.311 ± 15
$f_{\gamma(s)Z(t)}$	4.567	6.029 ± 0.002
$f_{\gamma(t)Z(t)}$	9.133	12.005 ± 0.005
$f_{Z(s)}$	8548.34	8609.96 ± 2.4
$f_{Z(s)Z(t)}$	17.410	-22.081 ± 10
$f_{Z(t)}$	3.205	4.163 ± 0.002

Table 6.2: Coefficients for the Bhabha cross section. Note the sign change in all the $Z(s)$ interference terms.

The systematic uncertainty in A_l for the Muon and Tau sample due to this variation is

$$\Delta A_e^\mu = 6 \cdot 10^{-4} \qquad \Delta A_e^\tau = 12 \cdot 10^{-4}$$

and

$$\Delta A_\mu^\mu = 17 \cdot 17^{-4} \qquad \Delta A_\tau^\tau = 10 \cdot 10^{-4}$$

Bibliography

- [1] M. Martinez (CERN), L. Garrido, R. Miquel (Barcelona, Autonoma U.), J.L. Harton (Wisconsin U., Madison), R. Tanaka (Ecole Polytechnique, LPNHE). CERN-PPE-90-109, Aug 1990. 22pp.
"Model independent fitting to the Z line shape" published in Z.Phys.C49: 645-656, 1991
- [2] M. Martinez, R. Miquel (CERN). CERN-PPE-91-87, Jun 1991. 26pp.
"Fitting the $e^+e^- \rightarrow e^+e^-$ lineshape", published in Z.Phys.C53: 115-126, 1992
- [3] M. J. Fero, SLD Note #249
unpublished

Chapter 7

Event selection

7.1. Events at SLD

There are five types of events at SLD relevant to this analysis(see figure 7.1): hadronic events, two-photon events, Bhabhas, mu-pairs and tau events. I divide each event into two hemispheres (defined by the highest momentum track) and assign each hemisphere to one of the two “leptons” produced in the “Z decay”. An event acollinearity is defined by the angle between the sum of the momenta in each hemisphere.

Hadronic events ($Z \rightarrow q\bar{q}$) usually show a high number of charged tracks(roughly 20). Figure 7.2 shows a typical hadronic event at SLD. I use a pre-selection (combination of angular acceptance cut and a cut on the charged track multiplicity) to remove most of the hadronic events out of the leptonic samples.

7. EVENT SELECTION

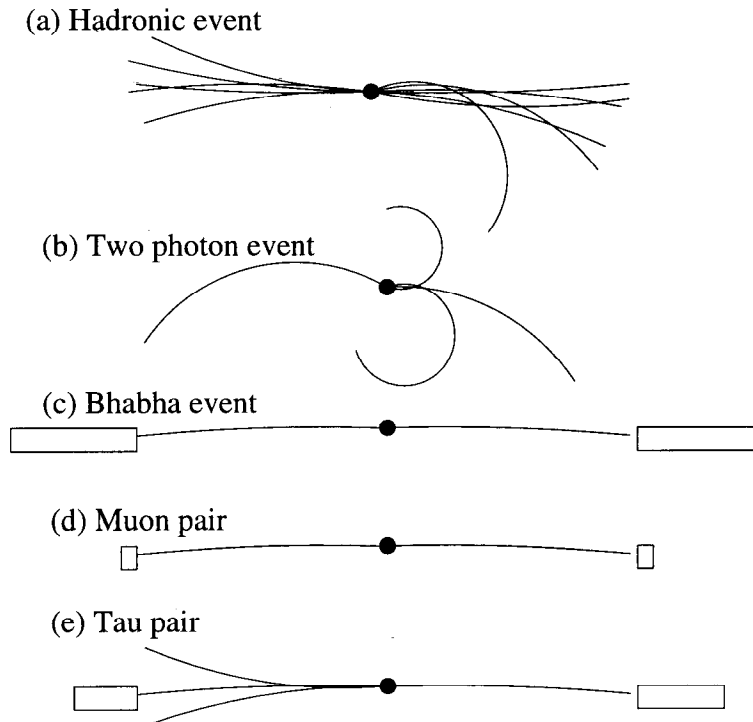


Figure 7.1: Sketch of event types at SLD. (a) Hadronic events have a large number of charged tracks (around 20). (b) Two-photon events are highly boosted (large acollinearity) and have low momentum tracks. (c) Bhabha events have high momentum tracks and deposit a large amount of energy in the (electromagnetic) calorimeter. (d) Muons have high momentum tracks and deposit little energy in the (electromagnetic) calorimeter. (e) Tau events show a small acollinearity and have more tracks than the other leptons.

In two-photon events, a fermion pair is produced by the fusion of a photon emitted by the beam electron and a photon emitted by the beam positron. The charged track multiplicity is low. Most of the energy is carried away by the initial-state particles. Usually, the event is highly boosted which leads to a large acollinearity.

7. EVENT SELECTION

Run 12576,	EVENT 2540
4-JUL-1992 19:18	
Source: Run Data	Pol: L

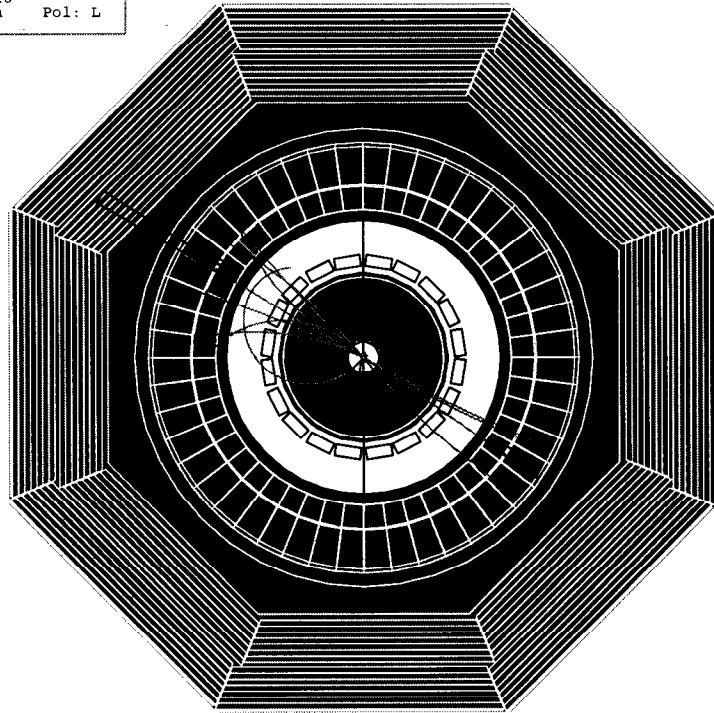


Figure 7.2: Typical hadronic event. Note the large number of charged tracks.

Bhabha events have a low number of charged tracks. Typically, there are two back-to-back high-momentum tracks in the event, which deposit a large amount of energy in the electromagnetic calorimeter. A typical Bhabha event is shown in figure 7.3.

Muon events look similar to Bhabha events, but the high-momentum tracks do not deposit a significant amount of energy in the electromagnetic calorimeter. A typical mu-pair is shown in figure 7.5.

7. EVENT SELECTION

Tau events have a larger charged track multiplicity than the other leptons and show a small acollinearity due to the neutrino emissions in the tau decays. The invariant mass of the event is reduced for the same reason. Typical tau events are shown in figures 7.9 and 7.11.

7.2. The Pre-Selection

The pre-selection selects leptonic events and rejects hadronic events. A typical hadronic event is shown in figure 7.2. It cuts on the acceptance of the detector ($|\cos\theta| < 0.7$) and on the charged particle multiplicity of the event ($2 \leq n_{\text{tracks}} \leq 8$). To insure good identification of the hemisphere charges q_1 and q_2 I want $q_1 \cdot q_2 = -1$. This leaves me with 14401 events (4550 from the 1993 run and 9851 from 1994/95), the purity is 71.48%. The lepton efficiencies within $|\cos\theta| < 0.7$ are $\epsilon_{\text{WAB}} = 92.72\%$, $\epsilon_{\mu} = 95.60\%$ and $\epsilon_{\tau} = 86.19\%$.

7.3. The Bhabha sample

The Bhabha sample is selected from the events passing the pre-selection cuts. A single additional cut is required to select the e^+e^- final state (Bhabha event). I add the LAC energies associated to the two highest momentum tracks in the event and this sum must be greater than 45 GeV. This removes about 8% of the true e^+e^- final state.

7. EVENT SELECTION

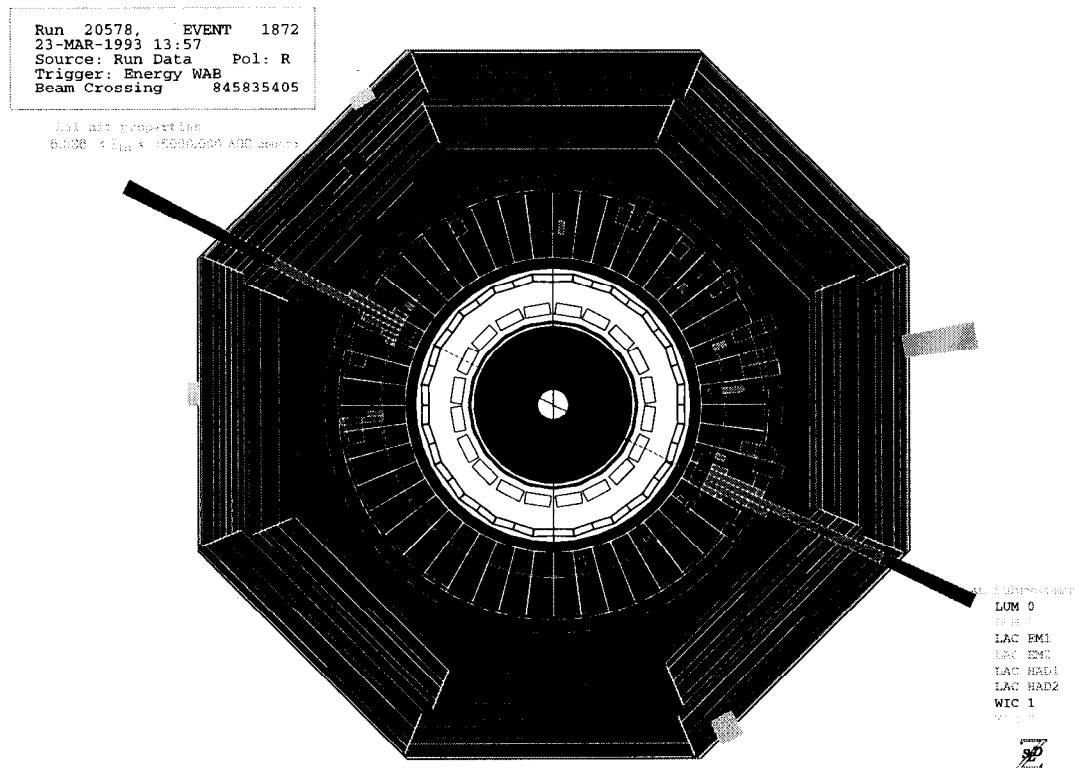


Figure 7.3: Typical Bhabha event. Note the large amount of energy deposited by the two back-to-back high-momentum tracks.

Figure 7.3 shows a typical Wide-Angle Bhabha (WAB) event. A plot of the cut quantity is shown in figure 7.4 The Bhabha selection has an efficiency of 92.45% within my angular acceptance. The purity is 99.29%. The Bhabha sample contains 4527 events.

7. EVENT SELECTION

Bhabha cut: Energy Cluster Sum

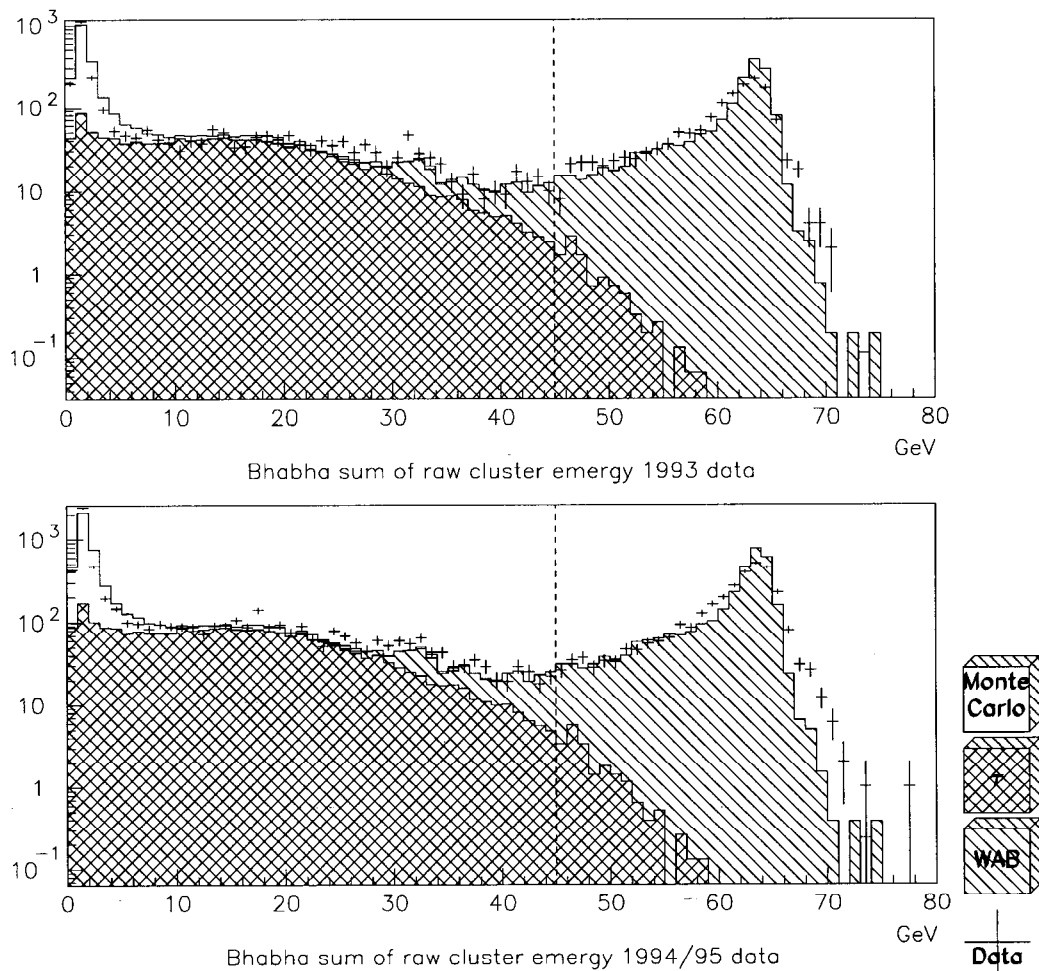


Figure 7.4: Bhabha selection cut on sum of the two largest energy clusters. This cut (indicated with the dashed line) sufficiently suppressed all studied background sources. The data is plotted with crosses, the histogram is Monte Carlo. The shaded areas correspond to τ and Bhabha Monte Carlo. For this plot, the cut has not been applied. Events are accepted to the right of the dashed line.

7. EVENT SELECTION

```
Run 11572, EVENT 3495
20-MAY-1992 08:55
Source: Run Data Pol: R
Trigger: CDC
Beam Crossing 1617986
```

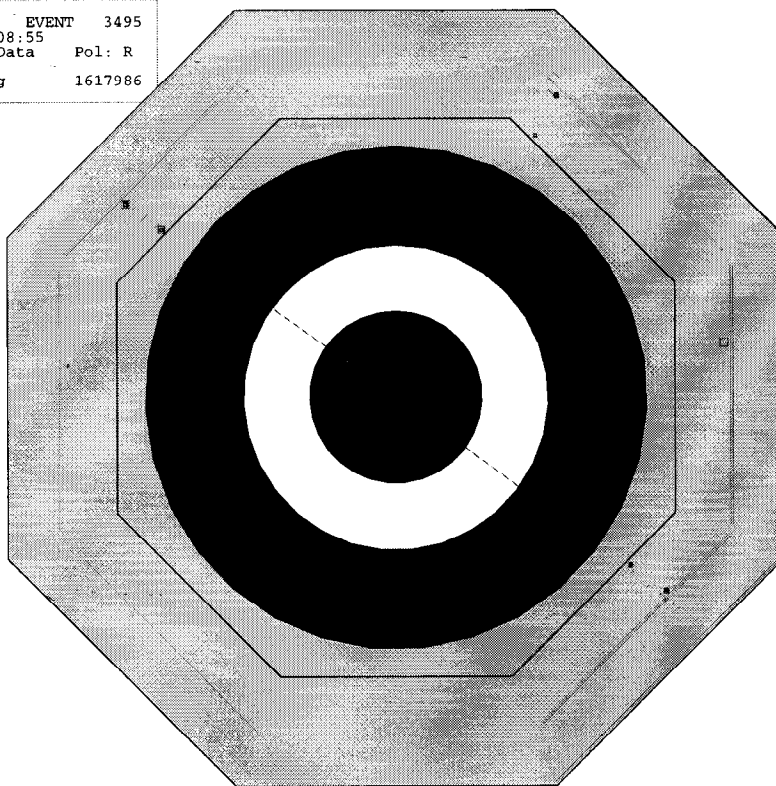


Figure 7.5: Typical mu-pair event. Note the small amount of energy deposited by the two back-to-back high-momentum tracks as indicated by small box symbols compared to figure 7.3.

7.4. The Muon sample

The Muon sample is selected from the events passing the pre-selection cuts by imposing only two cuts:

1. Invariant mass

I compute from the momenta of all charged tracks in an event its invariant mass assigning to each charged particle the pion mass and require this event mass

7. EVENT SELECTION

to be more than 70 GeV. The effect of this cut can be seen in figure 7.6. It removes most of the τ background from the sample.

2. Largest energy cluster

I cut on the largest LAC energy cluster that is associated with a charged track. I require it to be less than 10 GeV but bigger than 0. The effect of this cut is shown in figure 7.7. It removes most of the Bhabha background from the sample.

The μ selection is 95.79% efficient within my angular acceptance. The purity is 99.50%. The μ sample contains 3788 events. The efficiency of the acceptance cut ($|\cos\theta| < 0.7$) is 61.08%.

7.5. The Tau sample

The Tau sample is selected from the events passing the pre-selection cuts by imposing five requirements:

1. Invariant mass

I compute from the momenta of all charged tracks in an event its invariant mass assigning to each charged particle the pion mass and require this event mass to be less than 70 GeV. The effect of this cut can be seen in figure 7.8. It removes most of the μ background from the sample.

7. EVENT SELECTION

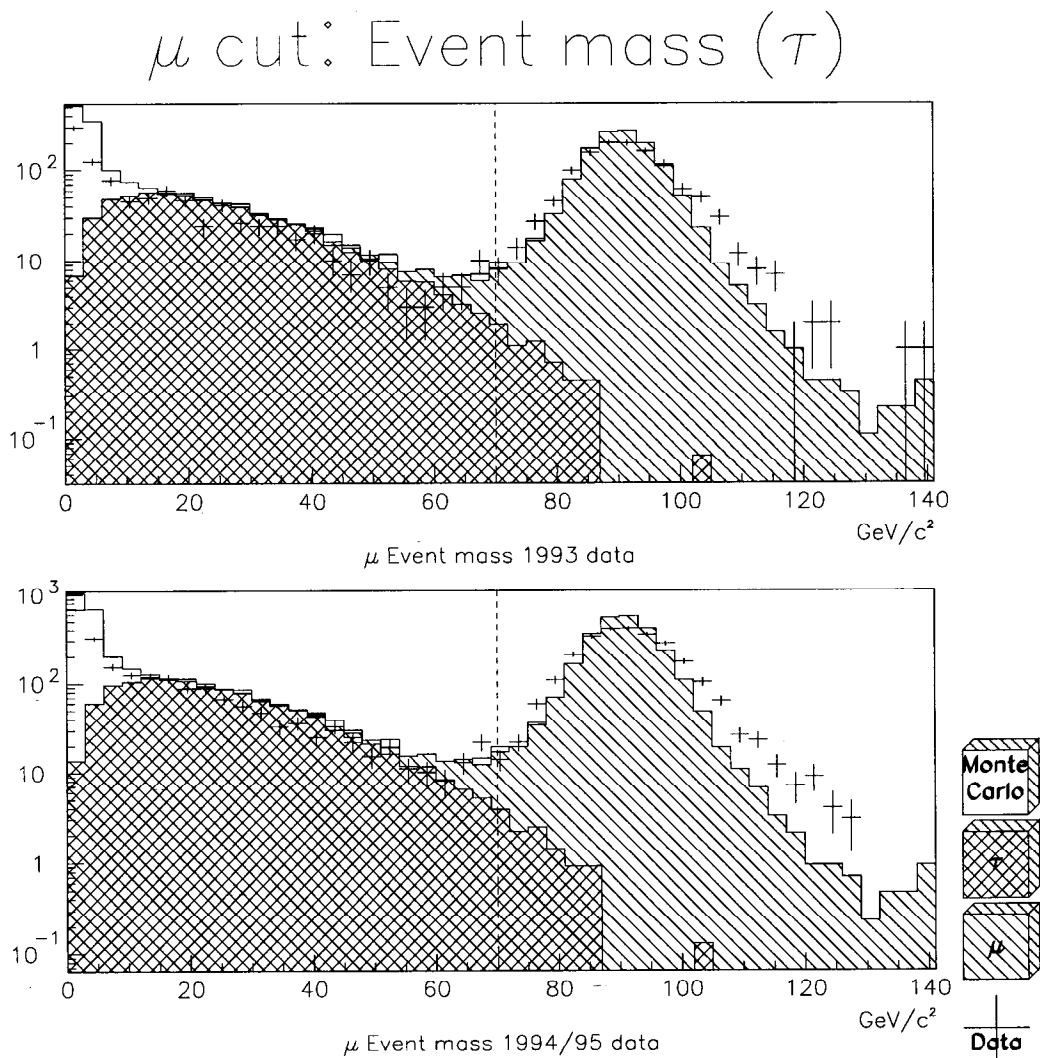


Figure 7.6: μ selection cut 1 on the invariant mass for all charged tracks. This cut (indicated with the dashed line) reduces the τ background. The data is plotted with crosses, the histogram is Monte Carlo. The shaded areas correspond to τ and μ Monte Carlo. All μ selection cuts have been applied except the cut on the invariant mass (1). Events are accepted to the left of the dashed line.

7. EVENT SELECTION

μ cut: max. Energy (WAB)

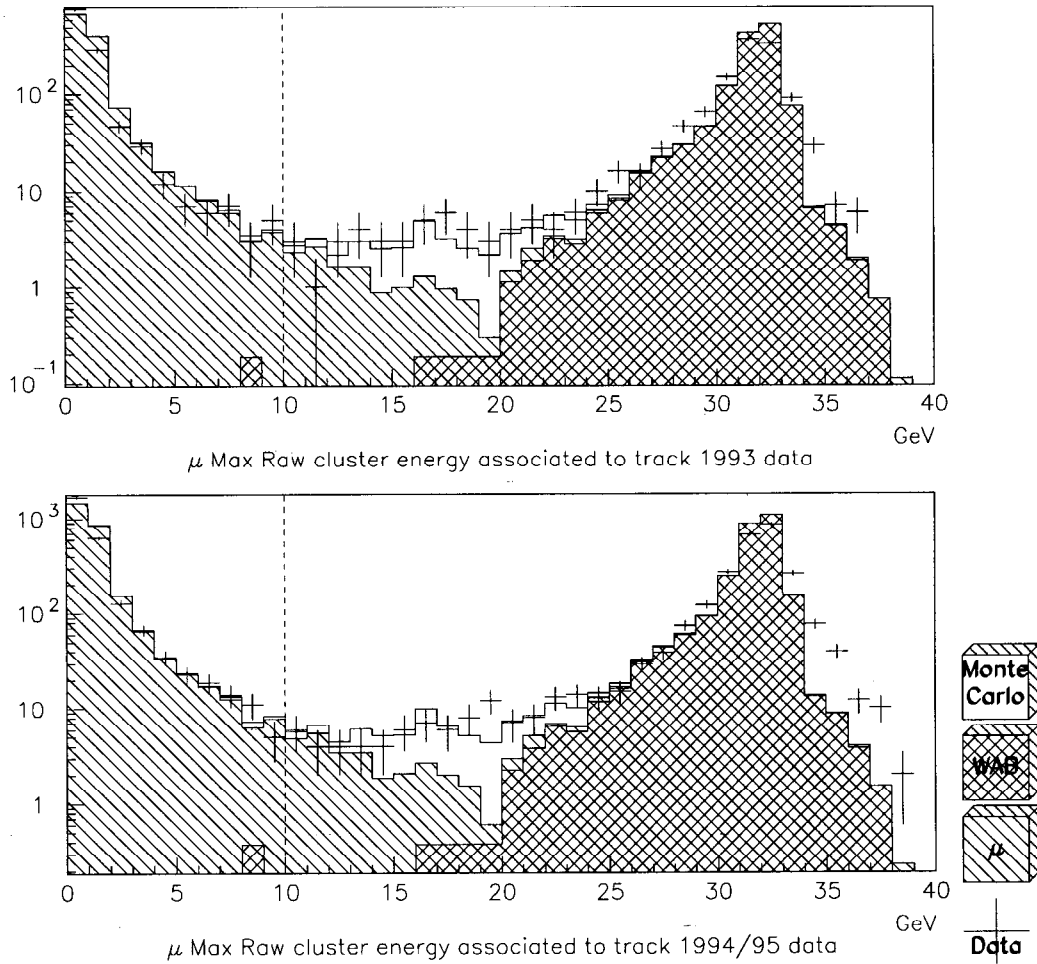


Figure 7.7: μ selection cut 2 on the largest energy cluster associated with a charged track. This cut (indicated with the dashed line) reduces the Bhabha background. The data is plotted with crosses, the histogram is Monte Carlo. The shaded areas correspond to WAB and μ Monte Carlo. The events in the area between 10 GeV and 25 GeV that is not shaded come from the τ Monte Carlo. All μ selection cuts have been applied except the cut on the largest energy cluster (2). Events are accepted to the right of the dashed line.

7. EVENT SELECTION

τ cut: Event mass (μ)

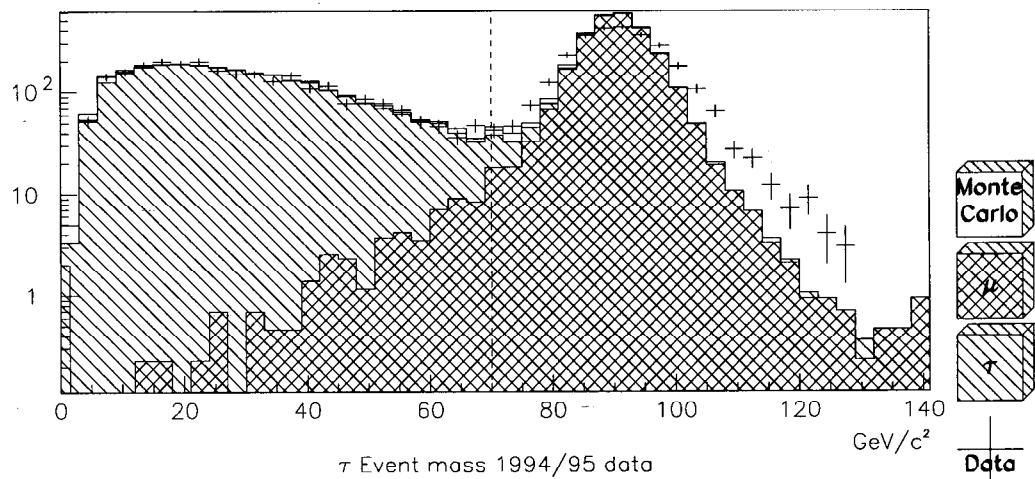
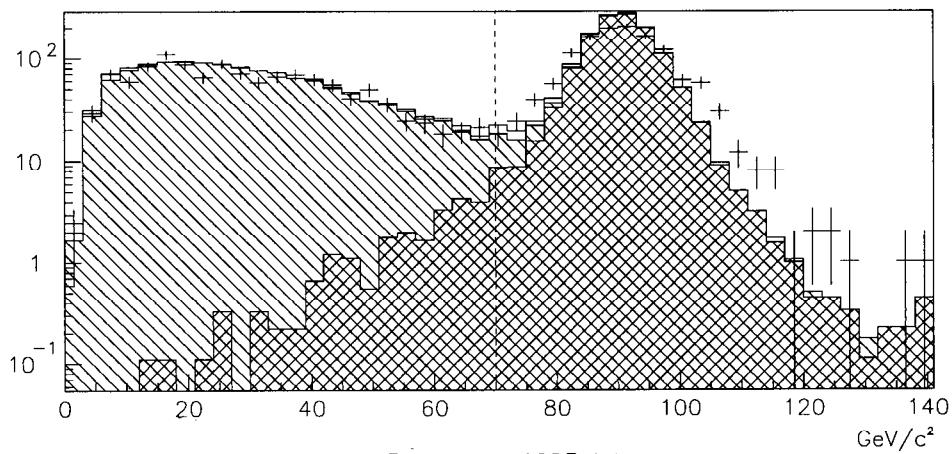


Figure 7.8: τ selection cut 1 on the invariant mass for all charged tracks. This cut (indicated with the dashed line) reduces the μ background. The data is plotted with crosses, the histogram is Monte Carlo. The shaded areas correspond to μ and τ Monte Carlo. All τ selection cuts have been applied except the cut on the invariant mass (1). Events are accepted to the right of the dashed line.

7. EVENT SELECTION

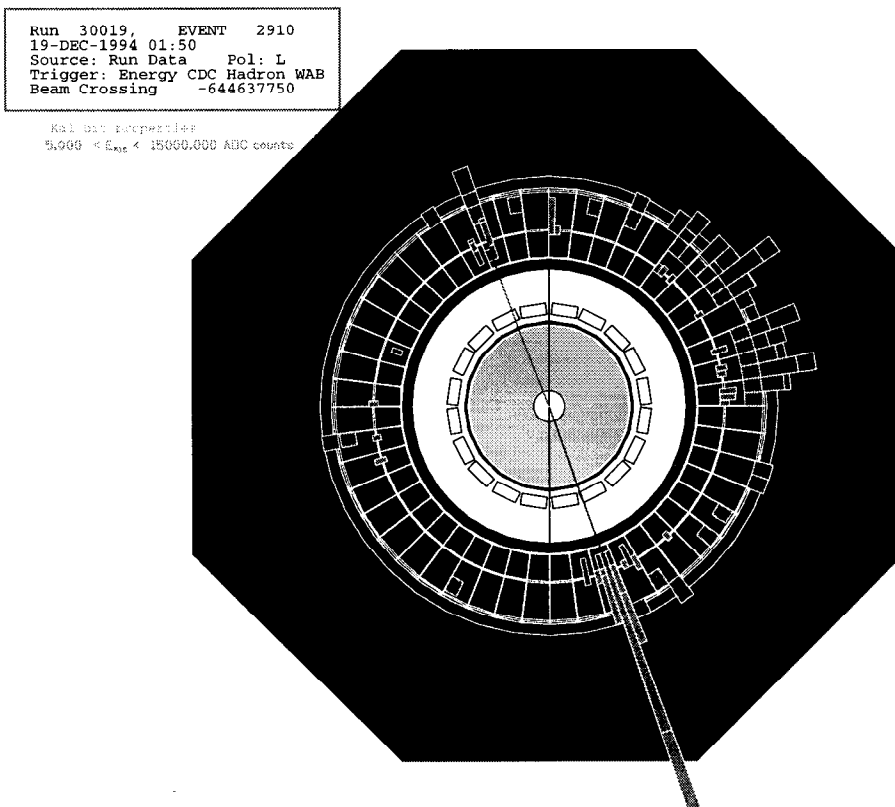


Figure 7.9: Typical Tau event in the 1-1 topology. Note the large amount of energy deposited by one of the two back-to-back high-momentum tracks. One τ probably decayed into a μ , the other into an electron.

2. Largest energy cluster

I cut on the largest energy cluster that is associated with a charged track. I require it to be less than 27.5 GeV but bigger than 0. The effect of this cut is shown in figure 7.10. It removes most of the Bhabha background from the sample.

7. EVENT SELECTION

τ cut: max. Energy (WAB)

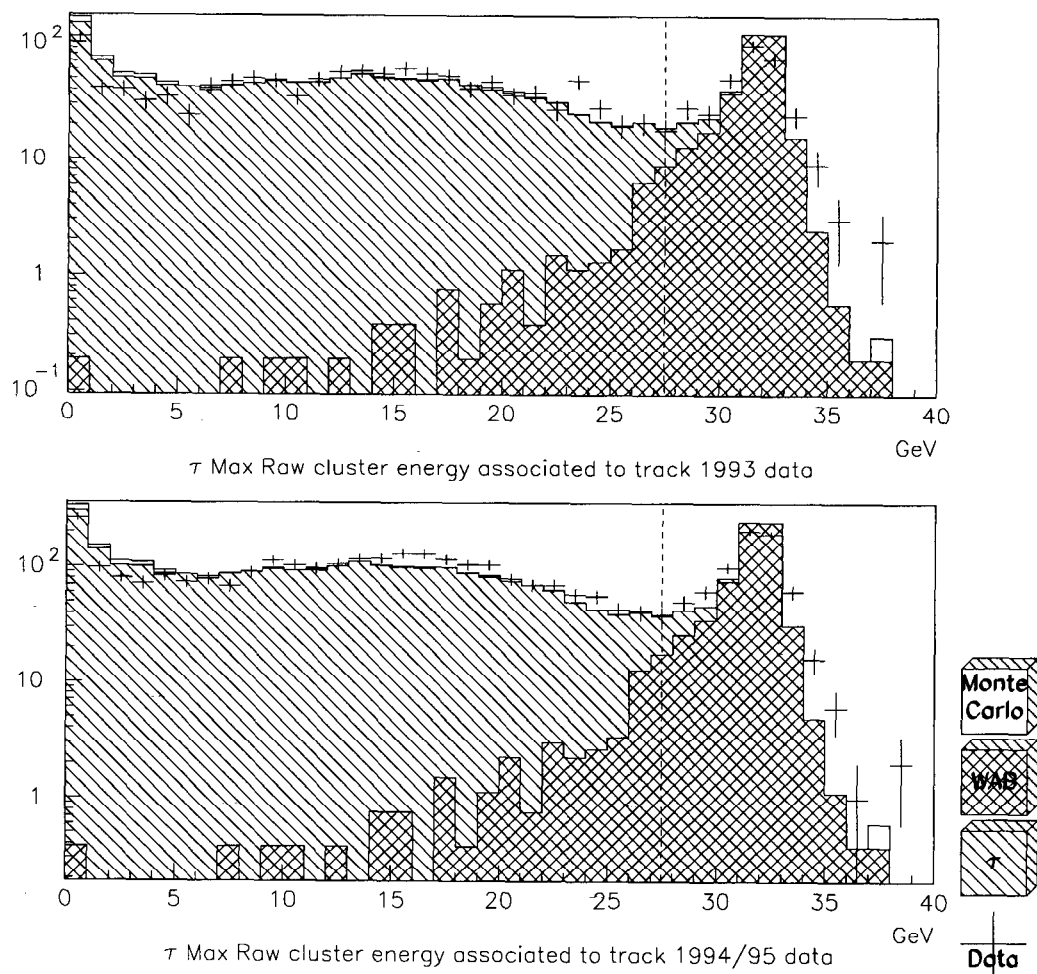


Figure 7.10: τ selection cut 2 on the largest energy cluster associated with a charged track. This cut (indicated with the dashed line) reduces the Bhabha background. The data is plotted with crosses, the histogram is Monte Carlo. The shaded areas correspond to WAB and τ Monte Carlo. All τ selection cuts have been applied except the cut on the largest energy cluster (2).

7. EVENT SELECTION

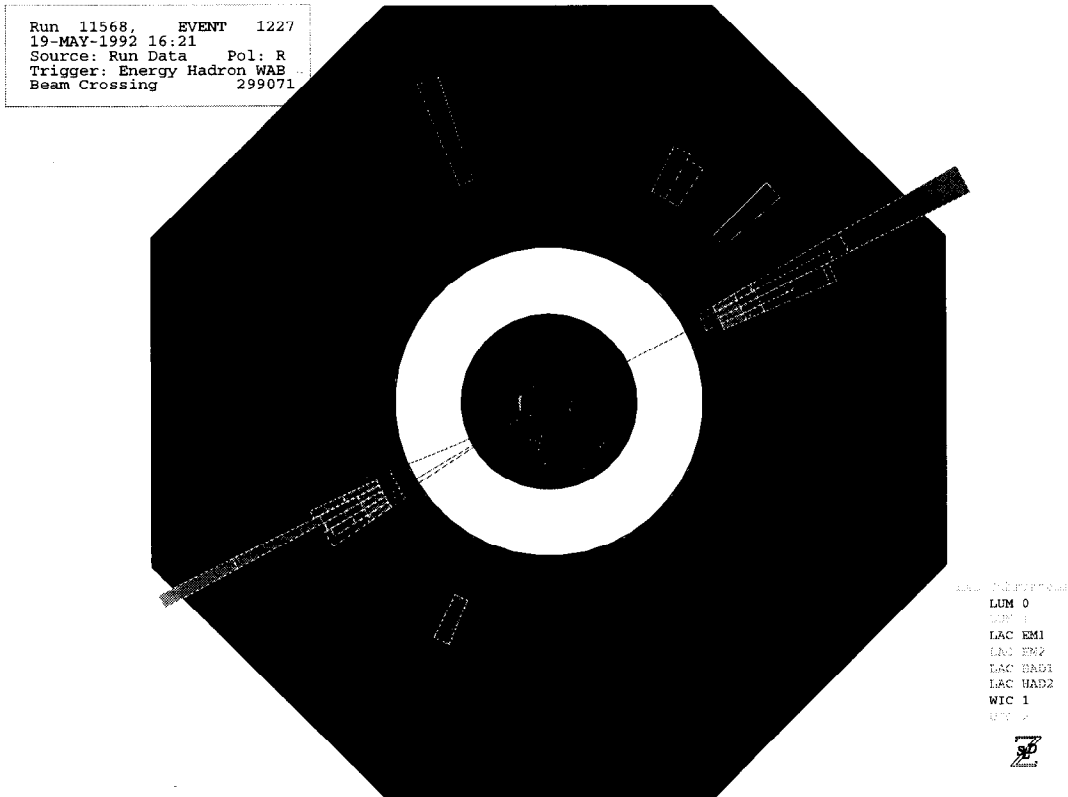


Figure 7.11: Typical Tau event in the 1-3 topology. Note the small acollinearity. An invariant mass can be formed in one hemisphere to cut against hadronic events.

3. Largest hemisphere mass

Dividing the event in two hemispheres I compute invariant masses for each of the hemispheres as described in 1. To reject hadronic events passing the pre-selection cuts, I want the larger of the two hemisphere invariant masses to be less than 1.8 GeV. The effect of this cut can be seen in figure 7.12. It removes most of the remaining hadronic background.

7. EVENT SELECTION

τ cut: Hemisphere mass (Hadron)

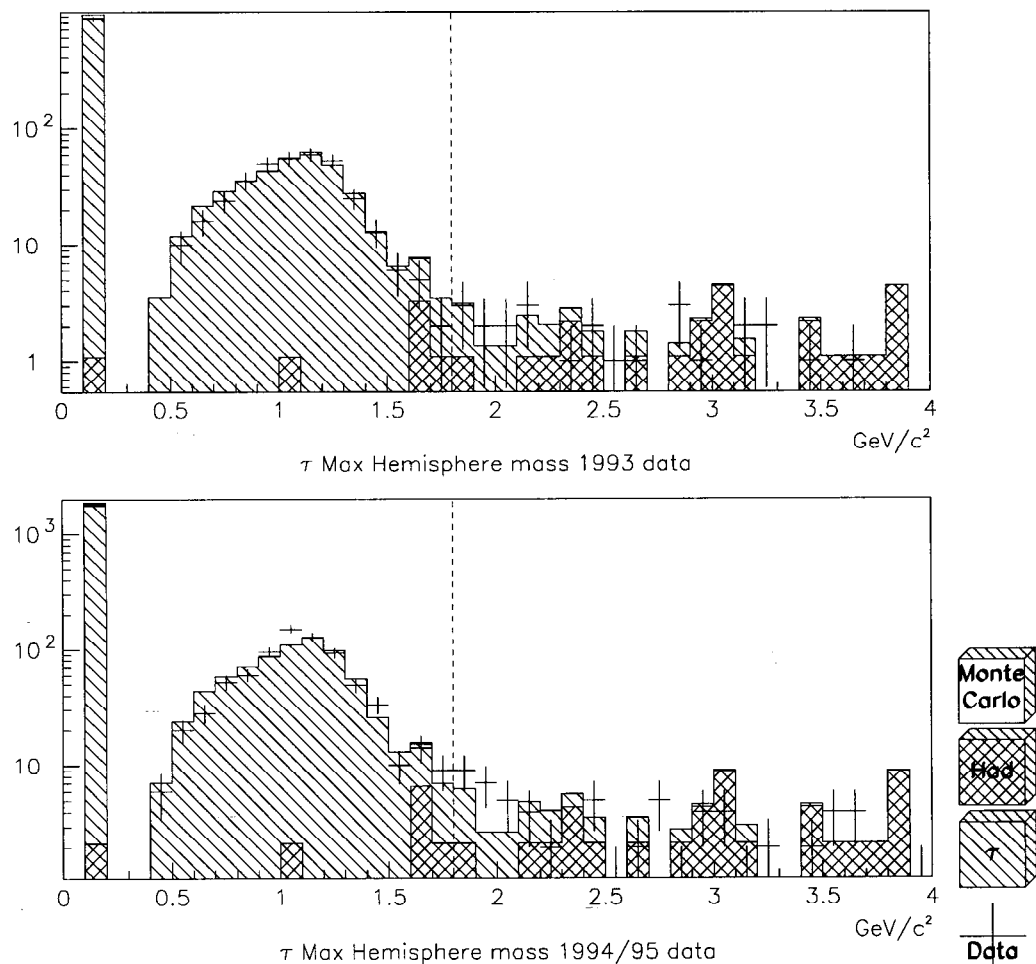


Figure 7.12: τ selection cut 3 on the larger hemisphere mass formed by charged tracks. This cut (indicated with the dashed line) reduces the hadronic background. The data is plotted with crosses, the histogram is Monte Carlo. The shaded areas correspond to hadron and τ Monte Carlo. All τ selection cuts have been applied except the cut on the larger hemisphere mass (3). Events are accepted to the right of the dashed line.

7. EVENT SELECTION

4. Largest momentum

The largest momentum of the charged tracks is required to be at least 3 GeV. This rejects two-photon events as well as events with a badly measured thrust axis. The effect of this cut is shown in figure 7.13 (the cut on the acollinearity (5) against two-photons has been applied) or in figure 7.14 (no acollinearity constraint is imposed).

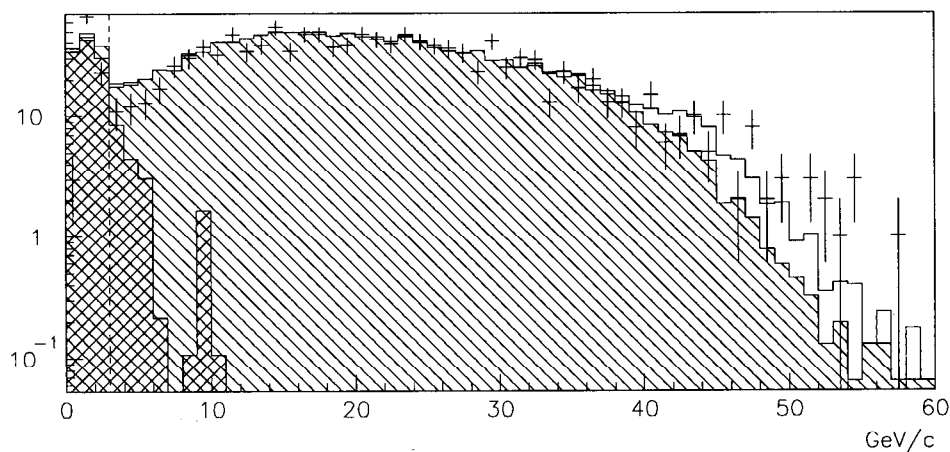
5. Acollinearity

Finally, I determine from each hemisphere the vector sum of the momentum based on charged tracks. From these two momenta, I compute the event acollinearity and require it to be greater than 160 degrees. The effect of this cut can be seen in figure 7.15) (the cut on the largest momentum (4) against two photon events has been applied) or in figure 7.16 (no momentum constrained is imposed).

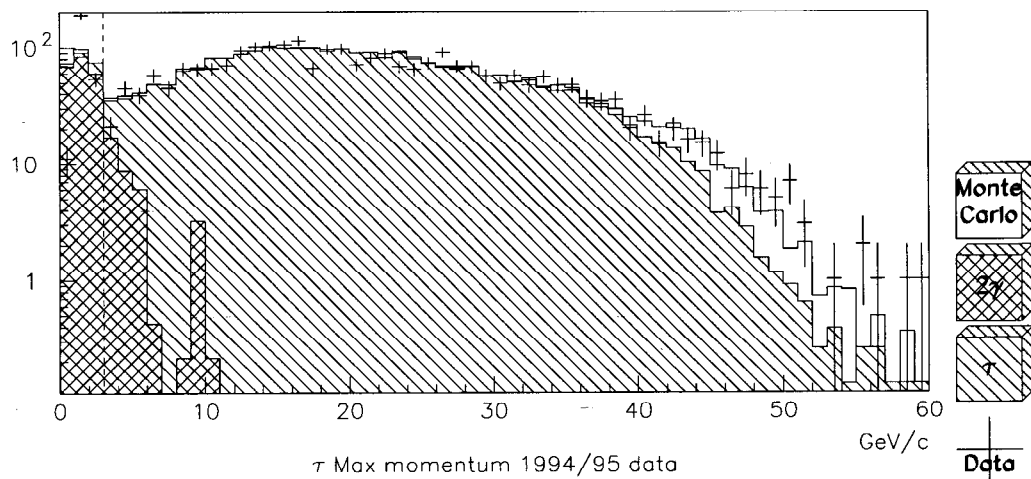
The τ selection efficiency within my angular acceptance is 89.57%. The purity is 94.75%. The τ sample contains 3748 events. The efficiency of the acceptance cut ($|\cos\theta| < 0.7$) is 61.08%.

7. EVENT SELECTION

τ cut: max. momentum ($\gamma\gamma$)



τ Max momentum 1993 data



τ Max momentum 1994/95 data

Figure 7.13: τ selection cut 4 on the largest momentum for the charged tracks. This cut (indicated with the dashed line) reduces the two photon background. The data is plotted with crosses, the histogram is Monte Carlo. The shaded areas correspond to $\gamma\gamma$ and τ Monte Carlo. All τ selection cuts have been applied except the cut on the maximum momentum (4). Events are accepted to the left of the dashed line.

7. EVENT SELECTION

$\gamma\gamma$: max. momentum

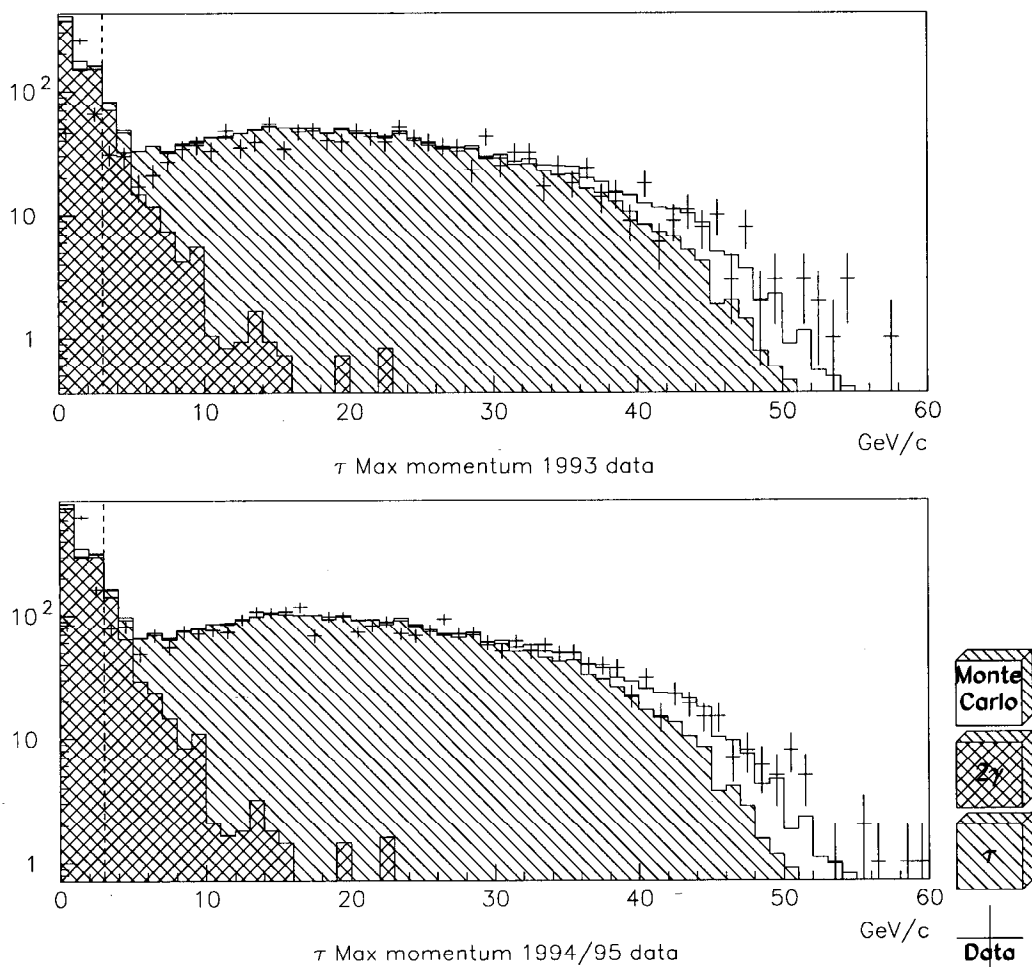


Figure 7.14: τ selection cut 4 on the largest momentum for the charged tracks. This cut (indicated with the dashed line) reduces the two photon background. The data is plotted with crosses, the histogram is Monte Carlo. The shaded areas correspond to $\gamma\gamma$ and τ Monte Carlo. No cut against $\gamma\gamma$ (4 or 5) was applied for this plot. Events are accepted to the left of the dashed line.

7. EVENT SELECTION

τ cut: Acolinearity ($\gamma\gamma$)

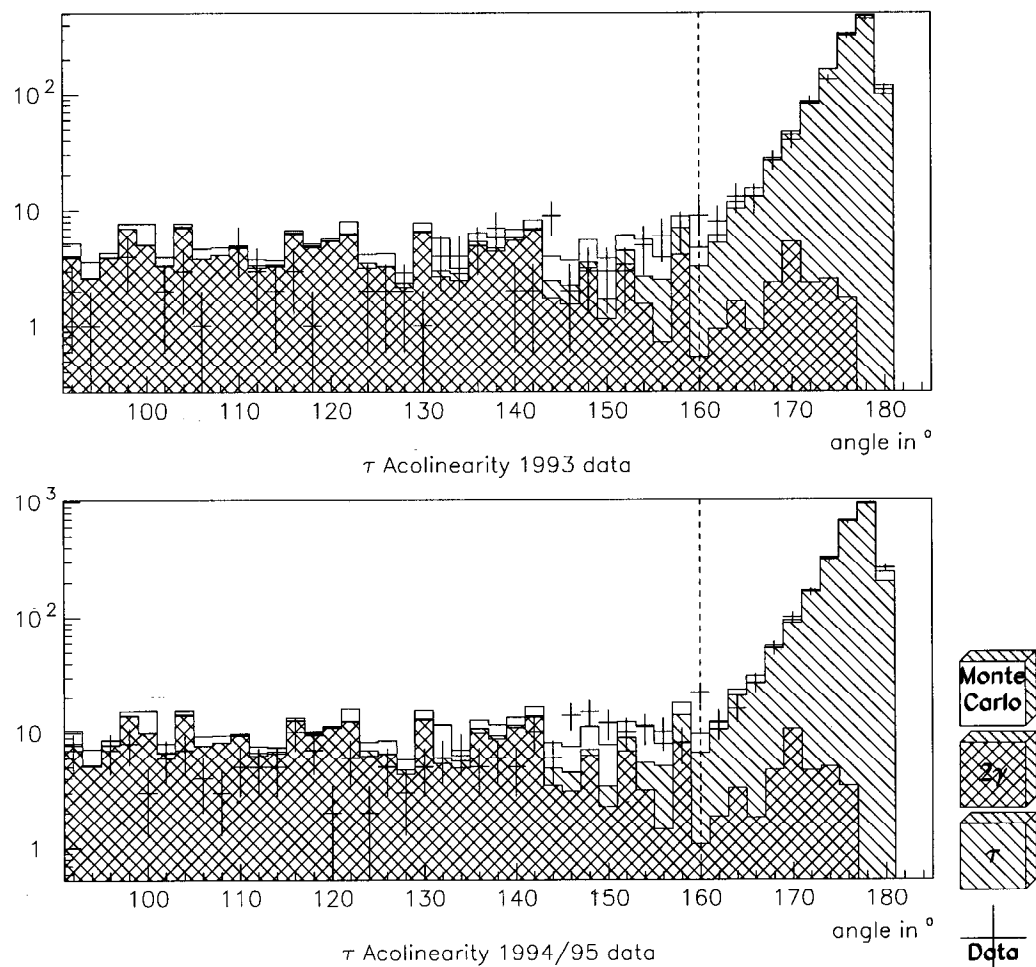


Figure 7.15: τ selection cut 5 on the acollinearity computed from the charged tracks. This cut reduces the two photon background. The data is plotted with crosses, the histogram is Monte Carlo. The shaded areas correspond to $\gamma\gamma$ and τ Monte Carlo. All τ selection cuts have been applied except the cut on the acollinearity (5). Events are accepted to the right of the dashed line.

7. EVENT SELECTION

$\gamma\gamma$: Acolinearity

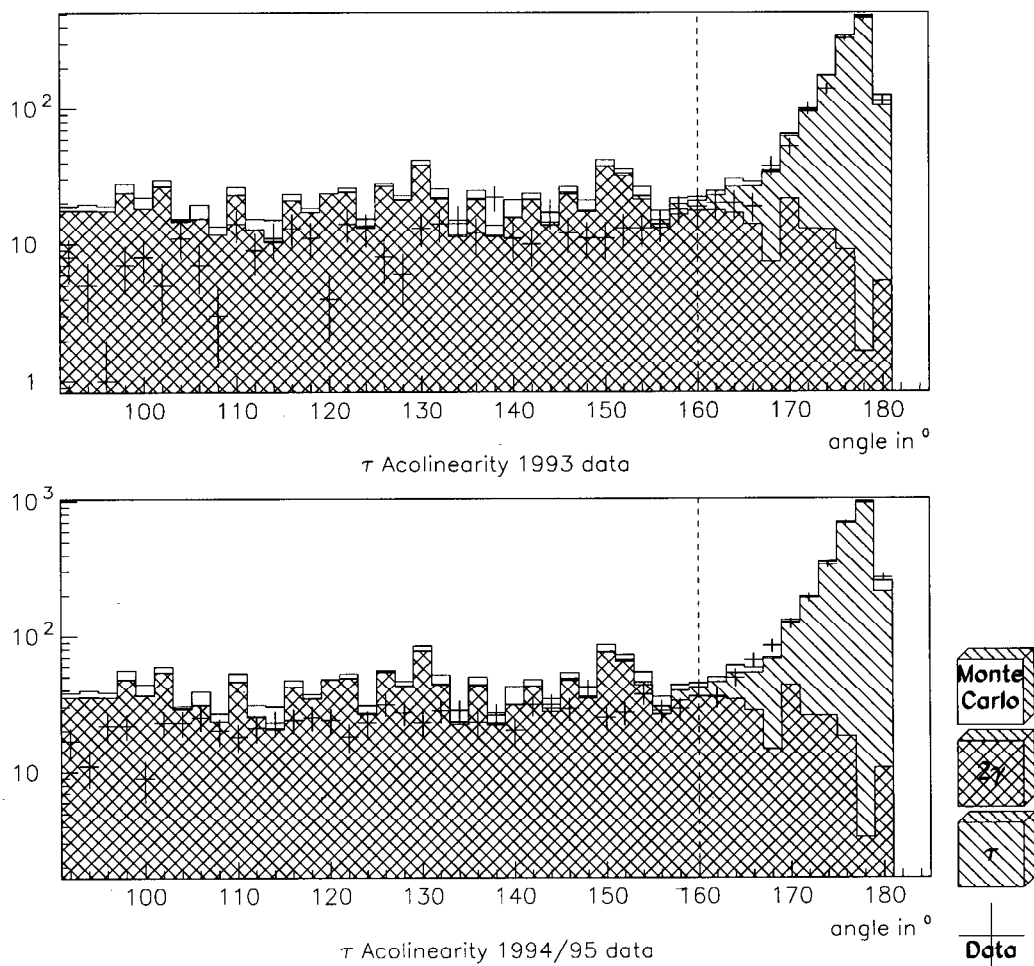


Figure 7.16: τ selection cut 5 on the acollinearity computed from the charged tracks. This cut reduces the two photon background. The data is plotted with crosses, the histogram is Monte Carlo. The shaded areas correspond to $\gamma\gamma$ and τ Monte Carlo. No cut against $\gamma\gamma$ (4 or 5) was applied for this plot. Events are accepted to the right of the dashed line.

Chapter 8

Backgrounds

Backgrounds in the sample that have different angular distributions will introduce a bias to the fitted asymmetry parameters. For example, a flat left-right symmetric background will wash out both the initial- and the final-state asymmetry. Therefore, I need to correct for the background effects. Since the exact level of background contamination (as well as the exact polarized angular distribution) is uncertain, this introduces systematic uncertainties in the measurement, which have to be estimated. To correct for possible biases in the lepton asymmetries A_l due to the presence of backgrounds I use the following procedure:

1. Assessing the backgrounds

I first compare the data with the detailed Monte Carlo simulations at each step in the process of making cuts to arrive at a final sample for each of the final states. Then, from each final sample, I relax the cuts one at a time to study the

8. BACKGROUNDS

effect of that cut. This is shown in figures 7.4-7.16. I compare the shape and number of events for the cut-on quantity above and below the cut value. If I find differences between data and Monte-Carlo, I correct the Monte Carlo estimates of the background level for these differences and take the difference as systematic uncertainty on the background level. If I find no obvious disagreement I use the Monte Carlo estimates for the background level and conservatively take all of the background to be systematically uncertain. In general, the agreement between data and Monte Carlo is good. Exceptions are discussed below.

2. Measuring the background's angular distribution

Starting from the events that passed the pre-selection cuts I use modified or inverted signal selection cuts to form event samples that are rich in the background being studied. (For μ 's and τ 's faking Bhabhas or Bhabhas faking μ 's and τ 's this is trivial, I just use the corresponding signal sample). I study the effects of the selection cuts for the signal suffering from this background on the background's angular distribution by relaxing or dropping cuts against the studied background to improve statistics. Being convinced that the selection cuts did not alter the background's angular distribution, I fit them with a suitable function.

8. BACKGROUNDS

3. Calculating the effect on the lepton asymmetries

The angular distributions obtained from the data are used as input to a fast simulation (“toy Monte Carlo”). The toy Monte Carlo consists of the function generating the signal (which is the same function used to fit the data) and, in addition, the background angular distribution function. Many “experiments” are run with the toy Monte Carlo where first the pure signal is fitted with the signal function, and then the signal diluted with different levels of background. Each fit is done in the same way as for the data. Since the fit function does not take the background into account, the fitted lepton asymmetries shifts from the undiluted value. I take this shift averaged over all the toy Monte Carlo experiments as the effect of the background being studied. I study three shifts for three different levels of background (0.25%, 0.5%, and 1%) and plot them against the background level. A linear fit provides me with the shift per % of background. Using the background estimates of 1, I compute a correction to be applied to the measured asymmetries.

Data sample/MC species	Bhabhas	Muons	Taus	$\gamma\gamma$	Hadrons
Bhabhas	99.29%	0.07%	0.64%	0.00%	0.00%
Muons	0.03%	99.50%	0.39%	0.00%	0.08%
Taus	1.47%	1.89%	94.75%	1.39%	0.50%

Table 8.1: Monte Carlo estimates of the composition for each sample. The numbers in the diagonals are the estimated purities, off diagonal numbers are background levels.

8. BACKGROUNDS

Data sample/Background	Bhabhas	Taus	$\gamma\gamma$	Hadrons
Bhabhas	-	$(0.7 \pm 0.7)\%$	0%	0%
Taus	$(1.5 \pm 1.5)\%$	-	$(1.0 \pm 0.5)\%$	$(0.5 \pm 0.5)\%$

Table 8.2: Corrected estimates of the background levels. Leptons faking other leptons are not considered to be background. The Muon sample has only negligible backgrounds.

8.1. Assessing the backgrounds

The Monte Carlo estimates for the backgrounds are listed in table 8.1. Data and Monte Carlo agree nicely in figure 7.4, so the τ background level in the Bhabha sample remains unchanged. All backgrounds in the μ sample are negligible since τ 's faking μ 's have no effect. There is no significant difference in the world-averaged measurements of A_μ and A_τ . Since A_μ is known within $13 \cdot 10^{-3}$ (and A_τ is known more precisely than that), the effect of τ background in the muons would be smaller than $5 \cdot 10^{-5}$. For the same reason, the μ background in the τ sample can be neglected. (Its effect is smaller than $2 \cdot 10^{-4}$. Figure 7.10 and 7.12 show no disagreement between data and Monte Carlo, so the Bhabha and hadronic background levels remain unchanged. On the other hand, in figure 7.13, 7.14, 7.15 and 7.16 data are consistently below Monte Carlo, so I correct the two-photon background level to 1%. This leaves me with the background levels printed in table 8.2

8.2. Measuring the background's angular distribution

To get the shape of the τ background in the Bhabha sample and the Bhabha background in the τ sample I used the τ sample and the Bhabha sample themselves. For the two-photon background and the hadronic background on the other hand, I needed two new data samples. The cuts for the samples are

1. The two-photon sample

The two-photon sample uses three cuts:

- I invert the τ acollinearity cut and require the event acollinearity to be smaller than 158 degrees. This cut removes most of the τ events.
- To reduce the amount of hadronic events which is the dominating contribution I impose a relaxed hemisphere mass cut ($\max(\text{mass1}, \text{mass2}) < 2 \text{ GeV}$)
- To reduce the number of τ events further, we want the maximum momentum to be less than 8 GeV.

2. The hadronic sample

I start from the τ sample and invert the cut on the larger hemisphere mass. I then relax the event mass cut to 79 GeV, the maximum cluster energy cut to 24 GeV, the maximum momentum cut to 2 GeV, and the acollinearity cut to 130 degrees.

8. BACKGROUNDS

Data sample/MC Species	Efficiency	Muon	Tau	Two-photon	Hadron
Pre-selection	19.50%, 1.42%	5.57%	6.31%	31.40%	61.34%
Two-photon	26.75%	0.00%	0.52%	91.14%	8.33%
Hadron	23.65%	0.60%	8.35%	0.00%	91.05%

Table 8.3: Efficiencies, Purities and Backgrounds for the two-photon and hadronic background data samples. The first efficiency listed for the pre-selection is the two-photon efficiency within $|\cos\theta| < 0.7$, the second is for hadronic events. All other efficiencies are within pre-selection. The four columns on the right give the fraction of events in the sample for the four Monte Carlo event types.

The efficiencies and purities of these samples are listed in table 8.3

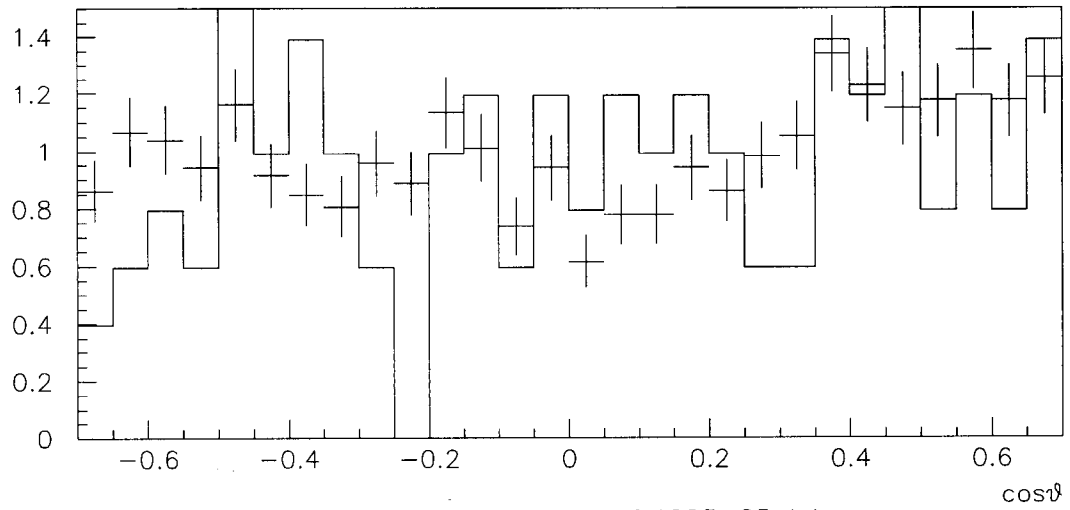
I studied the effect of the Bhabha cut on the angular distribution of the τ background. I did not find significant differences (see figure 8.1).

I also investigated the effect of the τ cuts on the Bhabha and the hadronic background and did not find significant differences as shown in figure 8.2.

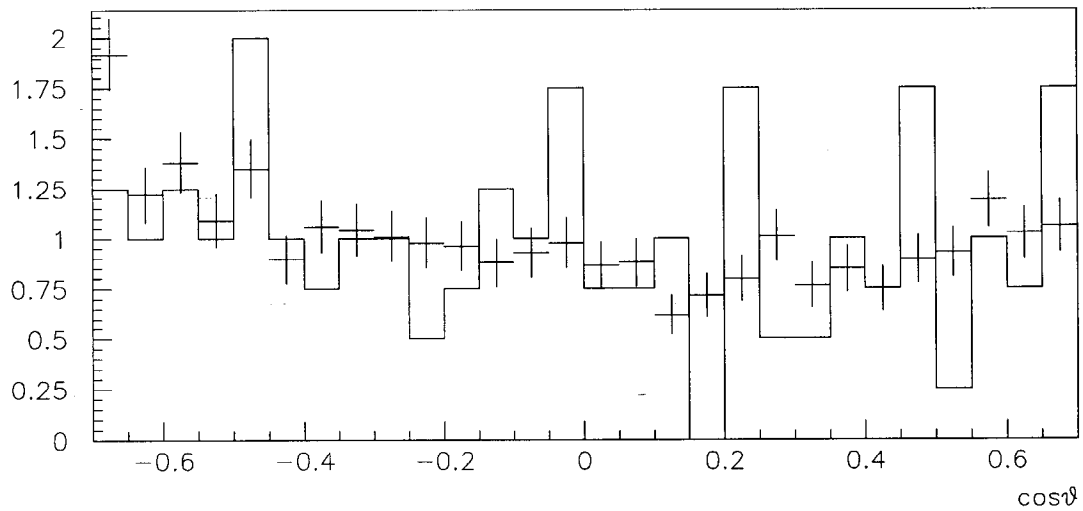
For the two-photon background (see figure 8.9) I saw differences between data and Monte Carlo. While Monte Carlo suggested a flat background profile, the data showed a fall off at large $|\cos\theta|$ (see figure 8.10 and 8.11). I think that the profile of the data is the correct one, but to investigate the possibility of changes in the distribution shape due to the τ cuts, I imposed the τ cuts on top of the two-photon ones. To increase statistics, I applied only one of the two cuts against two-photons, and then relaxed it. The observed data fall off for large $|\cos\theta|$ is visible in all the distributions (see figures 8.10-8.15).

8. BACKGROUNDS

τ shape



Bhabha left τ backgr. $\cos\vartheta$ 1993-95 data



Bhabha right τ backgr. $\cos\vartheta$ 1993-95 data

Figure 8.1: Shape of the angular distribution of the τ background in the Bhabha sample. The crosses use the background sample without the Bhabha cut, the histograms have a relaxed cut (sum of two largest energy clusters less than 35 GeV) applied. Figures 8.3 and 8.4 show a comparison for both samples between data and Monte Carlo.

8. BACKGROUNDS

WAB and Hadron shape

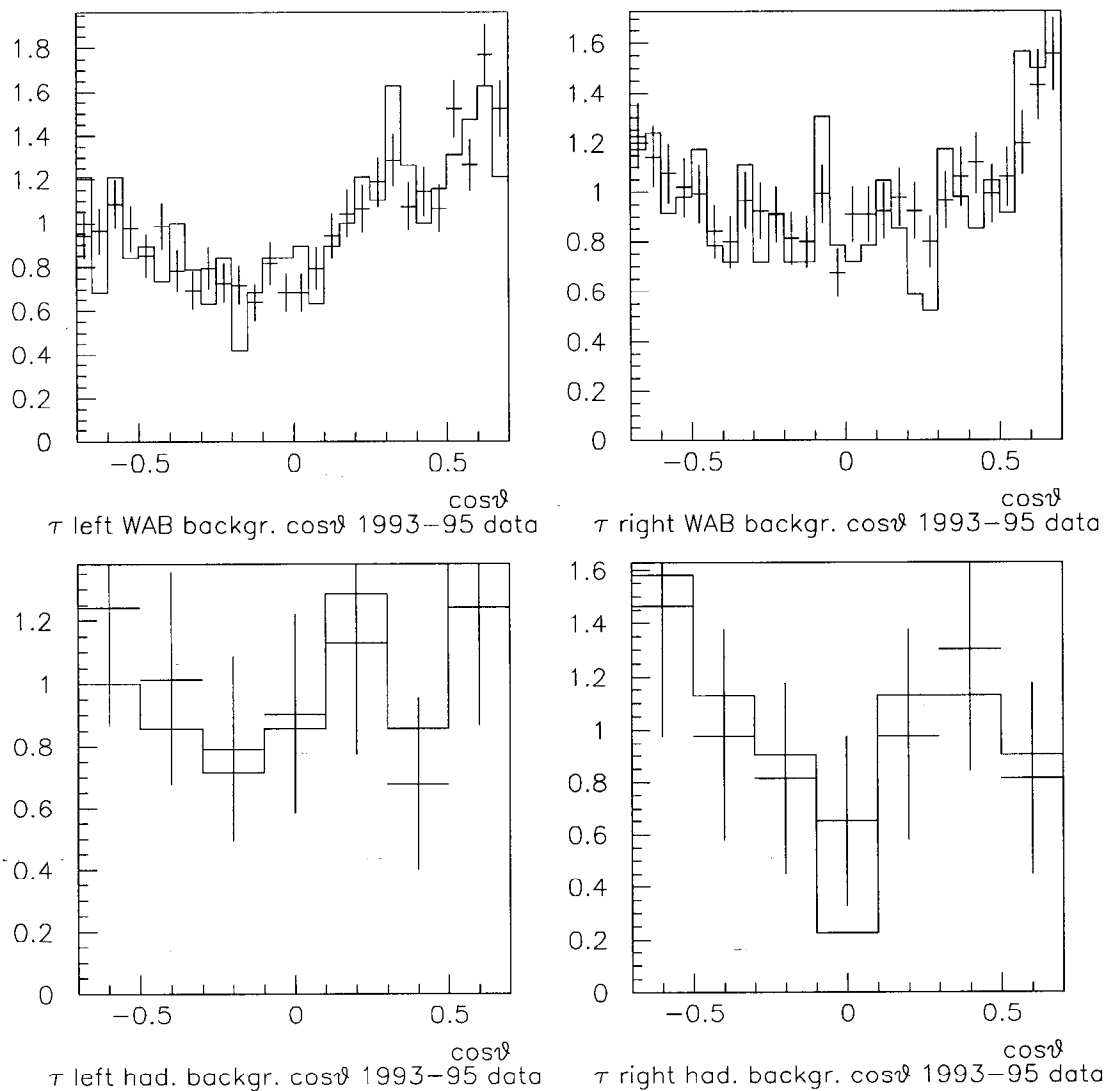


Figure 8.2: Shape of the angular distribution of the Bhabha and the hadronic background. The crosses use the background sample without any τ cut, the histograms have τ cuts applied, but not the one against the Bhabhas (hadrons). Figures 8.5 and 8.6 show a comparison for both Bhabha samples between data and Monte Carlo. Figures 8.7 and 8.8 show that comparison for both hadronic samples.

8. BACKGROUNDS

τ background

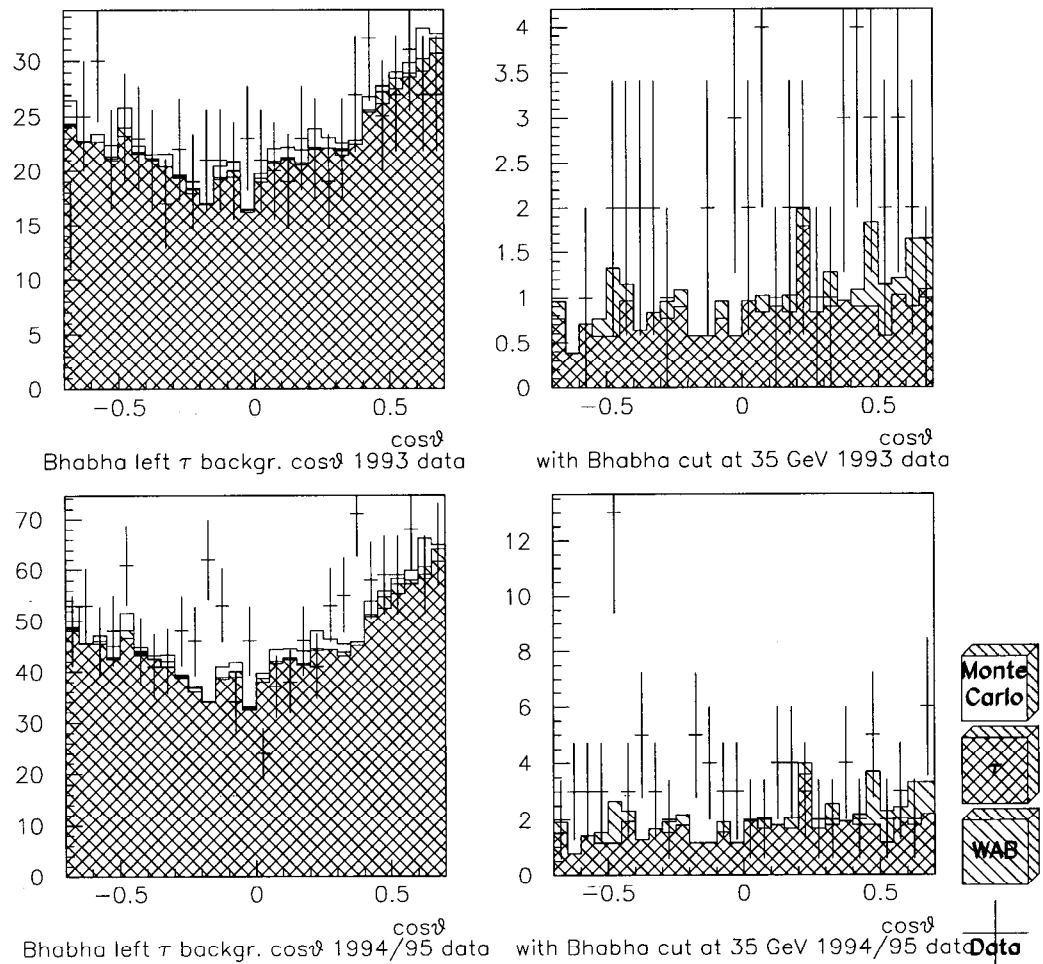


Figure 8.3: Shape of the angular distribution of the τ background in the Bhabha sample for left-handed events. The histograms on the left hand side are without Bhabha selection cut, the ones on the right hand side have a relaxed Bhabha cuts applied (sum of two largest energy clusters less than 35 GeV) The shape is the same in both cases.

8. BACKGROUNDS

τ background

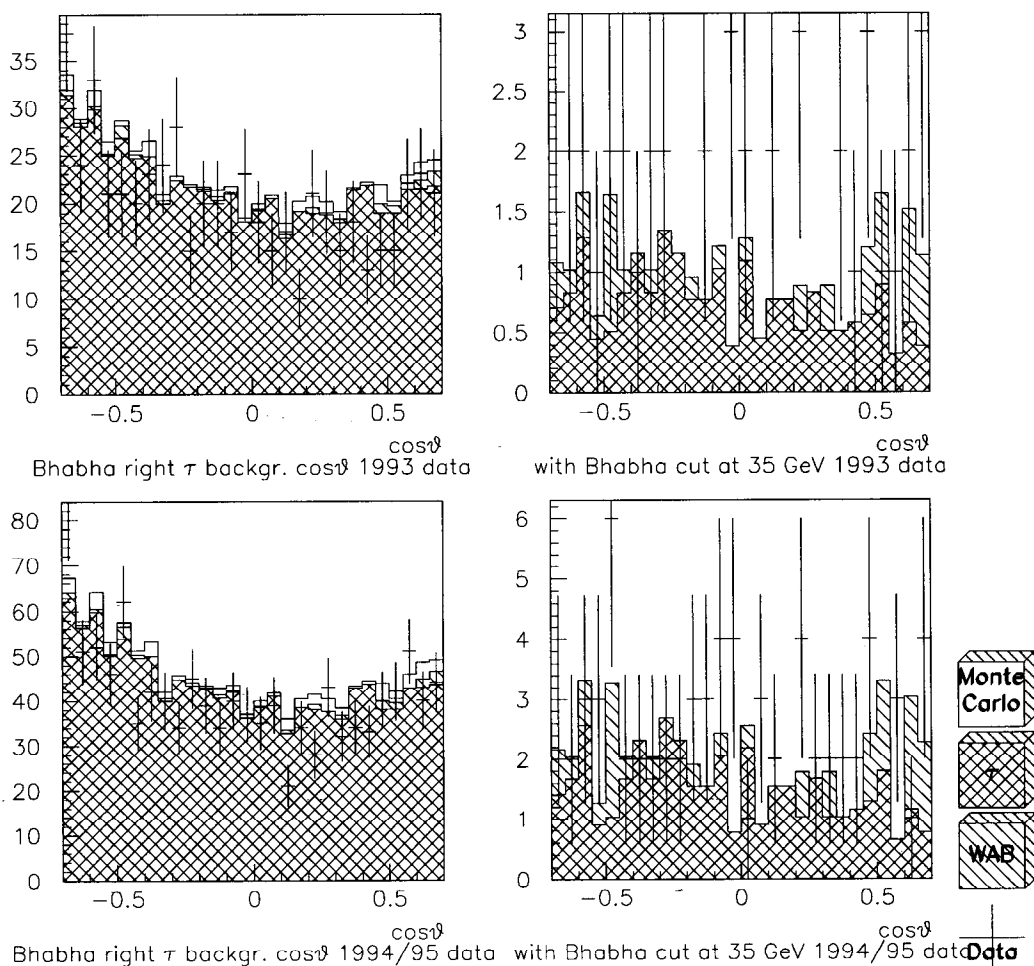


Figure 8.4: Shape of the angular distribution of the τ background in the Bhabha sample for right-handed events. The histograms on the left hand side are without Bhabha selection cut, the ones on the right hand side have a relaxed Bhabha cuts applied (sum of two largest energy clusters less than 35 GeV) The shape is the same in both cases.

8. BACKGROUNDS

WAB background

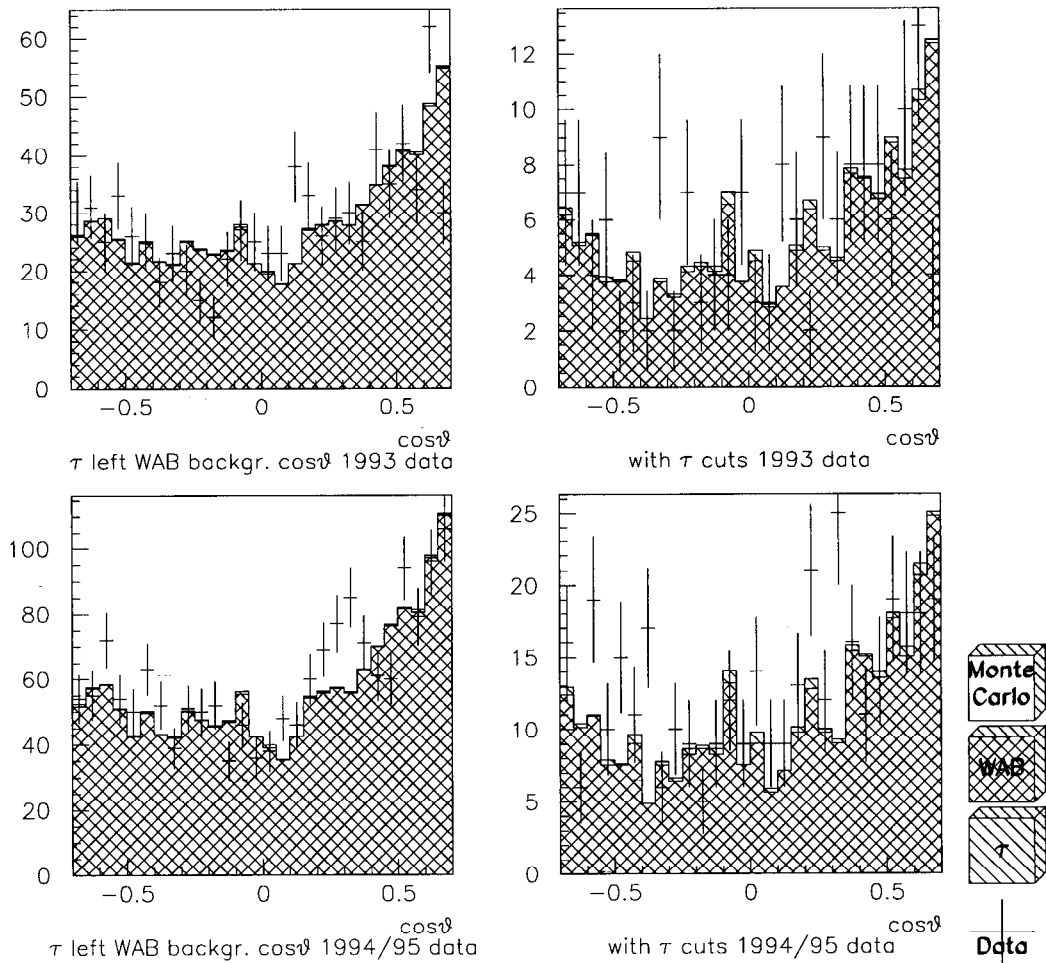


Figure 8.5: Shape of the angular distribution of the Bhabha background in the τ sample for left-handed events. The histograms on the left hand side are without any τ selection cuts, the ones on the right hand side have all τ cuts applied except for the one against Bhabha background (2). The shape is the same in both cases.

8. BACKGROUNDS

WAB background

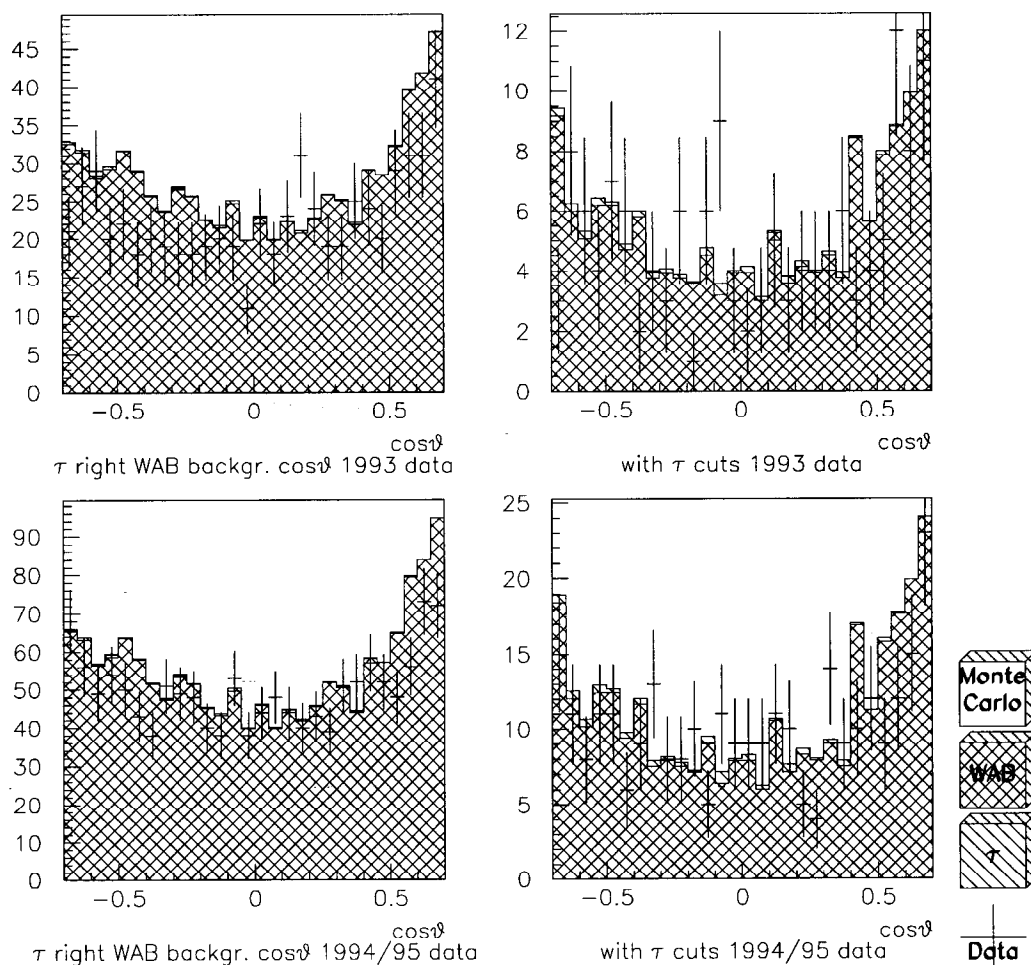


Figure 8.6: Shape of the angular distribution of the Bhabha background in the τ sample for right-handed events. The histograms on the left hand side are without any τ selection cuts, the ones on the right hand side have all τ cuts applied except for the one against Bhabha background (2). The shape is the same in both cases.

8. BACKGROUNDS

Hadr. background

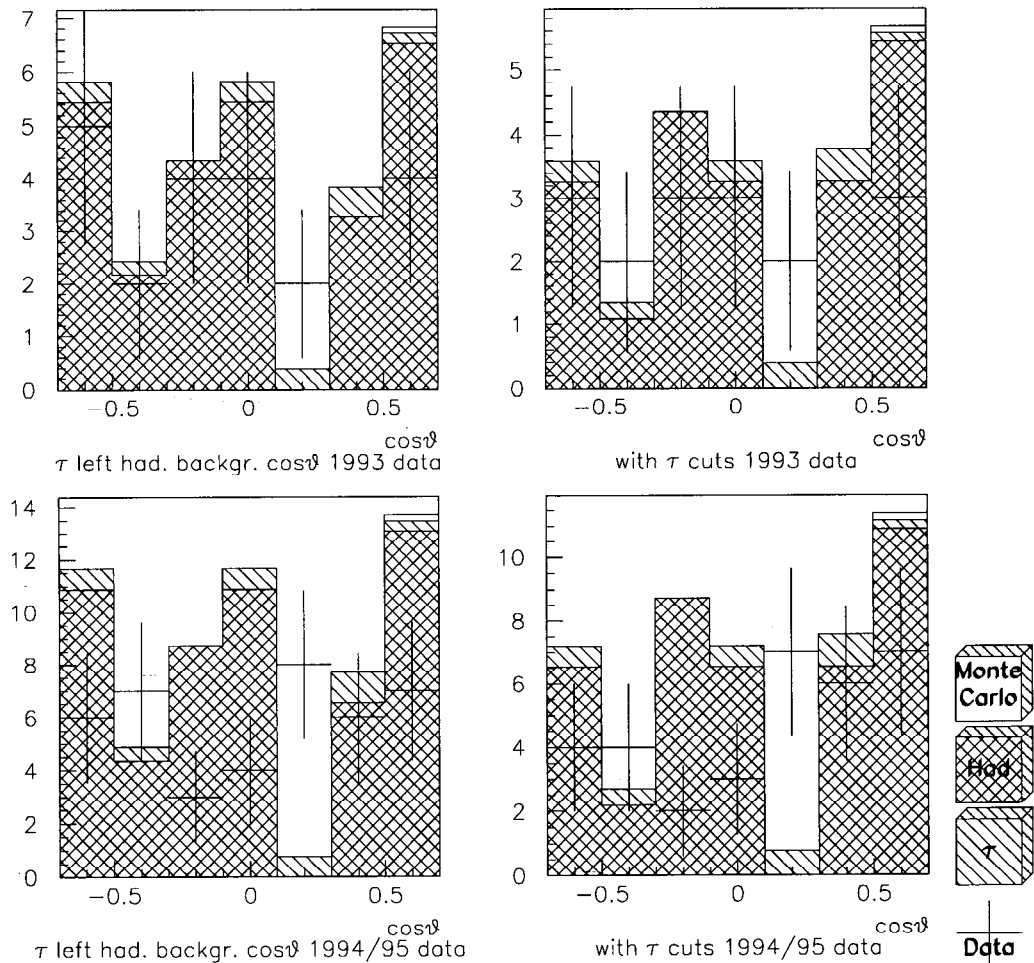


Figure 8.7: Shape of the angular distribution of the hadronic background in the τ sample for left-handed events. The histograms on the left hand side are without any τ selection cuts, the ones on the right hand side have all τ cuts applied except for the one against hadronic background. The shape is the same in both cases.

8. BACKGROUNDS

Hadr. background

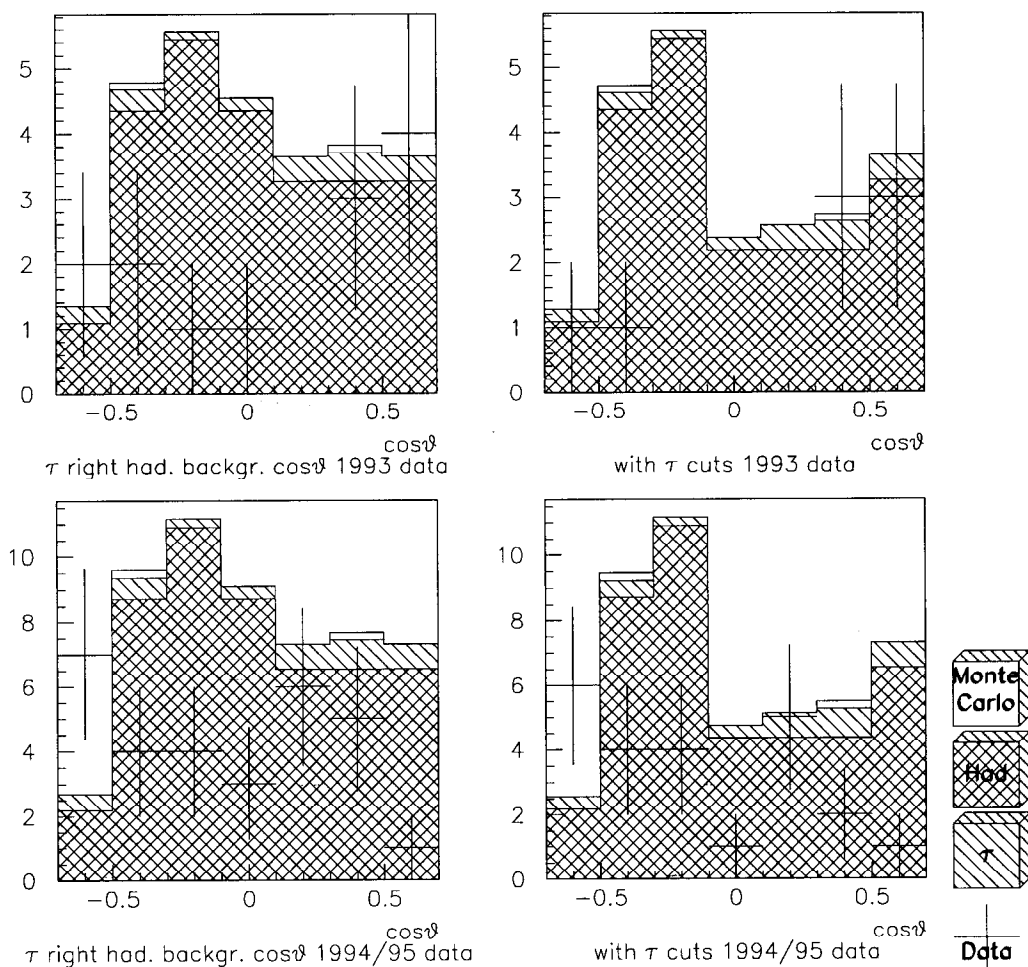


Figure 8.8: Shape of the angular distribution of the hadronic background in the τ sample for right-handed events. The histograms on the left hand side are without any τ selection cuts, the ones on the right hand side have all τ cuts applied except for the one against hadronic background. The shape is the same in both cases.

8. BACKGROUNDS

$\gamma\gamma$ shape

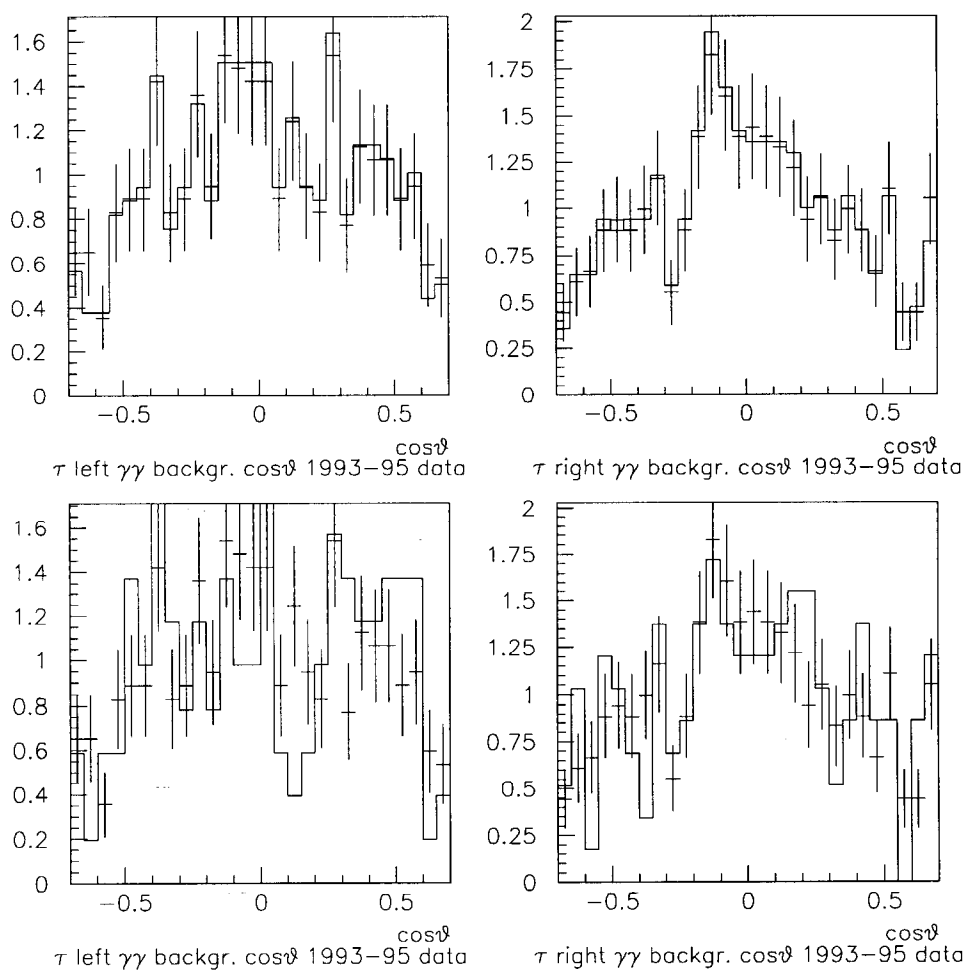


Figure 8.9: Shape of the angular distribution of the two-photon background. The crosses use the background sample without any τ cut, the histograms in the top two plots have τ cuts applied, but not the ones against the two-photon background. The histograms in the bottom two plots have in addition a relaxed maximum momentum cut (4': $\max(p) < 2$ GeV) applied. Figures 8.10 and 8.11 show Monte Carlo - data comparisons for the top two plots, figures 8.12 and 8.13 for the bottom two plots. Finally, figures 8.14 and 8.15 show Monte Carlo - data comparisons for the two-photon sample with τ cuts excluding the cut on the maximum momentum and relaxing the acollinearity cut (5) to 130 degrees

8. BACKGROUNDS

$\gamma\gamma$ background

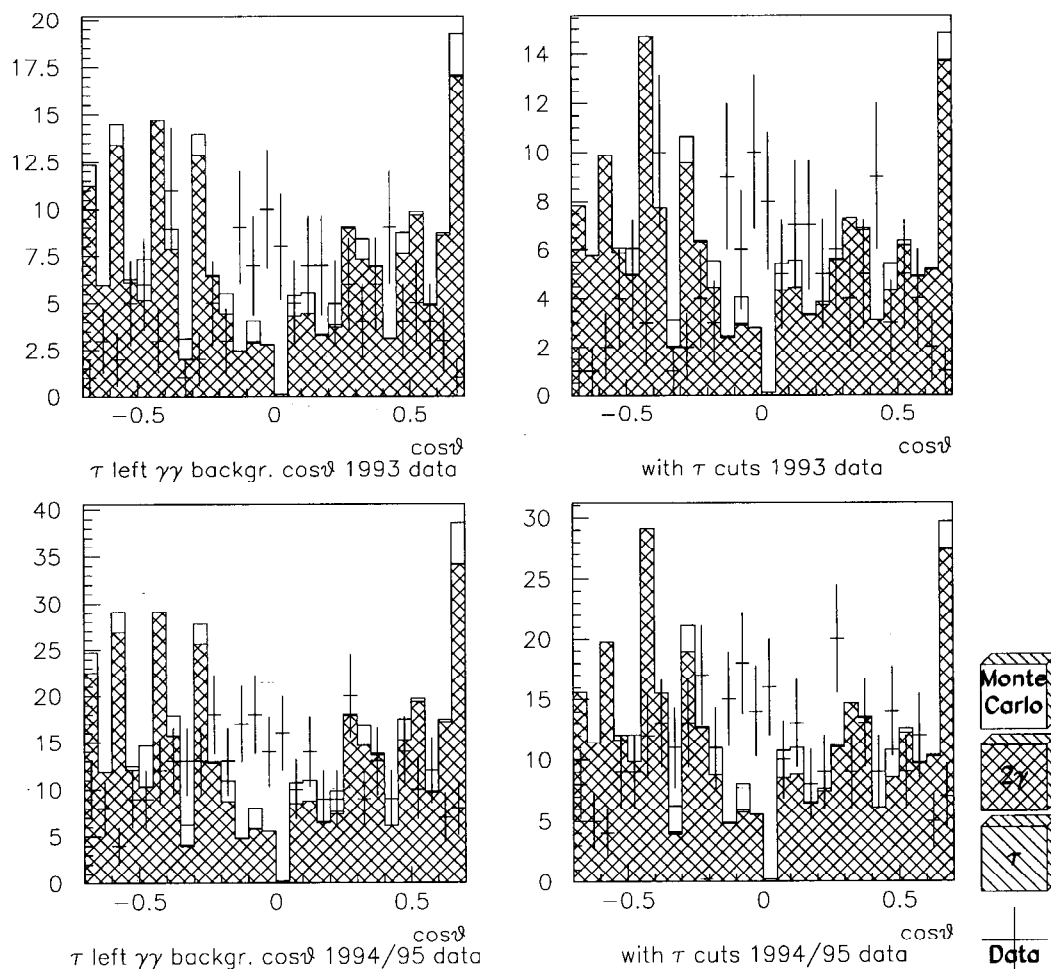


Figure 8.10: Shape of the angular distribution of the two photon background in the τ sample for left-handed events. The histograms on the left hand side are without any τ selection cuts, the ones on the right hand side have all τ cuts applied except for the ones against two photon background (4 and 5). The shape is the same in both cases.

8. BACKGROUNDS

$\gamma\gamma$ background

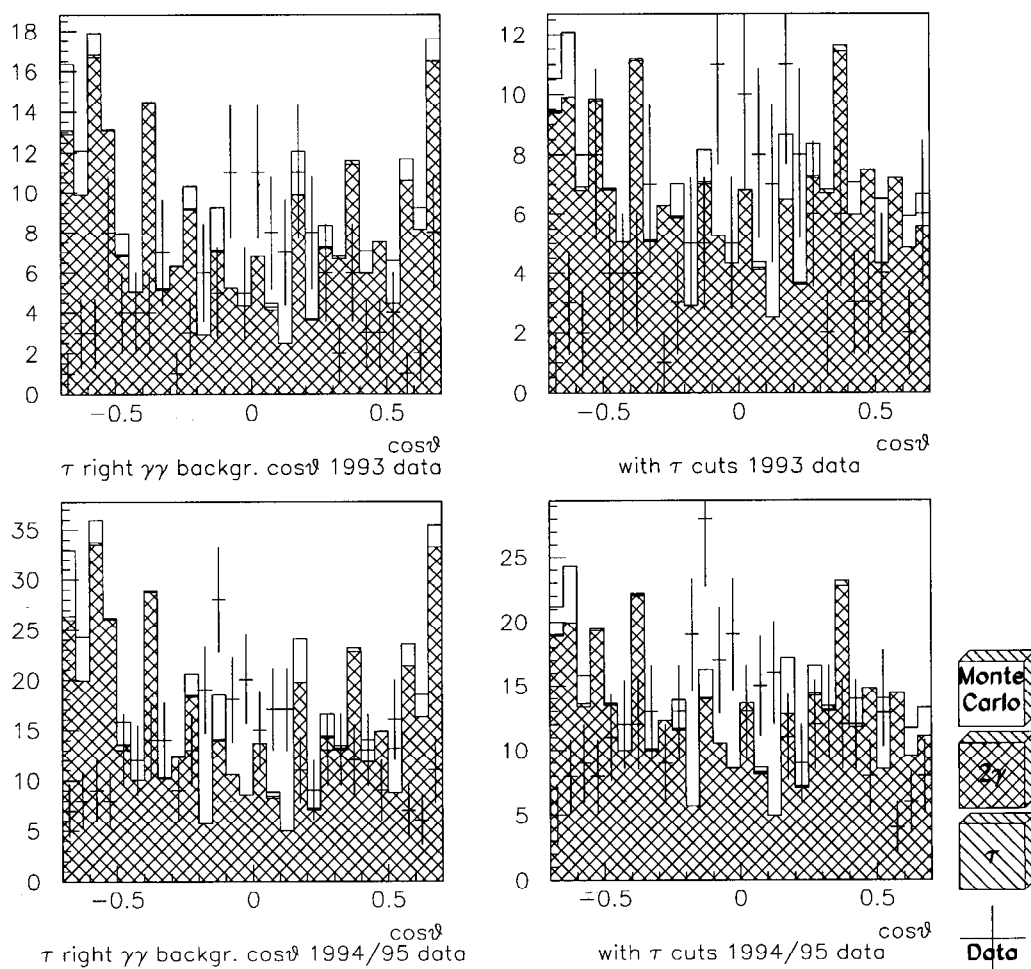


Figure 8.11: Shape of the angular distribution of the two photon background in the τ sample for right-handed events. The histograms on the left hand side are without any τ selection cuts, the ones on the right hand side have all τ cuts applied except for the ones against two photon background (4 and 5). The shape is the same in both cases.

8. BACKGROUNDS

$\gamma\gamma$ background

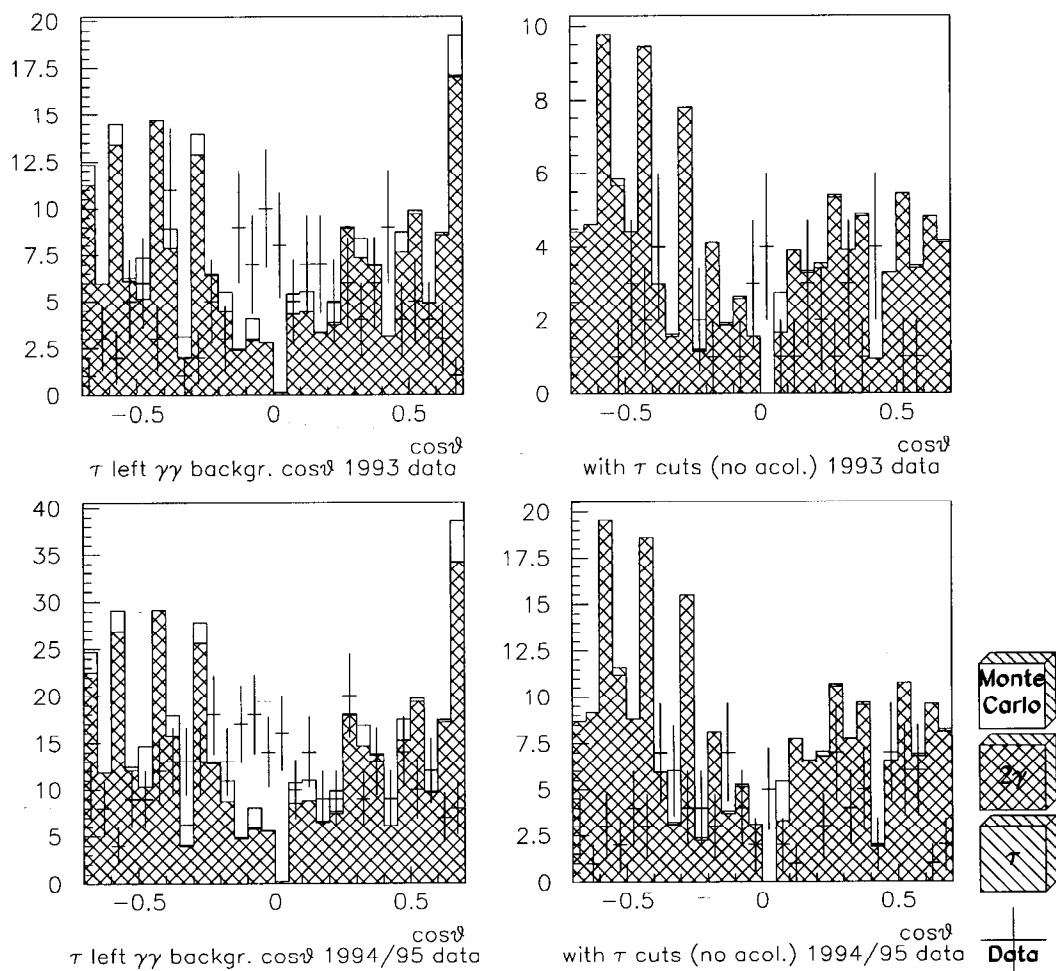


Figure 8.12: Shape of the angular distribution of the two photon background in the τ sample for left-handed events. The histograms on the left hand side are without any τ selection cuts, the ones on the right hand side have all τ cuts applied except for the acollinearity cut (5). The momentum cut has been relaxed to 2 GeV to increase statistics. The shape is the same in both cases.

8. BACKGROUNDS

$\gamma\gamma$ background

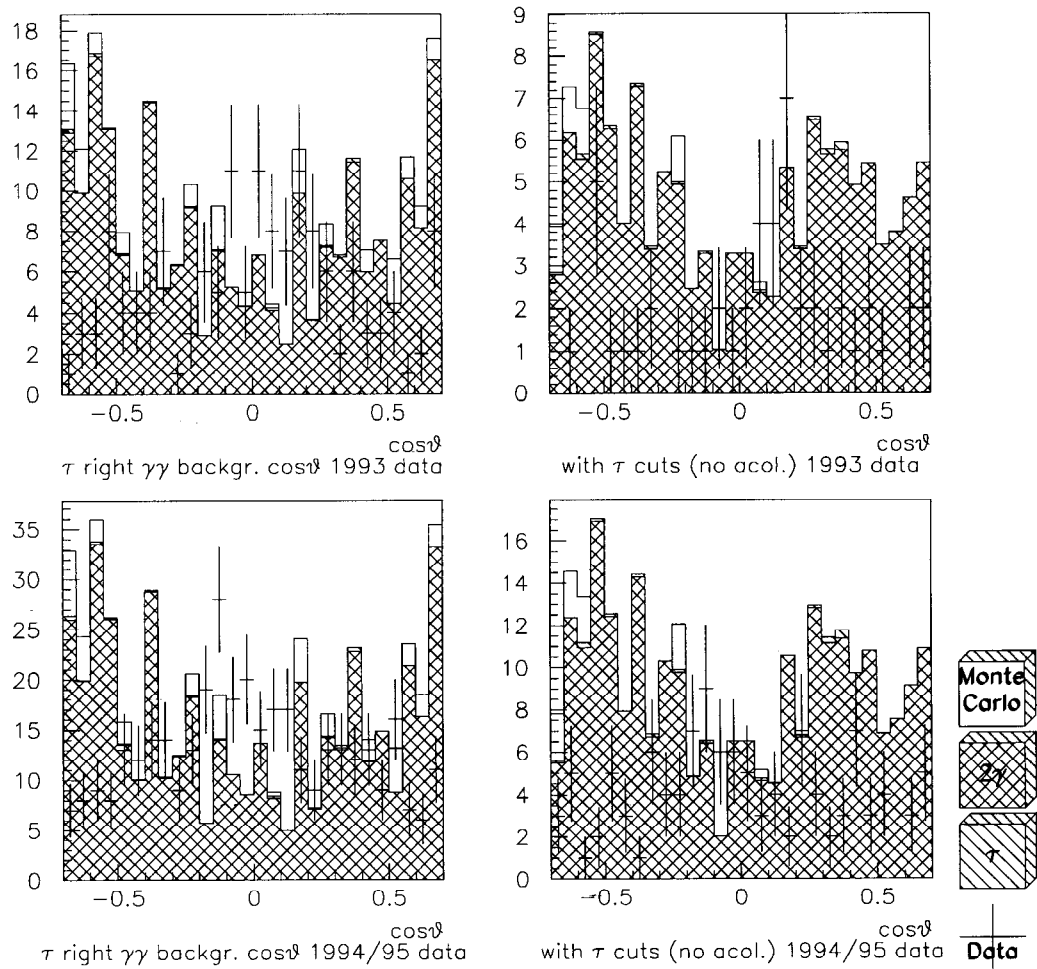


Figure 8.13: Shape of the angular distribution of the two photon background in the τ sample for right-handed events. The histograms on the left hand side are without any τ selection cuts, the ones on the right hand side have all τ cuts applied except for the acollinearity cut (5). The momentum cut has been relaxed to 2 GeV to increase statistics. The shape is the same in both cases.

8. BACKGROUNDS

$\gamma\gamma$ background

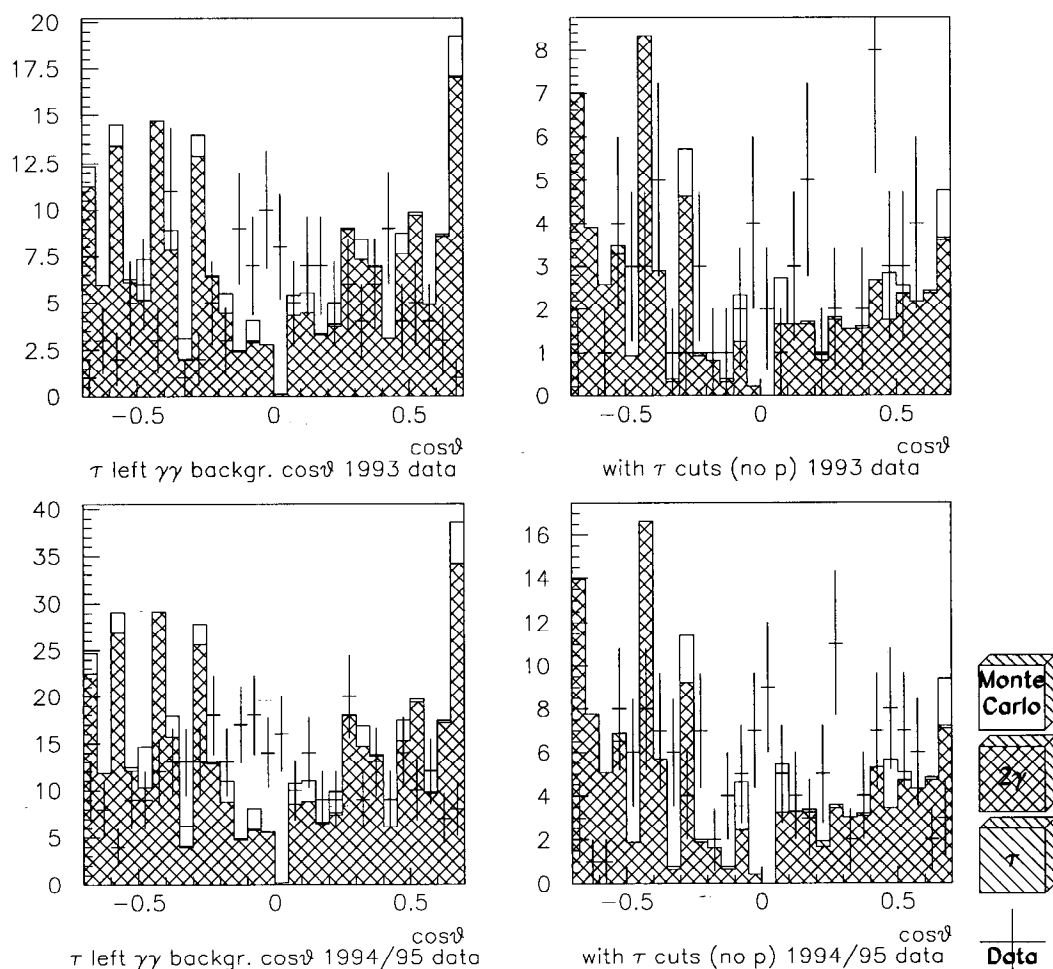


Figure 8.14: Shape of the angular distribution of the two photon background in the τ sample for left-handed events. The histograms on the left hand side are without any τ selection cuts, the ones on the right hand side have all τ cuts applied except for the maximum momentum cut (4). The acollinearity cut has been relaxed to 130 degrees to increase statistics. The shape is the same in both cases.

8. BACKGROUNDS

$\gamma\gamma$ background

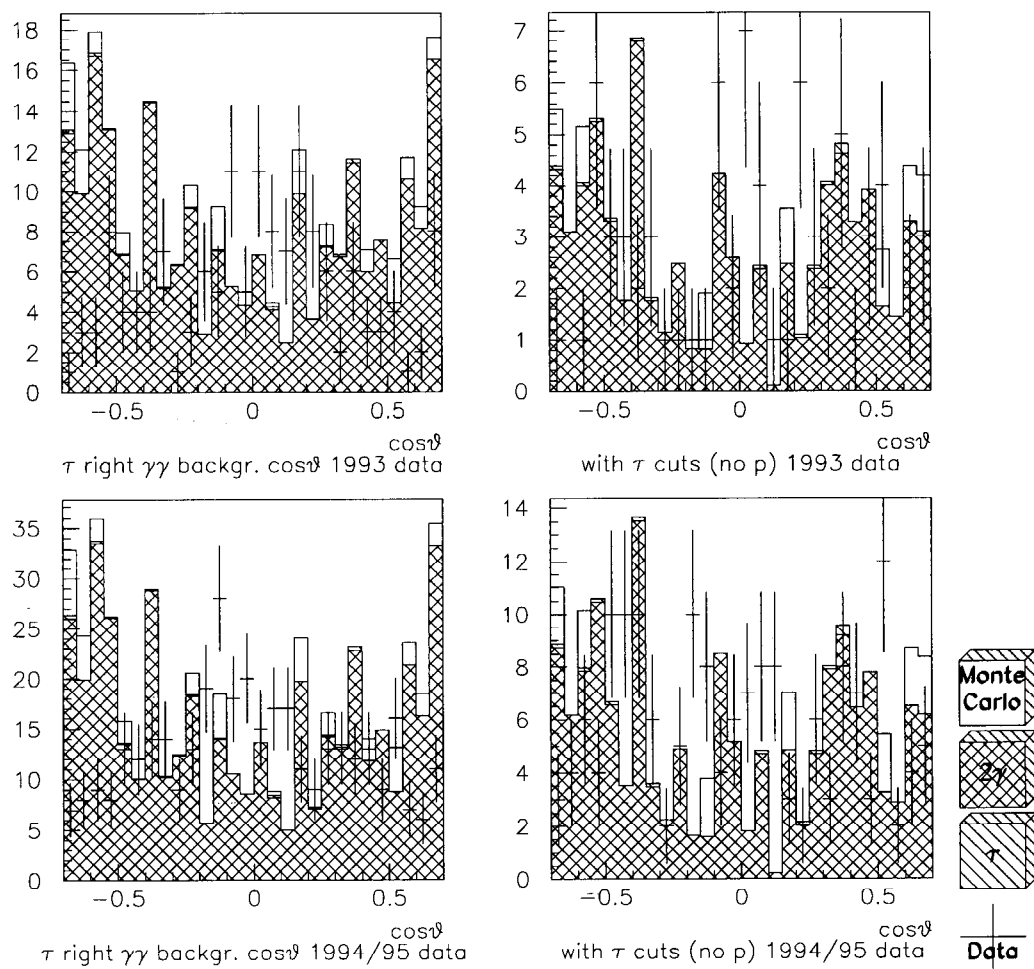


Figure 8.15: Shape of the angular distribution of the two photon background in the τ sample for right-handed events. The histograms on the left hand side are without any τ selection cuts, the ones on the right hand side have all τ cuts applied except for the maximum momentum cut (4). The acollinearity cut has been relaxed to 130 degrees to increase statistics. The shape is the same in both cases.

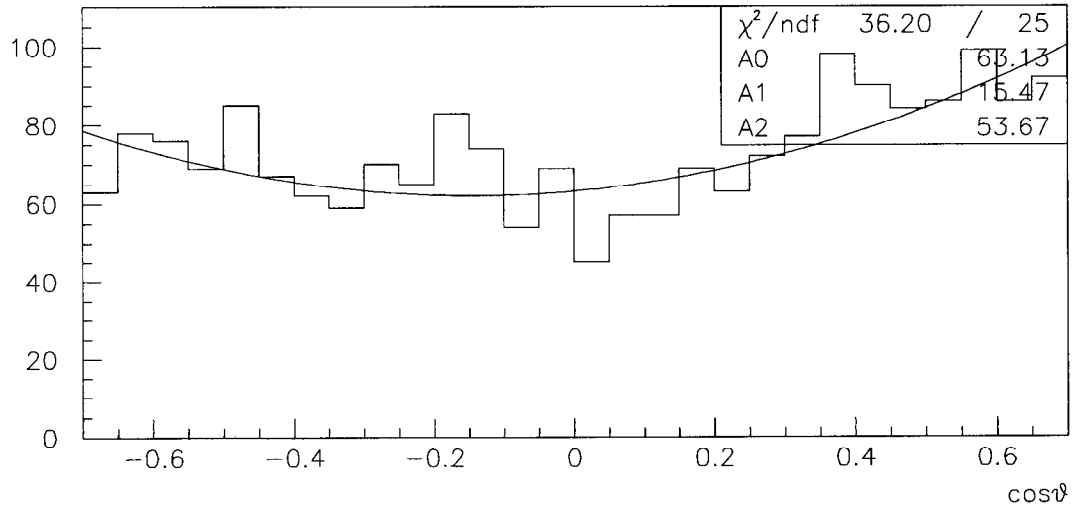
8.3. Calculating the effect on the lepton asymmetries

I now parameterize the background distributions. The τ distribution (as background in the Bhabha sample) is shown in figure 8.16. The parameterization function was chosen to be the one for s-channel single Z-exchange with an asymmetry of $A_e = A_\tau = 0.1551$. The Bhabha distribution (as background in the τ sample) uses the Bhabha measurement. ($A_e = 0.1563$) Photon and Z-exchange in both s- and t-channel are included. The fit is shown in figure 8.17. Figure 8.18 shows the two-photon distribution fit to a set of two second-order polynomials. Finally, Figure 8.19 shows the fit of the hadronic background to a set of two first-order polynomials. The hadronic background is consistent with being flat and shows a distinct left-right asymmetry. Since hadronic Z's with low multiplicity and a thrust axis within $|\cos\theta| < 0.7$ are very likely to have their real thrust somewhere along the beam pipe, the computed thrust axis gets randomized. Therefore, I expected a flat background with an asymmetry of $P \cdot A_e$. The data are consistent with that.

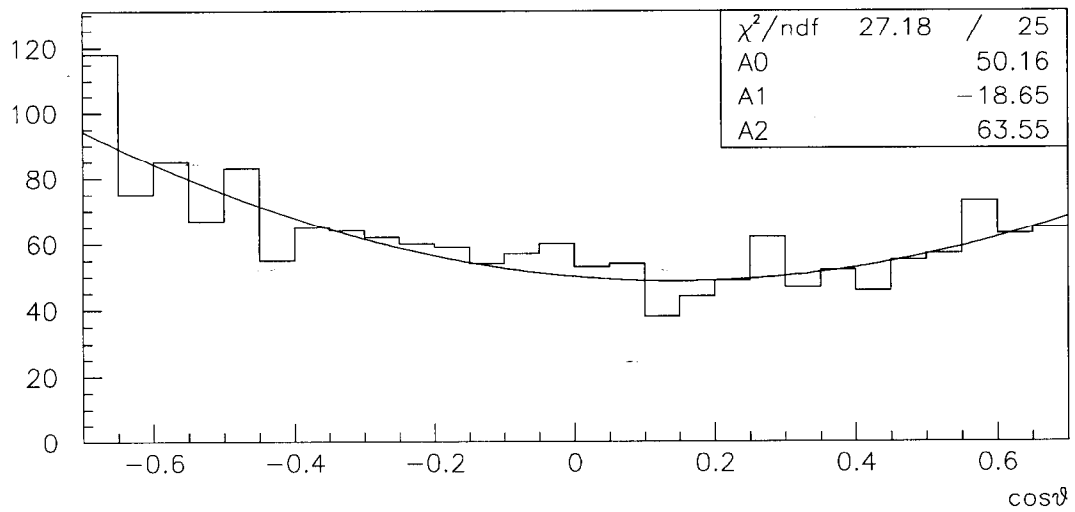
After that I generated roughly 10000 toy Monte Carlo Bhabha scattering experiments and 40000 toy Monte Carlo lepton production experiments and contaminated them with background at various levels. Figure 8.20 shows the effect of the τ background in the Bhabha sample. I observe a shift on the order of 10^{-4} which I neglect.

8. BACKGROUNDS

τ Background fit



Bhabha left τ backgr. $\cos\theta$ 1993-95 data



Bhabha right τ backgr. $\cos\theta$ 1993-95 data

Figure 8.16: Fit for the angular distribution of the τ background in the Bhabha sample. The top histogram is for left-handed polarization, the bottom one for right-handed polarization.

8. BACKGROUNDS

Bhabha Background fit

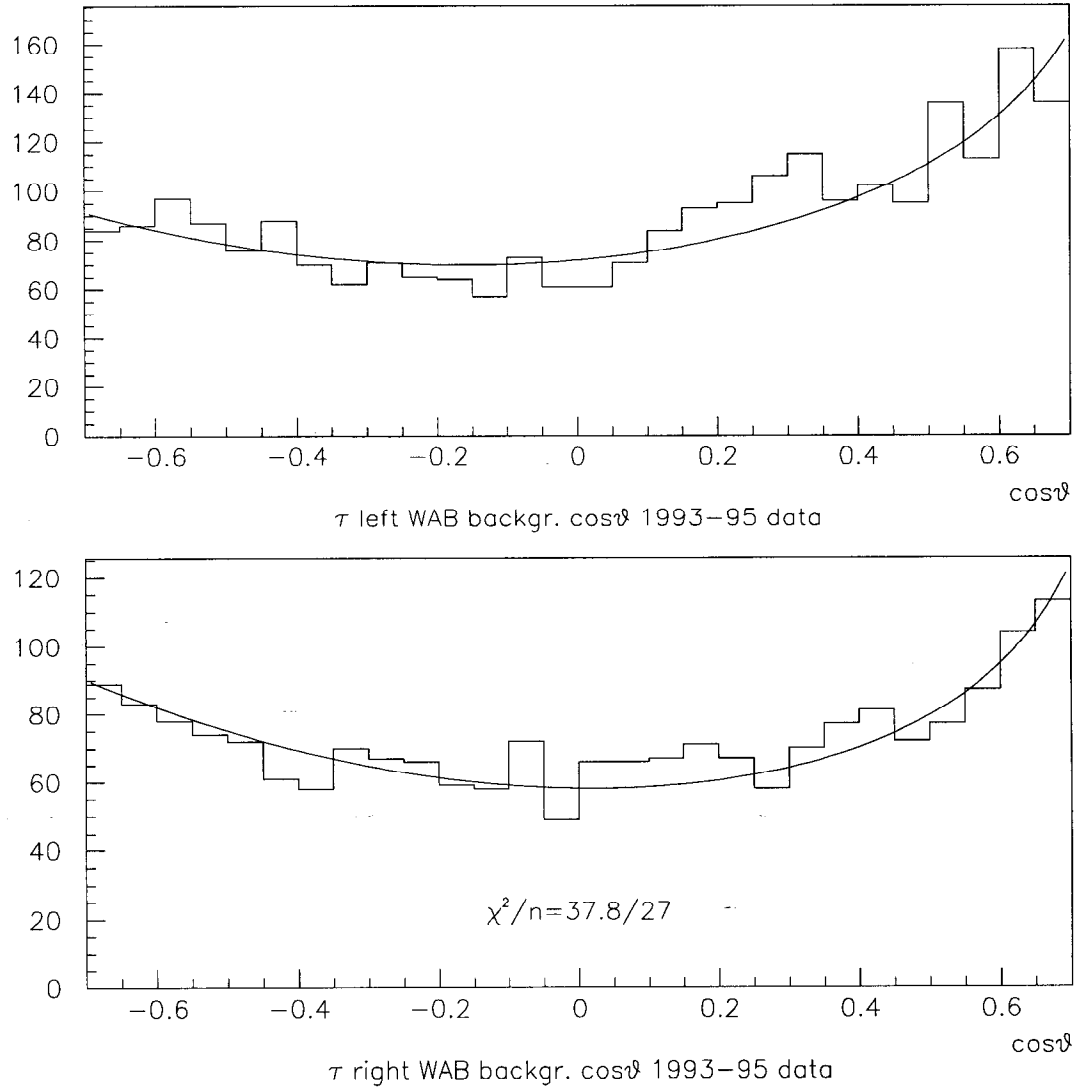


Figure 8.17: Fit for the angular distribution of the Bhabha background in the τ sample. The top histogram is for left-handed polarization, the bottom one for right-handed polarization.

8. BACKGROUNDS

$\gamma\gamma$ Background fit

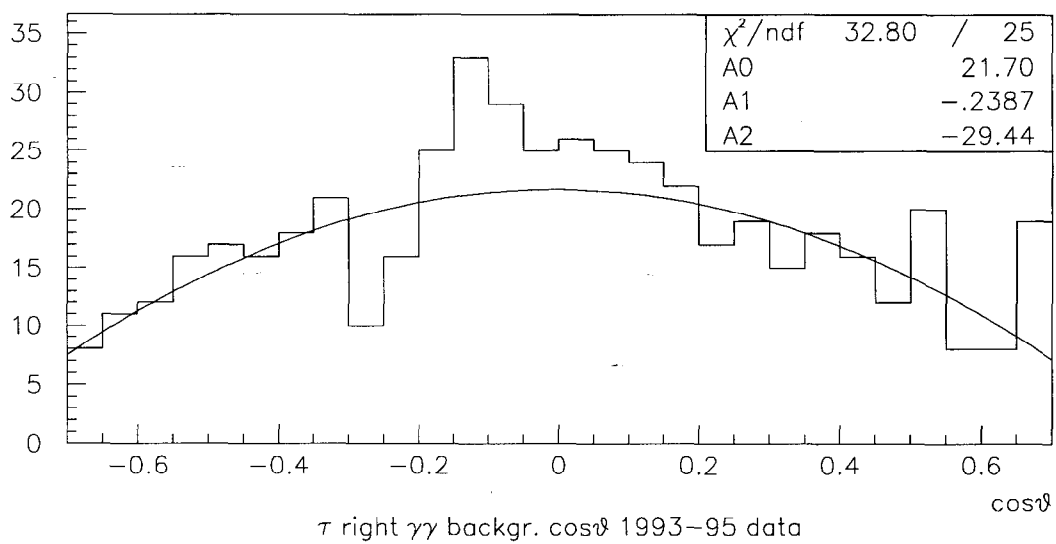
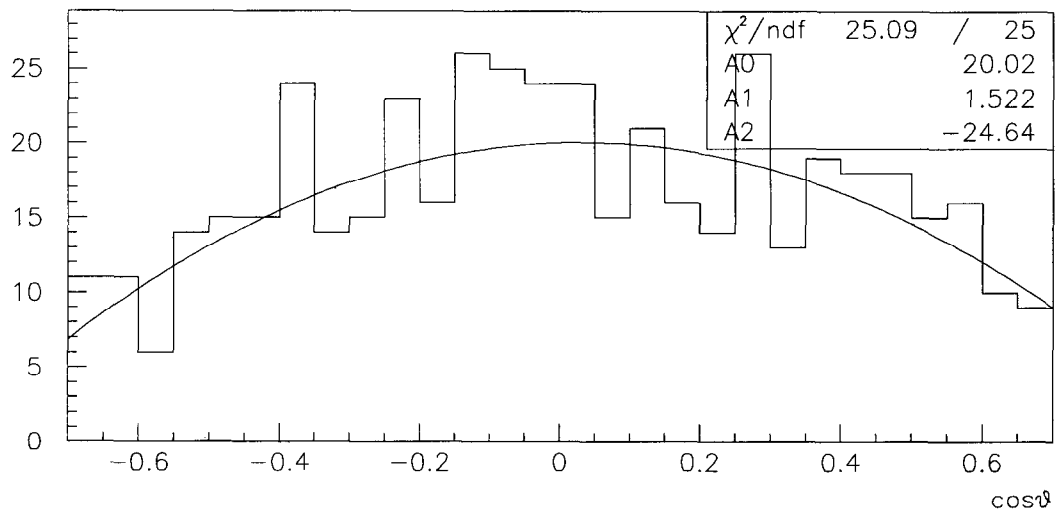


Figure 8.18: Fit for the angular distribution of the two-photon background in the τ sample. The top histogram is for left-handed polarization, the bottom one for right-handed polarization.

8. BACKGROUNDS

Hadronic Background fit

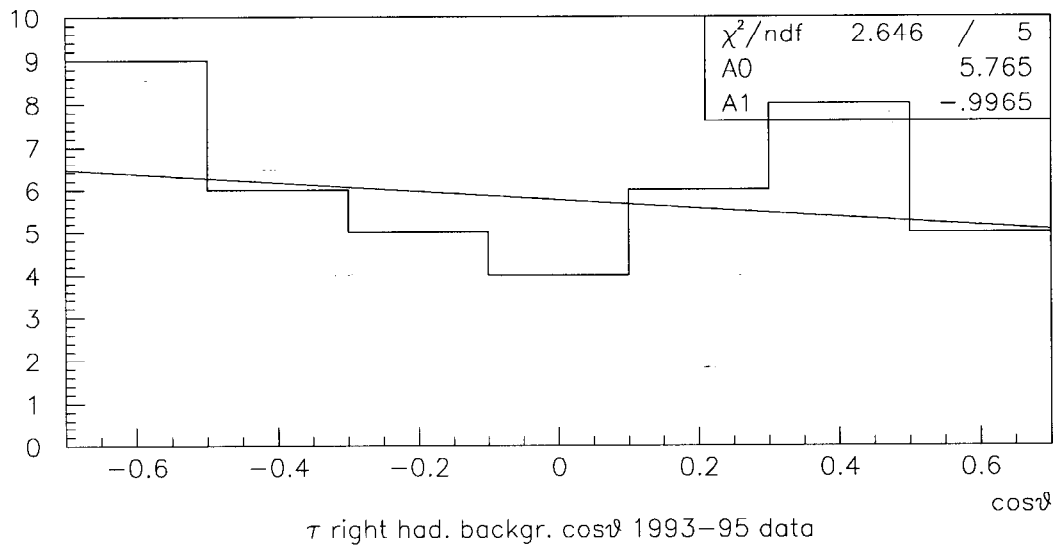
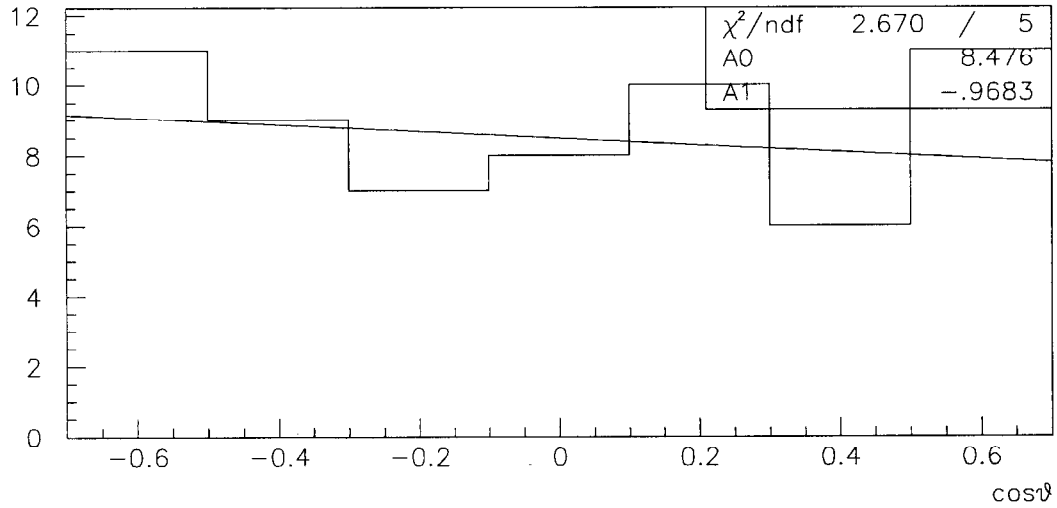


Figure 8.19: Fit for the angular distribution of the hadronic background in the τ sample. The top histogram is for left-handed polarization, the bottom one for right-handed polarization.

8. BACKGROUNDS

τ background shifts

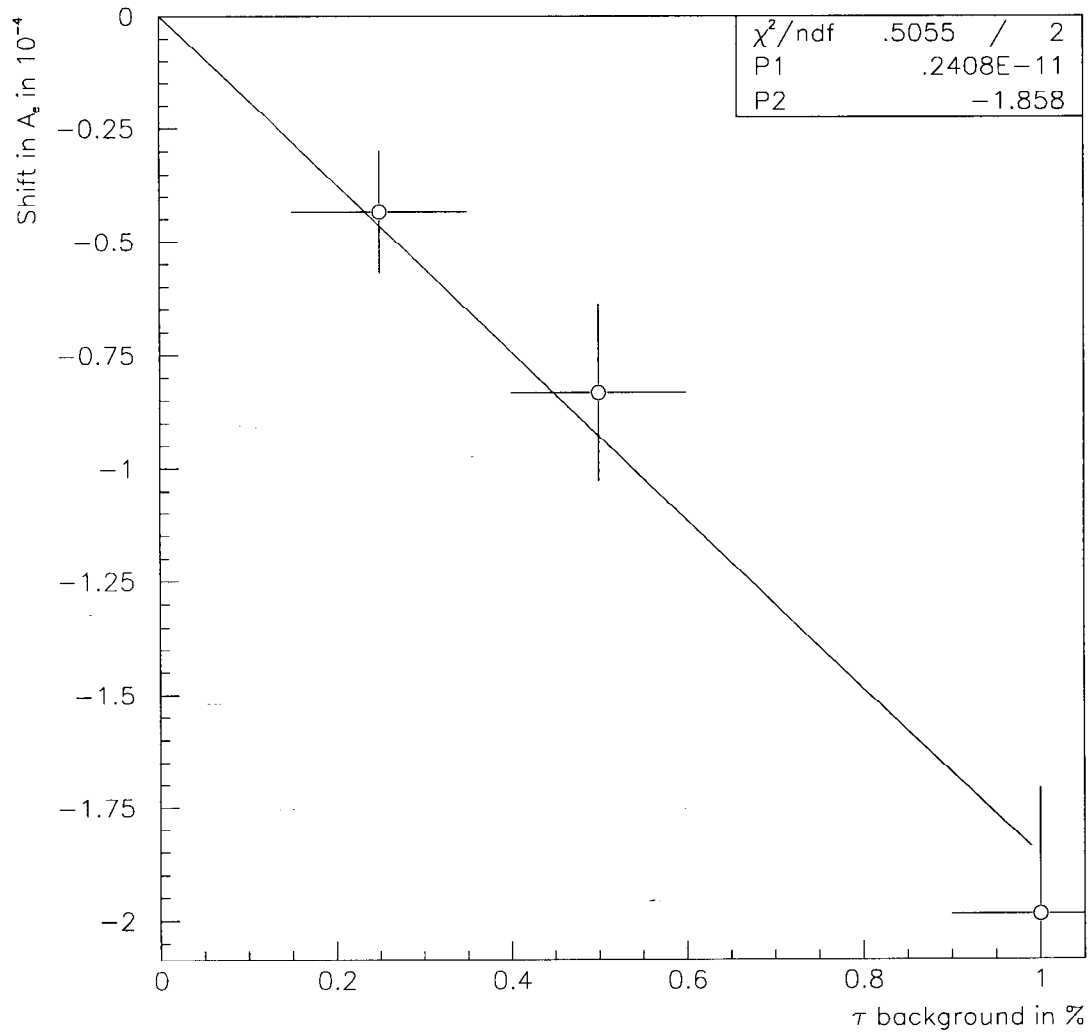


Figure 8.20: Fit for the shifts in A_e due to the presence of τ and μ background as a function of the amount of background. I observe a shift of $\Delta A_e = -1.3 \cdot 10^{-4}$ for 0.7% background. I neglect this correction because of its smallness with respect to the statistical error ($\Delta A_e^{stat} = -191 \cdot 10^{-4}$)

8. BACKGROUNDS

For the backgrounds in the τ sample it is possible to estimate the effects of the background analytically, if their polarized angular distribution is similar to the τ sample polarized angular distribution or if it is flat. The measured asymmetry parameter A_m with a background level b ($0 < b < 1$) is the weighted average of the true asymmetry A_t and the asymmetry in the background A_b .

$$A_m = bA_b + (1 - b)A_t \text{ or } \Delta A = A_m - A_t = b(A_b - A_t)$$

In this simple model, the background-induced shift ΔA is proportional to the background level b and to the asymmetry difference between background and signal. Figure 8.21 shows the effect of Bhabha background in the τ sample. The input values were $A_{LR}^\tau = 0.16$ and $\tilde{A}_{FB}^\tau = 0.14$. Because the Bhabhas have a left-right asymmetry of $A_{LR}^{\text{WAB}} = 0.1406$ and a polarized forward-backward asymmetry of $\tilde{A}_{FB}^{\text{WAB}} = 0.1362$ I expect the shifts ΔA_e and ΔA_τ for a Bhabha background level b to be

$$\begin{aligned} \Delta A_e = A_e - A_{LR}^\tau &= b(A_{LR}^{\text{WAB}} - A_{LR}^\tau) = -1.94 \cdot 10^{-4} \frac{b}{\%} \\ \Delta A_\tau = A_\tau - \tilde{A}_{FB}^\tau &= b(\tilde{A}_{FB}^{\text{WAB}} - \tilde{A}_{FB}^\tau) = -0.38 \cdot 10^{-4} \frac{b}{\%}. \end{aligned}$$

The toy Monte Carlo experiments result in shifts about 22% higher than the analytical prediction for A_e and 25% lower than the analytical prediction for A_τ . The difference in A_τ is not significant, it could be a statistical fluctuation. The difference in A_e

8. BACKGROUNDS

Bhabha background shifts

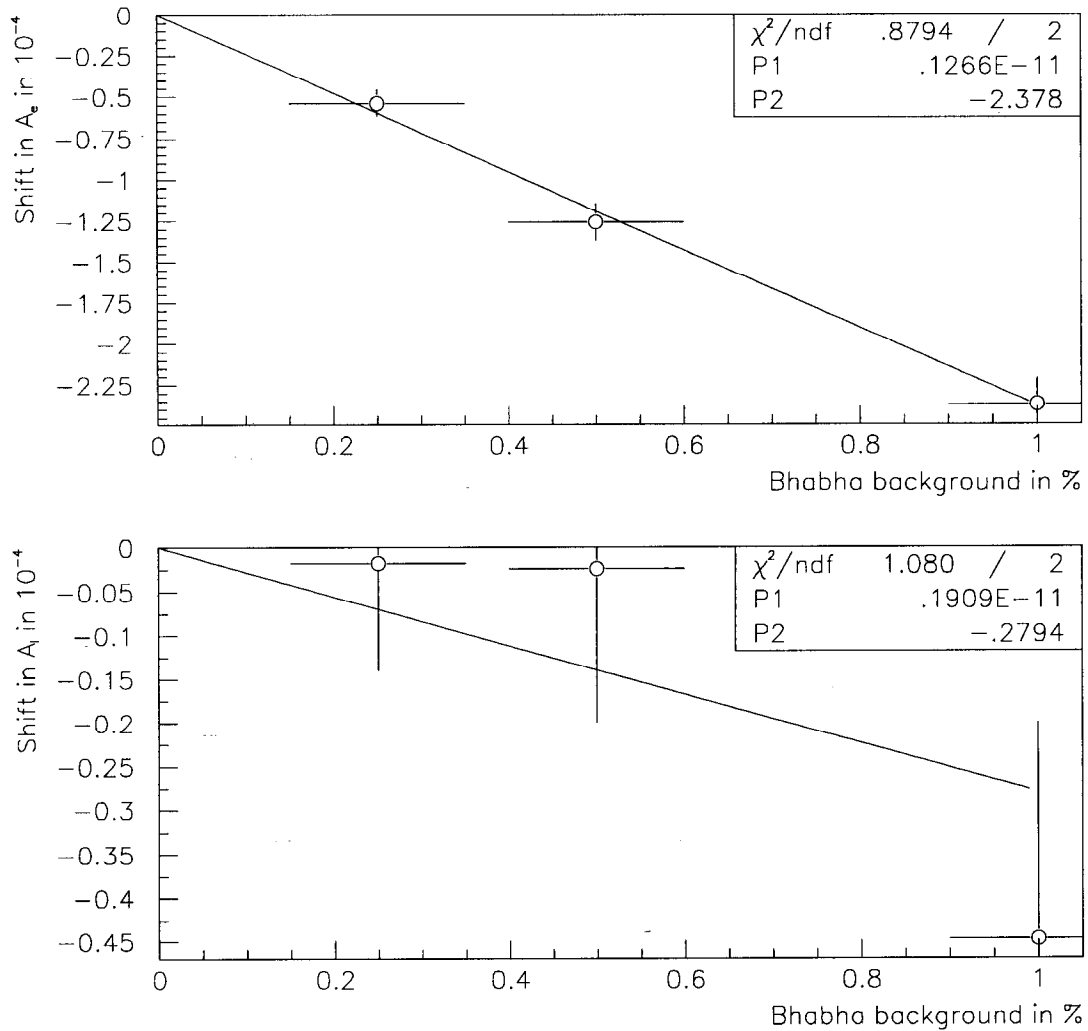


Figure 8.21: Fit for the shifts in A_e (top) and A_τ (bottom) due to the presence of Bhabha background as a function of the amount of background. From the left-right and the polarized forward-backward asymmetry of the Bhabha background one expects $-1.94 \cdot 10^{-4}/\%$ for A_e and $-0.38 \cdot 10^{-4}/\%$ for A_τ which is roughly 25% smaller (bigger) than observed. The difference is most likely a statistical fluctuation or due to the correlation term $A_e \cdot A_\tau$ in the cross section.

8. BACKGROUNDS

is more significant and might be due to the $A_e \cdot A_\tau$ term in the cross section, which cancels in the left-right asymmetry, but not in the maximum likelihood fit. Correcting the latter difference and using $A_{LR}^\tau = \tilde{A}_{FB}^\tau = 0.1542$ I calculate for $1.5\% \pm 1.5\%$ of Bhabha background:

$$\Delta A_e = -(3 \pm 3) \cdot 10^{-4}$$

$$\Delta A_\tau = -(3 \pm 3) \cdot 10^{-4}$$

Figure 8.22 shows the effect of two-photon background. There I cannot predict the shift in A_τ , because the shape of the polarized distribution is very different than the shape of the τ sample distribution. A_e on the other hand does not depend on the angular distribution and can therefore be predicted. Since $A_{LR}^{\gamma\gamma} = 0$, the analytical prediction is

$$\Delta A_e = -16 \cdot 10^{-4} \frac{b}{\%}$$

which is about 15% too low. Correcting for the difference and using $A_{LR}^\tau = \tilde{A}_{FB}^\tau = 0.1542$ I calculate for $1.0\% \pm 0.5\%$ of two-photon background:

$$\Delta A_e = -(18 \pm 9) \cdot 10^{-4}$$

$$\Delta A_\tau = -(7 \pm 4) \cdot 10^{-4}$$

8. BACKGROUNDS

$\gamma\gamma$ background shifts

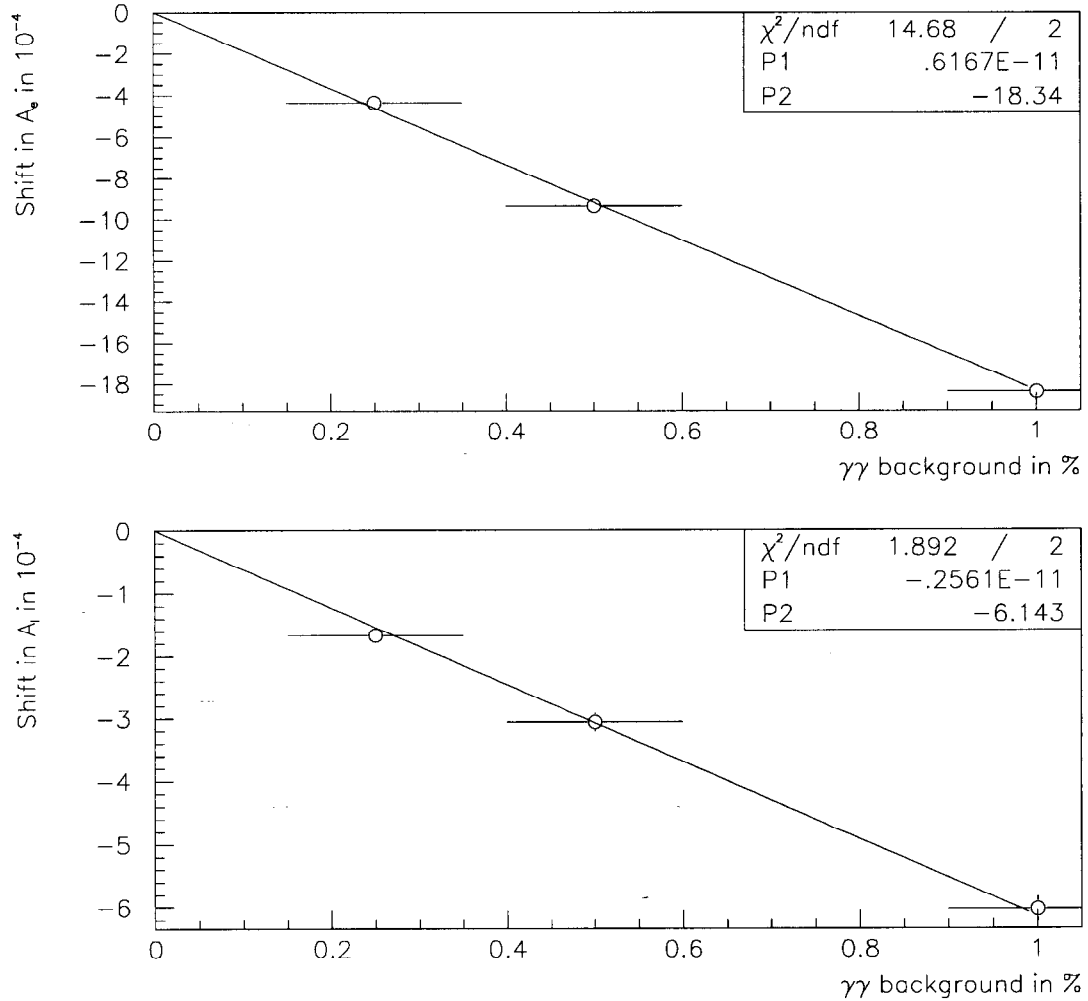


Figure 8.22: Fit for the shifts in A_e (top) and A_τ (bottom) due to the presence of two-photon background as a function of the amount of background. From the left-right asymmetry of the two-photon background one expects $-16 \cdot 10^{-4}/\%$ for A_e which is roughly 15% smaller than observed. The difference is most likely due to the $A_e \cdot A_\tau$ term in the cross section which cancels when calculating asymmetries.

8. BACKGROUNDS

Figure 8.23 shows the effect of hadronic background, which has the same left-right asymmetry as the τ sample, but is flat in $\cos\theta$. In the toy Monte Carlo, A_τ behaves as predicted analytically, but A_e shifted while I expected it to be unaffected. I take the observed shift as a systematic uncertainty:

$$\Delta A_e = -(0 \pm 3) \cdot 10^{-4}$$

$$\Delta A_\tau = -(8 \pm 8) \cdot 10^{-4}$$

8.4. Conclusion

In summary, I apply the corrections

$$-\Delta A_e = (20 \pm 9) \cdot 10^{-4}$$

$$-\Delta A_\tau = (18 \pm 9) \cdot 10^{-4}$$

to the asymmetry parameters measured in the τ sample and no correction to the asymmetry parameters measured in the Bhabha and μ sample. I have a systematic uncertainty of

$$\Delta A_e = 1.3 \cdot 10^{-4}$$

in the Bhabha sample that results from investigating different background shapes for the τ background.

8. BACKGROUNDS

Hadronic background shifts

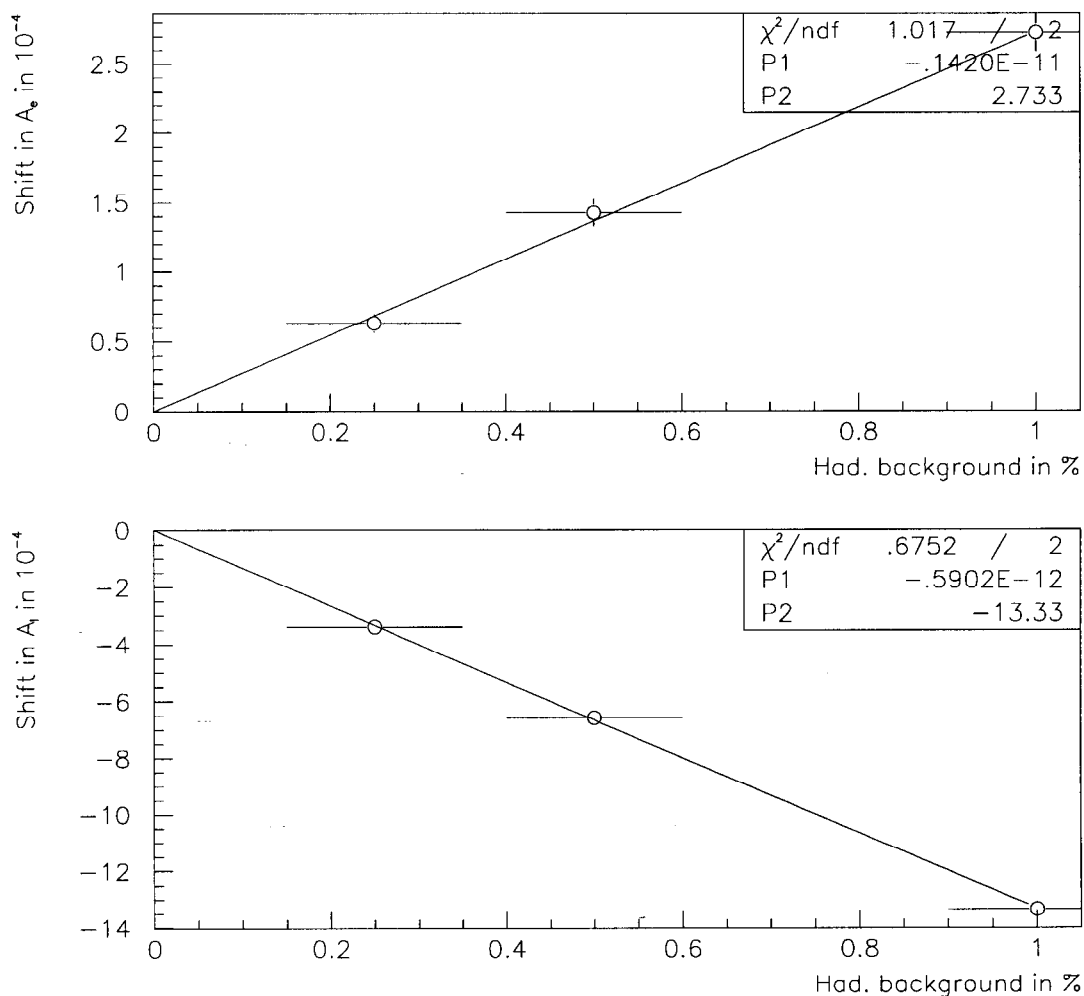


Figure 8.23: Fit for the shifts in A_e (top) and A_τ (bottom) due to the presence of hadronic background as a function of the amount of background. From the left-right and the polarized forward-backward asymmetry of the hadronic background one expects $0 \cdot 10^{-4}/\%$ for A_e and $-14 \cdot 10^{-4}/\%$ for A_τ . I take the apparent shift of A_e as systematic uncertainty as well as the 5% difference in the shift of A_τ even though the latter one is not statistically significant.

Chapter 9

Systematic effects from the τ Lorentz structure

Since this measurement uses left-right and polarized asymmetries in the polarized angular distributions, any selection efficiency difference (either between left- and right-handed events or between polarized forward and polarized backward events) will have a direct systematic effect on the measurement parameters. Electrons and muons are stable particles, so the selection efficiency does not depend on their helicity. The τ , however, decay weakly, and the V-A structure of their decay will introduce biases in the energy distribution of their decay products.

Since this effect is due to the polarization of the τ 's, I need to calculate this τ polarization at SLD/SLC. The cross sections for the four possible spin configurations for τ pair production as a function of $x = \cos \theta$ are

9. SYSTEMATIC EFFECTS FROM THE τ LORENTZ STRUCTURE

$$e^+e_L^- \rightarrow \tau_R^+\tau_L^-: \quad \frac{d\sigma}{dx} \propto c_L^e{}^2 c_L^\tau{}^2 (1+x)^2$$

$$e^+e_L^- \rightarrow \tau_L^+\tau_R^-: \quad \frac{d\sigma}{dx} \propto c_L^e{}^2 c_R^\tau{}^2 (1-x)^2$$

$$e^+e_R^- \rightarrow \tau_R^+\tau_L^-: \quad \frac{d\sigma}{dx} \propto c_R^e{}^2 c_L^\tau{}^2 (1-x)^2$$

$$e^+e_R^- \rightarrow \tau_L^+\tau_R^-: \quad \frac{d\sigma}{dx} \propto c_R^e{}^2 c_R^\tau{}^2 (1+x)^2$$

Because there is a fraction of $\frac{1 \pm P_e}{2}$ of left (right) handed events in a polarized electron beam of polarization P_e (where $P_e > 0$ means a left-handed beam) the production cross section for left-handed τ^- is

$$\frac{d\sigma_L}{dx} \propto c_L^\tau{}^2 ((1 + P_e A_e)(1 + x^2) + (A_e + P_e)2x).$$

The production cross section for right-handed τ^- is

$$\frac{d\sigma_R}{dx} \propto c_R^\tau{}^2 ((1 + P_e A_e)(1 + x^2) - (A_e + P_e)2x).$$

The τ polarization as a function of angle is therefore

$$P_\tau(x) = \frac{\frac{d\sigma_L}{dx} - \frac{d\sigma_R}{dx}}{\frac{d\sigma_L}{dx} + \frac{d\sigma_R}{dx}} = \frac{A_\tau + \frac{A_e + P_e}{1 + P_e A_e} \frac{2x}{1 + x^2}}{1 + A_\tau \frac{A_e + P_e}{1 + P_e A_e} \frac{2x}{1 + x^2}}$$

This function is shown in figure 9.1.

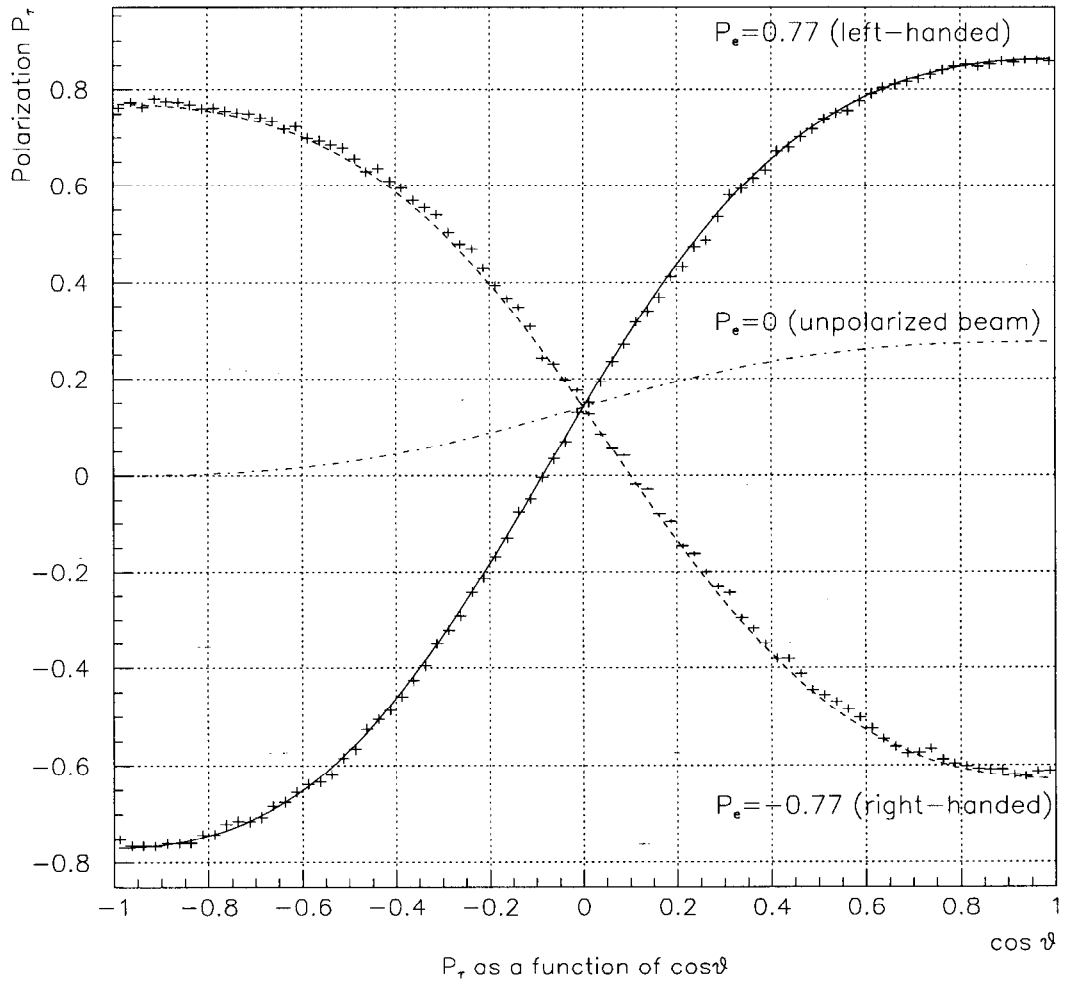
τ Polarization with polarized beams

Figure 9.1: τ polarization in KoralZ as a function of the scattering angle. The crosses are from KoralZ Monte Carlo used to investigate systematic effects on A_l due to the τ polarization. The smooth curves are analytical predictions of the polarization for $A_e = A_\tau = 0.141$

9. SYSTEMATIC EFFECTS FROM THE τ LORENTZ STRUCTURE

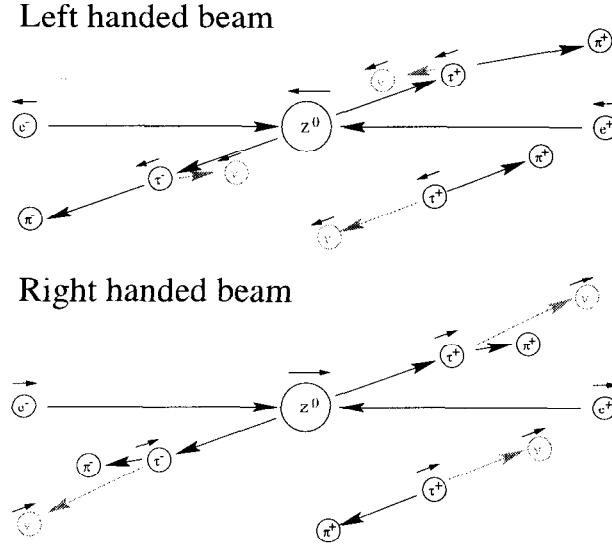


Figure 9.2: The beam polarization P_e influences the energy spectrum of the detected π in the τ decay channel $\tau \rightarrow \pi\nu$. The effect is due to the τ polarization and therefore (see figure 9.1) depends on $\cos \theta$. A left-handed beam (top) produces more hard π and a right-handed beam (bottom) more soft π . The small pictures in the right lower corner show the process in the τ rest frame

The reason why the energy distribution of the τ decay products depends on the τ polarization is the following. Since the τ neutrino that must be emitted in the τ^- decay is always left-handed, the decay products have preferred directions in the τ rest frame. For example, in the $\pi\nu$ decay mode (see figure 9.2) the probability for emitting the π at an angle ϕ with respect to the τ spin vector is $\propto \cos^2 \frac{\phi}{2} \propto E_\pi$ where E_π is the energy of the π measured in the lab frame. An energy dependent event selection can therefore produce a bias in the A_τ measurement since the τ polarization flips sign under parity and beam polarization sign reversal. I call this the ‘V-A effect’ since it arises from the ‘V-A’ structure of τ decays.

9. SYSTEMATIC EFFECTS FROM THE τ LORENTZ STRUCTURE

My event selection includes cuts on the energy deposited in the calorimeter (2) and on ‘tracking quantities’ like event mass (1), hemisphere mass (3), the maximum momentum (4) and acollinearity (5). Since the detector resolution induced errors of the ‘tracking quantities’ are small, they can be studied with generator-level Monte Carlo. I produced roughly $1 \cdot 10^6$ KoralZ [1] Monte Carlo events. To study the effect on the cut that involves the calorimeter I use GEANT [2] (a full detector simulation). I used about 70000 events from the 1994/95 SLD standard τ Monte Carlo.

9.1. The tracking cuts

I refer to the cuts on the event mass (1), the hemisphere mass (3), the maximum momentum (4) and the acollinearity (5) as ‘tracking cuts’. The KoralZ Monte Carlo used to study the effect of the tracking cuts shows indeed a different selection efficiency for left- and right-handed beam polarization (see figure 9.3). Because of the sign of the observed efficiency slopes, I expect an increase in the observed polarized forward-backward asymmetry and no effect for the left-right asymmetry. Figure 9.4 shows the measured and ‘true’ final state asymmetry A_l as a function of the scattering angle. I therefore need to apply a correction of

$$\Delta A_\tau^{track} = -(122.5 \pm 3.8) \cdot 10^{-4}$$

to the measured value of A_τ .

9. SYSTEMATIC EFFECTS FROM THE τ LORENTZ STRUCTURE

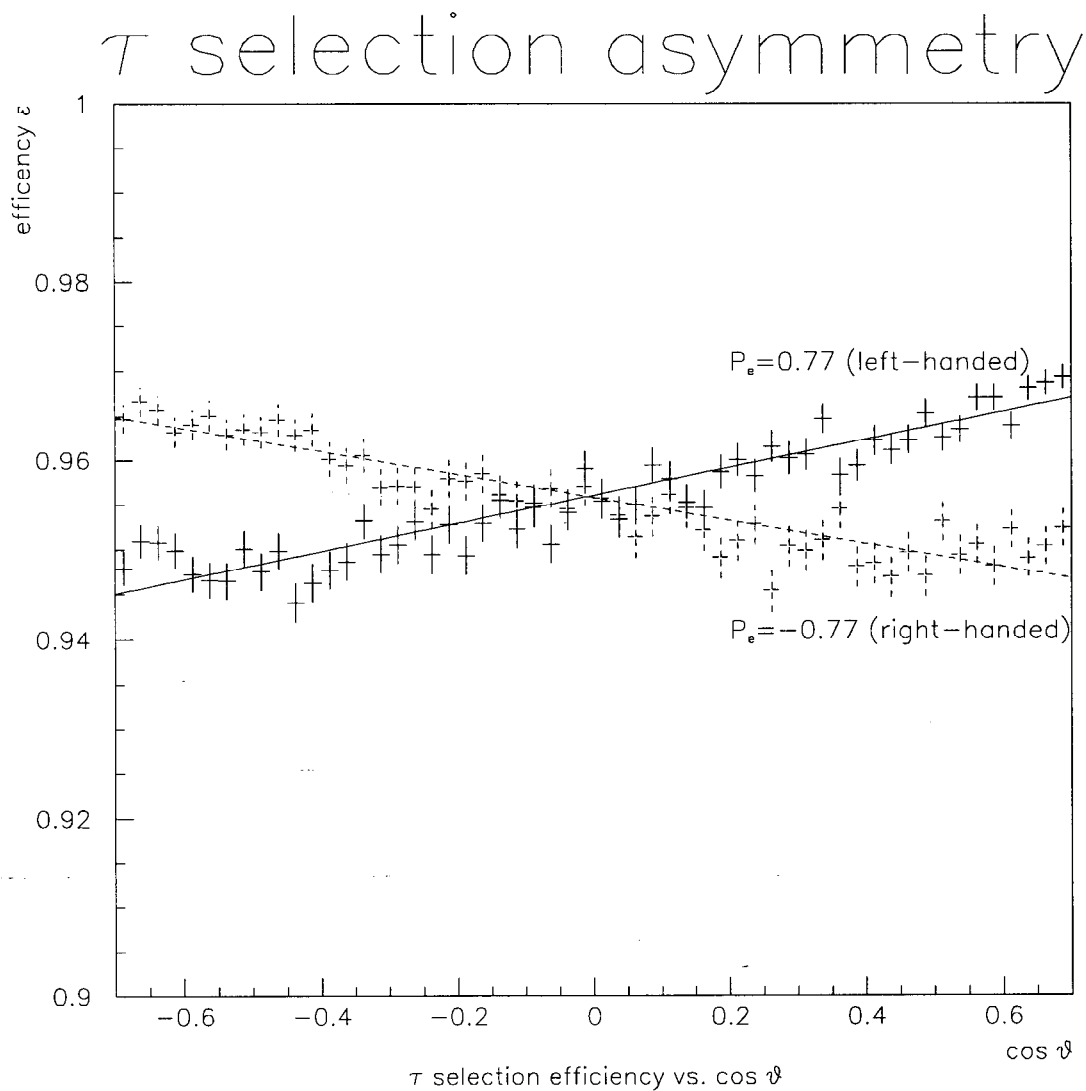


Figure 9.3: τ selection efficiency in KoralZ as a function of the scattering angle. I observe different slopes for left- and right-handed beams. From this I expect an increase in the measured polarized forward backward asymmetry. Since the average efficiency is equal for left- and for right-handed beams, I expect no effect for the left-right asymmetry. The efficiencies are for the tracking cuts (1, 3, 4 and 5) only.

9. SYSTEMATIC EFFECTS FROM THE τ LORENTZ STRUCTURE

V-A correction

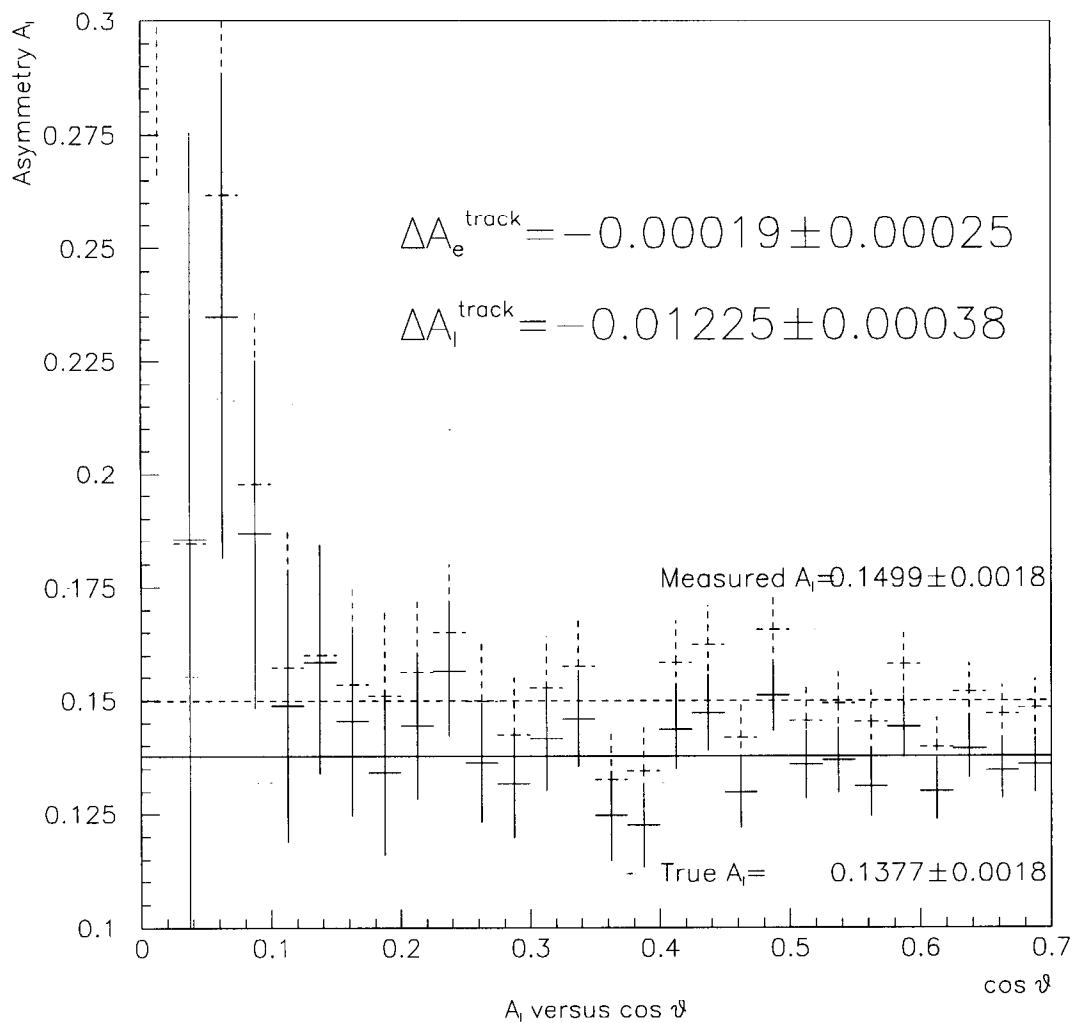


Figure 9.4: The final state asymmetry A_l as a function of the scattering angle. I observe a significant difference in the final state asymmetry of $(122.5 \pm 3.8) \cdot 10^{-4}$ while the left-right asymmetry is unchanged within the statistical error. The shown effect is from the tracking cuts (1, 3, 4 and 5) alone.

9.2. The calorimetric cut

I refer to the cut on the largest cluster associated with a charged track (2), the hemisphere mass (2) as the ‘calorimetric cut’. To study the effect of this cut I need to use a full detector simulation. I expect a decrease in the observed polarized forward-backward asymmetry and no effect for the left-right asymmetry, since I cut out decay products of higher energy. Figure 9.5 shows the measured and ‘true’ final state asymmetry A_l as a function of the scattering angle. I find a shift of

$$\Delta A_\tau = +(45 \pm 25) \cdot 10^{-4}$$

to the measured value of A_τ .

Since I did not observe a statistical significant shift (the effect could be a statistical fluctuation of 1.8σ), I changed the beam polarization to 1 to extract the highest precision from the Monte Carlo. Changing the beam polarization will change the τ polarization by a factor of about 1.25. I expect the effect to be linear in the τ polarization, so it should increase by a factor of 1.25 as well. I therefore expect a shift of about $56 \cdot 10^{-4}$. Figure 9.6 shows a shift of

$$\Delta A_\tau = +(54 \pm 19) \cdot 10^{-4}$$

To get the correction, I multiply this by 0.8 ± 0.2 that is, I treat all of the correction

9. SYSTEMATIC EFFECTS FROM THE τ LORENTZ STRUCTURE

V-A correction

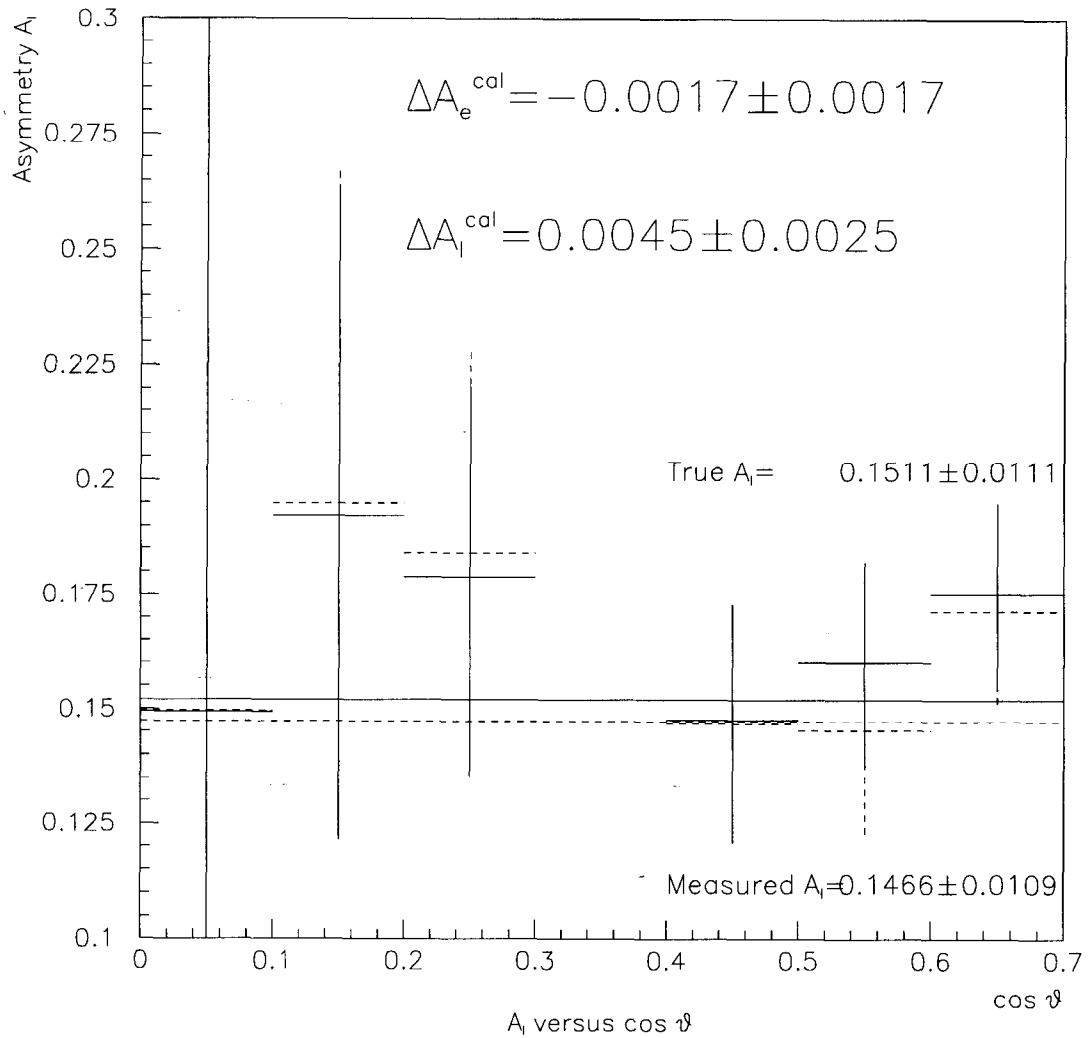


Figure 9.5: The final state asymmetry A_l as a function of the scattering angle. I observe a difference in the final state asymmetry of $(45 \pm 25) \cdot 10^{-4}$ while the left-right asymmetry is unchanged within the statistical error. The shown effect is from the calorimetric cut (2) alone.

9. SYSTEMATIC EFFECTS FROM THE τ LORENTZ STRUCTURE

V-A correction

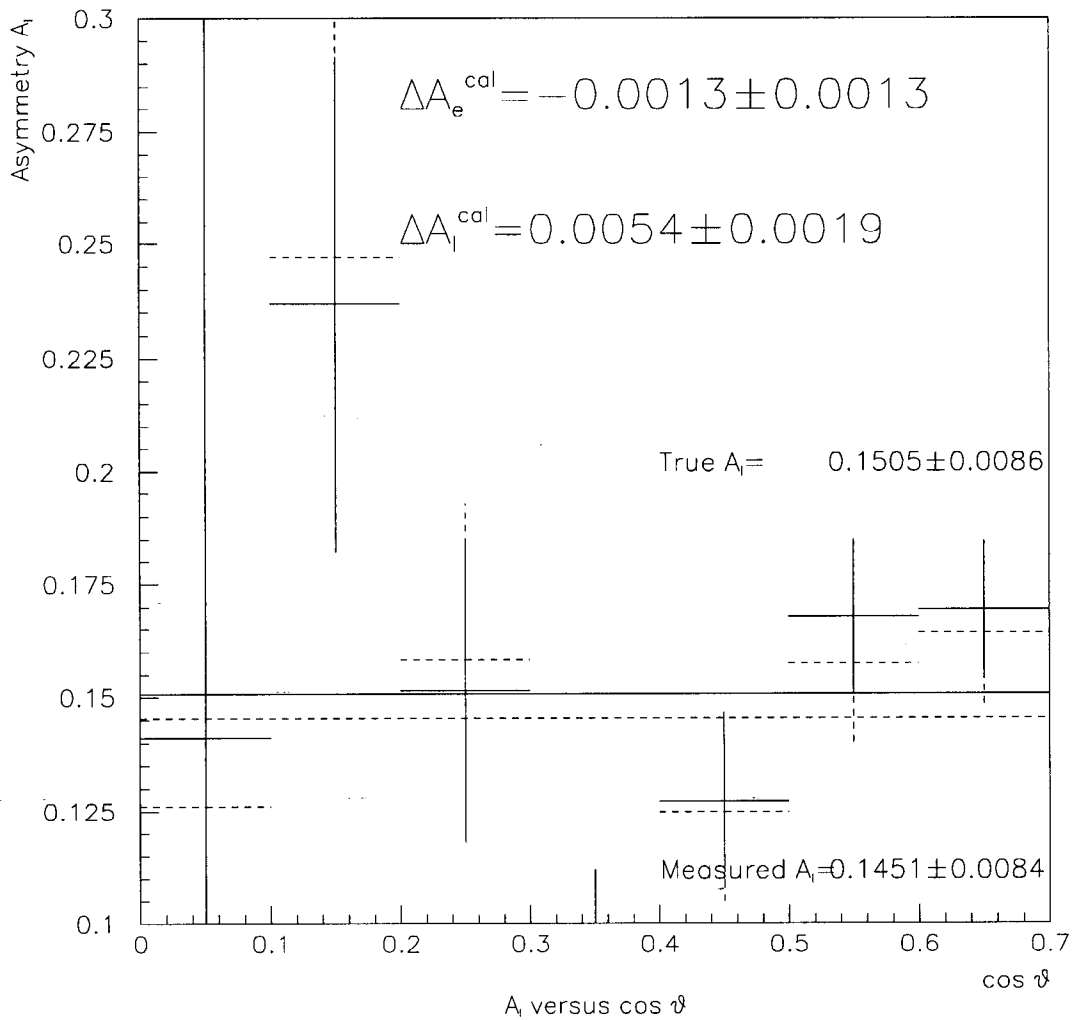


Figure 9.6: The final state asymmetry A_l as a function of the scattering angle for a beam polarization of magnitude 1. I observe a difference in the final state asymmetry of $(54 \pm 19) \cdot 10^{-4}$ while the left-right asymmetry is unchanged within the statistical error. To translate it to a beam polarization of magnitude 0.77 I multiply by 0.8 ± 0.2 and get $(43 \pm 19) \cdot 10^{-4}$. The shown effect is from the calorimetric cut (2) alone.

9. SYSTEMATIC EFFECTS FROM THE τ LORENTZ STRUCTURE

as uncertainty. I find the V-A correction due to the calorimetric cut to be

$$\Delta A_{\tau}^{cal} = +(43 \pm 19) \cdot 10^{-4}$$

The effect is now 2.3σ

Combining both the shift due to the calorimetric and the tracking cuts, the correction necessary due to the V-A effect is

$$\Delta A_{\tau} = -(80 \pm 19) \cdot 10^{-4}$$

9.3. Specific decay channels

It is interesting to investigate the effect of the separate decay channels. Figure 9.7 shows the efficiencies and corrections for $\tau \rightarrow \pi\nu$ and $\tau \rightarrow l\nu\nu$. Figure 9.8 displays the effect for $\tau \rightarrow \rho\nu$ and $\tau \rightarrow a_1\nu$. The effect is largest in the π decay mode. There the observed asymmetry is increased by roughly a factor of two. The lepton mode on the other hand shows no effect at all. (From the energy distribution of this mode I would expect a small effect of opposite sign. The Monte Carlo is consistent with that expectation but favors no effect at all.) Both ρ and a_1 show a modest-sized effect that is approximately equal to the one averaged over all decay modes. Table 9.1 summarizes the observed effects.

9. SYSTEMATIC EFFECTS FROM THE τ LORENTZ STRUCTURE

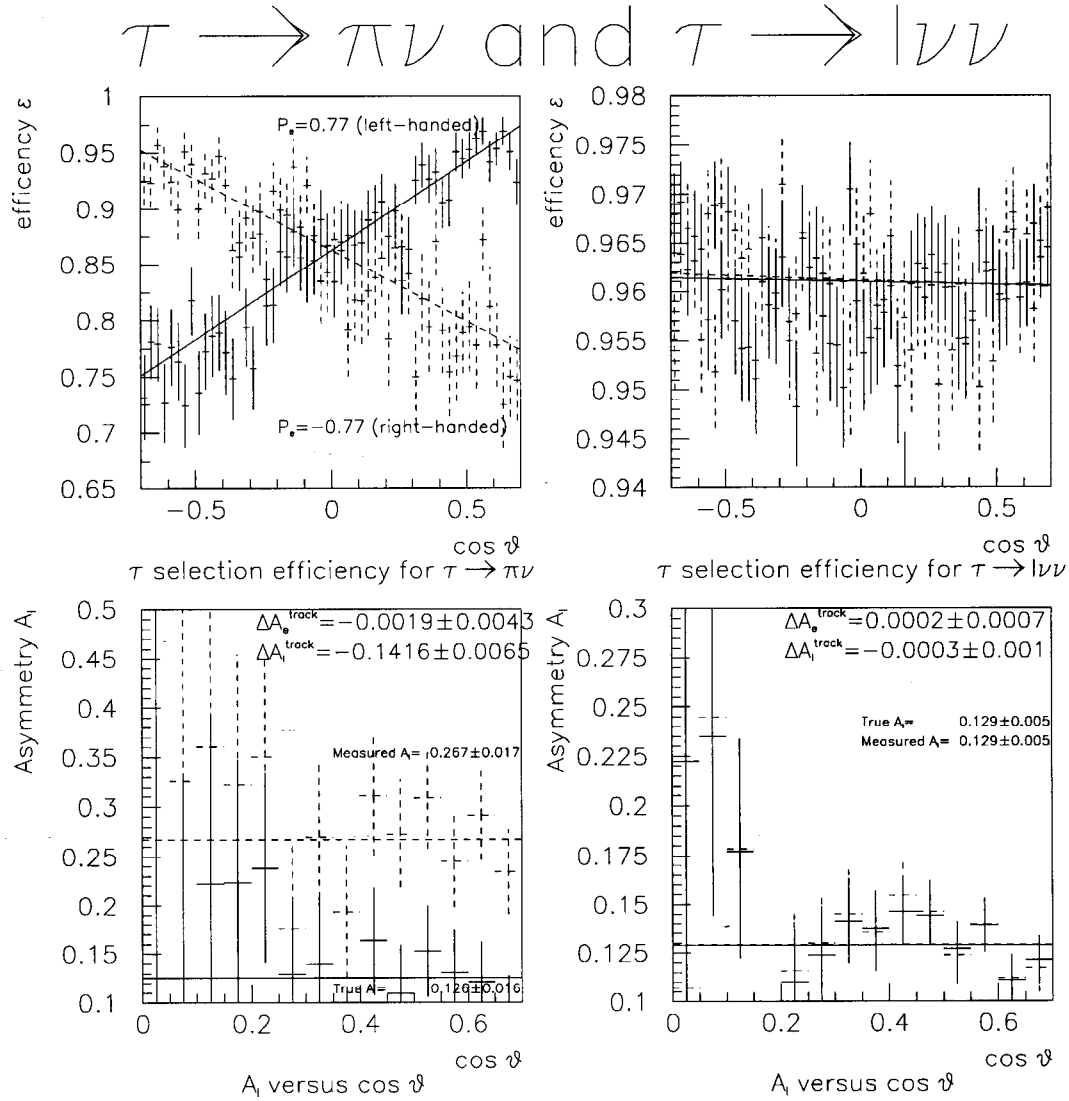


Figure 9.7: The efficiencies and the final state asymmetry A_l as a function of the scattering angle in the decay channels $\tau \rightarrow \pi\nu$ (left) and $\tau \rightarrow l\nu\nu$ (right). I observe a huge effect in the π mode and a negligible one in the lepton mode.

9. SYSTEMATIC EFFECTS FROM THE τ LORENTZ STRUCTURE

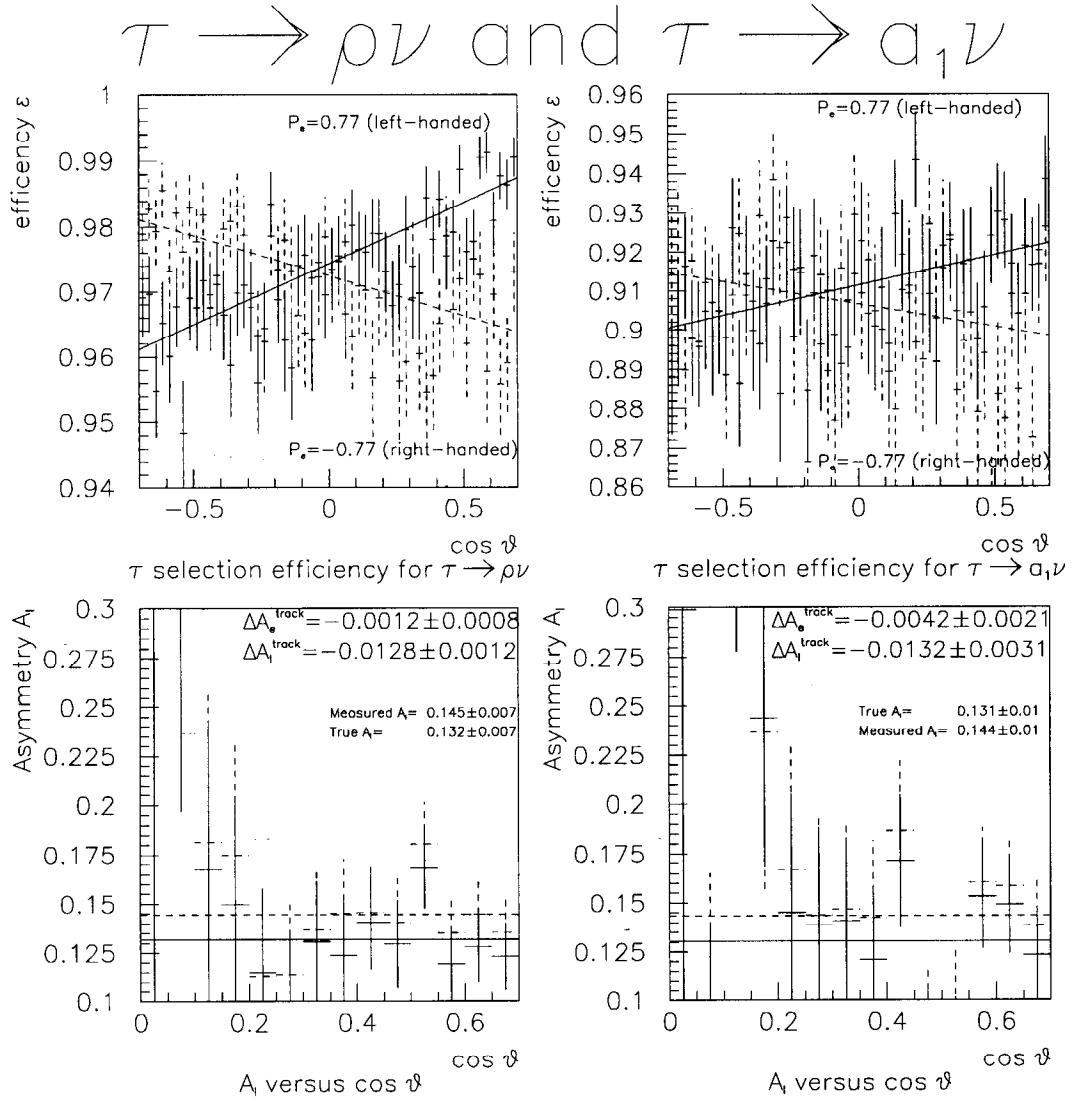


Figure 9.8: The efficiencies and the final state asymmetry A_l as a function of the scattering angle in the decay channels $\tau \rightarrow \rho\nu$ (left) and $\tau \rightarrow a_1\nu$ (right). I observe an average effect in both the ρ mode and the a_1 mode.

9. SYSTEMATIC EFFECTS FROM THE τ LORENTZ STRUCTURE

Decay mode	all	$\pi\nu$	$l\nu\nu$	$\rho\nu$	$a_1\nu$
ΔA_e in 10^{-4}	-1.9 ± 2.5	-19 ± 43	2 ± 7	-12 ± 8	-42 ± 21
ΔA_l in 10^{-4}	-122.5 ± 3.8	-1416 ± 65	-3 ± 10	-128 ± 12	-132 ± 31

Table 9.1: V-A effect for various τ decay modes. The largest effect comes from the π mode. ρ and a_1 show an average effect and I observe no effect in the lepton decay mode. There is no significant bias in A_e

9.4. Cross checks

I can of course use SLD Monte Carlo to investigate the effect of the tracking cuts.

As indicated in figure 9.9 I find

$$\Delta A_\tau^{track} = -(114 \pm 25) \cdot 10^{-4}$$

which is consistent with the KoralZ result. I therefore find the shift due to all five cuts to be

$$\Delta A_\tau = -(69 \pm 36) \cdot 10^{-4} \qquad \text{SLD Monte Carlo only}$$

I also fed the SLD Monte Carlo into the program with which I fit the data and observe a total shift of

$$\Delta A_\tau = -(71 \pm 36) \cdot 10^{-4} \qquad \text{SLD Monte Carlo only}$$

for the method using the polarized forward-backward asymmetry which is identical

V-A correction

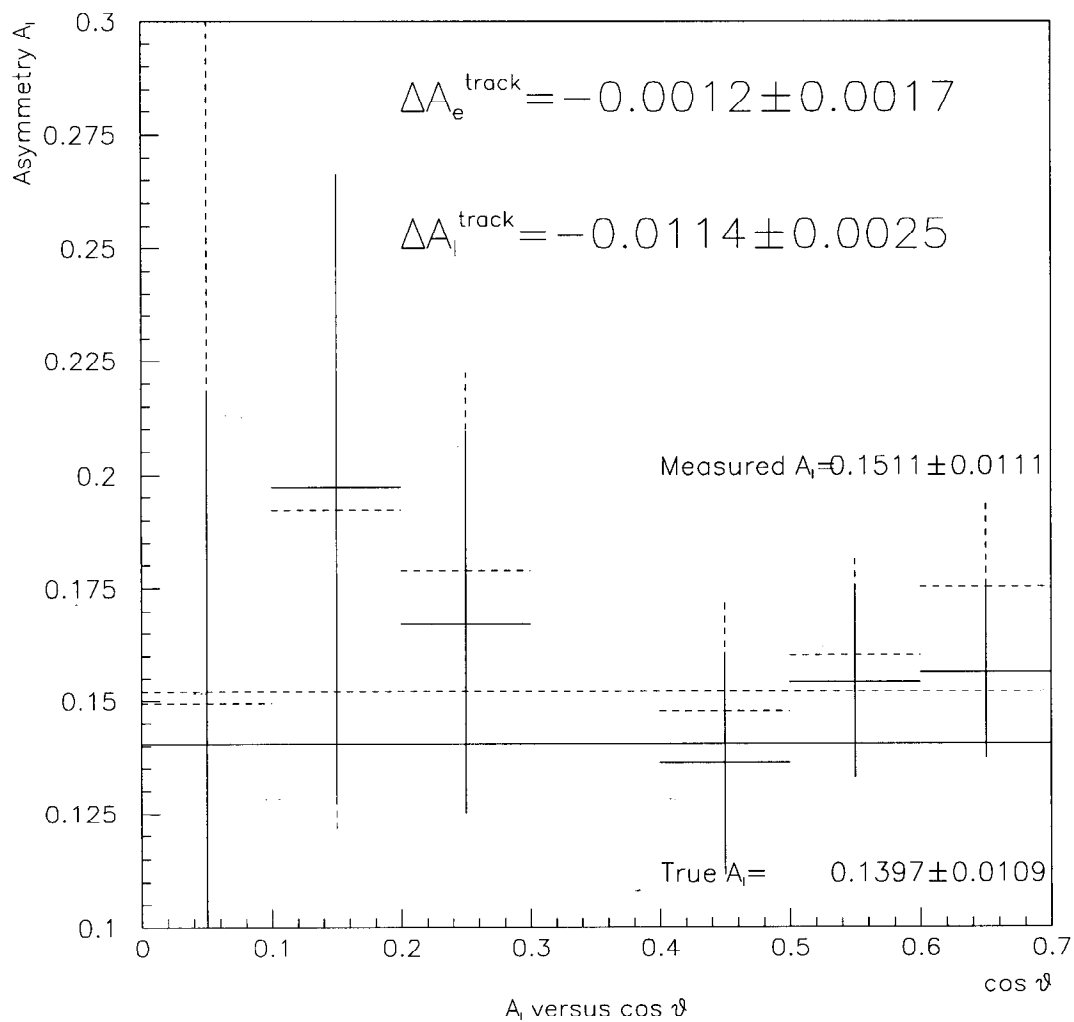


Figure 9.9: The final state asymmetry A_l as a function of the scattering angle. I observe a significant difference in the final state asymmetry of $(114 \pm 25) \cdot 10^{-4}$ while the left-right asymmetry is unchanged within the statistical error. The shown effect is from the tracking cuts (1, 3, 4 and 5) alone and has been investigated with the SLD Monte Carlo set.

9. SYSTEMATIC EFFECTS FROM THE τ LORENTZ STRUCTURE

to the finding above. The maximum likelihood method shifts its result by

$$\Delta A_\tau = -(72 \pm 37) \cdot 10^{-4} \qquad \text{SLD Monte Carlo only}$$

so I can't find a difference in the sensitivity to the V-A effect of the two analysis methods (polarized asymmetry method and maximum likelihood fit).

9.5. Conclusion

I measured the V-A effect due to the tracking cuts to be

$$\Delta A_\tau^{track} = -(122.5 \pm 3.8) \cdot 10^{-4}$$

and due to the calorimetric cut

$$\Delta A_\tau^{cal} = +(43 \pm 19) \cdot 10^{-4}.$$

Combining both, the correction necessary due to the V-A effect is

$$\Delta A_\tau = -(80 \pm 19) \cdot 10^{-4}$$

There is no effect on A_e and A_μ .

Bibliography

- [1] S. Jadach, B. F. L. Ward, Z. Was, *The Monte Carlo Program KoraiZ, Version 4.0, for the Lepton or Quark Pair Production at LEP/SLC Energies*
(Comut.Phys.Communic. **79**, 503-522, 1994)
- [2] R. Brun, R. Hagelberg, M. Hansroul, J. C. Lassalle, *GEANT: Simulation Program for Particle Physics Experiments. User Guide and Reference Manual*,
(CERN-DD/78/2 Rev., July 1978)

Chapter 10

Other systematic studies

There are a number of effects which I investigated, that can potentially affect the measurement. The systematic studies mentioned here have all negligible effects on the asymmetry parameter.

10.1. Thrust Axis Resolution

Since I look at polarized angular distributions, I need to reconstruct the lepton direction. For Bhabhas and mu-pairs this reconstruction is typically quite easy, because there are normally just two tracks. Tau events however have frequently more than two tracks, and there are at least two neutrinos (leading to a small acollinearity of the tau events) among the decay particles of the τ 's. I define a 'thrust axis' of the event (see figure 10.1) to reconstruct the lepton direction (in the center of mass) What I mean with 'thrust axis resolution' is the difference between lepton direction

10. OTHER SYSTEMATIC STUDIES

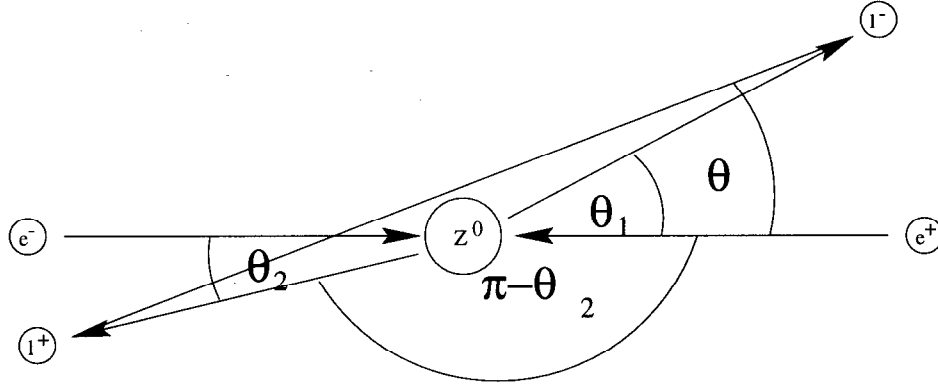


Figure 10.1: Thrust Axis for a lepton event. The momentum vector in each hemisphere defines an angle $\theta_{1,2}$. The angle θ combines both hemispheres and is used as the event angle, the difference between θ_1 and θ_2 measures the resolution.

and reconstructed thrust axis direction. I define (see figure 10.1)

$$x = \cos(\theta) = \frac{p_z}{|\vec{p}|} \text{ where } \vec{p} = \vec{p}_1 - \vec{p}_2 \quad (10.1)$$

and \vec{p}_i is the sum of the momenta of all charged tracks in hemisphere i the dividing plane of which is determined by the maximum momentum track. I can further define

$$x_{1,2} = \cos(\theta_{1,2}) = \pm \frac{p_{1z,2z}}{|\vec{p}_{1,2}|}$$

so the two momentum vectors are given by

$$\vec{p}_1 = p_1 \begin{pmatrix} \sqrt{1 - x_1^2} \hat{t}_1 \\ x_1 \end{pmatrix} \text{ and } \vec{p}_2 = p_2 \begin{pmatrix} -\sqrt{1 - x_2^2} \hat{t}_2 \\ -x_2 \end{pmatrix} \quad (10.2)$$

where $\hat{t}_{1,2}$ are the directions of the transverse momenta.

10. OTHER SYSTEMATIC STUDIES

I use now $x_1 - x_2$ as a measure of the uncertainty in x . For equal momenta magnitudes

$$p_1 = p_2 = p$$

I get

$$x = \frac{x_1 + x_2}{2} \frac{1}{\sqrt{\frac{1 - \cos \alpha}{2}}}$$

where α is the acollinearity angle. The second factor is close to one for τ events, since the acollinearity must exceed 160 degrees. (because this is one of the selection cuts)

Therefore, the resolution of x is

$$\sigma^2(x) = \frac{\sigma^2(x_1) + \sigma^2(x_2)}{4} = \frac{\sigma^2(x_1 - x_2)}{4} = \frac{\langle (x_1 - x_2)^2 \rangle}{4} \propto \langle (x_1 - x_2)^2 \rangle$$

10.1.1. τ events

Since any τ decay contains at least one neutrino (which escapes detection) I expect the difference between thrust axis and τ direction mostly due to stable neutral particles which are not taken into account when measuring the momenta p_1 and p_2 . Therefore, the resolution in θ should be independent of θ or

$$\sigma_\theta^2 = \langle (\Delta\theta)^2 \rangle = \langle (\theta - \theta_{true})^2 \rangle = \sigma_\theta^2.$$

10. OTHER SYSTEMATIC STUDIES

Therefore

$$\sigma_x^2 = \langle (\Delta x)^2 \rangle = \left\langle \left(\frac{\Delta x}{\Delta \theta} \Delta \theta \right)^2 \right\rangle \approx \langle (\Delta \theta)^2 \rangle \left(\frac{dx}{d\theta} \right)^2$$

and σ_x becomes a function of x :

$$\sigma_x^2(x) = \sigma_0^2(1 - x^2)$$

I plotted the τ thrust angle resolution for data, SLD Monte Carlo and KoralZ Monte Carlo in figure 10.2 and found that data and the two types of Monte Carlo agree well with each other and the above prediction. I found the 'conversion factor' between $\sigma^2(x)$ and $\langle (x_1 - x_2)^2 \rangle$ (from Monte Carlo) to be $\frac{1}{8}$. I assign a systematic error to the correction equal to its size. I extracted the proportionality constant and generated many toy Monte Carlo experiments with the thrust axis smeared by the amount mentioned above. I detected no shift in A_e and a shift of 0.0005 ± 0.0001 in A_τ . I conservatively treat the whole correction as systematic uncertainty as mentioned above, that is I apply the correction

$$\Delta A_\tau = (5 \pm 5) \cdot 10^{-4}$$

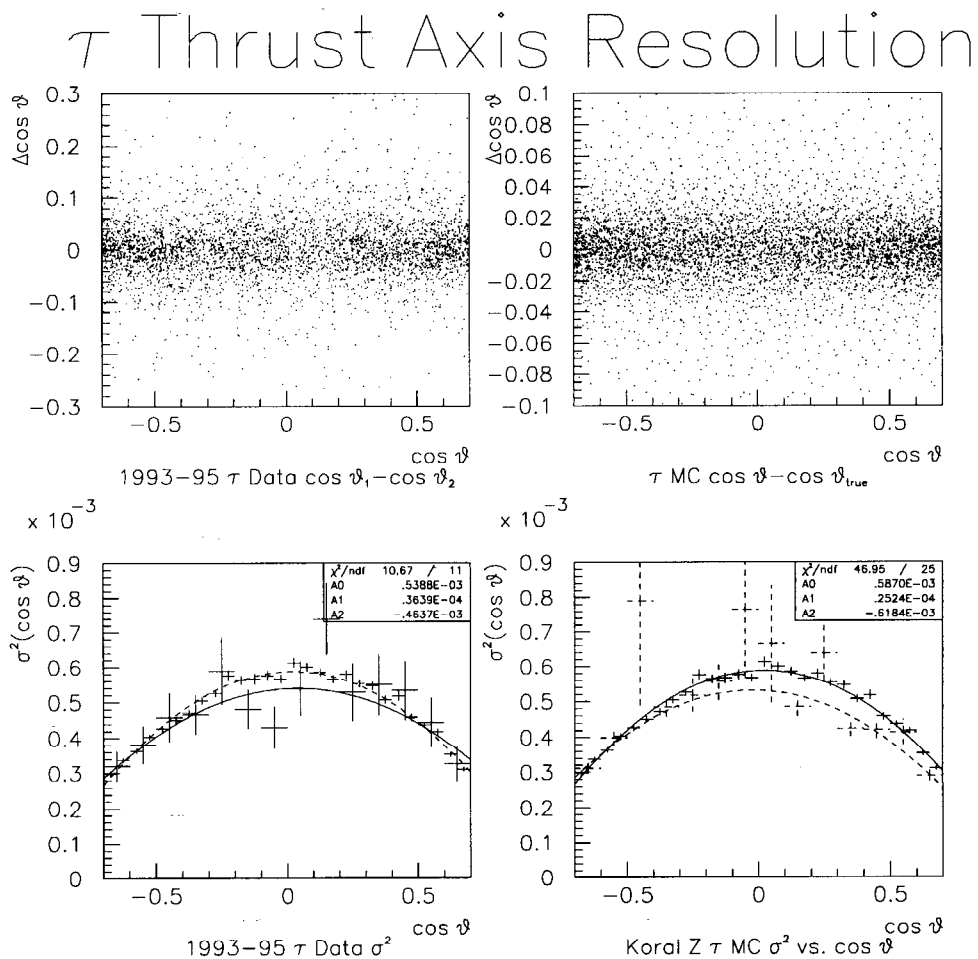


Figure 10.2: Thrust Axis Resolution for τ events. The upper left hand corner shows a scatter plot of $\cos(\theta_1) - \cos(\theta_2)$ versus $\cos(\theta)$ for the 1993-1995 data. The plot on the upper right shows the deviation of $\cos(\theta)$ from Monte Carlo truth for 1994/95 SLD Monte Carlo. The bottom plots show the variance in $\cos(\theta)$ as a function of $\cos(\theta)$. The lower left is a comparison between data (solid) and KoralZ Monte Carlo (dashed), the lower right compares KoralZ Monte Carlo (solid) with SLD Monte Carlo (dashed). All three relations have been fit to a second-order polynomial. Note that there is little difference between KoralZ and SLD Monte Carlo, so clearly the resolution is determined by the physics of the decay process and not by the SLD detector shortcomings. Agreement between data and Monte Carlo is very good, once the distribution in $\cos(\theta_1) - \cos(\theta_2)$ is normalized to the true residual in $\cos(\theta)$. Note also the size of the variance which is very small.

10.1.2. μ and Bhabha events

Figure 10.3 shows, that the thrust angle resolution for μ 's and Bhabhas is smaller than for τ events and can therefore be neglected. For these lepton species, SLD Monte Carlo suggests, that the conversion factor between $\sigma^2(x)$ and $\langle (x_1 - x_2)^2 \rangle$ is about 0.29 which was used in figure 10.3.

10.1.3. Initial/Final State Radiation

In addition to changing the Z line shape (see chapter 6), initial/final state radiation introduces a boost between the lab frame and the center of mass frame and therefore produces a non zero $x_1 - x_2$. Any correction due to that is therefore already taken care of in the two sections discussed previously. In principle, it could be corrected for by forming the thrust axis angle in the center of mass frame assuming that the initial state radiation photon is emitted along the beam pipe, that is the z -axis. Then the boosted four momenta are

$$\bar{p}_1 = \begin{pmatrix} \gamma(p_c + \beta p_{cz}) \\ \vec{p}_t \\ \gamma(\beta p_c + p_{cz}) \end{pmatrix} \text{ and } \bar{p}_2 = \begin{pmatrix} \gamma(p_c - \beta p_{cz}) \\ -\vec{p}_t \\ \gamma(\beta p_c - p_{cz}) \end{pmatrix}$$

where p_c is the magnitude of the momentum in the center of mass frame, p_{cz} the longitudinal and \vec{p}_t the transverse component of this momentum. Therefore, I can

10. OTHER SYSTEMATIC STUDIES

μ /WAB Thrust Axis Resol.

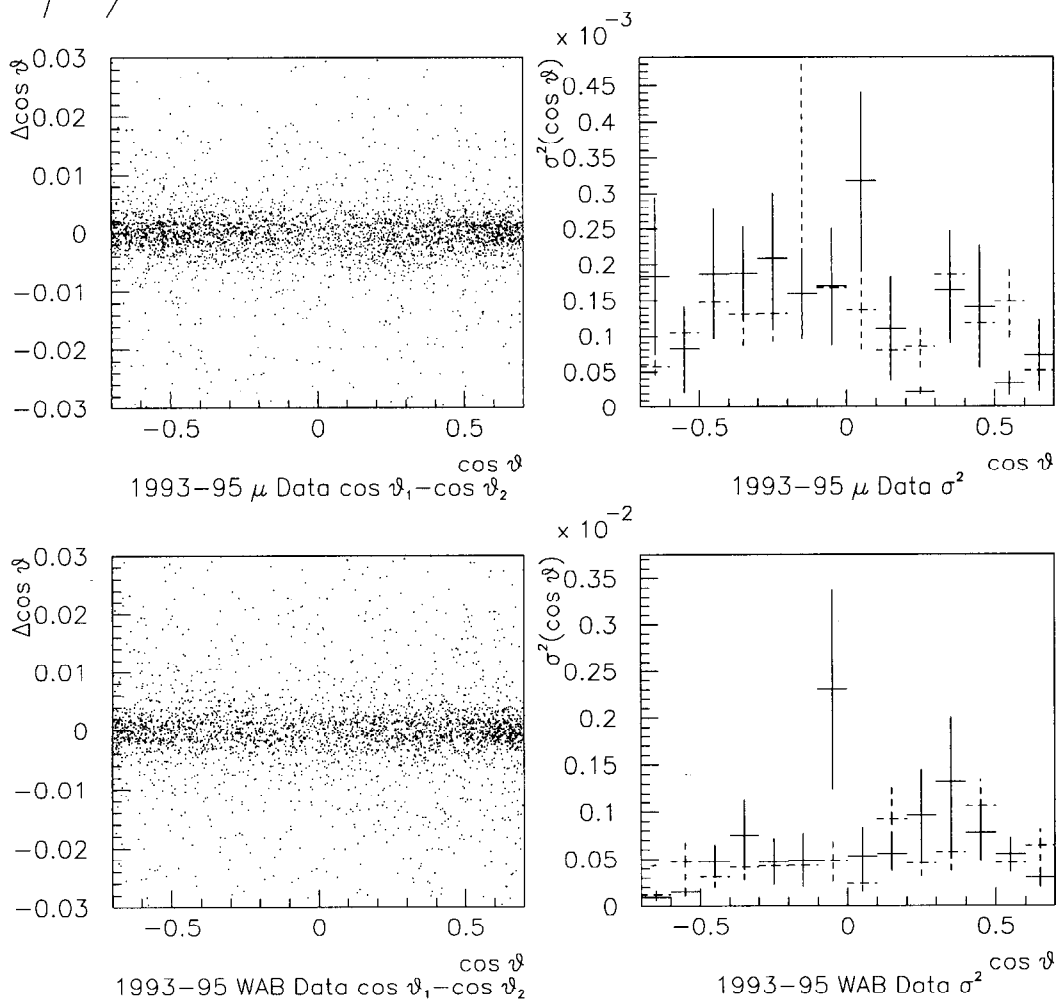


Figure 10.3: Thrust Axis Resolution for μ (top) and for Bhabha (bottom) events. The plots on the left-hand side are scatter plots of the residual versus $\cos(\theta)$, the ones on the right hand side show the variance. Note, that the resolutions are below the one for τ events and are therefore negligible.

10. OTHER SYSTEMATIC STUDIES

form

$$\cos(\theta^*) = \frac{p_{1z} - p_{2z}}{p_1 + p_2} = \frac{p_{1z} - p_{2z}}{E_1 + E_2} = \frac{2\gamma p_{cz}}{2\gamma p_c}$$

which is the correct angle in the center of mass frame. If there is just a longitudinal boost, then the transverse momenta in equation 10.2 balance, $p_1\sqrt{1-x_1^2}\hat{t}_1 = p_2\sqrt{1-x_2^2}\hat{t}_2$, that is $\hat{t}_1 = \hat{t}_2$ and $p_1 \sin \theta_1 = p_2 \sin \theta_2$ and (using $\sin \theta_1 + \sin \theta_2 = 2 \sin \frac{\theta_1 + \theta_2}{2} \cos \frac{\theta_1 - \theta_2}{2}$)

$$\cos(\theta^*) = \frac{p_1 \cos \theta_1 + p_2 \cos \theta_2}{p_1 + p_2} = \frac{\sin \theta_2 \cos \theta_1 + \sin \theta_1 \cos \theta_2}{\sin \theta_1 + \sin \theta_2} = \frac{\sin(\theta_1 + \theta_2)}{2 \sin(\frac{\theta_1 + \theta_2}{2}) \cos(\frac{\theta_1 - \theta_2}{2})}$$

which results in

$$\cos(\theta^*) = \frac{\cos(\frac{\theta_1 + \theta_2}{2})}{\cos(\frac{\theta_1 - \theta_2}{2})}$$

10.1.4. Charge Confusion

Since I require that the product of the two charges measured in the two hemispheres be -1 the only possible source of error is that the charges of both hemispheres have the opposite sign as the measured quantities. If I call p_{conf} the probability of this 'charge confusion' I can define the dilution D

$$D = \frac{1 - p_{conf} - p_{conf}}{1 - p_{conf} + p_{conf}} = 1 - 2p_{conf}.$$

10. OTHER SYSTEMATIC STUDIES

I measure then the product $A_{meas} = D \cdot A_l$ rather than A_l and have therefore a shift

$$\Delta A_l = A_l - A_{meas} = (1 - D)A_l = 2p_{conf}A_l$$

The probability p_{conf} can be estimated from the number of like-sign events (both hemispheres have the same charge sign) and the number of unlike-sign events (the hemispheres have the opposite charge sign)

$$p_{conf} = \left(\frac{n_{like}}{n_{unlike}} \right)^2$$

In figure 10.4 I plotted like-sign events for τ Monte Carlo as a function of $\cos \theta$. I get a charge confusion probability of

$$p_{conf} = 6.2 \cdot 10^{-5}$$

and therefore a shift of

$$\Delta A_\tau = 2.4 \cdot 10^{-5}$$

From this probability I would expect 1.2 events of the 19273 unlike-sign Monte Carlo events to have confused charges. I observed one event.

As seen in figure 10.5 I observe 47 like-sign events in the SLD τ sample (which are of course not used in the analysis). There is no preferred region in $\cos \theta$ in the

10. OTHER SYSTEMATIC STUDIES

MC τ Charge Confusion

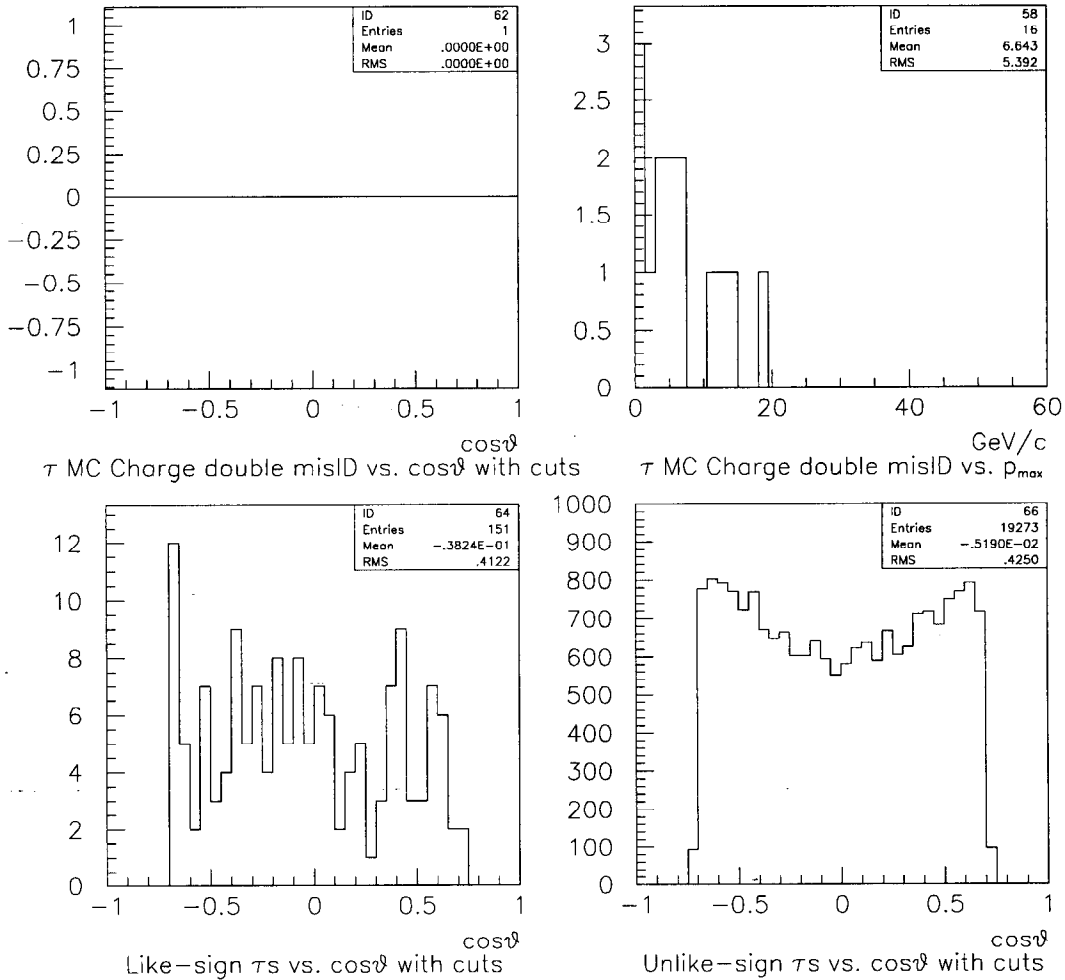


Figure 10.4: Charge confusion for τ Monte Carlo. The top plots show events for which the charge sign of both hemispheres was measured incorrectly as a function of the scattering angle and the maximum momentum for the charged tracks. The bottom two plots show events with equal (unequal) charge signs measured. The square of the ratio of the number of equal signs over the number of unequal signs should be roughly the probability of misidentification in both hemispheres.

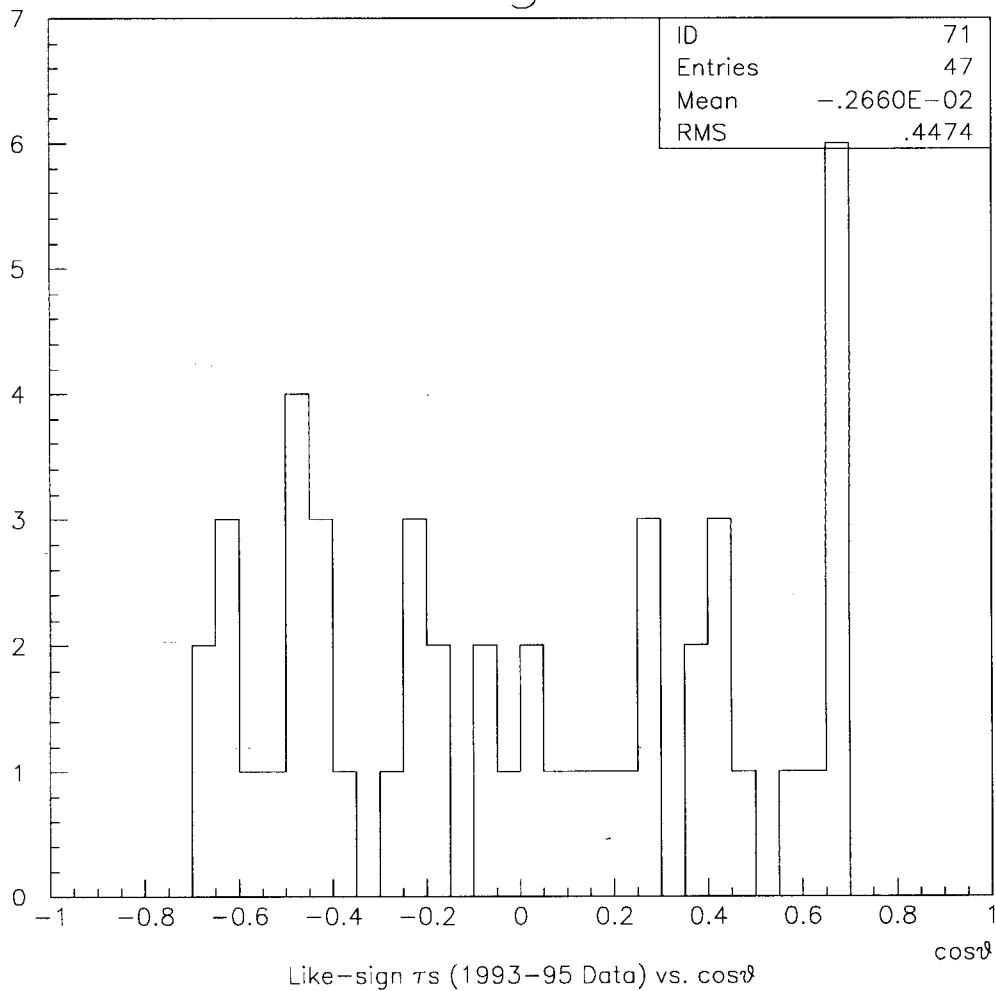
τ Data Charge Confusion

Figure 10.5: Like-sign events for τ data. I count only 47 events as opposed to 3748 unlike-sign events. There is no significant bias in any region of $\cos(\theta)$. The resulting effect on A_τ is negligible.

10. OTHER SYSTEMATIC STUDIES

sample. With a total sample size of 3748 events, the confusion probability

$$p_{conf} = 1.6 \cdot 10^{-4}$$

results in a shift of

$$\Delta A_\tau = 6.3 \cdot 10^{-5}$$

Both the Monte Carlo and the data determined shifts are very small and completely negligible. In figure 10.6 I see 7 like-sign events in the μ data (3788 events) preferring no angular region which corresponds to a confusion probability and a shift in A_μ of

$$p_{conf} = 3.4 \cdot 10^{-6}$$

$$\Delta A_e = 6.8 \cdot 10^{-7}$$

Finally, figure 10.7 shows 23 like-sign events in the Bhabha sample (4527 events) preferring no angular region;

$$p_{conf} = 2.6 \cdot 10^{-5}$$

$$\Delta A_e < 7.7 \cdot 10^{-6}$$

(A_e is also measured from the initial state coupling which is not affected by charge confusion in the final state.) In Monte Carlo, I don't observe any double charge confused muons or Bhabhas because of lack of statistics.

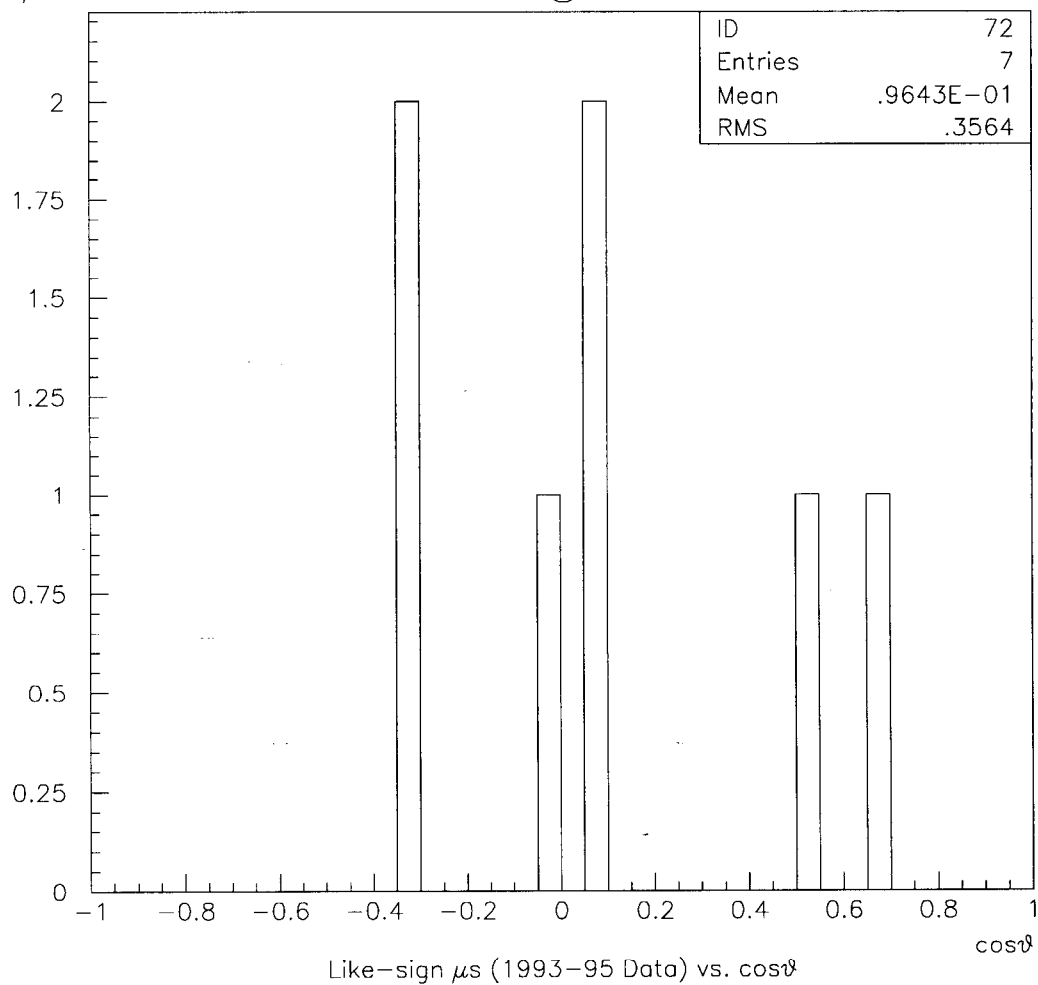
μ Data Charge Confusion

Figure 10.6: Like-sign events for μ data. I count only 7 events as opposed to 3788 unlike-sign events. There is no significant bias in any region of $\cos(\theta)$. The resulting effect on A_μ is negligible.

WAB Data Charge Confusion

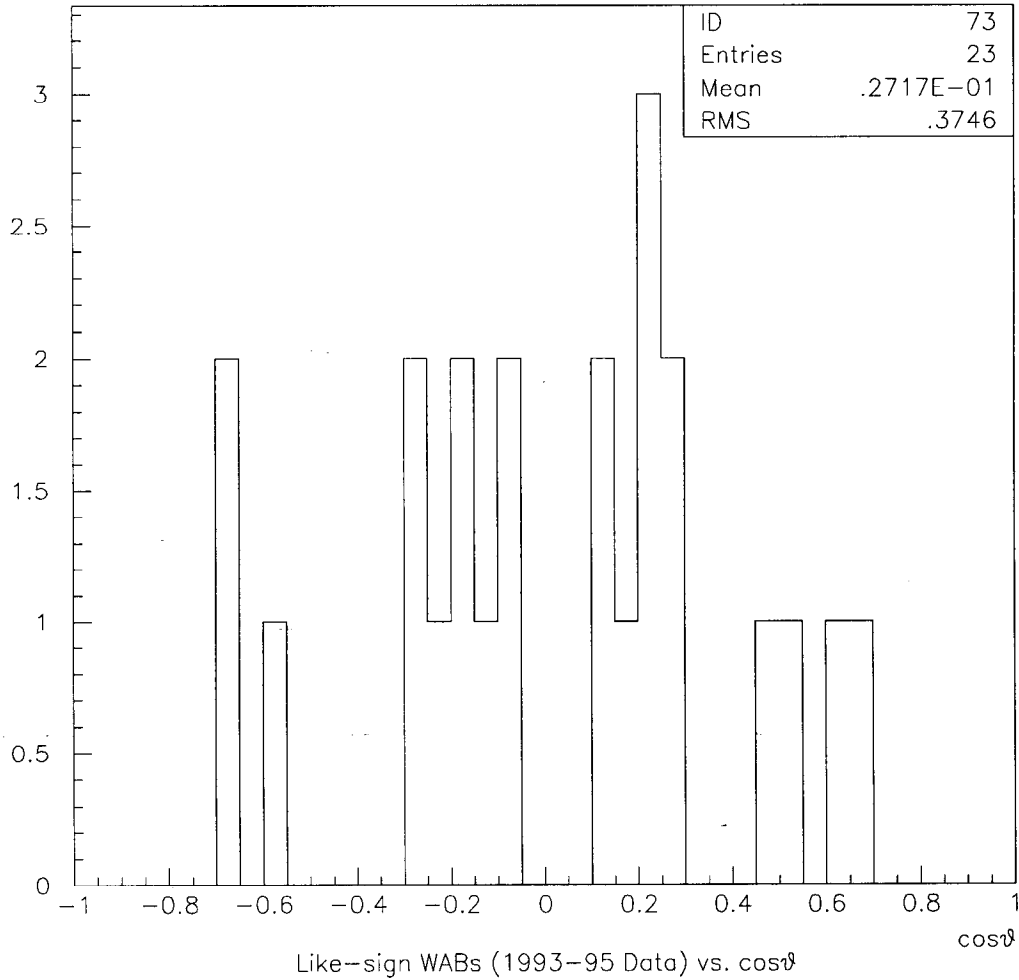


Figure 10.7: Like-sign events for Bhabha data. I count only 23 events as opposed to 4527 unlike-sign events. There is no significant bias in any region of $\cos(\theta)$. The resulting effect on A_T is negligible.

10.1.5. Conclusion

In summary, I apply a correction of

$$\Delta A_\tau = (5 \pm 5) \cdot 10^{-4}$$

to A_τ and effects on A_e and A_μ due to thrust axis resolution are negligible.

10.2. Detector efficiency systematics**10.2.1. Effect of a non-uniform selection efficiency for Bhabhas**

While the maximum-likelihood fit for muons and taus is insensitive to a dependence of the selection efficiency on $\cos \theta$ as long as it is symmetric in $\cos \theta$, the maximum-likelihood fit for Bhabhas requires a constant efficiency over the entire angular acceptance. The reason for this requirement is the presence of the photon t-channel term, which is asymmetric in $\cos \theta$. I used Monte Carlo to investigate possible efficiency differences, especially in the region around $|\cos \theta| \approx 0.5$, where the calorimeter performance is degraded. I did not see any significant changes in efficiency (see figure 10.8). I fit the distribution with a function and forced an efficiency drop at $|\cos \theta| \approx 0.5$ and at the edges of the angular acceptance. To increase the statistics, I assumed a symmetric efficiency dependence and fit the distribution in $|\cos \theta|$. I then used toy Monte Carlo to estimate the effect of such an efficiency

10. OTHER SYSTEMATIC STUDIES

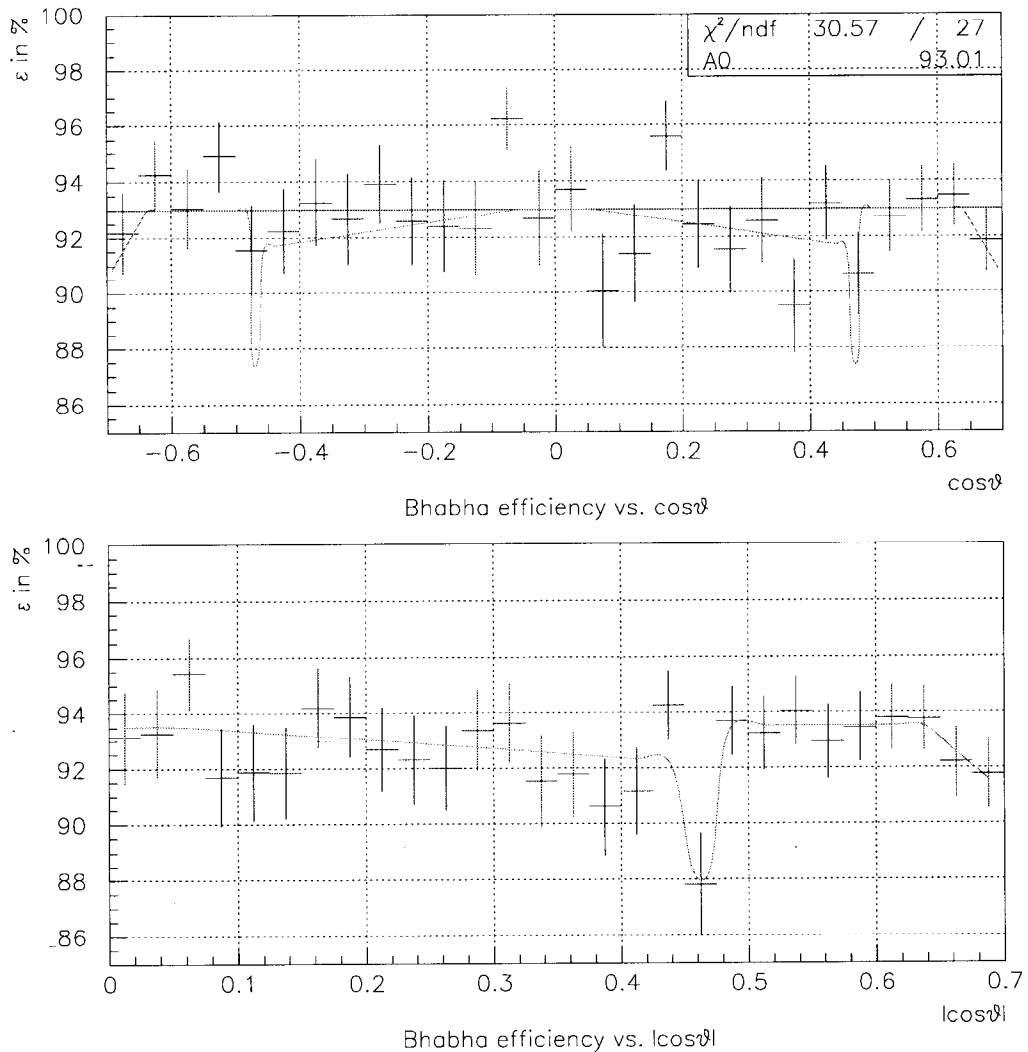


Figure 10.8: Bhabha selection efficiency versus $\cos \theta$. The top plot shows the result of a linear fit and compares the chosen fit function with the Monte Carlo histogram. Note, that the histogram is consistent with a flat efficiency. I actually did the fit to the distribution in $|\cos \theta|$ (lower plot) to increase the statistics. The effect of the chosen function on A_e is negligible.

function on A_e

$$\Delta A_e^{\text{eff}} = 1.3 \cdot 10^{-4}$$

which I neglected.

10.2.2. Effect of a detector-induced asymmetry in selection efficiency

I already studied a left-right difference in τ selection efficiency (see chapter 9) which was induced by the V-A structure of the τ decays.

In the study of detector-induced asymmetries in the selection efficiency, I assume no difference between left- and right-handed events. (It is hard to imagine how such a difference might arise; it would have to be a detector element sensitive to the spin of the final state) Therefore, there should not be any bias in the initial-state coupling A_{LR} .

However, a forward-backward detector efficiency asymmetry κ can be defined as $\kappa = \frac{\epsilon_F - \epsilon_B}{\epsilon_F + \epsilon_B}$. Then $\epsilon_F = \epsilon_0(1 + \kappa)$ and $\epsilon_B = \epsilon_0(1 - \kappa)$ ($\epsilon_0 = \frac{\epsilon_F + \epsilon_B}{2}$ is the symmetric efficiency), so

$$\begin{aligned} \Delta \tilde{A}_{FB} &= \frac{(1 + \kappa)\sigma_{LF} - (1 - \kappa)\sigma_{LB} - (1 + \kappa)\sigma_{RF} + (1 - \kappa)\sigma_{RB}}{(1 + \kappa)\sigma_{LF} + (1 - \kappa)\sigma_{LB} + (1 + \kappa)\sigma_{RF} + (1 - \kappa)\sigma_{RB}} - \tilde{A}_{FB} \\ &= \frac{\sigma_{LF} - \sigma_{LB} - \sigma_{RF} + \sigma_{RB} + \kappa(\sigma_{LF} + \sigma_{LB} - \sigma_{RF} - \sigma_{RB})}{\sigma_{LF} + \sigma_{LB} + \sigma_{RF} + \sigma_{RB} + \kappa(\sigma_{LF} - \sigma_{LB} + \sigma_{RF} - \sigma_{RB})} - \tilde{A}_{FB} \\ &= \frac{\tilde{A}_{FB} + \kappa A_{LR}}{1 + \kappa A_{FB}} - \tilde{A}_{FB} = \frac{\kappa}{1 + \kappa A_{FB}} (A_{LR} - A_{FB} \tilde{A}_{FB}) \\ &\approx \kappa A_{LR} \approx 0.12\kappa \end{aligned}$$

10. OTHER SYSTEMATIC STUDIES

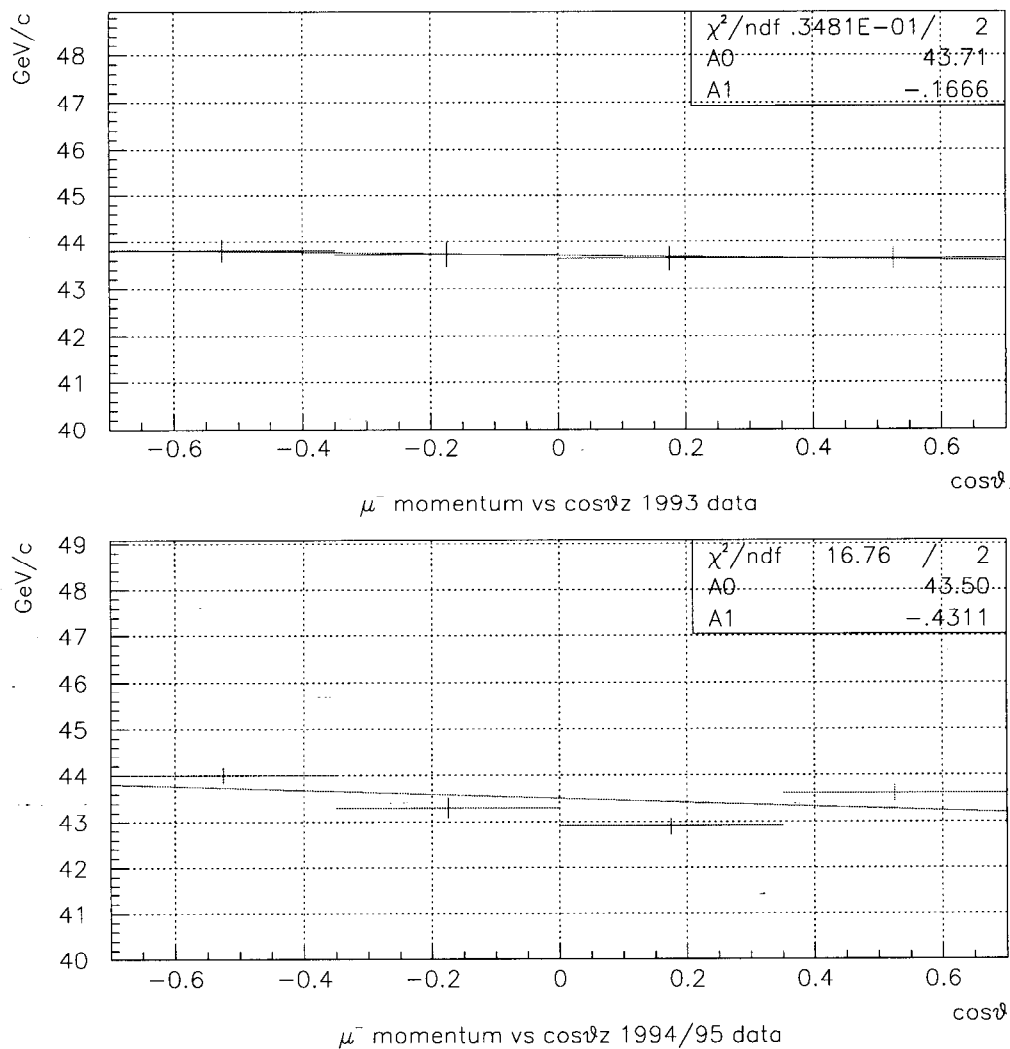


Figure 10.9: Maximum momentum of events with high maximum momentum ($\mu^+\mu^-$). The distribution is consistent with being flat, but for the 1994/95 data a 1% slope can be assumed.

10. OTHER SYSTEMATIC STUDIES

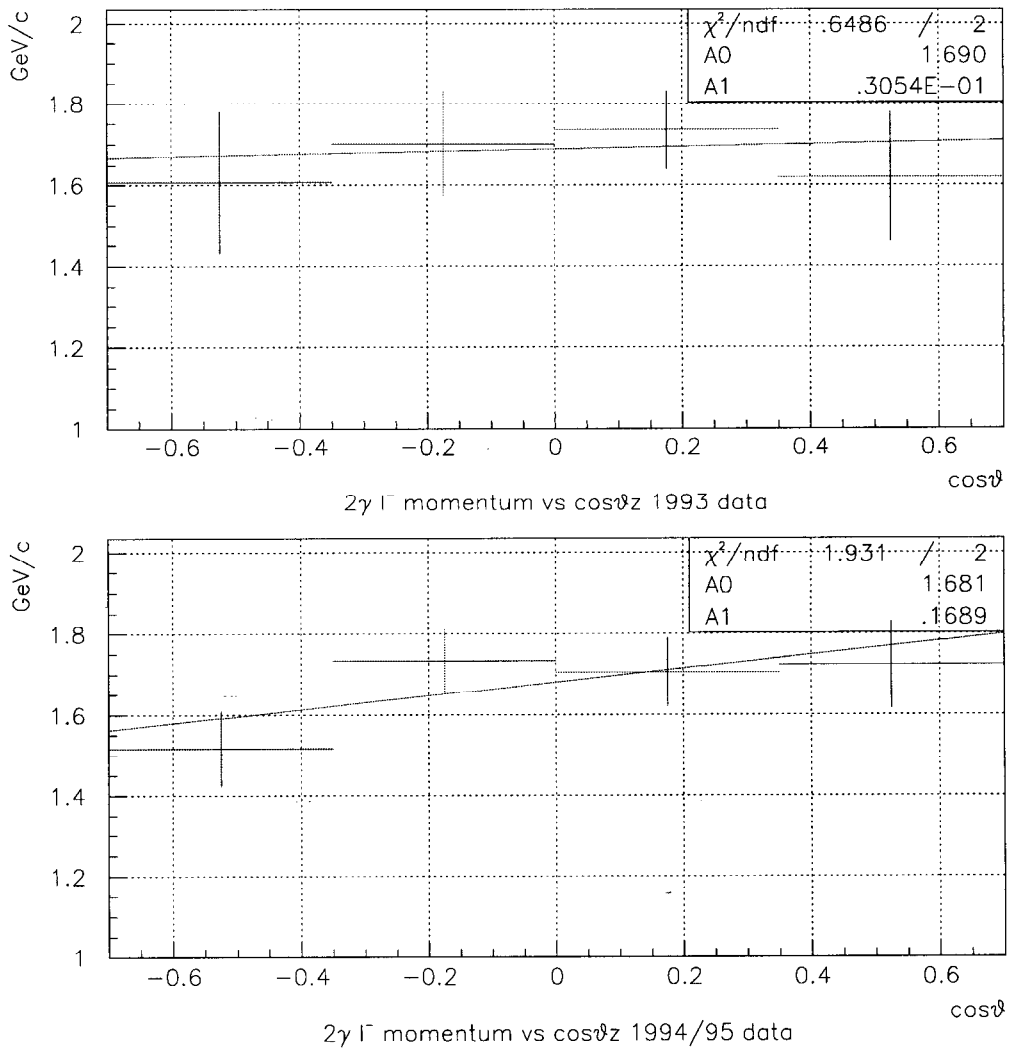


Figure 10.10: Maximum momentum of events with low maximum momentum ($\gamma\gamma$). The distribution is consistent with being flat, but for the 1994/95 data a 10% slope can be assumed.

10. OTHER SYSTEMATIC STUDIES

The search for a detector-induced efficiency asymmetry cannot use Monte Carlo, because the Monte Carlo model of the detector is symmetric. I plotted the momenta of events with a high maximum momentum (see figure 10.9: muons) and a low maximum momentum (see figure 10.10: two photons) versus the scattering angle and could not find any difference between the forward and the backward region. For the low momentum tracks, the data is consistent with a flat momentum distribution as well as a linear distribution with a 10% slope. In the two bins around the tau cut against low maximum momentum events, there are about 60 events in the 1994/95 data sample (see figure 7.13) out of about 2000 events. With the conservative assumptions, that the 10% slope is real, that there is a 10% difference in momentum between all forward and backward events (the true difference would be $|\cos \theta| \times 10\%$), that this momentum difference leads to a 10% difference in accepting these 60 events (and that all of them were taus) even though the average momentum (1.6 GeV) is well below the cut (3 GeV), the bias κ cannot exceed

$$\kappa < \frac{60 \times 10\%}{2000} = 0.003$$

and so the shift

$$\Delta \tilde{A}_{FB} < 4 \cdot 10^{-4}$$

is negligible.

10.3. Polarization Corrections

The event-by-event signed polarization values are of primary importance for this measurement as well as for the determination of the left-right cross section asymmetry A_{LR} from hadronic events. The polarization measurements and their errors are discussed along with SLD's A_{LR} measurement [1]. The most important correction that is not already done directly on SLD's data tapes is the so-called chromaticity correction. The Compton polarimeter [2] uses the asymmetry in polarized Compton scattering of circularly polarized photons with the electron beam to measure the electron beam polarization. It is effectively a measurement of the average polarization of the entire beam. Because of chromatic effects in SLC's final focus, electrons in the tails of the energy spectrum are not as well focused as the ones in the peak and don't contribute as much to the luminosity. Because the spin precession is energy-dependent (it is reasonable to optimize the spin rotators for the peak of the energy distribution), the tail electrons have a smaller polarization than the peak electrons. For measuring the polarized asymmetries I am interested in the luminosity-weighted average beam polarization. The Compton polarimeter measures a smaller polarization than that because it gives the tail electrons the same weight as the peak electrons. During the 1993 run the luminosity-weighted average beam polarization P_{lum} was a factor of

10. OTHER SYSTEMATIC STUDIES

about 1.017 higher than the one determined from the Compton polarimeter P_{Compt}

$$P_{lum} = 1.017 \cdot P_{Compt}$$

During the 1994-95 run the effective number of spin rotations in the arcs was reduced, therefore decreasing the dependence of the polarization on the energy. The resulting chromaticity correction is small and applied to SLD's data tapes directly.

For the 1993 data I increased each event polarization by 1.7% and observed a minor shift in the asymmetry parameters.

The uncertainty on the polarization leads to a systematic uncertainty of

$$\Delta A_e^{pol} = \Delta A_t^{pol} = 28 \cdot 10^{-4}$$

for 1993 [3] and

$$\Delta A_e^{pol} = \Delta A_t^{pol} = 10 \cdot 10^{-4}$$

for 1994/95 [2].

10.4. Overview over systematic uncertainties

The systematic uncertainties are listed in table 10.1. Assuming 100% of correlation between the polarization errors of 1993 and 1994-95 (that is the 1993 error is split up in $\pi_{uc} + \pi_c = 26 + 10$, where π_{uc} shows no correlation and π_c shows 100% correlation)

10. OTHER SYSTEMATIC STUDIES

I get the systematic uncertainties listed in table 10.2. Combining the results for A_e (with 100% correlation for the radiative corrections) gives a systematic error for A_e . Combining all results into $A_{e-\mu-\tau}$ results in a systematic error for $A_{e-\mu-\tau}$:

$$\Delta A_e = 13 \cdot 10^{-4}$$

$$\Delta A_{e-\mu-\tau} = 13 \cdot 10^{-4}$$

Systematics	A_e^e	A_e^μ	A_e^τ	A_μ	A_τ
Pol. 1993 $\pi_{uc} + \pi_c$ (see Section 10.3)	28	28	28	28	28
Pol. 1994-95 π_c (see Section 10.3)	10	10	10	10	10
Backgrounds (see Section 8.4)	4	-	9	-	9
Rad. Corr. (see Section 6.2)	8	6	12	17	10
V- Λ effect (see Section 9.5)	-	-	-	-	19
Thrust res. (see Section 10.1)	-	-	-	-	5

Table 10.1: Systematic Uncertainty Summary in units of 10^{-4}

Data Sample	A_e	A_μ	A_τ
Bhabha	15	-	-
Muon	13	21	-
Tau	19	-	26

Table 10.2: Systematic Uncertainty in units of 10^{-4}

Bibliography

- [1] SLD Collaboration (K. Abe et al.) SLAC-PUB-7291, Sep 1996. 15pp
“An Improved Measurement of the Left-Right Cross-Section Asymmetry” to be submitted to Physical Review Letters

- [2] M. Fero, P.L. Reinertsen, B.A. Schumm, M. Swartz, E. Torrence,
SLD note #249, June 1996 “Compton Polarization Measurement: 1995”, unpublished

- [3] SLD Collaboration (K. Abe et al.) SLAC-PUB-6456, Mar 1994. 15pp
“Precise Measurement of the Left-Right Cross-Section Asymmetry in Z Boson Production by e^+e^- collisions” published in Phys.Rev.Lett.73:25-29,1994.

Chapter 11

The Polarized Lepton Asymmetries

11.1. Extraction of the Asymmetries

To extract the asymmetry parameters I fit the selected μ 's and τ 's with the function described in Section 6.1. The function has A_e and A_μ (A_τ) as free parameters. I rely on the unbinned maximum likelihood method for the fitting. In addition, I form event-by-event asymmetries as described in Section 2.3.2 corrected as described in Section 2.3.1 which also give me A_e and A_μ (A_τ). The two methods agree in their results. A_e and A_τ from the τ samples are then corrected for backgrounds, the V-A effect and the thrust axis resolution. Figure 11.1 shows the two fits.

The Bhabha events are fit to the function described in Section 6.2. It has A_e (basically g_V^e/g_A^e) and $g_V^{e^2} + g_A^{e^2}$ (proportional to Γ_{ee}) as free parameters. Again, I rely on the unbinned maximum likelihood method. Figure 11.1 shows the fit.

11. THE POLARIZED LEPTON ASYMMETRIES

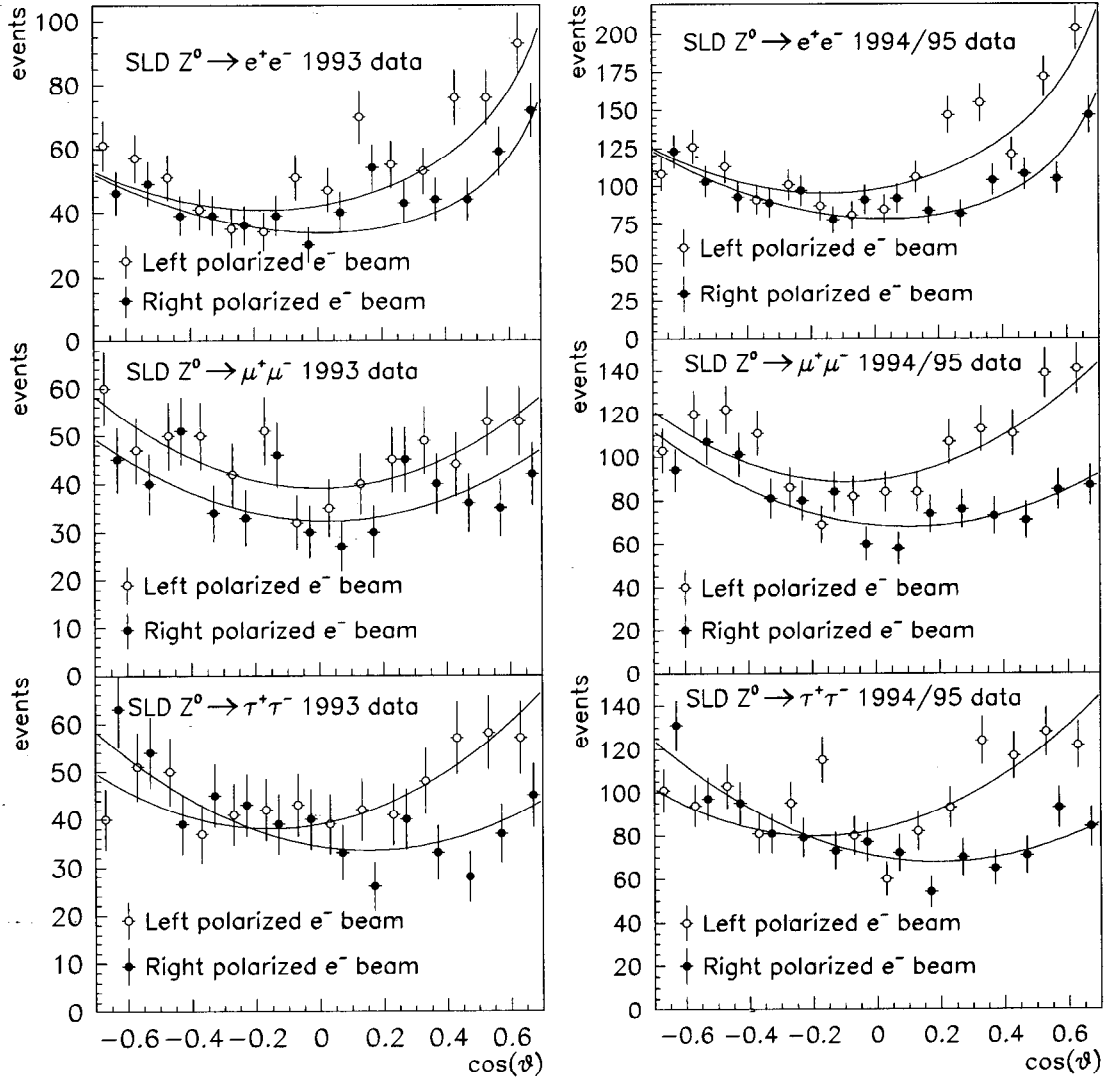


Figure 11.1: Polar angle distribution for Z decays to e , μ and τ . The 1993 data is shown on the right-hand side, the 1994/95 data on the left-hand side. The open (filled) circles are for left(right)-handed electron polarization. For the Bhabha events, the forward-backward asymmetry has the same sign for both polarizations, for the μ and τ events, the forward-backward asymmetry changes sign with polarization.

11. THE POLARIZED LEPTON ASYMMETRIES

Sample	Events	A_e	A_μ	A_τ
1993 e^-	1434	0.195 ± 0.041		
1993 μ^-	1185	0.155 ± 0.046	0.020 ± 0.070	
1993 τ^-	1211	0.110 ± 0.046		0.247 ± 0.069
1994/95 e^-	3093	0.145 ± 0.022		
1994/95 μ^-	2603	0.173 ± 0.026	0.127 ± 0.038	
1994/95 τ^-	2537	0.134 ± 0.026		0.178 ± 0.039

Sample	A_e	A_μ	A_τ
1993-95 e^-	$0.156 \pm 0.019 \pm 0.001$		
1993-95 μ^-	$0.169 \pm 0.022 \pm 0.001$	$0.102 \pm 0.034 \pm 0.001$	
1993-95 τ^-	$0.128 \pm 0.022 \pm 0.002$		$0.195 \pm 0.034 \pm 0.003$
1993-95 l^-	$0.152 \pm 0.012 \pm 0.001$		
1993-95 l^-	$A_l = 0.151 \pm 0.011 \pm 0.001$		

Table 11.1: Lepton Asymmetries from 1993-95 SLD data [1]. Systematic errors are only shown for the full data set. The last row combines all measurement on A_e . Combining all three measurement in a single asymmetry parameter A_l (assuming lepton universality) gives $A_l = 0.151 \pm 0.011 \pm 0.001$.

11.2. The Results

The corrected results are summarized in table 11.1. I measured the asymmetry parameters to be

$$\begin{aligned}
 A_e &= 0.152 \pm 0.012 & \frac{g_V^e}{g_A^e} &= 0.0764 \pm 0.0061 \\
 A_\mu &= 0.102 \pm 0.034 & \text{or } \frac{g_V^\mu}{g_A^\mu} &= 0.0511 \pm 0.0171 \\
 A_\tau &= 0.195 \pm 0.034 & \frac{g_V^\tau}{g_A^\tau} &= 0.0959 \pm 0.0175 \\
 A_l &= 0.151 \pm 0.011 & \frac{g_V^l}{g_A^l} &= 0.0759 \pm 0.0056
 \end{aligned}$$

11. THE POLARIZED LEPTON ASYMMETRIES

where A_l combines all three results with the assumption of lepton universality. The data supports the universality assumption with a confidence level of 15%. This assumption is crucial for the standard model of electroweak interaction, since $A_l = A_{LR}^0$ depends on the effective electroweak mixing angle only

$$\sin^2 \theta_W^{\text{eff}} = 0.2310 \pm 0.0014$$

and this mixing angle is a property of the neutral gauge bosons in this model. This is the first direct measurement of A_μ , since the four LEP experiments [2] can only measure $A_e \times A_\mu$. They can however measure A_e and A_τ independently, using the τ polarization as a function of polar angle which is induced by both the initial-state and final-state coupling asymmetry.

The four LEP experiments [2] measure the asymmetry parameters to be $A_e = 0.1465 \pm 0.0059$, $A_\mu = 0.1496 \pm 0.0140$ and $A_\tau = 0.1466 \pm 0.0062$. My results are consistent with that. Since SLD continues taking data at the Z^0 resonance and the uncertainties are dominated by statistics, I expect the uncertainty of the measurement (see figure 11.2) to reduce to ≈ 0.007 (for A_e) and ≈ 0.015 (for A_μ and A_τ). These estimates are based on 24,000 additional leptonic Z decays. (The 1996 data taking period lasting about 3 months produced about 50,000 hadronic Z decays, so I expect to find about 4,000 leptonic Z decays in this run. One more run is scheduled to last for an entire year.)

Future of A_1 Analysis

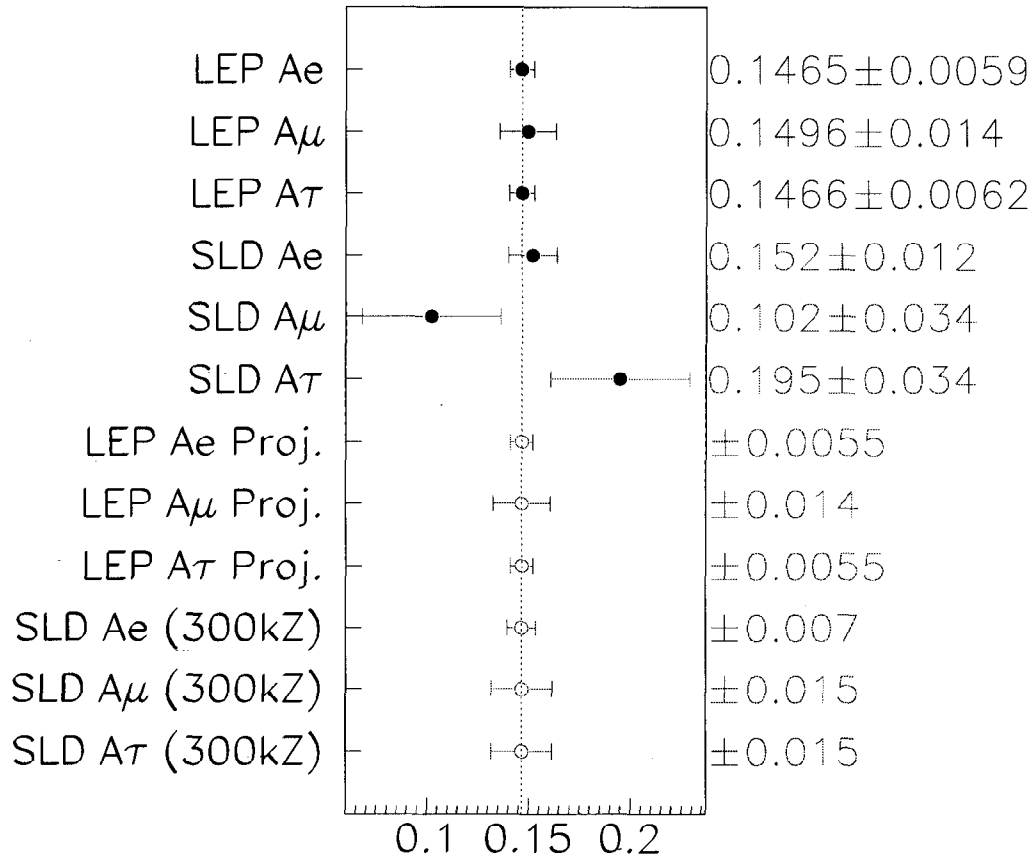


Figure 11.2: Future prospects of this analysis. Presently, the SLD's uncertainties on A_e and A_μ are comparable to a typical single LEP experiment. Since SLD continues to take data at the Z^0 resonance, its uncertainties will reduce considerably. In particular, the uncertainty of A_μ will be comparable to that of all four LEP experiments combined, if SLD collects 24,000 additional leptonic Z^0 decays. (corresponds to 300,000 hadronic Z^0 decays)

Bibliography

- [1] SLD Collaboration (K. Abe et al.) SLAC-PUB-7418
Submitted to Physical Review Letters (1997)
- [2] The LEP collaborations and the LEP electroweak working group, *A Combination of Preliminary Electroweak Measurements and Constraints on the Standard Model*
unpublished, see also *CERN-PPE/96-183*

Appendix A

The VXD3

Between the 1993 run and the 1994/95 run, SLD's pixel vertex detector was upgraded. While VXD2 achieved excellent tagging efficiencies and purities in heavy flavor physics, it had its limitations. VXD2 had 2.3 hits on the average in a region of solid angle $|\cos\theta| < 0.75$. The main motivation for an upgrade was to increase the covered solid angle and to increase the number of hits while reducing the amount of material. VXD3 has three completely overlapping layers. Its CCDs are longer than VXD2's and cover the solid angle up to $|\cos\theta| < 0.85$ with at least 3 hits. VXD3's single hit resolution is expected to be even higher than VXD2's.

A.1. VXD3 Geometry

An engineering drawing of VXD3 is shown in figure A.1. Like many other experiments, SLD relies on the GEANT program for an accurate Monte Carlo simulation.

A. THE VXD3

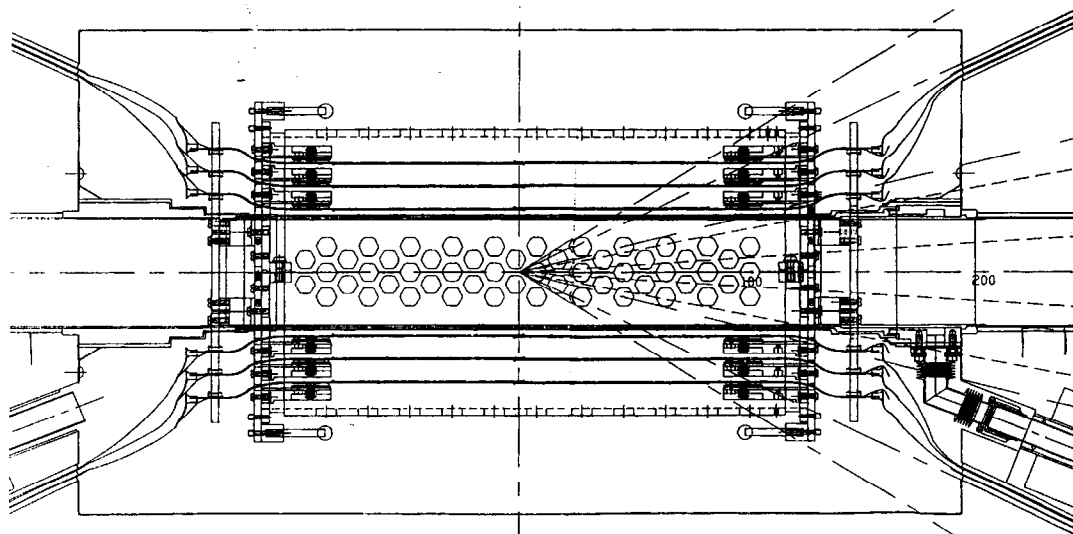


Figure A.1: VXD3 design geometry.

GEANT needs as input the amount of material in every part of the detector. For that reason, the detector is divided into regions of space, the 'GEANT volumes'. Each volume is filled homogeneously with a 'GEANT material'. A material is defined by specifying its density ρ , its effective atomic mass number A , its effective atomic charge number Z , its (electromagnetic) radiation length X_0 and its (nuclear) interaction length λ_0 . GEANT allows and encourages a hierarchical structure of volumes referred to as 'volume tree'. A 'daughter volume' replaces a section of the 'mother volume' material with its own. Daughter volumes have to be completely contained within their respective mother.

A. THE VXD3

A.1.1. The GEANT Volume Tree of VXD3

Obviously, it is not practical to incorporate every detail of the detector into GEANT, since GEANT's computation time increases with the complexity of the geometry. Therefore, material averages are computed when necessary. Still, it is necessary for the GEANT volume structure to resemble the design as closely as possible for a good detector simulation. The GEANT volume structure is shown in figures A.2 and A.3. All of the vertex detector resides in the logical GEANT domain 'SVTX'. (SLD's GEANT structure is divided in domains, one volume for each subsystem.) The tree is listed in table A.1 and A.2.

A.1.2. CCDs

VXD3 has three active, overlapping layers. Each layer contains a number of beryllium *ladders* which carry each 2 CCDs. Layer 1 has 12 ladders, layer 2 has 16 ladders and layer 3 has 20 ladders. The ladders lie parallel to the beam direction (z axis). On each ladder, there is a top (that is, larger radius) CCD covering the northern hemisphere of solid angle and a bottom (smaller radius) CCD which measures tracks in the southern hemisphere. The CCDs contain 4000×800 $20 \mu m \times 20 \mu m$ pixels each, so their active area has the dimension $8 \text{ cm} \times 1.6 \text{ cm}$. The CCD's active thickness is $20 \mu m$. The active areas of north and south CCD overlap by 1 mm in z . The CCD has the dimensions of $8.2400 \text{ cm} \times 1.6530 \text{ cm} \times 150 \mu m$. The two CCDs overlap

A. THE VXD3

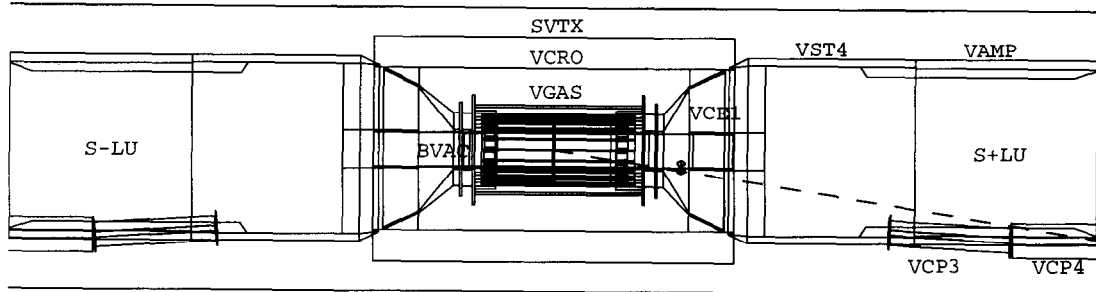


Figure A.2: VXD3 GEANT geometry in the xz plane.

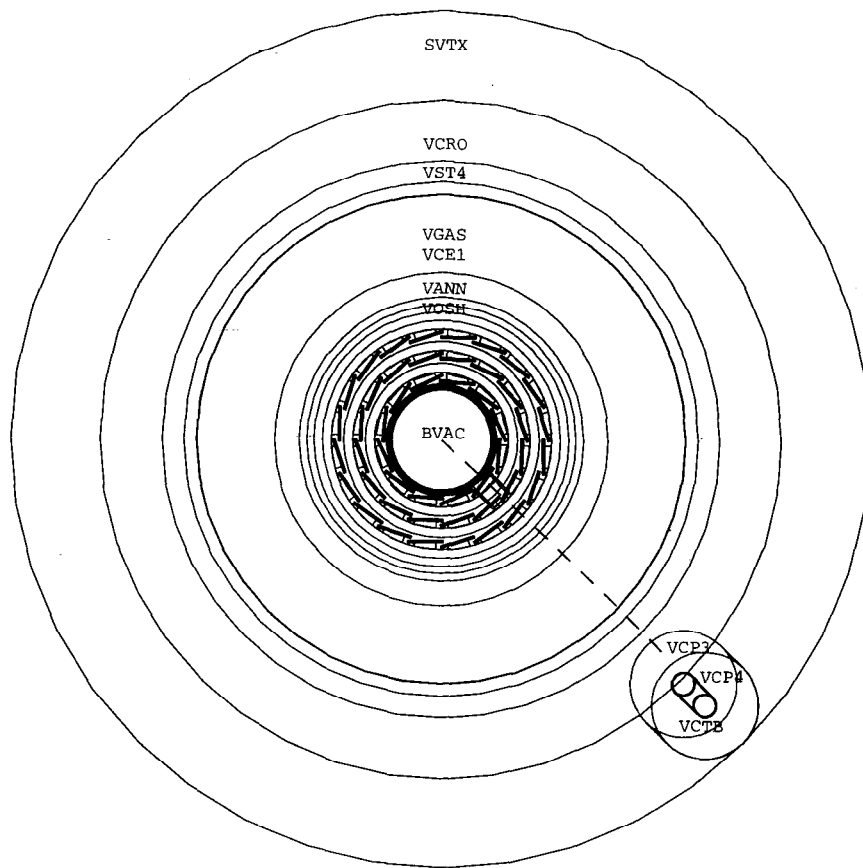


Figure A.3: VXD3 GEANT geometry in the xy plane. The beams move along the z axis.

A. THE VXD3

Name	Depth	Mother	Medium name
SVTX	0	SLD	AIR
VGAS	1	SVTX	N2AT180K
VBAR	2	VGAS	N2AT180K
VXL1	3	VBAR	N2AT180K (VXD3_LAY1_AVG)
VLM1	4	VXL1	N2AT180K
VLAD	5	VLM1	VXD3.LAD
VCBO	5	VLM1	VXD3.CAR
VSBO	5	VLM1	SILICON
VCCD	6	VSBO	SILICON
VCTP	5	VLM1	VXD3.CAR
VSTP	5	VLM1	SILICON
VLBK	4	VXL1	VXD3.MB.LADBLOCK
VXL2	3	VBAR	N2AT180K (VXD3_LAY2_AVG)
VXL3	3	VBAR	N2AT180K (VXD3_LAY3_AVG)
VARN	3	VBAR	VXD3_ANNULUS
VISH	2	VGAS	BERYLLIUM
VOSH	2	VGAS	VXD3_OUTER_SHELL
VANN	2	VGAS	VXD3_ENDPLATE
VCP1	2	VGAS	LIGHT_URETHANE
VCTB	3	VCP1	ALUMINUM
VMBC	2	VGAS	VXD3_MB_CONNECTOR
VST1	2	VGAS	VXD3_PIGTAIL
VST2	2	VGAS	VXD3_STRIPLINE
VSS1	2	VGAS	ALUMINUM

Table A.1: VXD3 GEANT volume tree 1.

A. THE VXD3

Name	Depth	Mother	Medium name
BVAC	1	SVTX	VACUUM
BPBE	2	BVAC	BERYLLIUM
BPLN	2	BVAC	TITANIUM
BPSS	2	BVAC	IRON
BSSO	1	SVTX	IRON
VCE1	1	SVTX	VXD_CRYOFOAM
VSTA	2	VCE1	VXD3_STRIPLINE
VCRO	1	SVTX	FLUFFY_URETHANE
VCP3	1	SVTX	LIGHT_URETHANE
VCP4	1	SVTX	LIGHT_URETHANE
VCP5	1	SVTX	LIGHT_URETHANE
VCIC	1	SVTX	ALUMINUM
VAMP	1	SVTX	VXD3_PREAMP
VST3	1	SVTX	VXD3_STRIPLINE
VST4	1	SVTX	VXD3_STRIPLINE

Table A.2: VXD3 GEANT volume tree 2.

by 1.7 mm. The CCDs rest on a flex circuit called the *chip carrier* which does the readout. A CCD is read out at all four corners (each corner reading a quadrant of the CCD). Near the northern (southern) end, the pixel size in the $r\phi$ direction is reduced continuously to 18μ , so the pixels there acquire a trapezoidal shape.

This geometry is reflected in GEANT in the following way. Each layer is contained in a (logical) volume filled with nitrogen gas at 170 K: VXL1, VXL2, VXL3. All three layers are contained in the logical volume VBAR (stands for *barrel*) that is also filled with nitrogen gas. VXL1, VXL2 and VXL3 have 12, 16 and 20 of (logical) volumes

A. THE VXD3

VLM1, VLM2 and VLM3 (LM stands for ladder mother volume) which are still filled with nitrogen gas. Each ladder mother volume contains the ladder VLAD (out of Beryllium), the top and bottom chip carriers (VCTP and VCBO) and the top and bottom silicon chip (VSTP and VSBO). The active part of the chip (VCCD) is a daughter volume to VSTP and VSBO and filled with silicon. The trapezoidal pixels are not reflected in the GEANT geometry.

A.1.3. Support structure

The ladders are hold on the north and the south end by the so-called ladder blocks, small pieces of plastic and Al_2O_3 which are supported by the six beryllium *annuli* (two for each layer). The annuli are screwed to the north and south *end plate* which is made of Beryllium again. The end plates rest on the beam pipe. Two beryllium cylinders connect the two end plates. The gas jacket (inner shell) has a radius that is smaller than that of layer 1 and the outer shell has a larger radius than layer 3.

This structure is reflected in the GEANT geometry as shown in figure A.4. The volume VGAS is filled with nitrogen gas and contains VBAR as well as the end plates (VANN), the inner shell (VISH) and the outer shell (VOSH). The annuli are part of VBAR and the ladder blocks (VBLK) are inside VXL1, VXL2 and VXL3, but outside of VLM1, VLM2 and VLM3. There are small gaps between the ladder blocks and annuli in GEANT, that is not present in the real geometry.

A. THE VXD3

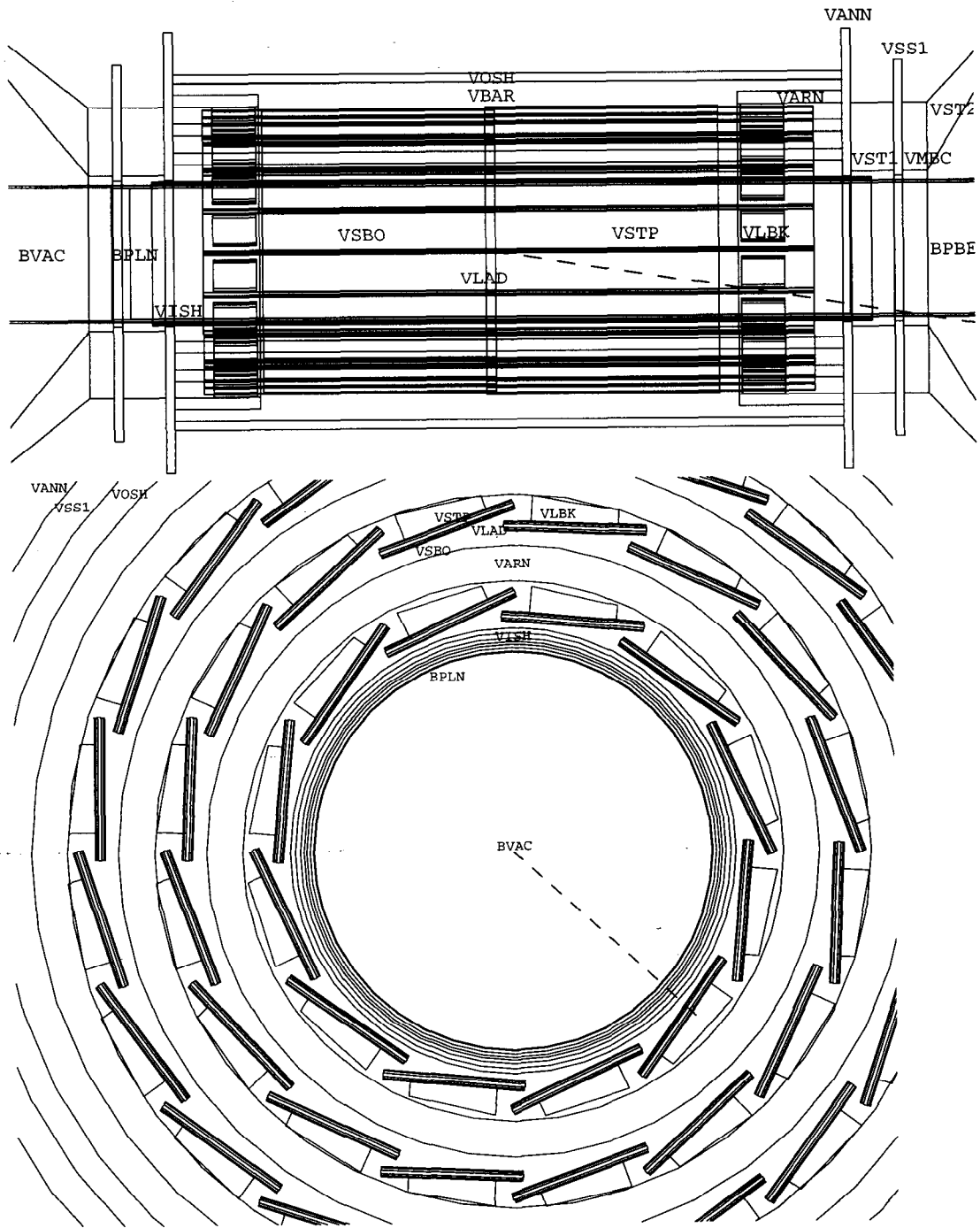


Figure A.4: Detailed VXD3 GEANT geometry.

A. THE VXD3

A.1.4. Beam pipe

The beam pipe has three regions. Near the interaction point it is made out of beryllium, further away it is made out of stainless steel. To improve the conductivity, the beryllium piece is lined with titanium. As shown in figure A.4 the GEANT geometry is the following. The beam pipe vacuum volume BVAC contains BPBE, the beryllium piece and BPSS, the stainless steel pieces as well as BPLN, the titanium liner. Outside the z interval occupied by BVAC, the stainless steel beam pipe is called BSSO.

A.1.5. Cryostat

The CCDs are cooled to limit the effects of radiation damage. Therefore VXD3 sits within a cryostat out of URETHANE. A pipe on the north ends supplies fresh cold nitrogen gas, a pipe on the south side acts as drain. The cryostat is coated with aluminum for electrical shielding. Figures A.5 and A.2 show the GEANT geometry of the cryostat. The cryostat pipes are split into 5 volumes VCP1 to VCP5 out of URETHANE that contain the tube aluminum tube VCTB. The barrel part of the cryostat is VCRO with the aluminum coating VCIC. The end pieces are called VCE1.

A. THE VXD3

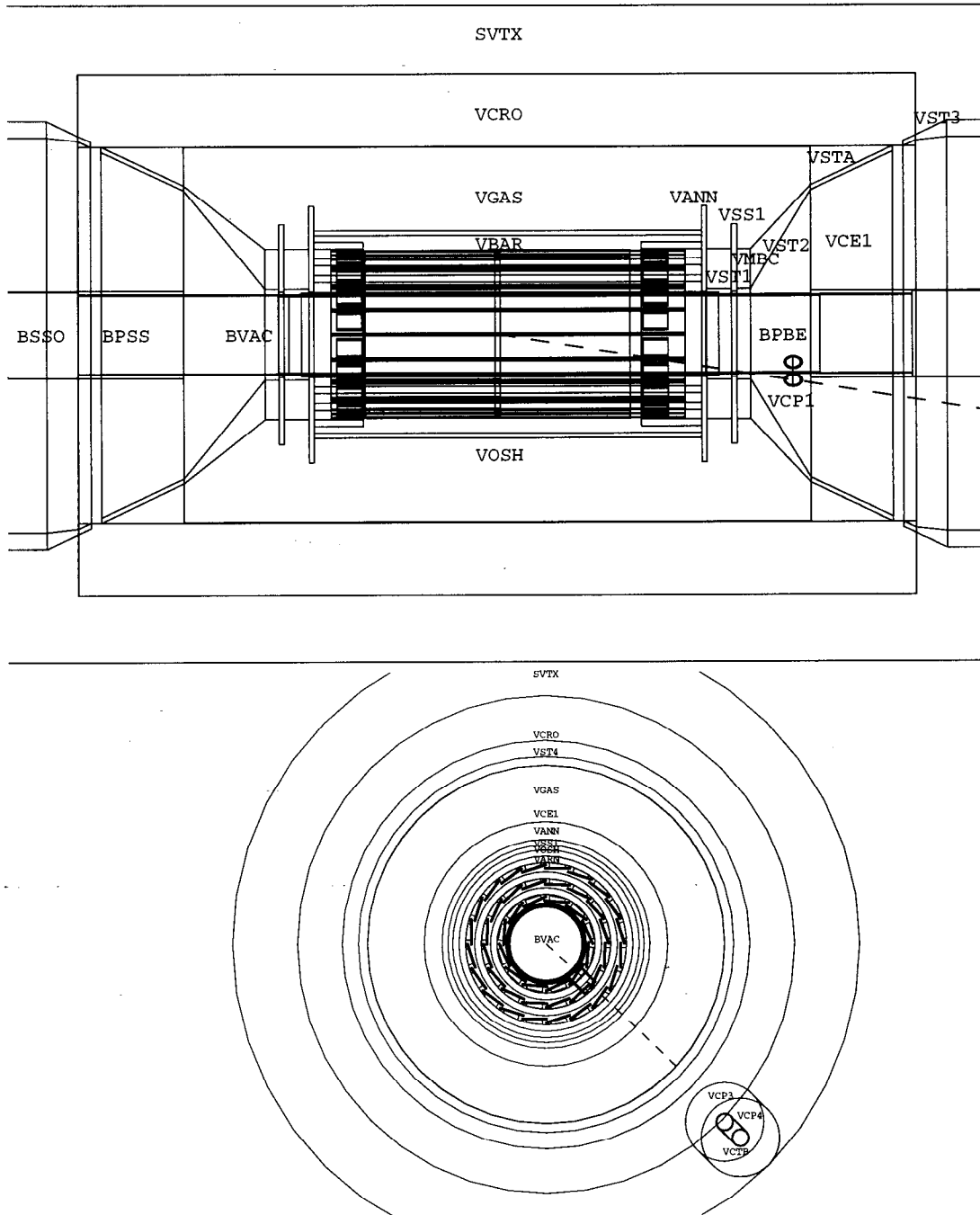


Figure A.5: VXD3 cryostat GEANT geometry.

A. THE VXD3

A.1.6. Cables and Electronics

The cables and electronics are implemented by means of material averages. VST1, VST2, VST3, VSTA and VST4 describe the cables (strip lines) and VSS1 and VMBC the support and the connectors. The electronics is implemented with VAMP. The geometry is shown in figures A.5 and A.2.

A.2. VXD3 Material in the GEANT simulation

SLD's GEANT description uses three types of materials: *Elements* are described by density, A , Z , X_0 and λ_0 . For all other material types these constants have to be calculated. Table A.3 lists all materials that are used for VXD3. *Compounds* are chemical bound states of elements and are defined by the molar weights n_i for their constituents and the density. Table A.5 lists all the compounds used for VXD3. *Mixtures* are used for volume averages when several elements/compounds occupy the same volume. They are convenient to simplify the design geometry. They are described by the volume percentage for each of the mixed elements or compounds. Table A.6 and A.7 lists all the mixtures used for VXD3.

A.2.1. SLD's element list

To calculate radiation and interaction lengths of materials, I look at a microscopic description. There the number of scattered particles N_{sc} from a target described by

A. THE VXD3

Element	Nr.	A in $\frac{g}{mol}$	Z	ρ in $\frac{g}{cm^3}$	X_0 in cm	λ_0 in cm
VACUUM	16	$100 \cdot 10^{-18}$	$100 \cdot 10^{-18}$	$100 \cdot 10^{-18}$	$10 \cdot 10^{15}$	$10 \cdot 10^{15}$
HYDROGEN	1	1.0100	1.0000	0.070800	865.00	790.00
BERYLLIUM	5	9.0100	4.0000	1.8480	35.300	36.700
CARBON	6	12.010	6.0000	2.2650	18.800	49.900
NITROGEN	7	14.010	7.0000	0.80800	44.500	99.400
N2AT180K	31	14.0100	7.0000	0.0019	19994.0	46211.0
AIR	15	14.610	7.3000	0.0012050	30423.0	67500.0
OXYGEN	17	16.000	8.0000	0.0014300	23944.0	63636.0
ALUMINUM	9	26.980	13.000	2.7000	8.9000	37.200
SILICON	21	28.090	14.000	2.3300	9.3600	45.490
SLCCD	32	28.090	14.000	2.3300	9.3600	45.493
TITANIUM	36	47.880	22.000	4.5400	3.5600	27.511
IRON	10	55.850	26.000	7.8700	1.7600	17.100
COPPER	11	63.540	29.000	8.9600	1.4300	14.800
SILVER	37	107.8682	47.000	10.5000	0.8543	15.077
G10	22	9.0000	6.0000	1.7000	19.400	53.100

Table A.3: List of VXD3's GEANT elements.

the cross section σ is given by

$$N_{sc} = \sigma * \frac{N_{incident}}{F}$$

where $N_{incident}$ is the number of incident particles in a beam and F is the beam's cross sectional area. Therefore, if N denotes the number of particles in the beam as

A. THE VXD3

a function of distance x then ($dN = -N_{sc}$ and $N_{incident} = N$)

$$d \log N = -\frac{\sigma}{F}$$

Macroscopically, in the volume Fdx there are $N_i * Fdx$ scattering targets (i.e. N_i is the density of targets of type i). Therefore

$$d \log N = -\sigma N_i dx$$

or

$$N(x) = e^{-\sigma N_i x} =:: e^{-\Sigma_i x} =:: e^{-\frac{x}{\lambda_i}}$$

λ is the interaction length of particles. If the targets i have the mass density ρ_i and the atomic mass A_i then

$$N_i = N_A * \frac{n}{Fdx} = N_A \frac{n}{m} \rho_i = N_A \frac{\rho_i}{A_i}$$

where n denotes the number of moles in Fdx . Therefore

$$\Sigma_i = N_A \sigma \frac{\rho_i}{A_i}$$

Since I could not find the interaction and radiation length of Silver in the literature

A. THE VXD3

I used Tsai's formula as quoted in the PDB [1] to calculate the radiation length. To use it I calculate

$$f(Z) = a^2((1 + a^2)^{-1} + 0.20206 - 0.0369a^2 + 0.0083a^4 - 0.002a^6),$$

$$L_{rad} = \log \left(\frac{184.15}{\sqrt[3]{Z}} \right),$$

$$L'_{rad} = \log \left(\frac{1194}{\sqrt[3]{Z^2}} \right)$$

For silver ($a^2 = (\alpha Z)^2 = 0.1176323$)

$$4\alpha r_e^2 \frac{N_A}{A} = 1.2940358 \cdot 10^{-5} \frac{cm^2}{g},$$

$$f(47) = 0.128523, L_{rad} = 3.9323681, L'_{rad} = 4.5182992,$$

From this, the radiation length can be calculated by Tsai's formula

$$\frac{1}{X_0} = 4\alpha r_e^2 \frac{N_A}{A} (Z^2(L_{rad} - f(Z)) + ZL'_{rad})$$

To get the nuclear interaction length, I approximated the nuclear inelastic cross section as $0.04993A^{2/3}barn$. This is optimized for heavy elements in the 'silver'-range. The value 0.04993 was obtained with a weighted average of the heavy elements (see table A.4. The weight was taken to be proportional to $A/\Delta A$. From this approxima-

A. THE VXD3

Element	Ti	Fe	Cu	Ge	Sn
σ/barn	0.637	0.703	0.782	0.858	1.21
appr./barn	0.658	0.729	0.795	0.869	1.206
deviation/%	+3.3	+3.7	+1.7	+1.3	-0.3
$100\sigma_{red}$	4.831	4.812	4.911	4.930	5.009
weight/%	5.213	6.012	7.056	8.870	31.746
Element	Xe	W	Pt	Pb	U
σ/barn	1.29	1.65	1.708	1.77	1.98
appr./barn	1.290	1.614	1.679	1.748	1.918
deviation/%	0.0	-2.2	-1.7	-1.2	-3.1
$100\sigma_{red}$	4.994	5.103	5.078	5.055	5.155
weight/%	16.252	7.016	6.485	6.048	5.302

Table A.4: Cross section comparison between the approximation formula and the interaction length for some heavy elements listed in PDB [1]. The value for $\sigma_{red} = \sigma A^{-2/3}$ is about constant. The weight for the weighted average is proportional to $A/\delta A$.

tion, I can calculate the interaction length of silver with

$$\lambda_{int} = \frac{A}{N_A \sigma}$$

A.2.2. SLD's chemical compound list

If the target is a (chemical) compound of different targets i , then

$$\Sigma = \sum_i \sigma(E, Z_i, A_i) N_i$$

A. THE VXD3

Compound	Nr	ρ in $\frac{g}{cm^3}$	Composition in mol			
URETHANE	17	0.0500	CARBON	1	HYDROGEN	1
			OXYGEN	2	NITROGEN	1
FLUFFY_URETHANE	20	0.0360	CARBON	1	HYDROGEN	1
			OXYGEN	2	NITROGEN	1
LIGHT_URETHANE	25	0.0320	CARBON	1	HYDROGEN	1
			OXYGEN	2	NITROGEN	1
VXD3_MB_LADBLOCK	24	5.1029	ALUMINUM	2	OXYGEN	3
KAPTON	21	1.4200	CARBON	2	OXYGEN	2
			NITROGEN	1	HYDROGEN	1
EPOXY	22	1.0000	CARBON	3	OXYGEN	2
			HYDROGEN	5		
ACRYLIC_GLUE	23	1.0500	CARBON	3	OXYGEN	2
			HYDROGEN	4		
SILVER_INK	26	3.5000	CARBON	3	HYDROGEN	4
			OXYGEN	2	SILVER	1.5588

Compound	Nr.	A in $\frac{g}{mol}$	Z	X_0 in cm	λ_0 in cm
URETHANE	54	14.459	7.2360	727.53	1815.2
FLUFFY_URETHANE	57	14.459	7.2360	1010.5	2521.1
LIGHT_URETHANE	62	14.459	7.2360	1136.8	2836.2
VXD3_MB_LADBLOCK	61	21.811	10.646	5.4781	18.766
KAPTON	58	14.045	7.0270	26.264	66.116
EPOXY	59	12.997	6.5302	39.223	96.067
ACRYLIC_GLUE	60	13.165	6.6077	37.168	92.421
SILVER_INK	63	79.455	34.881	3.3330	38.028

Table A.5: List of VXD3's GEANT compounds.

A. THE VXD3

where E is the beam energy and Z_i the charge of target i . If n_i describes the number of targets i per molecule and $n_i^{(0)}$ the number of moles in Fdx

$$\Sigma = N_A \sum_i \sigma(E, Z_i, A_i) \frac{n_i^{(0)}}{Fdx}$$

For a constant density ρ of all targets there is the relation

$$\rho = \sum_i n_i \frac{A_i}{V} = \sum_i n_i^{(0)} \frac{A_i}{Fdx}$$

where V is the molar volume. Also the relations

$$\frac{n_i}{V} = \frac{n_i^{(0)}}{Fdx}$$

hold and therefore

$$\begin{aligned} \Sigma &= N_A \sum_i \sigma(E, Z_i, A_i) \frac{n_i}{V} \\ \Sigma &= N_A \rho \frac{\sum_i n_i \sigma(E, Z_i, A_i)}{\sum_i n_i A_i} \end{aligned}$$

Defining the weight w_i with

$$w_i = \frac{n_i A_i}{\sum_i n_i A_i}$$

results in

$$\Sigma = N_A \rho \sum_i \frac{w_i}{A_i} \sigma(E, Z_i, A_i)$$

A. THE VXD3

The substitution

$$N_A \frac{\sigma(E, Z_i, A_i)}{A_i} = \frac{\Sigma_i}{\rho_i}$$

gives

$$\Sigma = \rho \sum_i w_i \frac{\Sigma_i}{\rho_i}$$

If the scattering process is dominated by the electromagnetic interaction, I can assume σ to be

$$\sigma(E, Z_i, A_i) = Z_i \sigma(E)$$

Therefore, I get

$$\Sigma = N_A \rho \sum_i \frac{w_i}{A_i} Z_i \sigma(E)$$

An effective A_{eff} and Z_{eff} should obey the relation

$$\Sigma = N_A \rho \frac{Z_{eff}}{A_{eff}} \sigma(E)$$

which results in

$$Z_{eff} = A_{eff} \sum_i \frac{w_i}{A_i} Z_i$$

For heavy elements, the nuclear interaction dominates and I can assume σ to be

$$\sigma(E, Z_i, A_i) = \left(\frac{A_i}{g/mol} \right)^{2/3} \sigma(E)$$

A. THE VXD3

Therefore, I get

$$\Sigma = N_{A\rho} \sum_i \frac{w_i}{\sqrt[3]{A_i}} \sigma(E) = N_{A\rho} \frac{\sigma(E)}{\sqrt[3]{A_i}}$$

which results in

$$A_{eff} = \frac{1}{\left(\sum_i \frac{w_i}{\sqrt[3]{A_i}}\right)^3}$$

and

$$Z_{eff} = \frac{\sum_i \frac{w_i}{A_i} Z_i}{\left(\sum_i \frac{w_i}{\sqrt[3]{A_i}}\right)^3}$$

Since GEANT uses only the interaction lengths (and not A and Z) SLD's GEANT simulation uses the more simple relations

$$A_{eff} = \sum_i w_i A_i \text{ and } Z_{eff} = \sum_i w_i Z_i$$

Three of the compounds are URETHANE with different densities. Their compositions are straight forward. I defined the compound VXD3_MB_LADBLOCK to describe the so-called *ladder block*, that connects each ladder with VXD3's support structure. The ladder block is a box with dimensions $0.303 \times 1.0160 \times 1.5240 \text{ cm}^3$, so the volume is 0.469 cm^3 . Because of GEANT volume overlaps, I had to chip off an edge of the box which changes the thickness from 0.303 to 0.1651 on one side. The volume is then $0.5(0.303 + 0.1651) \times 1.0160 \times 1.524 \text{ cm}^3$ or 0.362 cm^3 . Therefore, I increased the density of the material by a factor of 1.29. The ladder block consists

A. THE VXD3

mostly out of Al_2O_3 (I neglected screws and springs), which has a density of $3.965 \frac{g}{cm^3}$.

The compositions of the three glues are again straight forward. A problem arises for the compound SILVER_INK. This is the product CB028 Silver Conductor from DuPont Electronic Materials. The manufacturer refuses to disclose the chemical composition. However, he states, that 70% of the ink's mass is Silver, the rest solvent. The ink has a density of $3.5 \frac{g}{cm^3}$. I assume, that the solvent is like ACRYLIC_GLUE, that is 3 Carbon, 2 Oxygen and 4 Hydrogen. The molar weight is

$$A_s = 3A_C + 2A_O + 4A_H = 72.064 \frac{g}{mol}$$

The mass percentage is proportional to the mol percentage times the atomic/molar weight:

$$A_C \frac{3}{9+x} + A_O \frac{2}{9+x} + A_H \frac{4}{9+x} = \frac{A_s}{9+x} = \frac{0.3}{N}$$

and $A_{Ag}x/(9+x) = 0.7/N$. Dividing the equations gives $x = 0.7A_s/0.3A_{Ag} = 1.5588$.

(N turns out to be 0.04396, the mass percentage of Carbon in the ink is 15.00%, the one of oxygen 13.32%, the one of hydrogen 1.68%).

A. THE VXD3

Average	Nr	Composition	in	vol%	
VXD_CRYOFOAM	29	URETHANE	1.0	URETHANE	1.0
VXD3_LAD	20	BERYLLIUM	1.0	VXD3_CAR	0.0
VXD3_CAR	19	N2AT180K	10.0	KAPTON	1.5
		EPOXY	1.0	COPPER	0.28
		ACRYLIC_GLUE	1.0		
VXD3_ANNULUS	35	N2AT180K	1.0	BERYLLIUM	3.0839
VXD3_ENDPLATE	36	IRON	1.0	BERYLLIUM	23.47
VXD3_OUTER_SHELL	38	BERYLLIUM	2.0	N2AT180K	1.797
VXD3_MB_CONNECTORS	39	KAPTON	8.0	COPPER	0.7
		G10	16.0	N2AT180K	328.5
VXD3_PIGTAIL	37	KAPTON	3.0	COPPER	0.7
		N2AT180K	301.75		
VXD3_STRIPLINE	34	KAPTON	3.0	COPPER	0.7
		AIR	221.51	SILVER_INK	2.0
VXD3_PREAMP	40	SILVER	1.0	G10	30.6743
		AIR	240.8156		
VXD3_LAY1_AVG	21	SLCCD	0.05757	VXD3_CAR	0.03838
		VXD3_LAD	0.21744	N2AT180K	0.68661
VXD3_LAY2_AVG	22	SLCCD	0.06659	VXD3_CAR	0.04439
		VXD3_LAD	0.25149	N2AT180K	0.63752
VXD3_LAY3_AVG	23	SLCCD	0.07309	VXD3_CAR	0.04873
		VXD3_LAD	0.27604	N2AT180K	0.60214

Table A.6: Composition of VXD3's GEANT mixtures.

A. THE VXD3

Element	Nr.	Λ in $\frac{g}{mol}$	Z	ρ in $\frac{g}{cm^3}$	X_0 in cm	λ_0 in cm
VXD_CRYOFOAM	92	14.459	7.2360	0.050000	727.53	1815.2
VXD3_LAD	83	9.0100	4.0000	1.8480	35.300	36.700
VXD3_CAR	82	33.814	15.796	0.46745	45.314	229.57
VXD3_LAY1_AVG	84	14.433	6.8042	0.55521	75.805	135.64
VXD3_LAY2_AVG	85	14.433	6.8042	0.64188	65.572	117.32
VXD3_LAY3_AVG	86	14.434	6.8042	0.70434	59.758	106.91
VXD3_ANNULUS	98	9.0117	4.0010	1.3960	46.720	48.588
VXD3_ENDPLATE	99	16.204	7.3788	2.0941	19.845	35.058
VXD3_OUTER_SHELL	101	9.0146	4.0028	0.97430	66.911	69.625
VXD3_MB_CONNECTORS	102	17.855	9.4439	0.12870	215.99	740.89
VXD3_PIGTAIL	100	41.997	19.435	0.036357	493.60	3079.1
VXD3_STRIPLINE	97	57.219	25.729	0.078337	187.61	1529.6
VXD3_PREAMP	103	25.571	12.872	0.22990	99.026	423.12

Table A.7: List of VXD3's GEANT mixtures.

A.2.3. SLD's material mixture list

For material mixtures, the weights

$$w_i = \frac{n_i A_i}{\sum_i n_i A_i}$$

are mass fractions, so they can be replaced by

$$w_i = \frac{m_i}{M} = \frac{\rho_i V_i}{\sum_i \rho_i V_i}$$

A. THE VXD3

where M is the total mass of the mixture. The density ρ can be calculated by

$$\rho = \frac{\sum_i V_i \rho_i}{\sum_i V_i}$$

the relations mentioned before apply after that.

The mixtures VXD_CRYOFOAM and VXD3_LAD are trivial (they are in the list for historic reasons only; in the first design of VXD3, the ladders were out of beryllium oxide and no carrier was necessary) VXD3_CAR is the average to describe the flex circuit on which the CCD chips rest. This flex circuit is called the *chip carrier* and has a width of 1.6530 *cm*. It consists out of layers which are listed in table A.8. It has 0.5 *oz/ft*² = 0.01526 *g/cm*² of copper traces, which corresponds to a thickness ($\rho_{Cu} = 8.95 \text{g/cm}^3$) of 0.67 mill. There are 20 traces, which are 10 mills wide, and 5 traces of 5 mills thickness, so the fill factor is 225 *mill*/1.653 *cm* = 34%. There are 1.8498 mills of N2AT180K, 1.5 mills of KAPTON, 0.8 mills of EPOXY, 0.5 mill ACRYLIC_GLUE and 0.232 mill of copper, so both sides of the chip carrier together have a thickness of 9.7638 mill=248 μm , which is the thickness of the GEANT volume.

VXD3_ANNULUS is the material average for the *annuli*, the parts of the support structure that holds the ladder blocks. There are six of them, three on the south side and three on the north side. The annuli cover the radial spaces from 3.1423 *cm* to 3.5560 *cm*, 4.1537 *cm* to 4.5720 *cm* and 5.2583 *cm* to 5.5880 *cm*. I measured the length and the masses of the south annuli. Their length is 2.9972 *cm*. They

A. THE VXD3

Layer Nr.	Layer	Thickness	Material
1	CCD		Silicon
2	gap	1.8498 mill	Nitrogen
3	passivation	0.5 mill	Kapton
4	adhesive	0.4 mill	epoxy
5	traces	0.6712 mill	copper (fill factor 34%: 0.2320mill)
6	adhesive	0.4 mill	epoxy
7	isolation	1.0 mill	Kapton
8	adhesive	0.5 mill	acrylic glue
9	ladder		Beryllium

Table A.8: Layers of the chip carrier.

have the masses 36.4 g, 48.0 g and 57.8 g. The densities of the first two are close together, I decided to calculate the average density of the first two ($1.396 \frac{g}{cm^3}$) and adjust the third outer radius to 5.5682 cm. (The volumes are $\pi(r_1^2 - r_2^2)l$, that is $26.093 cm^3$, $34.368 cm^3$ and $41.400 cm^3$). This results in masses of 36.424 g, 47.976 g and 57.793 g. The density of Be is $1.848 \frac{g}{cm^3}$, the density of N2AT180K is $0.0019 \frac{g}{cm^3}$.

The density of a mixture can be calculated by

$$\rho = \frac{m_1 + m_2}{V_1 + V_2} = \rho_1 \frac{V_1}{V_1 + V_2} + \rho_2 \frac{V_2}{V_1 + V_2} = \rho_1 v_1 + \rho_2 v_2$$

where v_1 and v_2 are the volume percentages of the mixture: $v_1 + v_2 = 1$. Therefore I can calculate $v_1 = (\rho - \rho_2)/(\rho_1 - \rho_2) = 75.5\%$ (Be) and $v_2 = 24.5\%$ (N2AT180K) or 3.0839 volume parts Be and 1 part N2AT180K.

The annuli are supported by the two end plates. The material they consist of is

A. THE VXD3

called VXD3_ENDPLATE. An end plate has 88.4 g of Be and 16.04 g of steel. There is therefore 84.64 mass % of Be and 15.36 mass % of steel. The density of the mixture obeys the relation

$$\frac{1}{\rho} = \frac{V_1 + V_2}{m_1 + m_2} = \frac{\frac{m_1}{\rho_1} + \frac{m_2}{\rho_2}}{m_1 + m_2} = \frac{m_1}{m_1 + m_2} \frac{1}{\rho_1} + \frac{m_2}{m_1 + m_2} \frac{1}{\rho_2}$$

The density of the mixture is then ($\rho_1 = 1.848 \frac{g}{cm^3}$, $\rho_2 = 7.87 \frac{g}{cm^3}$) $\rho = 2.094 \frac{g}{cm^3}$ and the total volume $49.874 cm^3$. This gives a volume percentage of $v_1 = 95.9\%$ (Be) and $v_2 = 4.1\%$ (Iron) or 23.47 : 1 as the ratio of volumes. An end plate has a thickness of 0.3048 cm, an inner radius of 2.5908 cm and an outer radius of 7.4676 cm giving a volume of only $46.97 cm^3$, I therefore needed to increase the outer radius. An outer radius of 7.6679 cm gives the correct volume.

VXD3_OUTER_SHELL is the material of the outer cylinder that connects the two end plates. It is out of Beryllium and has hexagonal holes that cover 47.3% of the area. A hole is 0.312" high and varies in width from 0.18" to 0.36". It has therefore an area of 0.08424 square inch or $0.543 cm^2$. There are 11 + 11 rings of 36 holes each, so the total area is $430.438 cm^2$. Using the average radius of 6.128 cm and cylinder length of 23.622 cm, the cylinder area is $909.489 cm^2$.

The connectors that connect the chip carrier with the 'pig tails' is made out of VXD3_MB_CONNECTOR. These connectors have a Kapton backing of additional 5 mill, so there is 3 mill + 5 mill = 8 mill of Kapton. In addition there is 16 mill of G10.

A. THE VXD3

The amount of copper is assumed to be the same as for the strip lines (0.7 mill). With the densities of Kapton ($1.42 \frac{g}{cm^3}$), G10 ($1.7 \frac{g}{cm^3}$) and Copper ($7.87 \frac{g}{cm^3}$), the density of the mixture is $1.78417 \frac{g}{cm^3}$. In GEANT there is a cross sectional area of 59.730 cm^2 reserved for it ($r_1 = 5.1583 \text{ cm}$, $r_2 = 2.756 \text{ cm}$). One connector has the cross sectional area of $0.0254 \cdot 2.54 \times 0.531 \cdot 2.54 \text{ cm}^2 = 0.087 \text{ cm}^2$ and there are 48 of them, covering in total of 4.177 cm^2 or 7.0% of the total area. A proportion of 328.5 mills of N2AT180K will cover 93.0% of the total area.

VXD3_PIGTAIL is the material of the flex circuit that connects the chip carrier with the strip lines. The Kapton is 3 mill thick, there is 1.4 mill of Copper covering around 50% of the area. GEANT has a cross sectional area of 59.730 cm^2 for it ($r_1 = 5.1583 \text{ cm}$, $r_2 = 2.7560 \text{ cm}$). One connector has a cross sectional area of $0.0044 \cdot 2.54 \times 0.531 \cdot 2.54 \text{ cm}^2 = 0.0151 \text{ cm}^2$ and there are 48 of them, covering in total 0.724 cm^2 or 1.2% of the total area. A proportion of 301.75 mills of N2AT180K will cover 98.8% of the total area.

The strip lines, that go out to the pre-amplifiers are made out of VXD3_STRIPLINE. The composition is like the one of the 'pigtail', only there is a 2 mill thick coating of silver ink to shield them. The GEANT volume is a bit difficult to calculate, because it involves conic pieces. The volume of a hollow cone is

$$V = \pi \frac{h}{3} (r_2^2 + r_2 r_4 + r_4^2 - r_1^2 - r_1 r_3 - r_3^2)$$

A. THE VXD3

	r_2/cm	r_4/cm	r_1/cm	r_3/cm	length/cm	Volume/cm ³
VST2	5.1583	9.0338	2.7560	8.7163	4.2658	210.96094
VSTA	9.0338	12.1035	8.7163	11.7860	6.3500	131.86935
VST3	12.1035	13.0175	11.7860	12.0000	1.8907	97.34463
VST4	13.0175		12.0000		23.5093	1880.0435
total volume						2320.21843

Table A.9: Pieces of strip line implemented in GEANT.

where r_2, r_4 describe the outer cone and r_1, r_3 the inner one. GEANT has four pieces of strip lines listed in table A.9. There are 48 strip lines of dimensions $18.5 \cdot 2.54 \cdot 5/8 \times 2.54 \times 0.0064 \cdot 2.54 \text{ cm}^3$ with a total volume of 58.207 cm^3 or 2.5% of the GEANT volume. An air layer of 221.51 mill will cover 97.5% of the GEANT volume.

VXD3.PREAMP is used to describe the material of the electronics. The GEANT volume ($r_1 = 11.7475 \text{ cm}$, $r_2 = 13.0175 \text{ cm}$, length=25.4000 cm) is 2509.722 cm^3 . In reality, there are 8 boards of dimensions $9.161 \times 0.154 \times 25.4 \text{ cm} = 35.834 \text{ cm}^3$ with a measured mass of $2.5 \text{ oz} = 70.87 \text{ g}$ giving a density of $\rho = 1.978 \frac{\text{g}}{\text{cm}^3}$. I assume, that it consists out of Silver and G10 with densities ($\rho_1 = 10.5 \frac{\text{g}}{\text{cm}^3}$ and $\rho_2 = 1.7 \frac{\text{g}}{\text{cm}^3}$), therefore it contains 3.157vol% Silver or 30.67 parts G10 per Silver. There are also 8 trapezoidal shaped pieces with a volume of $0.136 \times 0.4967 \times (11.22 + 7.497)/2 \text{ cm}^3 = 0.632 \text{ cm}^3$. The volume of all pieces together is therefore 291.73 cm^3 or 11.6% of the GEANT volume. Adding 240.82 parts of air will cover 88.4% of the volume.

A. THE VXD3

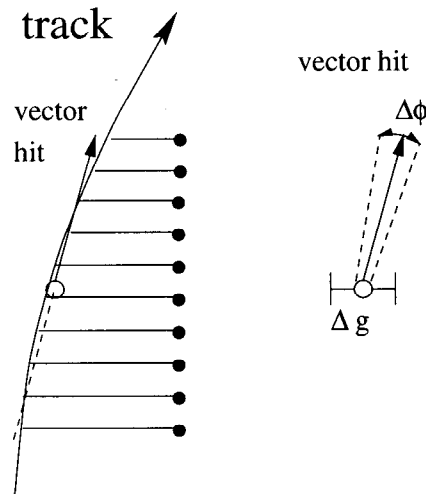


Figure A.6: Drift chamber vector hit in the xy plane. It is formed from a linear approximation of the track segment. It is assigned a position error Δg roughly perpendicular to its direction and a direction error $\Delta \phi$.

A.3. Pattern Recognition

The reconstruction of tracks with VXD3 is done differently than with VXD2. With VXD2 the reconstruction code began by forming vector hits from each (axial) drift cell. A vector hit (see figure A.6) is described by a position and direction. Then the pattern recognition code links the vector hits into reconstructed tracks. A Billoir fit to the hits of each wire is extrapolated into VXD2. Then we try to link the VXD2 hits to the track and do a combined fit which results in the reconstructed track.

While it was necessary to link VXD2 hits only after tracks are reconstructed by the drift chamber, the larger number of hits in VXD3 allows the formation of a vector hit of its own. The pattern recognition links all the vector hits (including the ones coming from VXD3) into tracks. Finally, the Billoir fit to all hits is done. Since

A. THE VXD3

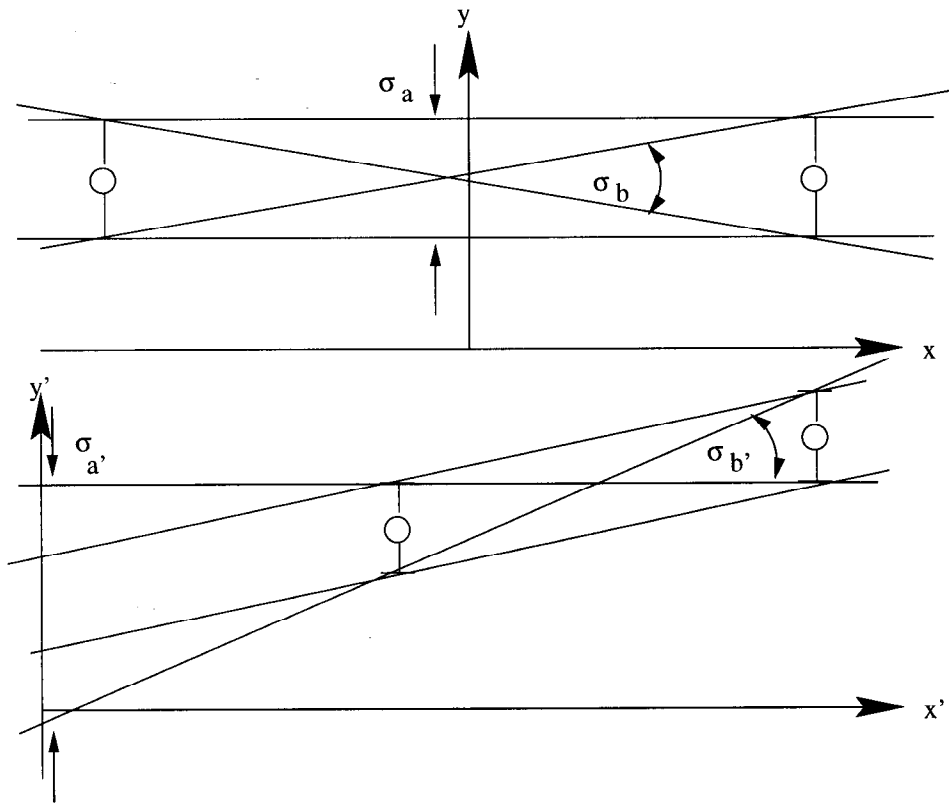


Figure A.7: VXD vector hit in different coordinate systems. If we describe the vector hit by $y=a+bx$, then the error in a will correspond to Δg and the error in b to $\Delta\phi$ only if the vector hit is described in a centered coordinate system.

VXD3 gives x , y and z information for each hit with equal precision, it would be possible to form a three dimensional vector hit. However, for compatibility with the old pattern recognition code, we form vector hits in the xy plane and include the z information later. Figure A.7 shows that the vector hit is best described in a local coordinate system centered around the vector hit. Figure A.8 shows the coordinate system chosen to describe the vector hit: SLD's coordinate system is rotated and its origin shifted.

A. THE VXD3

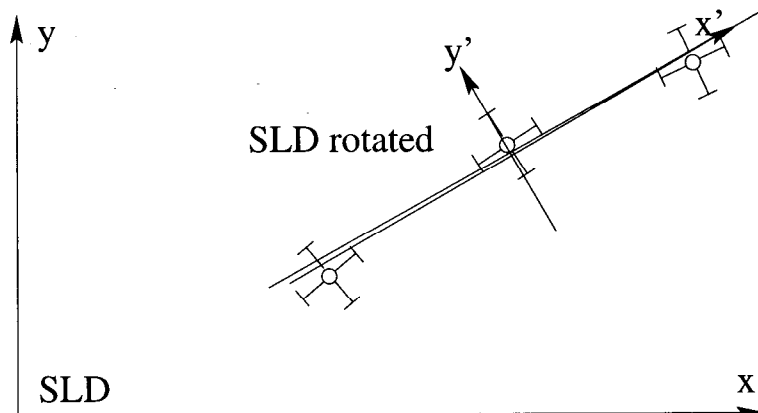


Figure A.8: Coordinate system for VXD vector hit. SLD's coordinate system is rotated by the average ϕ angle of the hits and its origin is shifted to the average r distance.

In addition to the line fit in the $r(r\phi)$ plane, we fit for another line in the rz plane. This gives the dip angle of the vector hit (and therefore the track) and supplies it with a z position. For the drift chamber vector hits, the z information is obtained from charge division and stereo layer hits.

A.4. Reconstruction Efficiency

To investigate effects like radiation damage, it is interesting to look at the reconstruction efficiency for each layer (CCD). To measure this efficiency, reconstructed tracks with at least two VXD hits are used. A CCD that should be intersected by that track and did not produce a hit is recorded as inefficiency. Figure A.9 shows the efficiency as a function of polar angle for each layer in the north and the south part of the detector.

A. THE VXD3

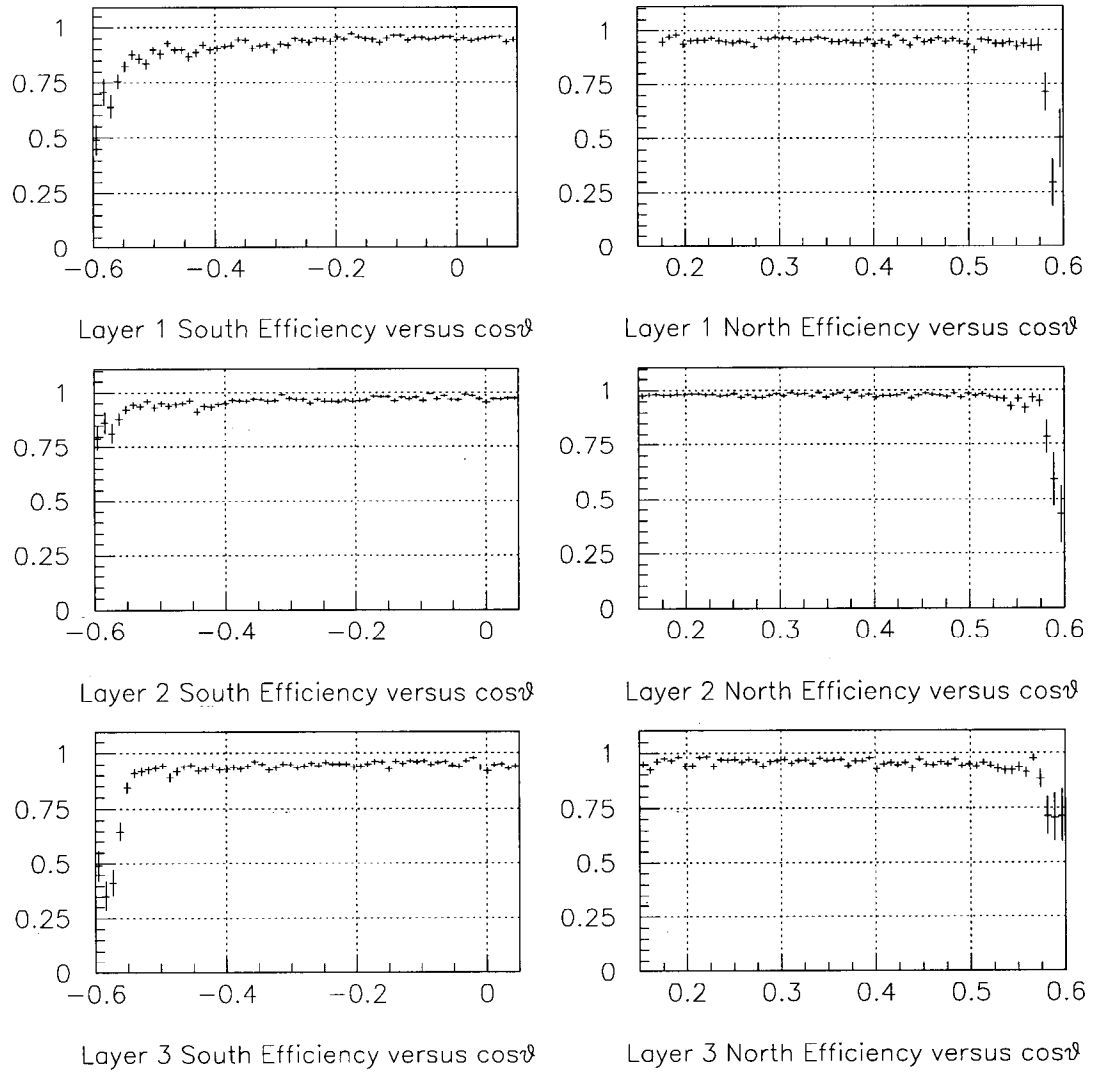


Figure A.9: Reconstruction efficiency for VXD3 as a function of polar angle. The southern part shows a reduced efficiency especially in the inner layers. This is probably due to radiation damage.